Design and setup of the Tritium Adsorption Desorption Experiment (TRIADE)

Diplomarbeit

von

Fabian Lukas Schneck

bei Prof. Dr. Guido Drexlin
Institut für Experimentelle Kernphysik, Fakultät für Physik,
Karlsruher Institut für Technologie

Korreferent Prof. Dr. Ulrich Husemann
Institut für Experimentelle Kernphysik, Fakultät für Physik,
Karlsruher Institut für Technologie

FAKULTÄT FÜR PHYSIK

KARLSRUHER INSTITUT FÜR TECHNOLOGIE

ABGABE: 6. FEBRUAR 2013
STAND: MAI 2013

Erklärung

Hiermit versichere ich, die vorliegende Arbeit selbständig angefertigt, alle dem Wortlaut oder Sinn nach entnommenene Inhalte anderer Werke an den entsprechenden Stellen unter Angabe der Quellen kenntlich gemacht, die Satzung des KIT zur Sicherung guter wissenschaftlicher Praxis beachtet und keine weiteren Hilfsmittel verwendet zu haben.

Fabian Lukas Schneck
Karlsruhe, den 06. Februar 2013

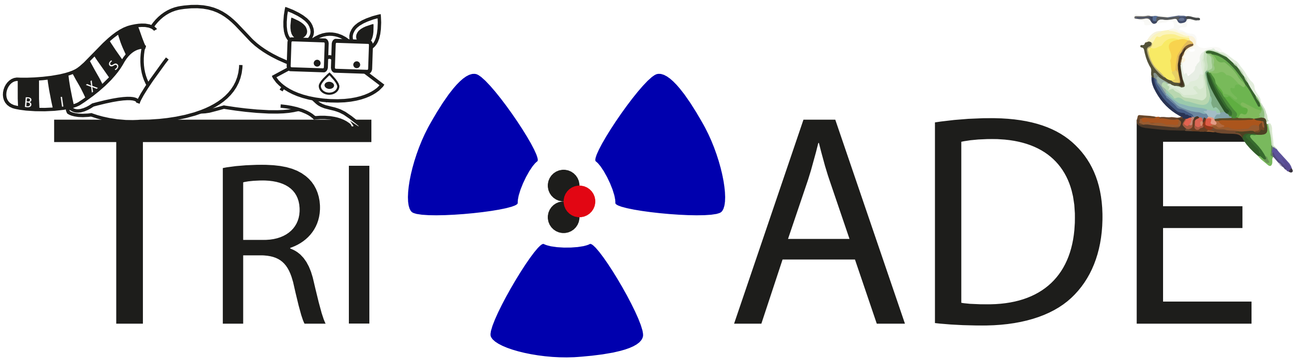

Tritium Adsorption Desorption Experiment

Deutsche Zusammenfassung

Tritium steht am Tritiumlabor Karlsruhe (TLK) aus zwei Gründen im Fokus wissenschaftlichen Interesses. Ein Grund ist die mögliche Verwendung von Tritium in zukünftigen Fusionskraftwerken, die in einigen Jahrzehnten einen Beitrag zur sicheren und nachhaltigen Energieversorgung beitragen könnten [Gam09]. Zum anderen ist Tritium aufgrund seiner Eigenschaften als β-Emitter die beste Wahl für die modellunabhängige Messung der Neutrinomasse [Alt03]. Tritium ist mit zwei Neutronen und einem Proton im Kern das schwerste Wasserstoffisotop und zerfällt in Helium-3, ein Elektron und ein Elektron-Antineutrino. Die Zerfallsenergie beträgt 18,6 keV.

Das TLK wurde am Karlsruher Institut für Technologie[1] als zentrale Einrichtung zur Entwicklung eines geschlossenen Brennstoffkreislaufes für Fusionskraftwerke im Rahmen des europäischen Fusionstechnologieprogramms geplant [Sch91]. Forschung und Entwicklung auf dem Gebiet der Fusionstechnologie waren und sind wichtige Aufgaben des TLK. Des Weiteren stellt das TLK die Tritiuminfrastruktur für das Karlsruhe Tritium Neutrino Experiments (KATRIN). Entwicklung und Aufbau der tritiumführenden Komponenten von KATRIN sind die zweite wichtige Aufgabe des TLK. Das KATRIN Experiment hat das Ziel, die Neutrinomasse $m_{\bar{\nu}}$ mit einer Sensitivität von $0.2\ \text{eV}/c^2$ zu bestimmen [KAT05]. Sowohl in der Fusionstechnologie, als auch im Kontext von KATRIN ist die Adsorption von Tritium von Bedeutung.

Die Akkumulation von Atomen oder Molekülen eines Gases an der Oberfläche eines Festkörpers bezeichnet man als Adsorption. Diese tritt auch bei gasförmigem Tritium auf, welches auf vielen Oberflächen, die in der Tritiumtechnologie vorkommen, adsorbieren kann. Aus folgenden Gründen ist es dabei wichtig, die Tritiummenge abschätzen zu können, die unter definierten Bedingungen auf bestimmten Materialien adsorbiert, und zu verstehen, wie sich Tritiumadsorption unter verschiedenen Bedingungen verhält:

- Adsorbiertes Tritium steht als Gas für den Prozess nicht mehr zur Verfügung.
- Adsorbiertes Tritium kann im Material gelöst werden und durch es hindurch diffundieren. Dies muss zum Beispiel beim Design der Kühlsysteme von „Breeder Blankets“ in Fusionsreaktoren berücksichtigt werden.
- Die Bauteile, auf denen Tritium adsorbiert ist, sind kontaminiert und müssen nach ihrer Verwendung aufwändig entsorgt werden.
- Aus Gründen der Prozessüberwachung und -steuerung ist eine akkurate Bilanzierung der Tritiummenge in der Tritiumtechnologie unerlässlich. Darüber hinaus ist sie auch aus rechtlicher Sicht obligat. Durch Adsorption in einem System gebundenes Tritium muss dabei berücksichtigt werden.

---

[1] damals noch Kernforschungszentrum Karlsruhe

Für das KATRIN Experiment gibt es wichtige, speziellere Fragestellungen in Bezug auf Tritiumadsorption. Diese sind die wichtigste Motivation für diese Arbeit, deshalb werden im Folgenden KATRIN und die entsprechenden Fragestellungen näher beschrieben:

Neutrinos sind ungeladene Leptonen, deren Masse im Standardmodell der Elementarteilchenphysik freie Parameter darstellen, welche dort auf Null gesetzt werden. Experimentell wurden jedoch Flavoroszillationen beobachtet, die nicht mit masselosen Neutrinos vereinbar sind. Bis heute konnten nur Obergrenzen für die Masse der Neutrinos bestimmt werden. Neutrinos sind nur sehr schwer nachzuweisen, da sie nur über die schwache Wechselwirkung interagieren. Die heute gültige Obergrenze der Neutrinomasse von 2.05 eV/c^2(95%C.L.) wurde aus der Untersuchung der Kinematik des β-Zerfalls von Tritium bestimmt [Ase11].

Die Bestimmung der Neutrinomasse aus dem Betaspektrum basiert auf der Energieerhaltung. Die Energie, die zur Erzeugung eines massiven Neutrinos beim Zerfall eines Tritiumatoms (vgl. Gleichung 1.2) benötigt wird, steht für die anderen beteiligten Teilchen nicht zur Verfügung. Der Einfluss dieser Tatsache auf das Betaspektrum ist in Abbildung 1.1 dargestellt.

Die Bestimmung der Neutrinomasse in KATRIN geschieht durch die hochpräzise Vermessung des Betaspektrums von Tritium, basierend auf der MAC-E Filter[2] Methode. Die Zerfallselektronen werden von einem Magnetfeld adiabatisch in Richtung des Detektors geleitet und müssen dabei ein elektrostatisches Retardierungspotential überwinden (dargestellt in Abbildung 1.2). Elektronen, deren kinetische Energie ausreicht, können das Retardierungspotential überwinden und werden im Detektorsystem registriert. Elektronen, deren kinetische Energie nicht ausreicht, werden vom Retardierungspotential reflektiert. Der Aufbau wirkt demnach wie ein Hochpassfilter. Für eine Messung wird das Retardierungspotential variiert und dabei die Zählrate am Detektor gemessen. Hiermit lässt sich ein integrales Spektrum bestimmen [KAT05].

Die präzise Vermessung des Betaspektrums mit Hilfe des MAC-E Filters erfordert ein wohldefiniertes und zeitlich konstantes Potential der Tritiumquelle. Das Potential des Plasmas in der gasförmigen Tritiumquelle (WGTS) von KATRIN wird im Wesentlichen durch den Abschluss des Strahlrohrs auf der Quellseite, der „Rear Wall“ definiert. Tritiumadsorption auf der Rear Wall verändert deren Oberflächenpotential, was zu systematischen Effekten bei der Bestimmung der Neutrinomasse führen kann [KAT12].

Weiterhin ist es für die präzise Vermessung des Betaspektrums wichtig, dass die Aktivität in der Quelle genau bekannt ist. Diese wird beim KATRIN Experiment unter anderem durch β-induzierte Röntgenspektroskopie (BIXS) bestimmt [KAT12]. Dies ist auch die wichtigste Messmethode im TRIADE Experiment, weshalb sie weiter unten näher erläutert wird. Die verwendeten Detektoren werden mit goldbeschichteten Berylliumfenstern vor direkter Kontamination durch Tritium geschützt. Die Adsorption von Tritium auf diesen Fenstern kann das Signal-zu-Untergrund-Verhältnis so weit senken, dass die Aktivitätsüberwachung auf dem 0,1%-Level nicht mehr möglich ist. Deshalb muss die zu erwartende Menge Tritium auf diesen Fenstern bekannt sein. Die Rear Wall und die Fenster der BIXS-Detektoren sind im Modell in Abbildung 1 dargestellt.

Um die Tritiumadsorption auf den genannten Oberflächen messen zu können, wurde das TRItium Adsorption Desorption Experiment (TRIADE) entwickelt und aufgebaut. Es wird in der Lage sein, die Tritiummenge zu messen, welche unter kontrollierbaren

---

[2] Magnetic adiabatic collimation combined with an electrostatic filter

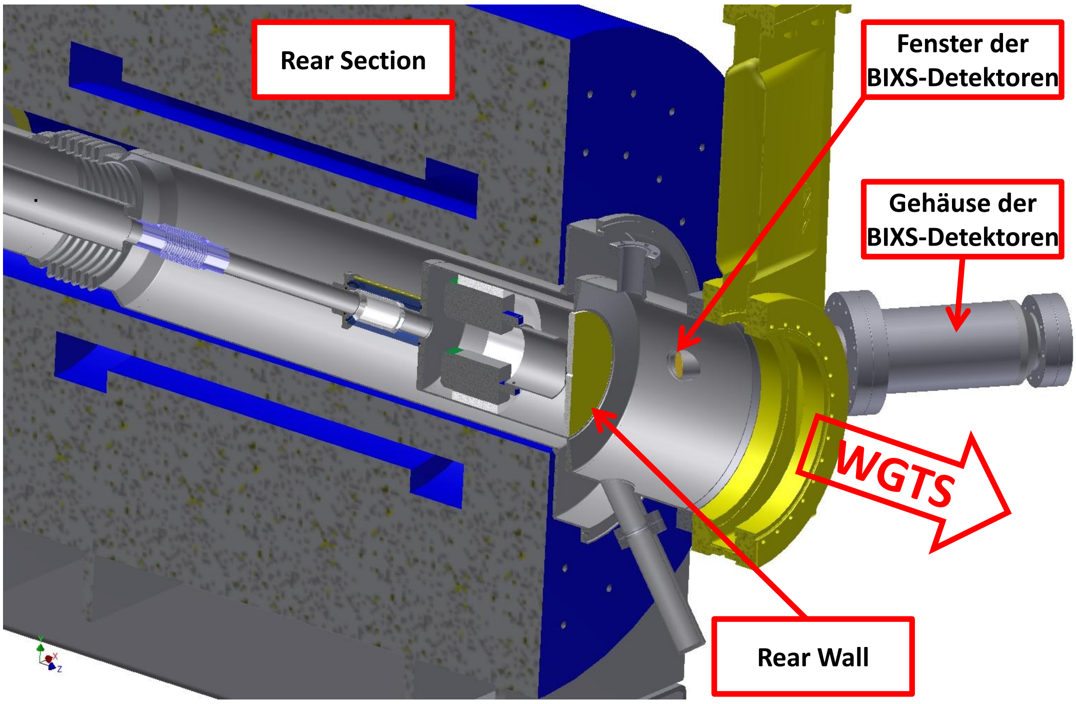

Abbildung 1: KATRIN Rear Section. Zu sehen ist ein Schnitt durch das CAD-Modell der KATRIN Rear Section. Adsorption von Tritium auf den Oberflächen der Rear Wall und der Fenster der BIXS-Detektoren spielt eine besondere Rolle für das KATRIN Experiment, wie im Text näher beschrieben wird. Die Rear Section ist über das Schieberventil (gelb) direkt mit der fensterlosen gasförmigen Tritiumquelle (WGTS) von KATRIN verbunden. Die Rear Wall bildet den Abschluss des Strahlrohres auf der Quellseite.

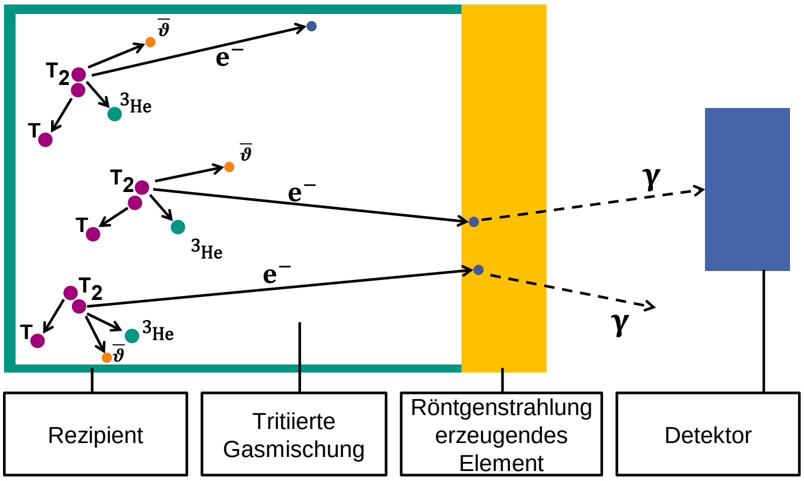

Abbildung 2: Vereinfachtes BIXS-Schema. Die Schemazeichnung verdeutlicht das Prinzip der β-induzierten Röntgenspektroskopie. Zerfallselektronen produzieren in einem Röntgenstrahlung erzeugenden Element Bremsstrahlung, die mit einem Detektor nachgewiesen werden kann. Von der Detektorzählrate lässt sich auf die Aktivität im Rezipienten schließen.

Bedingungen auf einer beliebigen Probe[3] adsorbiert. Dabei wurde eine Nachweisgrenze unter einer Monolage adsorbierten Tritiums angestrebt.

Das TRIADE Experiment verwendet β-induzierte Röntgenspektroskopie als zentrale Messmethode. Das Prinzip ist in Abbildung 2 dargestellt. Zerfallselektronen erzeugen in einem Röntgenstrahlung erzeugenden Element Bremsstrahlung. Ein Teil dieser Bremsstrahlung wird von einem Detektor registriert. Von der Detektorzählrate lässt sich auf die Aktivität schließen, welche im Rezipienten vorhanden ist.

Durch Berücksichtigung der Beiträge zur Detektorzählrate, die durch unterschiedliche Prozesse zustande kommen, kann aus der Zählrate auf die Aktivität in einem Adsorbat und damit auch auf die darin vorhandene Tritiummenge geschlossen werden. Der entsprechende Aufbau des TRIADE Experiments ist in Abbildung 4.3 schematisch dargestellt. Das Modell der Kernkomponenten ist in Abbildung 3 zu sehen. Um aus der Detektorzählrate die Aktivität auf der Probenoberfläche bestimmen zu können, wurde das TRIADE Experiment mit folgenden konstruktiven Merkmalen ausgestattet:

- Maximierung der Probenoberfläche und Beschränkung des Sichtfeldes des Detektors auf die Probenoberfläche,
- Beschichtung aller Oberflächen im Rezipienten mit Gold, wodurch die Adsorption von Tritium auf diesen Oberflächen und ein daraus resultierendes Untergrundsignal minimiert werden soll,
- Ausstattung mit einem ausheizbaren Vakuumsystem, das den Druck im Rezipienten auf $P < 10^9$ mbar reduzieren kann,
- Verwendung eines rauscharmen Siliziumdriftdetektors.

---

[3] Die Probe muss lediglich als vakuumtaugliche Scheibe mit einem Durchmesser von 70 mm und einer Dicke von 1 mm vorliegen.

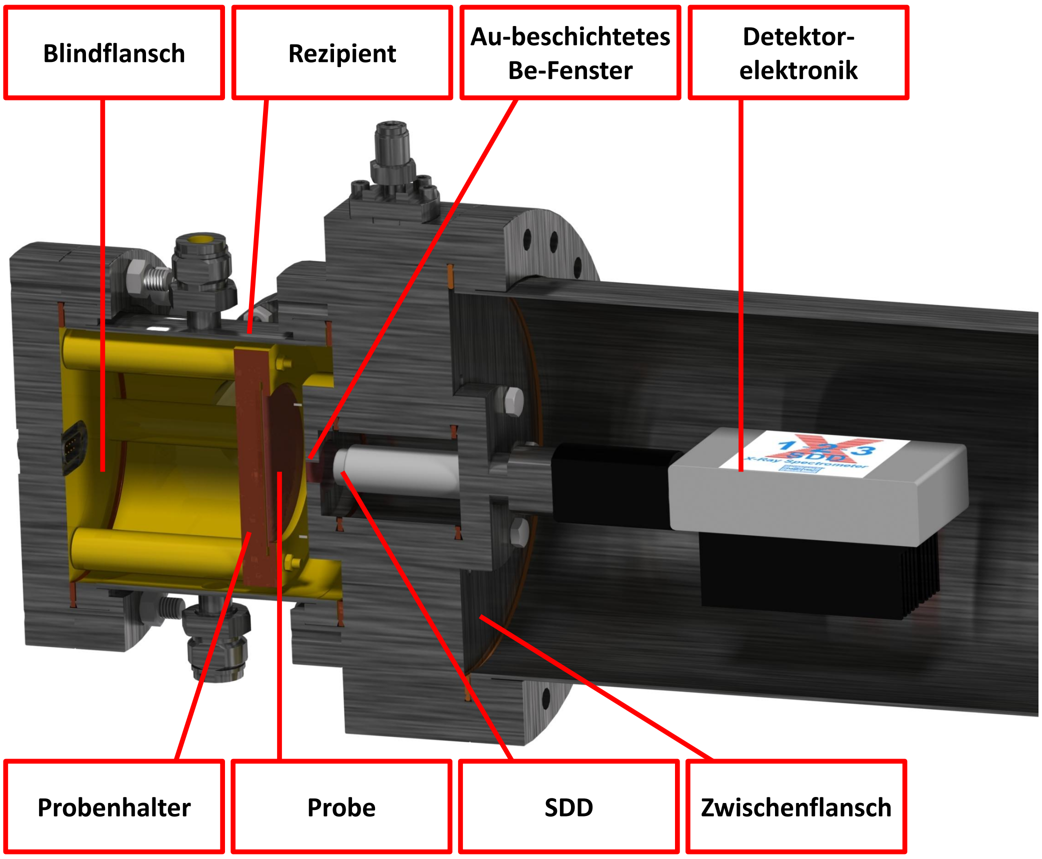

Abbildung 3: Kernkomponenten des TRIADE Aufbaus. Zu sehen ist der von innen vollständig mit Gold beschichtete Rezipient mit Probenhalter und Probe. Der Detektor (SDD) befindet sich in einem eigenen Volumen im so genannten Zwischenflansch, die Detektorelektronik ist in einem weiteren Volumen untergebracht.

Um die Aktivität auf einer Probenoberfläche bestimmen zu können, wurde mit Hilfe von Monte-Carlo-Simulationen bestimmt, mit welcher Effizienz die Zerfälle auf der Probenoberfläche messbare Ereignisse im Detektor erzeugen. Des Weiteren wurden die zu erwartenden Beiträge von zwei Untergrundquellen bestimmt (Tritium im Restgas und Tritium, welches auf dem Berylliumfenster adsorbiert). Die ermittelte Nachweisgrenze aus diesen Simulationen beträgt 0,1 Monolagen absorbiertes Tritium.

Das TRIADE Experiment wurde so geplant, dass es in der Lage ist, Tritiumadsorption in einem Probentemperaturbereich von ca. -100°C bis ca. 200°C zu untersuchen. Die Temperierung der Probe erfolgt über die Temperierung des Blindflansches, auf dem der Probenhalter montiert ist. Zur Optimierung der Wärmeleitung wurde die Probenhalterung aus Kupfer gefertigt. Die Temperierung des Blindflansches erfolgt mit Hilfe einer Heizmanschette, beziehungsweise über einen Wärmetauscher, welcher von Kühlgas durchströmt wird. Das Konzept wurde in zwei Testexperimenten verifiziert. Der Wärmetauscher zur Kühlung des Blindflansches wurde eigens entwickelt und gefertigt. Das Kühlgas wird von einer Kaltgasanlage durch Verdampfen von flüssigem Stickstoff zur Verfügung gestellt.

Mit dem Vakuumsystem von TRIADE ist es möglich, im Rezipienten einen Druck im Bereich von ca. 10^{-9} mbar bis zu 800 mbar einzustellen. Der Aufbau beinhaltet des Weiteren ein Quadrupol-Massenspektrometer, das zur Analyse von Gasgemischen im Rezipienten eingesetzt werden kann. Damit verfügt das Experiment zudem grundsätzlich über alle Komponenten zur Durchführung von Thermodesorptionsspektroskopie-Messungen (TDS). Da der Aufbau nicht für TDS, sondern für die Messung mit BIXS optimiert ist, werden Testmessungen zeigen müssen, welche Aussagekraft diese Messungen mit TRIADE haben können. Im Rahmen dieser Arbeit wurde eine vorbereitende Literaturrecherche für die Auswertung von TDS-Spektren durchgeführt.

Innerhalb dieser Arbeit wurde das TRIADE Experiment vollständig geplant und aufgebaut. Die Inbetriebnahme des Experiments wurde bis zur Fertigstellung dieser Arbeit weitgehend abgeschlossen. Die Betriebsparameter des verwendeten Detektors wurden optimiert und es wurde eine Energiekalibrierung durchgeführt. Die Verbindungen des Vakuumsystems wurden auf Lecks getestet. Alle Verbindungen erfüllen die Anforderung einer Leckrate $< 10^{-9}$ mbar·l/s. Derzeit wurden noch Untergrundmessungen mit dem Detektor durchgeführt. Nach dem Schließen der Handschuhbox, in dem das Experiment aufgebaut wurde, können erste Experimente mit Tritium beginnen.

Erste Proben wurden für Messungen vorbereitet (vgl. Abbildung 7.1). Das Experiment wird voraussichtlich im März 2013 damit beginnen, die Fragestellungen bezüglich Tritiumadsorption, die für KATRIN relevant sind, zu untersuchen. Im Anschluss steht das Experiment für Untersuchungen von Materialen, die an anderer Stelle in der Tritiumtechnologie interessant sind, zur Verfügung.

Für ausführlichere Angaben und entsprechende Literaturverweise sei auf den (englischen) Haupttext verwiesen. Die Arbeit ist in 7 Kapitel aufgeteilt. Kapitel 1 motiviert zunächst das Interesse an Tritiumadsorption im Kontext von KATRIN und Fusionstechnologie. In Kapitel 2 werden die Grundlagen von Adsorption und Desorption, sowie ihre experimentelle Untersuchung erläutert. Des Weiteren wird ein Überblick über Literaturdaten zur Adsorption von Wasserstoff und Tritium gegeben. Das Kapitel schließt mit den Fragestellungen, die im Rahmen des TRIADE Experiments beantwortet werden sollen. In Kapitel 3 werden die physikalischen Grundlagen der β-induzierten Röntgenspektroskopie erläutert. In Kapitel 4 wird der experimentelle Aufbau des Experiments beschrieben. Die Inbetriebnahme des Experiments und die durchgeführten Testmessungen werden in Kapitel 5 beschrieben, die durchgeführten Simulationen und ihre Ergebnisse werden in Kapitel 6 präsentiert. In Kapitel 7 wird die vorliegende Arbeit zusammengefasst und es wird ein Ausblick auf das geplante weitere Vorgehen gegeben. Im Anhang finden sich alle wichtigen Datenblätter, Zeichnungen und Konfigurationsdaten.

Abbildung 4: Das TRIADE Experiment. Das Bild zeigt die wichtigsten Komponenten des TRIADE Experiments. Folgende Komponenten sind abgebildet: (1) Rezipient, (2) Zwischenflansch, (3) Detektorelektronikvolumen,(4) Volumen des Massenspektrometers, (5) Leybold SL80 Turbomolekularpumpe, (6) Druckinstrumentierung und (7) Divac 0.8T Vakuumpumpen. Im unteren Teil der Handschuhbox, der nicht abgebildet ist, befindet sich Infrastruktur, wie weitere Pumpen und ein Pufferbehälter. Abbildung B.2 zeigt die gesamte Handschuhbox.

Contents

List of Figures

List of Tables

Chapter 1

Introduction: Adsorption and desorption in tritium technology

Tritium is in the focus of scientific interest for mainly two reasons[4]. The first reason is that tritium can be used for the determination of the neutrino mass, which is the aim of the KArlsruhe TRItium Neutrino experiment (KATRIN), which is currently being set up at the Karlsruhe Institute of Technology. The other important reason for the interest in tritium is its use in future fusion reactors [Bor11]. The processes of adsorption and desorption of gaseous tritium are relevant for both fields of research. Therefore, both are described in the following introduction.

Tritium (abbreviated by T or ^{3}H) is the heaviest hydrogen isotope, its nucleus[5] contains one proton and two neutrons. It decays into ^{3}He$^+$, an electron and an electron antineutrino by negative β decay with a half-life of 12.3 years [Alt03].

Fusion technology

A tritium nucleus can fuse with a deuterium nucleus (D or ^{2}H), which is the second heaviest hydrogen isotope, under the release of energy according to [Dem10b]:

$$\mathrm{T} + \mathrm{D} \;\rightarrow\; {}^4\mathrm{He} + \mathrm{n} + 17.6\ \mathrm{MeV}\ . \tag{1.1}$$

The use of this reaction on large scales in future fusion power plants has the potential to make a major contribution to a sustainable and secure energy supply in a few decades from now [Gam09]. Therefore, great research and development efforts are made in fusion technology in order to meet the huge technological challenges in this field.

The Tritium Laboratory Karlsruhe (TLK) was planned as a central facility of the Karlsruhe Institute of Technology [6] for the research in the field of tritium technology for the European Fusion Technology Program [Sch91]. The TLK holds a license for storage and handling of 40 g of tritium and currently has 23 g on site. The initial mission of the TLK was and still is the development of tritium technologies for the fuel cycle of fusion reactors.

---

[4] Tritium has further applications as a tracer in medical and geological science [Ein74], [Che10] and for self-sufficient illumination. Furthermore, tritium has a military use in thermonuclear weapons.

[5] often referred to as "triton"

[6] former Kernforschungszentrum Karlsruhe

Numerous important subsystems, required for the closed fuel cycle of a fusion reactor, have been realized on a technical scale at TLK. A reference process for the Tokamak Exhaust Processing (TEP) system of the International Thermonuclear Reactor (ITER) has been realized at TLK, which is called CAPER[7] [Bor11]. This system is required for the separation of hydrogen isotopes from other components (e.g. helium) of the off-gas from the torus and the purge gas from the breeder blankets. The isotope separation system (ISS) is able to separate tritium from deuterium and protium. Other important subsystems of the fusion fuel cycle, which have been realized at TLK, are the storage and delivery system (SDS), the water detritiation system and the atmosphere and vent detritiation systems [Bor11].

Another very important aspect in tritium technology are the analytical systems, which also are developed at TLK [Dem12]. Analytical methods are crucial for process monitoring and control. Furthermore, tritium accountancy is required for legal reasons [Vei12]. The analytical methods at TLK cover tritium concentrations over 12 orders of magnitude (from 10^4 Bq/m^3 up to 10^{17} Bq/m^3). The most important analytical method for the work at hand is the beta induced X-ray spectroscopy (BIXS), which is described in detail in chapter 3. Examples of other methods, which are being developed at TLK, are Laser-Raman spectroscopy [Stu10] and ionization chambers. Research and development in the field of fusion technology is continued with high priority at TLK [Bor11].

With the systems mentioned above, the TLK has a closed tritium loop. This was the reason for the decision in 2001 to locate the KATRIN experiment at the TLK [KAT05]. The KATRIN experiment today requires the technology, which has been developed for future fusion reactors, since the tritium source of KATRIN requires a throughput of 40 g of tritium per day, as it will be explained in the following.

Motivation for the Karlsruhe Tritium Neutrino Experiment

Neutrinos, which were postulated by Pauli in 1930 [Pau30] and discovered by Reines and Cowan in the Poltergeist experiment in 1956 [Rei56], are part of today's Standard Model of particle physics. The 12 fermions of the Standard Model are listed in table 1.1. The interactions between these fermions are mediated by bosons of an integer spin. Neutrinos only interact weakly, therefore their detection is challenging [Gru08].

The masses of the three neutrinos are free parameters, which were set to zero in the Standard Model. However, there is experimental evidence for flavor oscillations of neutrinos and therefore for non-zero neutrino masses [Alt03]. This evidences are seen as a clear indication for physics beyond the Standard Model [KAT05]. Knowledge of the neutrino masses may therefore be a key to a theory beyond the Standard Model.

Furthermore, neutrinos play an important role in astrophysics and cosmology. There are about 10^9 times more neutrinos left from the Big Bang than baryons. The absolute neutrino mass is an important parameter for cosmological models, which explain the evolution of the universe [Han10],[KAT05].

The methods for the determination of the absolute neutrino mass can be divided into the indirect measurements (neutrinoless double β decay and cosmological observations) and the direct measurements (e.g. time-of-flight measurements from supernova neutrinos and the study of weak decays). The measurement of the neutrino mass by the study of weak decays is model-independent and gives the most stringent results [Alt03].

---

[7] CAPER is an acronym for CAprice and PERmcat.

Table 1.1: Fermions of the Standard Model of particle physics. The table lists the fermions (spin=1/2) of the Standard Model. The Standard Model furthermore contains the antiparticles of these fermions, as well as gauge-bosons with integer spin [Dem10b].

	Generation			Electric charge	Interaction
	1	2	3		
Leptons	ν_e	ν_μ	ν_τ	0	Weak
	e^-	μ^-	τ^-	$-\vert e\vert$	Weak, electromagnetic
Quarks	u	c	t	$+2/3\,\vert e\vert$	Weak, electromagnetic, strong
	d	s	b	$-1/3\,\vert e\vert$	Weak, electromagnetic, strong

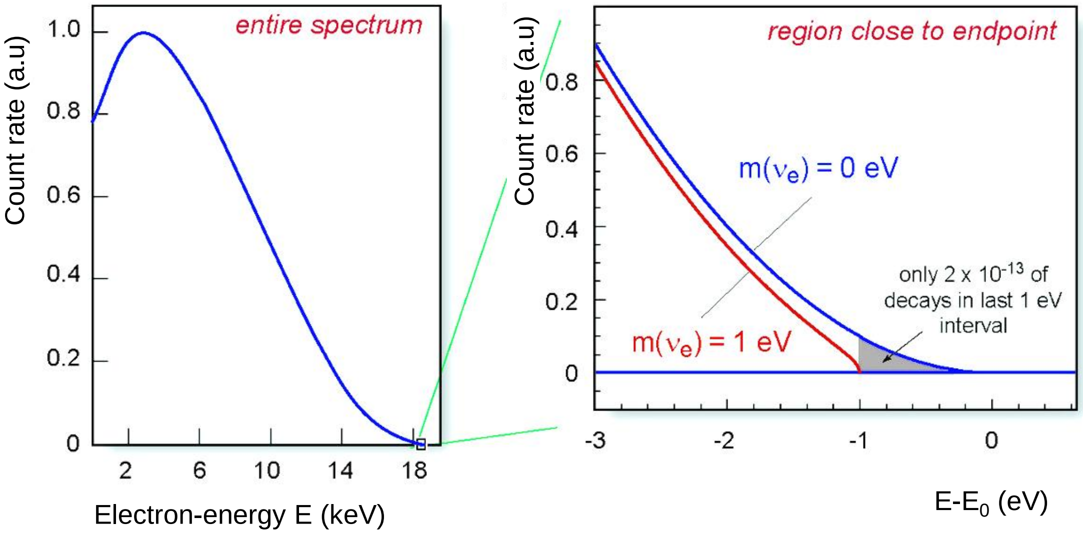

Figure 1.1: Tritium beta spectrum. The entire beta spectrum of tritium is shown on the left side. The endpoint region for a neutrino mass of 0 and 1 eV is shown on the right side. In this region, the influence of a non-zero neutrino mass becomes most distinct. The probability that the energy of the electron is in the last eV below the kinematic endpoint is $2 \cdot 10^{-13}$ [KAT05].

The measurement of the neutrino mass using the weak β^- decay is based on the laws of energy conservation and momentum conservation. The energy released in the decay is split upon the involved particles (compare section 3.2). The energy required for the production of a massive neutrino is not available as kinetic energy for the decay products, which has an impact on the shape of the resulting electron energy spectrum. This impact of the neutrino mass on the beta spectrum of tritium is shown in figure 1.1.

Tritium decays by the weak negative β decay, according to [Alt03]:

$$\mathrm{T} \rightarrow {}^3\mathrm{He}^+ + \mathrm{e}^- + \bar{\nu}_\mathrm{e} + \mathrm{Q}\ . \tag{1.2}$$

The Q-value of approximately 18.6 keV is the energy released in the tritium decay [Alt03]. Tritium is the most suitable β emitter for the determination of the neutrino mass because of its low Q-value[8], the short half-life of approximately 12.3 years [Alt03], the simple electron shell structure of tritium and its decay product (^{3}He) and further reasons [Alt03], [KAT05].

The current limit on the neutrino mass was determined based on the tritium beta decay [Ase11]:

$$m_{\bar{\nu}_e} < 2.05\ \mathrm{eV}/c^2\ (95\%\mathrm{C.L.}). \tag{1.3}$$

The KATRIN experiment

The aim of the KATRIN experiment is the determination of the electron antineutrino mass $m_{\bar{\nu}_e}$. The KATRIN experiment has a discovery potential of 5σ (3σ) for a neutrino mass $m_{\bar{\nu}_e} = 0.35\ \mathrm{eV/c^2}$ ($m_{\bar{\nu}_e} = 0.3\ \mathrm{eV/c^2}$). The upper limit, if no neutrino mass signal is observed, is $m_{\bar{\nu}_e} < 0.2\ \mathrm{eV/c^2}$. In the following, the design of the KATRIN experiment is described briefly [KAT05].

Tritium decay experiments for the determination of the neutrino mass require the following basic components with the following tasks:

- The source, which contains tritium, provides a constant flux of β electrons with a constant energy distribution.
- The transport section adiabatically guides the electrons towards the detector and prevents tritium from entering the spectrometer.
- The spectrometer analyzes the energy of the electrons.
- The detector counts the electrons, which passed the spectrometer.

The KATRIN experiment will measure the tritium beta spectrum with a so-called MAC-E filter (magnetic adiabatic collimation combined with an electrostatic filter). The principle of this method is described in figure 1.2.

---

[8] The endpoint of ^{187}Re (2.6 keV) is lower than that of tritium , but still tritium is more suitable because of the long half-life of ^{187}Re, which is $5 \cdot 10^{10}$ years.

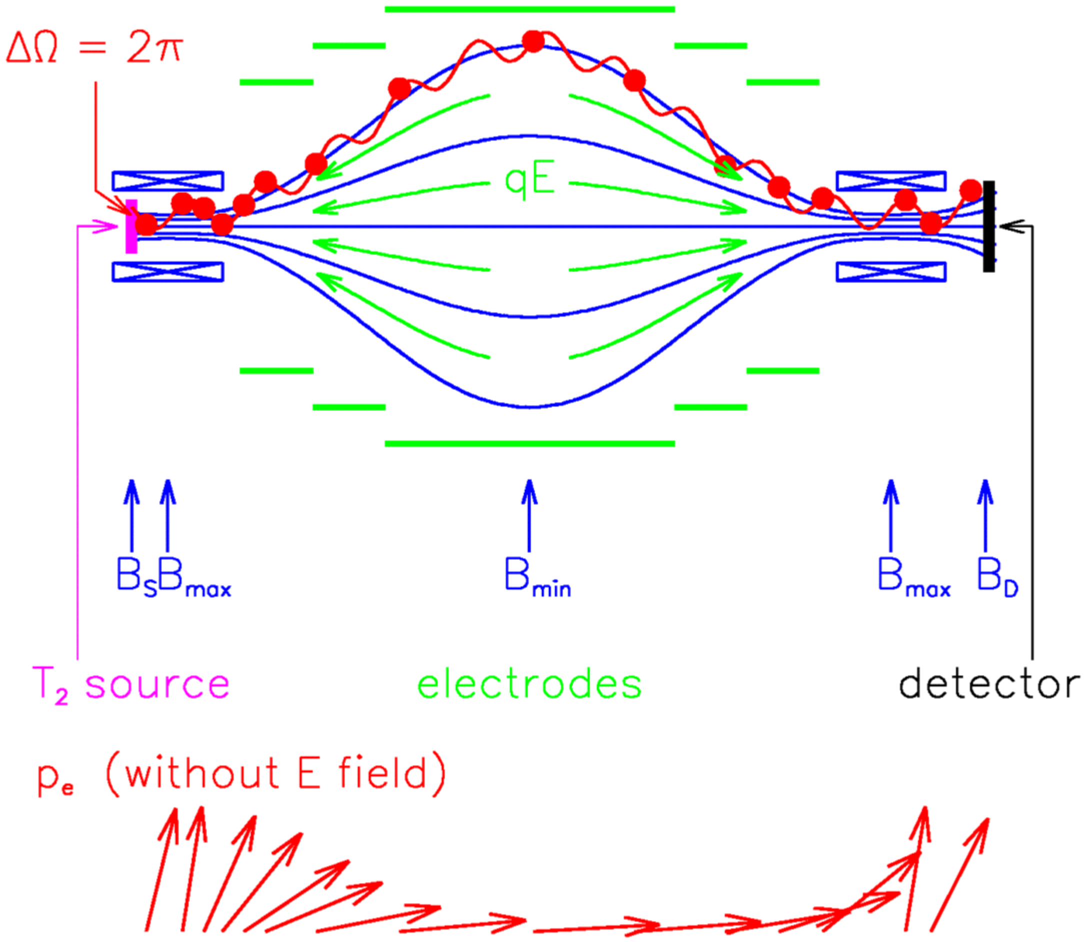

Figure 1.2: Principle of the MAC-E filter. Electrons, which are emitted in the source (left side) under a solid angle of almost 2π are adiabatically guided on a spiral trajectory along the magnetic field lines (blue) towards the detector (right side). The magnetic field is maximal at source and detector and drops by many orders of magnitude towards the center of the spectrometer (minimum magnetic field in analyzing plane B_A). This causes the transversal momentum of the electrons to be transferred into the longitudinal direction in the analyzing plane, as shown in the lower part of the figure. The retarding potential has its maximum in the analyzing plane. Hence, electrons with an energy larger than $|eU|$, where U is the retarding voltage and e is the electron's charge, can pass the analyzing plane. They are then re-accelerated by the electrostatic field and counted by the detector. Electrons with lower kinetic energy are reflected by the retarding potential. Therefore, the MAC-E filter works as an energetic high pass filter and an integral spectrum is measured. An integral β spectrum can be measured by varying the retarding potential [KAT05].

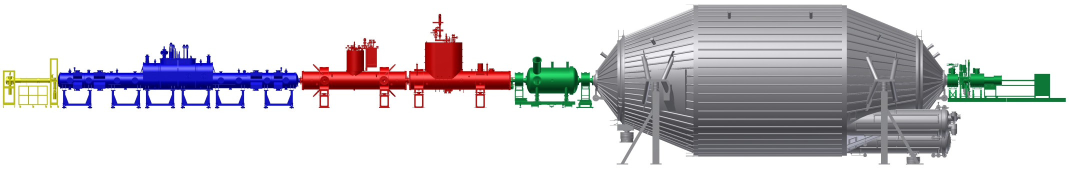

Figure 1.3: Setup of the KATRIN experiment. The picture shows the rear section in yellow, the windowless gaseous tritium source and its surrounding cryostat (WGTS) in blue, the differential pumping section (DPS) and the cryogenic pumping section (CPS) in red, the pre-spectrometer in green (in the middle), the main spectrometer in gray and the detector system in green (on the right). The whole setup has a length of approximately 70 m.

Figure 1.3 gives an overview of the experimental setup of KATRIN. The KATRIN experiment consists of the following main components (from left to right in figure 1.3) [KAT05], [KAT12]:

- The rear section is attached to the tritium source, it physically limits the source and is used for monitoring and calibration purposes. This is further described below.
- The Windowless Gaseous Tritium Source (WGTS): The WGTS consists of a source tube with a stabilized gas column. It is surrounded by the WGTS cryostat, which is used for the temperature stabilization of the WGTS and the tritium loops, which are required for the stable injection of tritium into the WGTS.
- The transport section: The transport section adiabatically guides the electrons to the pre-spectrometer and reduces the tritium flow rate by 11 orders of magnitude between WGTS and pre-spectrometer. This is achieved by differential pumping. The transport system consists of the Differential Pumping Section (DPS) and the Cryogenic Pumping Section (CPS).
- The MAC-E type main and pre-spectrometer: The pre-spectrometer is used to reduce the number of electrons entering the main spectrometer. The actual energy analysis with a resolution of $\Delta E = 0.93$ eV takes place in the main spectrometer, which has a diameter of 10 m and a length of 23.3 m.
- The detector system is placed in a superconducting magnet. It consists of a segmented PIN-diode array.

The tritium related parts of the KATRIN-experiment are the rear section, the WGTS and the transport section. These parts of the more than 70 m long experimental setup will be located in the TLK. For the work at hand, the WGTS and the rear section are relevant, therefore they are described in further detail.

The WGTS is an approximately 10 m long tube of 9 cm diameter. It contains a stable gas column of tritium molecules with an isotopic purity kept at $\epsilon_T > 95$ %. In order to maintain the stable gas column in the WGTS, tritium molecules are injected with a constant injection rate into the WGTS in the middle of the source tube. The tritium molecules are pumped off at the ends of the source tube by turbomolecular pumps with a constant pumping speed. The number of tritium molecules inside the WGTS is given by:

$$N(\mathrm{T}_2) = \rho d \cdot A \cdot \epsilon_\mathrm{T} \ , \tag{1.4}$$

where $N(\mathrm{T}_2)$ is the number of tritium molecules, A is the cross section of the source tube and ϵ_T is the isotopic purity of tritium. ρd is the source column density, which is expected to be the main systematic uncertainty in the WGTS. Therefore, relative fluctuations need to be known to a precision of 0.1 %. The column density in the WGTS will be kept at $\rho d = 5 \cdot 10^{17}$ molecules/cm^2 [Bab12], [KAT05].

The required stable isotopic purity and column density are maintained with the help of closed tritium loops containing a T_2 recovery and isotope separation system, as well as a controlled injection system. The injection rate will be set to $1.7 \cdot 10^{11}$ Bq/s, which equals a tritium throughput of 40 g per day. The source will be temperature stabilized at 27 K with a stability of ±30 mK [KAT05].

The rear section contains the rear wall, which physically limits the WGTS and which is the first conducting surface intersecting the magnetic field lines. The rear wall is shown in the CAD model of the rear section in figure 1.4. Beta decays and ionization cause a plasma in the WGTS, which is highly conductive in the direction of the magnetic field, and highly nonconductive in the transverse directions. The plasma potential is defined by the rear wall. Hence, the electric properties of the rear wall are required to be well defined and stable in time. The variation of the work function is aimed for to be lower than 20 mV RMS within one detector pixel, as the detector integrates over this area [KAT12].

Another important task of the rear section, besides providing the defined rear wall potential, is the monitoring of the activity of the WGTS. Fluctuations in the column density of the WGTS, which are not accounted for, result in systematical uncertainties for the determination of the neutrino mass. Therefore, the activity has to be monitored with a precision of 0.1 %. The activity will be monitored by β induced X-ray spectroscopy. This is also the measurement principle of the Tritium Adsorption Desorption Experiment (TRIADE), therefore it is described in detail in chapter 3.

Some of the β decay electrons impinging on the rear wall produce bremsstrahlung in a gold layer on the rear wall. A fraction of this radiation can be measured by silicon drift detectors, which are located in the rear section (compare figure 1.4). The activity in the WGTS can be calculated from the count rate measured by the silicon drift detectors. The principle of monitoring the source activity with β induced X-ray spectroscopy was tested using a rear-wall-like surface in the TriReX experiment [Röl12b]. The design of the TRIADE experiment was strongly influenced by this experiment, therefore TriReX is further described in section 3.9.

Adsorption and desorption

If a solid surface is exposed to gas, a certain amount of gas particles accumulate on the surface. This process is called adsorption. Adsorption often occurs in an equilibrium state with the inverse process of desorption. Hence, both processes have to be known, if the amount of adsorbed gas in the equilibrium state is of interest. The amount of adsorbed gas particles is strongly dependent on the involved elements (gas and surface), temperature and pressure. After adsorbing on a surface, the gas particles can often diffuse into the bulk material ("absorption"). This also applies to tritium and the multiple surfaces of systems in tritium technology. Adsorption and desorption will be discussed in detail in chapter 2.

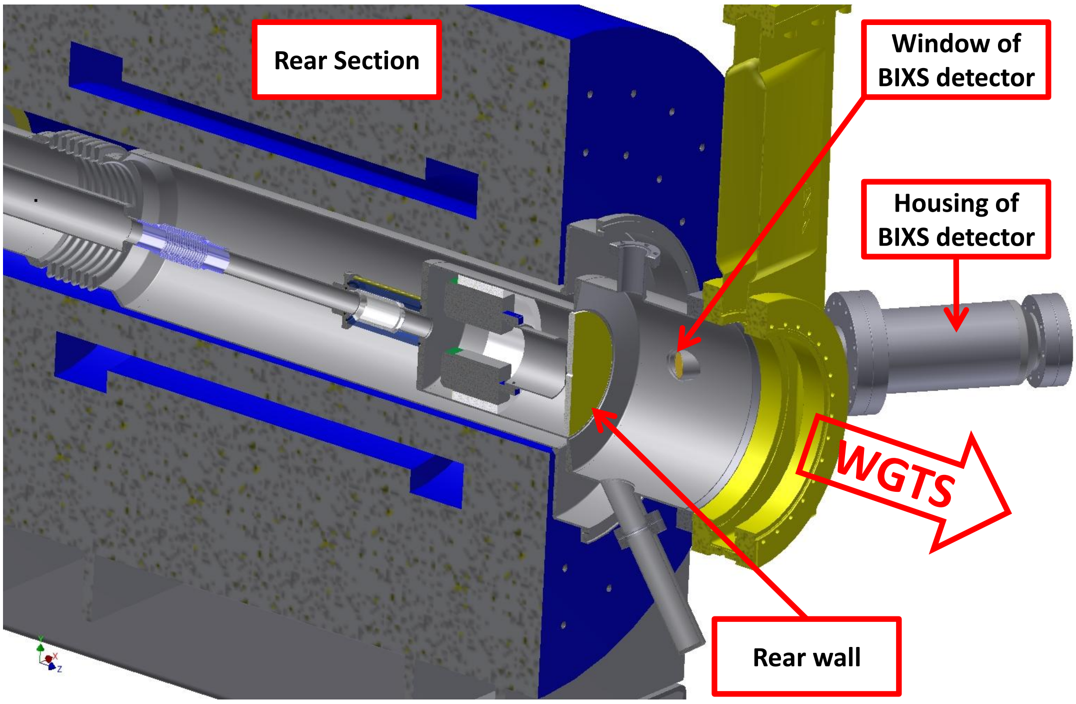

Figure 1.4: CAD model of the rear section. The picture shows a cut through the current model of the rear section, which is the area on the left and in the middle of the picture. Adsorption of tritium on the surfaces of the rear wall and the windows of the BIXS detectors needs to be investigated for the KATRIN experiment. The BIXS detectors are not visible in the picture. The rear section is terminated by a gate valve (yellow), the WGTS, which is not displayed, is connected to the rear section on the right side of the picture.

Adsorption and desorption in the context of KATRIN

Adsorption of tritium on two surfaces in the KATRIN setup is of special concern. The first important surface is that of the rear wall. Hydrogen isotope adsorption on the rear wall may change the work function of the surface locally up to 1 eV [KAT12]. Therefore, the amount of atomic tritium adsorbed on the rear wall is required to be less than $5 \cdot 10^{14}$ atoms/cm^2 and the amount of molecular tritium adsorbed on the rear wall is required to be less than $5 \cdot 10^{13}$ atoms/cm^2 [KAT12]. One monolayer corresponds to approximately $6 \cdot 10^{14}$ particles/cm^2 (compare equation A.1 in appendix A). Based on the literature data, which is presented in chapter 2, it is assumed that this can be achieved by the choice of a suitable surface material. Polycrystalline gold with a dominant (111)-surface on a substrate with well-prepared surface at room temperature is considered suitable [KAT12]. This assumption requires experimental verification. Different layer configurations and crystalline structures of the gold layer are still under consideration.

The BIXS-detectors, which monitor the activity in the WGTS, are protected from tritium contamination by gold coated beryllium windows. Tritium adsorption on these surfaces also needs to be investigated, because tritium adsorption on the windows could decrease the signal-to-background ratio of the detectors. This might make it impossible to measure changes of the activity in the WGTS on the 0.1%-level. The amount of tritium which is expected to be adsorbed on these windows needs to be known.

Adsorption and desorption in tritium technology

The Tritium Adsorption Desorption Experiment (TRIADE) was initiated in order to face the needs to investigate the adsorption of tritium in the context of KATRIN. But knowledge about tritium adsorption is of interest in all fields of tritium technology for the following reasons:

- The tritium adsorbed on a surface or diffused into the bulk material might be lost for the process it is intended for.
- The tritium diffusing into the bulk material can escape from the system into the environment. This has to be taken into account for example in the design of cooling systems for the breeder blankets of fusion reactors.
- The material on which tritium is adsorbed is contaminated. Depending on the surface activity, these materials require special treatment when disposed.
- The handling of an amount of 40 g of tritium is only allowed, if an adequate accountancy of the tritium inventory is possible [Vei12]. Tritium adsorbed in a system has to be taken into account.

These aspects apply for KATRIN as well as for fusion technology. After investigating the tritium adsorption on the materials, which are important for KATRIN, other materials, which are used in tritium technology in general, can be investigated.

The TRIADE experiment

TRIADE is capable of investigating tritium adsorption on any solid material[9], which might be interesting for tritium technology, using β induced X-ray spectroscopy. Furthermore, it is possible to investigate adsorption under a wide range of conditions (tritium concentrations, temperatures, pressures) which may occur in tritium technology. The design of the TRIADE experiment takes account of experience at TLK from prior experiments using BIXS [Röl12b]. The experimental setup is supposed to reach a detection limit of < 1 monolayer of adsorbed tritium. The possibility to measure tritium adsorption also enables the investigation of decontamination processes. Therefore, a decontamination process using purge gas is implemented in the experimental setup. The aim of the work at hand was to provide the experimental setup ready for first measurements.

This thesis is structured as follows: In chapter 2, the basics of adsorption, desorption and their investigation are discussed, followed by a summary of what has been found about hydrogen and tritium adsorption up to now. The chapter concludes with the open questions, which are to be answered by the TRIADE experiment. Chapter 3 describes the β induced X-ray spectroscopy (BIXS), which is the main measurement method used in TRIADE. Chapter 4 contains the physical and technical requirements for the TRIADE experiment, followed by the design and setup of the experiment. The commissioning of the experiment and first test measurements are described in chapter 5. The simulations which are necessary for the interpretation of data taken in the TRIADE experiment are described in chapter 6, followed by the summary and the outlook in chapter 7.

---

[9] which is vacuum compatible

Chapter 2

Physics of adsorption and desorption

In general, adsorption can occur on any interface between two phases. In the context of this work only interfaces between a solid state body and a gas are of interest. In this case the term adsorption refers to the accumulation of atoms or molecules of the gaseous adsorbt on a solid material, which is called the adsorbent. The particles enriched on the surface are called adsorbate. The processes of adsorption and desorption are schematically illustrated in figure 2.1. The sticking of adsorbed particles to a surface can be caused by several different interactions, which are described in section 2.1. The term desorption refers to the inverse transition of adsorbed particles back into the gaseous phase. Desorption is discussed in section 2.2. Adsorption and desorption can occur in an equilibrium state, which is described in section 2.3. Adsorbed atoms or molecules can often move along the surface or diffuse into the bulk material. This is not dealt with in the context of this work. The technique of thermal desorption spectroscopy (TDS) for the study of adsorption and desorption is presented in section 2.4. Special characteristics and literature data for systems of interest are presented in sections 2.5 and 2.6.

2.1 Physical aspects of adsorption

The enrichment of atoms or molecules on solid surfaces is caused by an interaction potential provided by the surface. This potential has a local minimum close to the surface. In figure 2.5 the interaction potential is given for the example of hydrogen adsorption on a gold surface. Impinging atoms or molecules might be scattered elastically and be reflected by the surface or they might be trapped in the potential well. The trapping can be a process consisting of several steps, for example the dissociation of a molecule before adsorption of the atoms. The probability of an impinging gas particle to be trapped on the surface is called sticking probability S [Chr88].

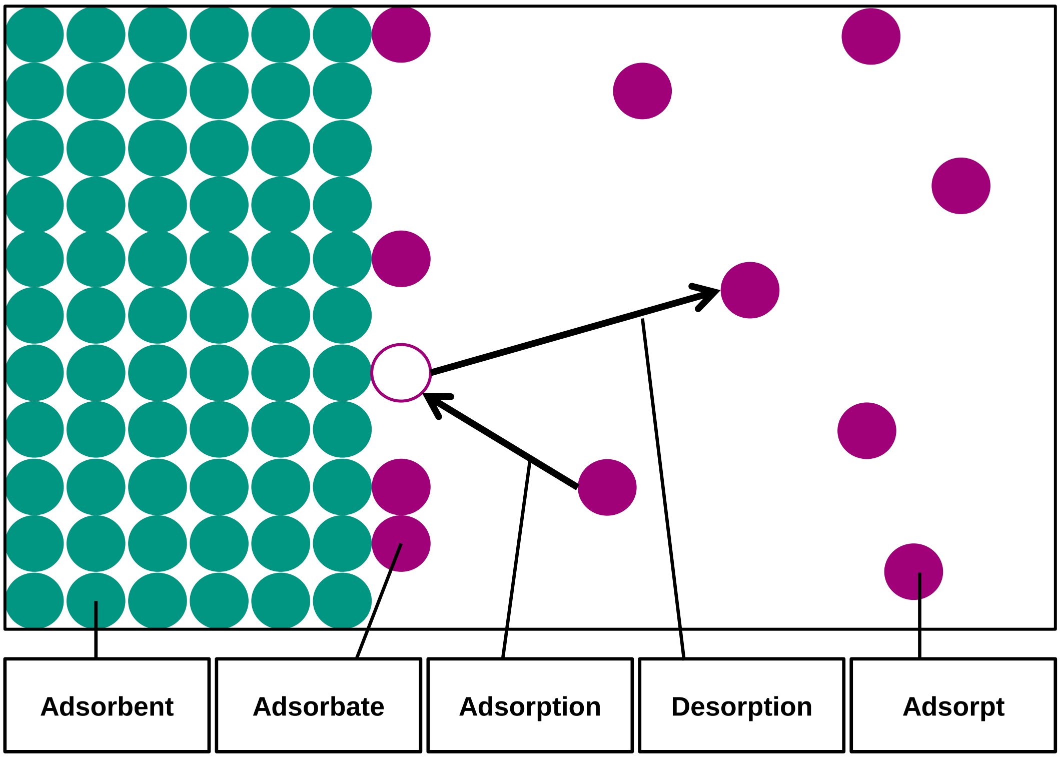

Figure 2.1: Adsorption and desorption. The schematic illustrates the greatly simplified processes of adsorption and desorption of a gaseous adsorpt on a solid adsorbent. The shown particles might be atoms or molecules. In some cases the molecules of an adsorpt might also dissociate upon adsorption (compare section 2.5). The situation is often more complicated as adsorption might form multiple adsorbate layers and there may be different elements adsorbed on a surface. Furthermore, the surface usually is not as homogenous as shown. Diffusion of particles of the adsorbate into the bulk material is not shown.

The minimum of the surface potential can be caused by different bonding forces, such as

- Van-der-Waals forces (which are always present),
- hydrogen bonding forces,
- ionic bonding forces,
- covalent bonding forces,
- metallic bonding forces.

The forces which occur and their ratio are determined by the system (the elements involved), temperature and pressure. Interactions might only occur in certain pressure or temperature ranges [Cla70]. The experimental distinction of these forces is difficult, as the surface and pressure and temperature distributions usually are not uniform. Therefore adsorption is usually not characterized by the occurring interactions.

A common categorization is the distinction between physisorption and chemisorption [Chr91]. If the adsorbate particles are weakly bound to the adsorbent surface, usually by Van-der-Waals forces, one speaks of physisorption. This corresponds to binding energies of <50 kJ/mol (0.5 eV/particle) [Hen91]. If the adsorbed particles are strongly bound to the adsorbent surface, one speaks of chemisorption. This corresponds to binding energies above 50 kJ/mol [Hen91]. Chemisorption can only occur, if the adsorbate consists of ions or chemical radicals, or if those are formed during the process of adsorption, for example during catalytic dissociation of molecules. The border between physisorption and chemisorption is not distinct. There are different definitions of the threshold binding energy between physisorption and chemisorption [Bar11], other authors distinguish physisorption and chemisorption based on the interactions taking place [Iba06].

The adsorption can further be categorized as being (sub-) monolayer or multilayer. Chemisorption is limited to one monolayer, while physisorption may occur in several layers and on top of a chemisorbed monolayer [Bar11]. Usually layers upon the first monolayer are less strongly bound to the surface than the first monolayer, as the interaction potential seen by the particles adsorbing onto the first layer is influenced by the this layer [Bar11].

Further characteristics which adsorption can be categorized by are reversibility and the conditions (temperature, pressure) of adsorption and the mobility of adsorbed atoms, which is important for catalytic reactions and desorption (compare section 2.2) [Bar11].

2.2 Physical aspects of desorption

Desorption is the reversal process of adsorption. It is characterized by the breaking of the bonds between adsorbent and adsorbate particle and the release of the adsorbate particle into the gas phase. As the adsorbate particle resides at the bottom of a potential well, energy is required which enables it to leave the potential well. Desorption can be induced by different causes [Hen91]:

- The required energy can be provided by thermal excitation. This is used in thermal desorption spectroscopy (compare section 2.4).
- A gradient in the chemical potential between adsorbed particles and gas phase causes an isothermal desorption. This occurs for example if a vacuum chamber containing a gas previously adsorbed on a sample is suddenly pumped down.
- Desorption can be caused if the required energy is provided by impinging ions ("ion impact desorption"), electrons ("electron impact desorption") or photons ("photo desorption").
- High electric fields influence the interaction potential and may cause desorption ("field desorption").
- Chemical reactions of adsorbate particles with other adsorbate particles or particles from the gas phase.

The desorption process is often a complicated series of microscopic processes. Therefore, a macroscopic quantitative description of the desorption process is not easy. The desorption rates can often be described formally by the kinetic equation of desorption (also referred to as "Wigner-Polanyi equation") [Hen91], [Chr91]:

$$R_{\mathrm{des}} = -\frac{\mathrm{d}N^{\mathrm{ad}}}{\mathrm{d}t} = \nu_x \cdot \exp\left(-\frac{E_{\mathrm{A,des}}}{\mathrm{R}T}\right) \cdot \left(N^{\mathrm{ad}}\right)^x \quad , \tag{2.1}$$

where R_{des} is the desorption rate, N^{ad} is the number of adsorbed particles on a defined surface, ν_x is the pre-exponential factor of the order x, $E_{\mathrm{A,des}}$ is the activation energy of desorption, R is the gas constant and T is the temperature.

The pre-exponential factor and the activation energy can be determined experimentally (compare section 2.4). The activation energy of desorption is the sum of adsorption energy and activation energy of adsorption:

$$E_{\mathrm{A,des}} = Q_{\mathrm{ad}} + E_{\mathrm{A,ad}} \ . \tag{2.2}$$

The adsorption energy Q_{ad} is the energy released upon adsorption and $E_{\mathrm{A,ad}}$ is the height of the activation barrier for the adsorption process. If the adsorption process is not activated, $E_{\mathrm{A,ad}}$ equals zero. Both quantities are illustrated by the example of hydrogen adsorption on gold in figure 2.5.

If no experimental data is available, the activation energy of desorption can often be estimated by standard quantum methods [Wan01]. Literature data is available for some systems [Wan01], [Zhu89]. The order of the desorption process can also be determined experimentally. In practice four reaction types occur more frequently than others, namely $x = 0,\frac{1}{2},1,2$ [Chr91]. In some cases one step of the desorption process is rate-limiting and thereby determines the order of the desorption process. Other cases are more complicated.

Equation 2.1 contains three assumptions, neither one of them is fulfilled in reality: The approximation of constant $E_{\mathrm{A,des}}$ and ν_x might not be applicable in most cases. They might depend on temperature and coverage [Hen91]. Furthermore, the dependency of R_{des} on N^{ad} can be significantly more complicated than assumed in equation 2.1 [Iba06]. More sophisticated theoretical models have been developed (e.g. the Eyring theory, [Hen91]).

A precise quantitative description of desorption requires deeper knowledge of the reaction kinetics. For example desorption can be caused by the following mechanisms:

- The Langmuir-Hinshelwood mechanism: Two adsorbed particles (which may be of the same or different species) can react chemically with each other in the adsorbed state. An energy released during this process can cause desorption. Furthermore, the product of the reaction possibly does not stick to the surface. The desorption via this mechanism can be described by the Wigner-Polanyi equation (eq. 2.1). If the reaction of the adsorbed particles is the rate-limiting process, the desorption is of second order. If the desorption of the product of the reaction is rate-limiting, the overall process of desorption is of first order. The Langmuir-Hinshelwood mechanism is illustrated in figure 2.2 [Chr91], [Hen91], [Bar11].

- The Eley-Rideal mechanism: Adsorbed particles can also react with particles from the gas phase. This can also cause desorption, as it is illustrated in figure 2.2 [Chr91], [Bar11]. In this case the desorption rate is determined by the flux of impinging gas atoms (compare equation 2.11).

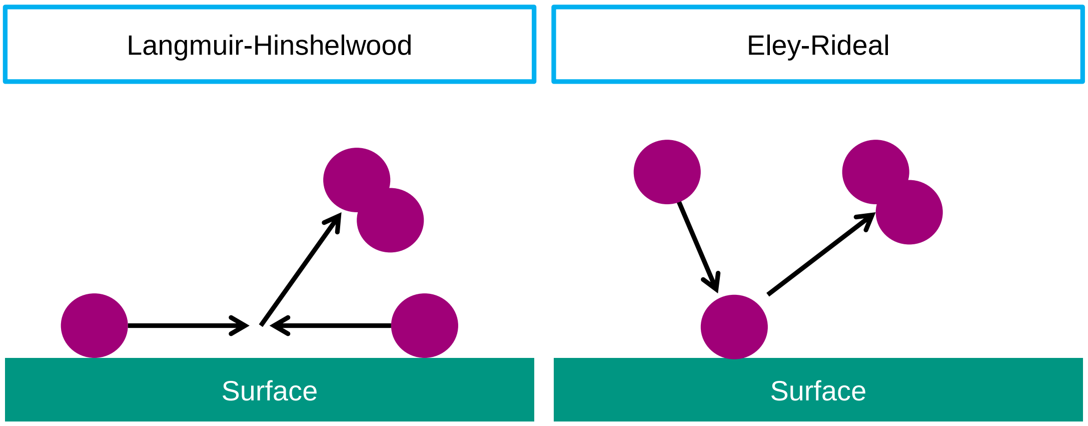

Figure 2.2: Langmuir-Hinshelwood and Eley-Rideal desorption mechanisms. The picture illustrates these two desorption mechanisms.

Several techniques are available for the quantitative investigation of desorption. They are based on the different causes for desorption listed above. The most important standard technique for the characterization of binding energies is the thermal desorption spectroscopy (TDS) [Hen91], which is further described in section 2.4.

2.3 The equilibrium of adsorption and desorption

Typically adsorption and desorption occur in an equilibrium state. That means that atoms are adsorbed on the surface, remaining on the surface for an average time τ and desorbing again. In this equilibrium state at constant temperature and pressure the surface is covered with a constant amount of adsorbate particles. This is described by the surface coverage[10] of the adsorbent [Chr91]:

$$\Theta = \frac{N^{\mathrm{ad}}}{N_{\mathrm{sites}}} , \tag{2.3}$$

where N_{sites} is the number of adsorption sites per area [Hen91], which can be determined experimentally [Sto92].

The coverage which is formed when an adsorbent is exposed to an adsorpt strongly depends on the materials of adsorbent and adsorpt. The properties of the surface play an important role, such as crystal structure, topology and impurities. Sometimes even the "history" of the surface matters, if previously adsorbed adsorbate layers are present. Furthermore, the coverage is strongly dependent on temperature and pressure.

A thermodynamic description of an adsorption/ desorption system is only possible, if the surface coverage is a distinct function of temperature and pressure, which is not the case for every system [Hen91]. The relation between surface coverage and pressure at a given temperature is characterized by an adsorption isotherm. Various models with different model assumptions were developed in order to describe the isotherms of different systems.

---

[10] There are different definitions of surface coverage in the literature. Sometimes the coverage is also defined as adsorbate atoms per adsorbent atoms, so values above $\Theta = 1$ are possible [Hen91].

The most important isotherm, which is widely applicable to experimental data, is the Langmuir isotherm [Chr91]:

$$\Theta = \frac{b_{(T)}P}{1 + b_{(T)}P} , \tag{2.4}$$

where Θ is the coverage, P is the gas pressure and $b_{(T)}$ is given by:

$$b_{(T)} = \frac{S \cdot \exp\left(-\left(E_{\mathrm{A,ad}} - E_{\mathrm{A,des}}\right)/\mathrm{k}T\right)}{\nu_1 \sqrt{2\pi m \mathrm{k}T}} , \tag{2.5}$$

where S is the sticking probability, $E_{\mathrm{A,ad}}$ is the activation energy for adsorption (which might be zero), k is the Boltzmann constant, T is the temperature and m is the mass of the adsorbent particles.

The Langmuir isotherm is based on model assumptions like assuming constant values for $E_{\mathrm{A,ad}}$,$E_{\mathrm{A,des}}$ and ν_1. This is not fulfilled in reality. Nevertheless experimental data from many systems can be fitted to isotherms described by equation 2.4, adjusting the parameter b. Isotherms based on more realistic model assumptions were developed, like the BET isotherm[11] or the Tiomkin isotherm (compare section 2.5).

2.4 Thermal desorption spectroscopy (TDS)

Thermal desorption spectroscopy[12] (TDS) is one of the oldest and the most important method for the investigation of desorption processes [Iba06]. The aim of TDS measurements is the determination of the parameters introduced in equation 2.1, namely the activation energy of desorption ($E_{\mathrm{A,des}}$), the pre-exponential factor (ν_x) and the order of the desorption process (x) [Chr91]. In the following paragraphs the idea and the setup of a TDS experiment are described, followed by an introduction into the possibilities of the analysis of TDS spectra.

The principle of TDS studies is to heat a sample (an adsorbent with an adsorbate of interest) with a constant heating rate[13] and to detect the desorbing products either with a mass spectrometer or an ion gauge. If the vacuum chamber is constantly pumped during the process, the desorption at its maximum rate leads to a maximum partial pressure of the desorbing products. Example spectra are given in figure 2.4. The idea behind TDS is that the maximum rate of desorption appears right at the temperature where the most adsorbate-adsorbent bonds are thermally dissociated. The temperature the maximum desorption rate appears at has to be determined experimentally [Chr91], [Hen91].

Setup of a TDS experiment

A TDS setup needs the possibility to expose a sample of a material of interest to a gas of interest in order to let the gas adsorb on the sample surface. Furthermore, the experimental setup requires the possibility to heat the sample with different constant heating rates[14] of adequate magnitude. A possibility to detect the desorbing atoms or

---

[11] Introduced by Brunauer, Emmett and Teller [Bru38].

[12] Sometimes also referred to as "thermal desorption mass spectroscopy" (TDMS) or "temperature programmed desorption " (TPD). The method was also referred to as "flash filament technique", because of the used filaments [Iba06].

[13] as introduced by P.A. Redhead [Red62]

[14] Different heating rates are required due to reasons concerning the analysis of spectra, which is discussed below.

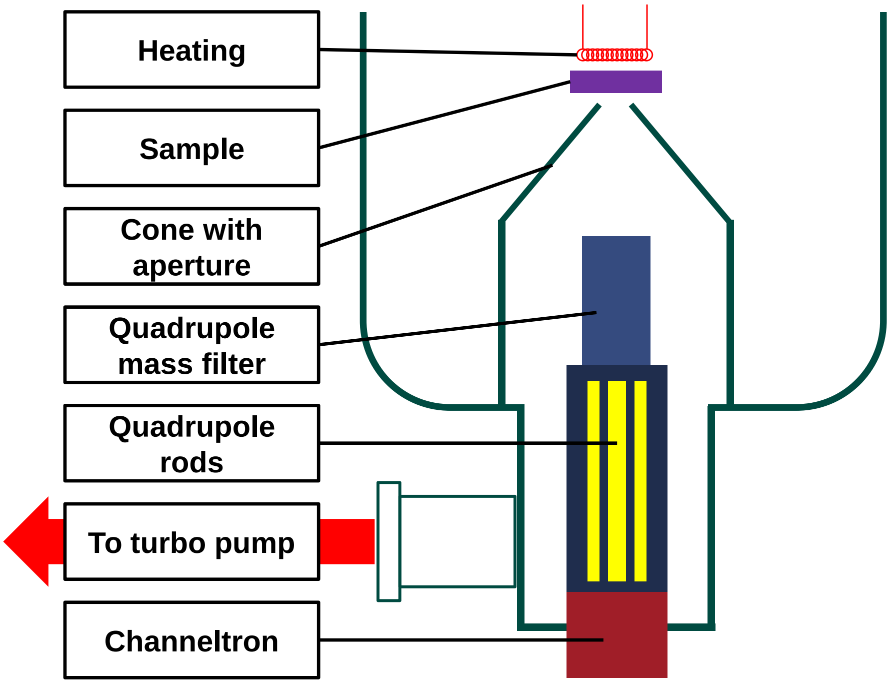

Figure 2.3: Schematic setup of a TDS experiment. Typical experimental setup for TDS using a quadrupole mass spectrometer, differentially pumped by a turbomolecular pump (according to [Chr91]).

molecules is required, such as a quadrupole mass spectrometer. If re-adsorption should be avoided, an adequate pumping system is required.

In TDS experiments it is of interest that a maximum fraction of the atoms or molecules desorbing from the sample surface are detected. Simultaneously contributions originating from the sample holder, support structure and vacuum chamber should be minimized, as they can simulate desorption spectra or give rise to background effects. A commonly used solution to this problem is illustrated in figure 2.3. The flux of desorbing atoms or molecules has to pass the mass spectrometer, which is differentially pumped, in order to be analyzed. The cone with an aperture of a typical diameter of $d \approx 0.5$ mm $-$ 1 mm at the entrance of the mass spectrometry setup maximizes the fraction of atoms or molecules which originate from the sample surface [Chr91], [Iba06].

As most surfaces other than single crystals are not uniform and consist of sites with broad distributions of adsorption energies and irregular surface patterns [Cla70], even the small aperture can not guarantee unambiguous results in every case. Heterogeneous surfaces lead to several separated desorption peaks in the best case. In the worst case they can lead to broad and uncharacteristic desorption peaks, making the analysis of the spectrum impossible. The same applies if the contributions of sample holder, support structure and vacuum chamber are not negligible [Chr91].

Analysis of TDS spectra

As mentioned before, the aim of TDS measurements is the determination of the activation energy of desorption ($E_{\mathrm{A,des}}$), the pre-exponential factor (ν_x) and the order of the desorption process (x). The order of the desorption process (x) can usually be determined from the shape of the desorption spectrum (compare figure 2.4). For example the peak position does not depend on the initial coverage for $x = 1$ but does so for $x = 2$, as shown below.

In case of large effective pumping speeds of the pumping system[15], the partial pressure of the desorbing species is proportional to the desorption rate. In this case the initial coverage can be determined from the area below the desorption spectra [Hen91].

A relation between peak position T_{max}, $E_{\mathrm{A,des}}$, ν_x and β can be obtained for given x and constant heating rate β from equation 2.1. The temperature derivation of the desorption rate is zero at the rate maximum [Chr91]:

$$\left.\frac{\mathrm{d}R_{\mathrm{des}}}{\mathrm{d}T}\right|_{T=T_{\mathrm{max}}} = 0 \ . \tag{2.6}$$

For x =1 one obtains the relation:

$$\frac{E_{\mathrm{A,des}}}{\mathrm{R}T_{\mathrm{max}}^2} = \frac{\nu_1}{\beta} \cdot \exp\left(-\frac{E_{\mathrm{A,des}}}{\mathrm{R}T_{\mathrm{max}}}\right) \ , \tag{2.7}$$

for x =2 one obtains:

$$\frac{E_{\mathrm{A,des}}}{\mathrm{R}T_{\mathrm{max}}^2} = \frac{2N^{\mathrm{ad}}_{T=T_{\mathrm{max}}}\nu_2}{\beta} \cdot \exp\left(-\frac{E_{\mathrm{A,des}}}{\mathrm{R}T_{\mathrm{max}}}\right) \ . \tag{2.8}$$

The activation energy of desorption ($E_{\mathrm{A,des}}$) and the pre-exponential factor (ν) can be determined from experiments with varied heating rate. The activation energy of desorption ($E_{\mathrm{A,des}}$) can be determined from the slope of a plot of $\ln(T_{\mathrm{max}}^2/\beta)$ vs. T_{max}^{-1}, whereas ν can be determined from the intercept using $E_{\mathrm{A,des}}$ determined before [Chr91]. In order to reduce the error of the measurements, the heating rates should be different by at least two orders of magnitude [Iba06]. As mentioned above these equations are based on unrealistic model assumptions of constant parameters $E_{\mathrm{A,des}}$, ν_x and x, which may also depend on temperature or coverage.

Further considerations require knowledge about the kinetics of the desorption process. Diatomic molecules for example frequently dissociate upon adsorption and desorb after recombination. A more sophisticated expression for the desorption rate can be obtained from an ansatz for the chemical potential of the adsorbed phase. For more details see [Iba06].

2.5 Literature data for hydrogen adsorption

The amount of literature data for the adsorption of tritium on different surfaces is not sufficient in order to dependably estimate the amount of adsorbed tritium on the KATRIN rear wall or other materials of interest in tritium technology (compare chapter 1). Some of the existing literature about tritium adsorption is summarized

---

[15] This is favorable because re-adsorption can be avoided by large pumping speed.

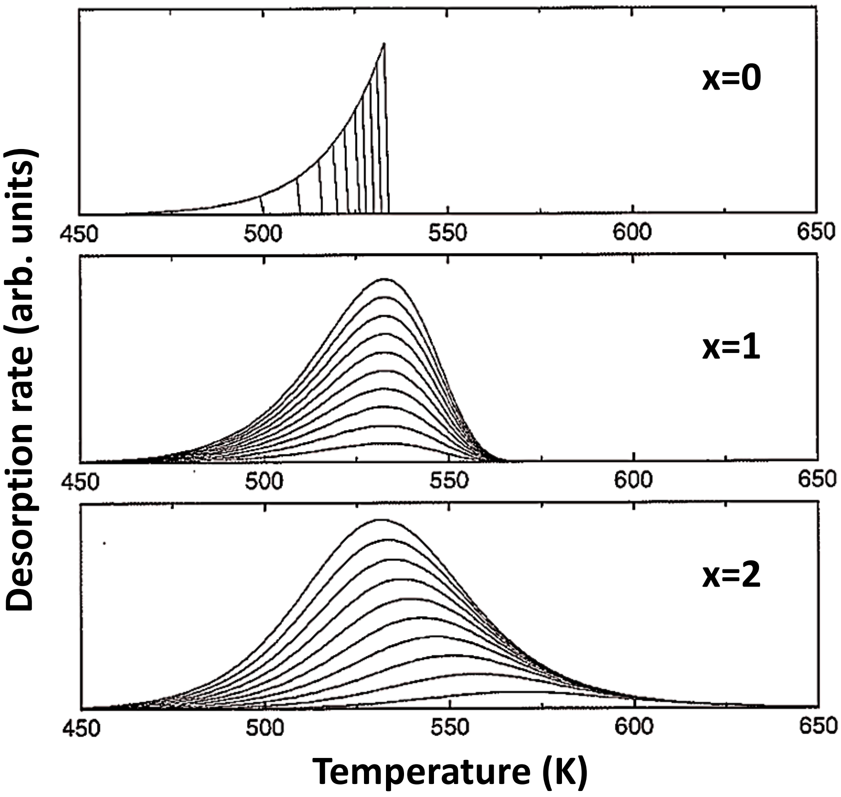

Figure 2.4: Calculated TDS example spectra. The plots show spectra calculated according to equation 2.1 for the desorption order $x = 0,1,2$, a heating rate of $\beta = 1$ K/s, a pre-exponential factor of $\nu_x = 10^{13}$ s^{-1} and an activation energy of $E_{\mathrm{A,des}} = 1.5$ eV. Every line corresponds to an initial coverage between $\Theta = 0.1$ and $\Theta = 1$ in steps of 0.1. The higher the initial coverage, the higher is the rate maximum. Figure according to [Iba06]. As the temperature is increased with a constant heating rate, the x-axis also corresponds to the time elapsed.

in section 2.6. Tritium is an isotope of hydrogen. Therefore, this section gives an insight into what has been found about the behavior of hydrogen in adsorption and desorption processes. Taking into account the special characteristics of tritium (compare section 2.6) one may form hypotheses about the behavior of tritium, based on the knowledge about hydrogen.

Because of the special interest into tritium and hydrogen adsorption on gold (compare chapter 1) this section focuses on the adsorption of hydrogen on gold. A detailed report on the interaction of hydrogen with solid surfaces in general is given in [Chr88]. A large amount of pre-exponential factors and desorption energies for different systems is summarized in [Wan01].

It is known that molecular hydrogen does not adsorb on solid surfaces at temperatures above 20 K [Chr88]. So only atomic hydrogen occurs in the adsorbed state at temperatures above 20 K. It is known as well that desorption only occurs if adsorbed hydrogen atoms recombine [Chr88]. This can happen via the Eley-Rideal or the Langmuir-Hinshelwood mechanism (compare section 2.2).

Chemisorption is possible if an hydrogen molecule is dissociated, which requires an activation energy of 435 kJ/mol ($\approx$4.5 eV/molecule) [Chr88]. The resulting potential for dissociative adsorption is the superposition of the potential of a H_2 molecule and the potential of the dissociated molecule approaching the surface. Depending on the adsorbent, this potential can contain a barrier, meaning that an activation energy is required for dissociative adsorption (compare figure 2.5 for hydrogen on gold at $T = 78$ K). Easy dissociation is not provided by deep lying d-bands, as they are the case for gold [Chr88]. This is one reason, why gold is considered to be a suitable coating material for reducing tritium adsorption on surfaces.

Hydrogen adsorption on gold at 78K

The most comprehensive study of hydrogen adsorption on gold were carried out at 78 K. Adsorption was investigated by pressure decrease (caused by adsorption) and TDS measurements [Sto94],[Sto92], [Sto96]. The results are summarized in the following.

Hydrogen adsorption was studied on thin gold films for low atomic hydrogen pressures and short exposition times. The measured isotherms are probably well described by Tiomkin's type of isotherm, as they can be fitted to the equation [Sto94]:

$$\Theta = A \cdot \ln\left(B \cdot p_{\mathrm{H}}\right) \ , \tag{2.9}$$

where Θ is the coverage, A and B are parameters and p_{H} is the hydrogen partial pressure. The heat of atomic hydrogen adsorption was determined by measurement of the isotherms of the coverage dependent on the atomic hydrogen pressure. The heat of adsorption Q_{ad} was determined as 21 kJ/mol ($\approx$ 0.2 eV/molecule H_2) [Sto94] using the Tiomkin isotherm:

$$\Theta = \frac{\mathrm{R}T_{\mathrm{Au}}}{\alpha}\ln\left\{\left(\frac{\mathrm{R}T_{\mathrm{Au}}}{Q_{\mathrm{ad}}\alpha}\ln\left[\frac{S_0}{\nu\left(2\pi m_{\mathrm{H}}\mathrm{k}T_{\mathrm{Au}}\right)^{1/2}}\right]+\frac{1}{\alpha}\right)p_{\mathrm{H}}\right\} \ , \tag{2.10}$$

where T_{Au} is the temperature of the gold surface, α is the fine structure constant and S_0 is the initial sticking probability for hydrogen on the thin gold film surface at 78 K.

It was found that recombination via the Eley-Rideal mechanism (compare section 2.2) occurs [Sto92], [Sto94]. With increasing of the temperature, hydrogen or deuterium adatoms may recombine according to the Langmuir-Hinshelwood mechanism [Sto96]. Taking both mechanism into account, one can describe the rate of adsorption as:

$$\frac{\mathrm{d}N_{\mathrm{ad}}}{\mathrm{dt}} = J_{\mathrm{H}}S_0(1-\Theta) - J_{\mathrm{H}}\gamma\Theta - \nu\exp\left(-\frac{E^{\mathrm{LH}}_{\mathrm{A,des}}}{\mathrm{R}T}\right)\cdot\left(N^{\mathrm{ad}}\right)^2 \ , \tag{2.11}$$

where N_{ad} is the number of adsorbed hydrogen atoms on a defined gold surface area, t is the time, J_{H} is the total atomic hydrogen stream impinging the thin gold surface per second and Θ is the surface coverage. The first negative term takes into account the recombination and desorption via the Eley-Rideal mechanism, where γ is the probability of recombination via this mechanism. The second negative term describes the recombination and desorption via the Langmuir-Hinshelwood mechanism as a second order process according to the Wigner-Polanyi equation (eq. 2.1).

The activation energy of thermal desorption of mono-atomic hydrogen is dependent on surface coverage:

$$E_{\mathrm{A,des}}(\Theta) = E^0_{\mathrm{A,des}}(1-\Theta) \ , \tag{2.12}$$

where $E_{\mathrm{d}}(\Theta)$ is the activation energy for desorption. E^0_{d} was determined as 57 ± 5 kJ/mol from TDS measurements. This is the desorption energy at low coverages ($\Theta \cong 0.01$) [Sto92].

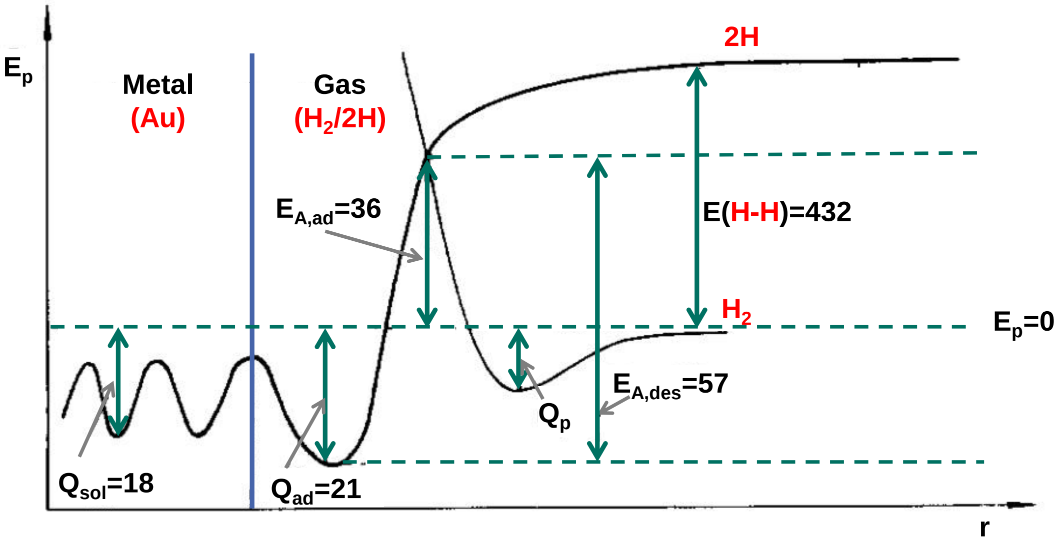

Figure 2.5: Model of dissociative H_2 adsorption on thin gold films at 78 K. The figure illustrates the potential energy for a complete (H_2) and a dissociated (2H) hydrogen molecule near a thin gold film surface at 78 K and in the bulk material. The H_2 molecule can dissociate and the two hydrogen atoms can be chemisorbed. They can recombine and desorb with an activation energy of $E_{\mathrm{A,des}} = 57$ kJ/mol, which was determined by TDS measurements. Q_{ad} is the heat of adsorption, $E_{\mathrm{A,ad}}$ is the activation energy of adsorption, E(H-H) is the dissociation energy of a hydrogen molecule, Q_{P} is the heat of physisorption of the hydrogen molecule, and Q_{sol} is the potential barrier for diffusion into the bulk material. All quantities are given in kJ/mol. Model according to [Sto94].

It was found that dissociative adsorption of molecular hydrogen is activated. The activation energy of the dissociative adsorption was calculated from the activation energy of associative desorption and the heat of adsorption [Sto94]. With these values the model of dissociative hydrogen adsorption on thin gold films, which is shown in figure 2.5, was developed[16].

Furthermore, it was found that adsorption of hydrogen on gold is dependent on the nanostructure of the gold surface [Sto99].

All known measurements were taken far below room temperature. Therefore, only few assumptions can be made concerning hydrogen or tritium adsorption at room temperature. Isotope effects have been observed for hydrogen and deuterium [Sto96]. Furthermore, the special characteristics of tritium have to be taken into account, which are described in the following section.

---

[16] An analogue model of the adsorption of hydrogen on aluminium at 150 K is described in [Boh98].

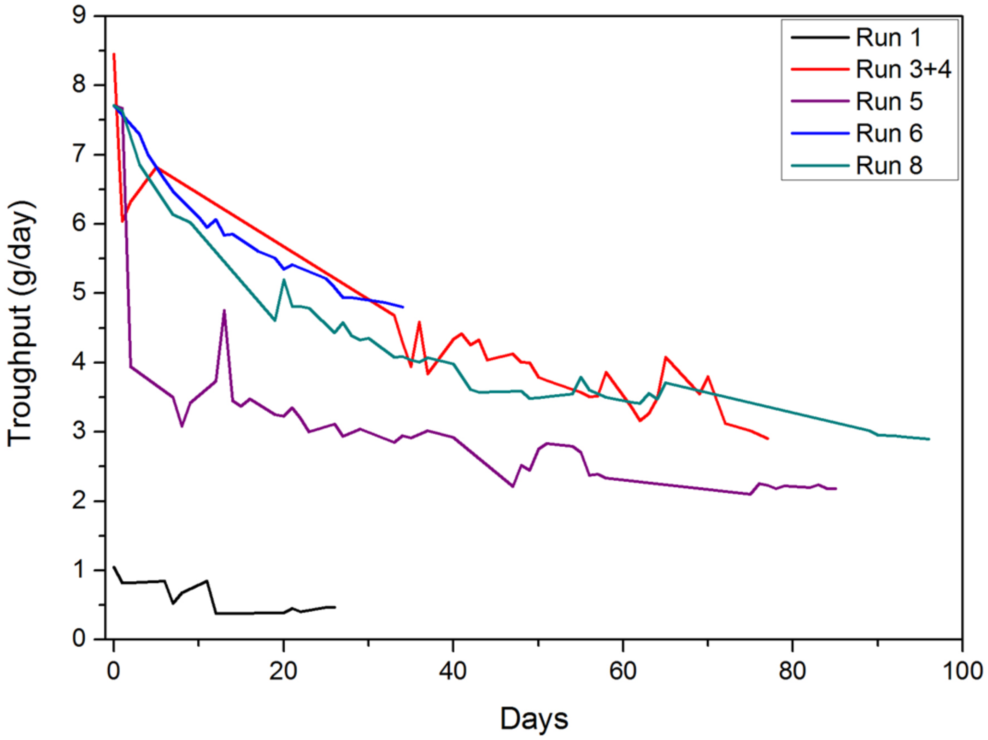

Figure 2.6: T_2 throughput in the TriToP experiment. Tritium was pumped in a closed cycle by a turbomolecular pump. The plots show a decreasing throughput in several runs. The missing tritium is expected to be sorbed somewhere in the system [Pri12].

2.6 Special characteristics of tritium adsorption/ desorption

Tritium adsorption on materials and absorption in materials, which are of interest in tritium technology, occurs. For example, it has been shown that tritium at room temperature sorbes on the surface of 316L stainless steel, which is frequently used in tritium technology. The amount of adsorbed tritium in the form of HTO is strongly dependent on the amount of reactive oxygen on the surface [Hir84].

In the TriTop experiment at TLK, it was shown that the amount of tritium which was pumped in a closed cycle with a Oerlikon Leybold MAG W 2800 turbomolecular pump decreased over time. Figure 2.6 shows the tritium throughput in the Tritop experiment. The missing tritium could be sorbed in the stainless steel, replacing hydrogen [Pri12].

There is no literature data available about the adsorption of tritium on relevant materials at the conditions of interest. It was found that HT does not adsorb on gold surfaces at room temperature and there is no catalytic exchange reaction between H_2O and HTO [Mat85]. Therefore, gold is considered to be the most suitable coating material for the reduction of tritium adsorption on surfaces of experimental setups (compare chapter 4).

One may suppose that tritium behaves similarly to hydrogen, but one has to take into account the following characteristics of tritium, which differentiate tritium from hydrogen:

- The tritium nucleus contains an additional neutron and is thereby heavier than hydrogen or deuterium is unknown. As an isotope effect was observed between hydrogen and deuterium, it is expected that this effect also occurs for tritium.
- The influence of radiochemical effects on adsorption. A tritiated gas mixture always contains atomic tritium. When a tritium atom bound in a T_2 molecule decays, the molecular bond is broken, leaving a tritium and a helium atom, of which at least one is ionized. The stream of impinging ions on a surface (compare equation 2.11) is determined by the number of ions generated by tritium decay and secondary ionization.
- If the β decay takes place in a magnetic field in a closed vacuum system, as it is the case in the KATRIN experiment (compare chapter 1), the $^3He^+$ or T^+ ions, which have a kinetic recoil energy, are guided towards a surface of the closed vacuum system, such as the KATRIN rear wall. The effect of the impinging ions on the coverage of this surface is currently unknown.

This leaves some open questions concerning tritium adsorption, which are important to the KATRIN experiment and tritium technology in general (compare chapter 1):

- How much tritium is expected to be adsorbed on rear wall candidate materials in the equilibrium state at the expected conditions?
- How much tritium is expected to be adsorbed on the windows of the BIXS activity monitor detectors in the equilibrium state at the expected conditions?
- Can the assumption be verified that gold is the most suitable material to reduce tritium adsorption?
- Which material is most suitable in order to reduce tritium adsorption?

The TRIADE experiment is designed to answer these questions. It uses β induced X-ray spectroscopy (BIXS), which is capable of detecting small amounts of tritium. The BIXS method is described in the following chapter.

Chapter 3

Basics of beta induced X-ray spectroscopy (BIXS)

In this chapter, the basics of BIXS, which is the main measurement principle used in TRIADE, are described. After a short introduction into the BIXS process in section 3.1, the physical processes which take place in a BIXS system are described in the sections 3.2 to 3.4. An example spectrum is discussed in section 3.5. Sections 3.6 and 3.7 give an insight into the applications of the BIXS method, as they will be implemented in TRIADE. Section 3.8 presents a type of detector which is suitable to be used for BIXS. In section 3.9 a former experiment (TriReX) using BIXS at TLK is described, as the TRIADE design was strongly influenced by this experiment.

3.1 Overview

BIXS is a method for the non-invasive detection of β activities. Therefore, it can be used for the detection of any β emitter. It has been used for the detection of β emitters in solids [Tor05], liquids [Wes60] and gases [Röl11]. Since tritium is the only β emitter of interest in this work, the following discussion refers only to tritium.

The basic principle of the BIXS method is shown in figure 3.1. Tritium decays into ^{3}He, an electron antineutrino and an electron. A fraction of the emitted electrons hit a body which will be referred to as the "X-ray producing element" in the following. A fraction of the β electrons produces X-rays in the X-ray producing element and part of the produced X-rays can be detected by an X-ray detector. The rate detected by the detector is related to the activity of the β source. The resulting spectrum allows conclusions concerning the type of β source and materials used in the system.

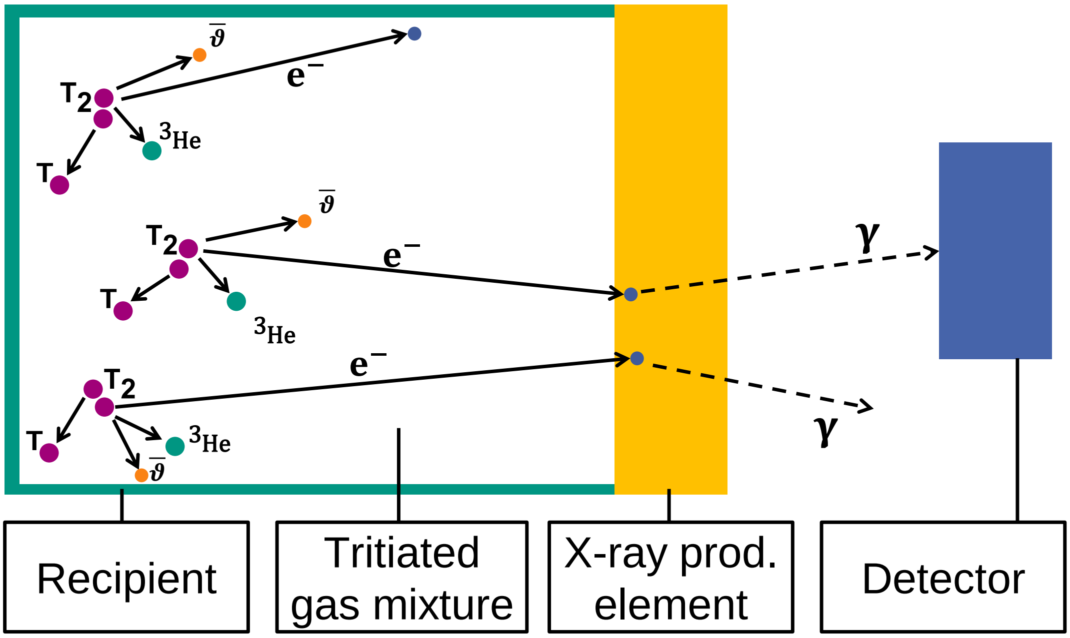

Figure 3.1: Simplified BIXS schematic. The schematic illustrates the principle of BIXS: Tritium inside the recipient decays, the emitted electrons enter a solid state body in which they produce bremsstrahlung which can be detected by a detector.

A simple BIXS-system for monitoring a system containing tritium requires three essential components:

1. A recipient, which contains the tritiated sample: Due to the hazards of tritium, which is a radioactive isotope of hydrogen, this recipient (and all of the needed instrumentation and infrastructure attached to it) needs to meet safety criteria, in order to prevent tritium from escaping the setup. In the context of this work, the recipient will contain a solid material sample and a gas mixture with variable tritium content[17]. Usually the recipient will be a certified stainless steel vacuum vessel with flanges for the fully metalic sealed connection of instrumentation and infrastructure.

2. An X-ray producing element: In order to achieve a low detection limit for the activity in the recipient, the conversion of the kinetic energy of the electrons into X-rays should be as efficient as possible. At the same time the element should be as transparent to photons as possible, in order to avoid the produced X-rays to be absorbed by the element itself[18]. Additionally this body needs to safely prevent tritium from leaking out of the recipient.

3. An X-ray detector: The detector should have a large absorption probability for photons with $E_\gamma \leq 18.6$ keV. In order to achieve a detection limit of < 1 monolayer of adsorbed tritium on a sample surface, combined with short measurement periods, it should have a low noise level. It should be able to process high count rates.

---

[17] concentration approximately up to 90%, variable pressure between 10^{-10} mbar and 800 mbar

[18] The solution to this apparent contradiction is described in section 4.3.2.1.

The three processes taking place in a BIXS-system are:

1. The β decay of a tritium atom (see section 3.2),
2. the interaction of electrons with matter, as they take place in the X-ray producing element (see section 3.3),
3. the interaction of photons with matter, as they take place in the detector and the X-ray producing element (see section 3.4).

The following subsections will give an overview of the physical fundamentals of these processes, which are essential for the design of a BIXS system and the selection of suitable materials.

3.2 The tritium beta decay

Tritium decays into ^{3}He emitting an electron. The β decay electrons are emitted with a continuous energy distribution, although a discrete amount of energy is set free. In order to explain the continuous spectrum and to solve the apparent contradiction to the law of energy conservation, Pauli postulated the neutrino [Pau30] in 1930, which carries a variable fraction of the released energy [Ott08]:

$$\mathrm{T} \;\rightarrow\; {}^3\mathrm{He}^+ \;+\; \mathrm{e}^- \;+\; \bar{\nu}_\mathrm{e} \;+\; \mathrm{Q}\ . \tag{3.1}$$

The so called Q-value is the surplus energy released, which is shared between the kinetic energy of the β particle (E), the total energy of the neutrino ($E_{\mathrm{tot}\ \bar{\nu}_\mathrm{e}}$), the recoil energy carried by the daughter nucleus (E_rec) and its final state excitation energy (V_j) [Ott08]:

$$Q = E + E_{\mathrm{tot}\ \bar{\nu}_\mathrm{e}} + E_\mathrm{rec} + V_\mathrm{j}\ . \tag{3.2}$$

The Q-value for the decay of atomic tritium is 18589 eV [Nag06]. In the case of zero neutrino mass and the ^{3}He$^+$ nucleus produced at rest in the ground state, the Q-value represents the maximum kinetic energy of the emitted electron. This kinetic energy of the electron is available for the production of X-rays in an X-ray producing element of a BIXS-system. The energy spectrum of the β decay electrons is given by[19] [Alt03]:

$$\begin{aligned}\frac{\mathrm{d}^2N}{\mathrm{d}t\mathrm{d}E} &= C\cdot F\left(E,Z+1\right)\ \cdot\ p_\mathrm{e}\ \cdot\ \left(E+m_\mathrm{e}\right)\cdot\left(E_0-E\right)\\ &\cdot\sqrt{\left(E_0-E\right)^2-m_\nu^2}\ \cdot\ \theta\ \cdot\ \left(E_0-E-m_\nu\right)\ ,\end{aligned} \tag{3.3}$$

where $F\left(E,Z+1\right)$ is the Fermi function which takes into account the Coulomb interaction of the emitted electron with the daughter nucleus, E is the kinetic energy of the electron, E_0 is the maximum energy of the electron with $m_\nu = 0$ and p_e is the momentum of the electron. Energy conservation is represented by the theta function. The constant C is given by:

$$C = \frac{G_\mathrm{F}^2}{2\pi^3\hbar^7}\cos^2\theta_\mathrm{c}\left|M_\mathrm{nuc}\right|^2\ , \tag{3.4}$$

where G_F is the Fermi constant, θ_c is the Cabibbo angle and M_nuc is the nuclear matrix element.

---

[19] with the vacuum speed of light set to $c = 1$.

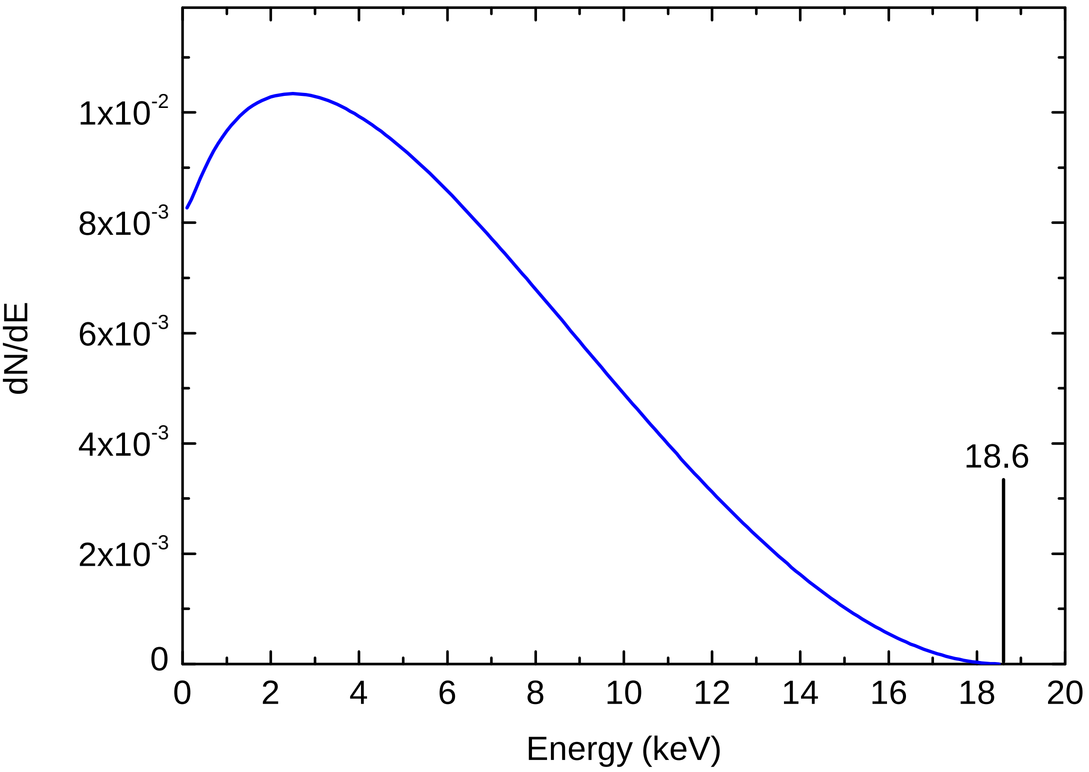

Figure 3.2: Energy distribution of tritium β decay electrons. The maximum energy of the tritium β decay electrons is 18589 eV, the mean electron energy is 5.7 keV. Tritium decays with a half-life of 12.3 y [Alt03].

3.3 Interactions of electrons with matter

If electrons enter matter, their interaction is dominated by electromagnetic interaction, which is described by Coulomb's law. The energy loss of electrons impinging matter is dominated by ionization and bremsstrahlung [Dem10b], which are described in the following. Elastic scattering processes are not of interest for the BIXS method as no photons are produced during these processes. Therefore, they are not further described in this work.

Ionization and characteristic γ-radiation

When an electron is scattered inelastically on an atomic electron, the atom can be ionized. The incident electron loses a part of its energy during this process. The energy loss can be described by [Dem10b]:

$$\frac{\mathrm{d}E}{\mathrm{d}x} \approx \frac{Z^2 e^4 n_\mathrm{e}}{4\pi\epsilon_0^2 m_\mathrm{e} v^2} \ln \frac{m_\mathrm{e} v^2}{2\left\langle E_\mathrm{b}\right\rangle} \ , \tag{3.5}$$

where $\langle E_\mathrm{b}\rangle$ is the mean binding energy of the atomic electrons, Z is the atomic number of the medium, n_e is the electron density in the medium, v is the velocity of the electron, e is the elementary charge, m_e is the mass of the electron and ϵ_0 is the electric field constant.

If atoms are ionized by electrons or photons, the vacant energy level of the electron which is released from the atom can be filled up by either an electron of a higher energy level or a free electron. In this process a discrete amount of energy is set free and a photon of the released energy is emitted. The energy of these characteristic X-rays is given by the energy difference between the two shells and is described by Moseley's law [Gru08]:

$$E_\gamma = Ry(Z-1)^2\left(\frac{1}{n^2}-\frac{1}{m^2}\right) \ , \tag{3.6}$$

where E_γ is the released photon energy, $Ry = 13.6$ eV is Rydberg's constant, Z is the atomic number and n and m are the principal quantum numbers characterizing the atomic shells. As the energy levels of the electron shells are specific for every element, characteristic radiation can be used for the identification of elements. In the following, the "Siegbahn" notation will be used, where the Kα_1-line means the transition:

$$E_\gamma = E_{\text{bind, }(n=2,l=1,j=3/2)} - E_{\text{bind, }(n=1,l=0,j=1/2)} \ , \tag{3.7}$$

where n is the principal quantum number, l is the angular quantum number and m is the magnetic quantum number. A list of characteristic X-ray energies can be found in [Tho09]. The characteristic radiation results in Gaussian peaks, which superimpose the continuous bremsstrahlung spectrum. The full width at half maximum (FWHM) of these peaks is mainly determined by the energy resolution of the detector. Characteristic peaks in the spectrum allow conclusions concerning the elements in the system. Furthermore, an energy calibration can be performed based on identifiable characteristic peaks. Therefore, a good energy resolution of the detector is of interest in a BIXS system.

Bremsstrahlung

Electrons which enter matter can be scattered inelastically by nuclei and produce a continuous spectrum of bremsstrahlung. The energy loss by bremsstrahlung can be described by [Kri12]:

$$\left(\frac{\mathrm{d}E}{\mathrm{d}x}\right)_{\text{brems}} = \frac{\rho\ \alpha\ Z^2\ r_\mathrm{e}^2\ E_\mathrm{tot}}{u\ A_\mathrm{r}}\left(R_{\mathrm{rad,n}}+\frac{1}{Z}R_{\mathrm{rad,e}}\right) \ , \tag{3.8}$$

where E_tot is the total energy of the electrons, x is the penetration depth, ρ is the density of the material, α is the fine structure constant, Z is the atomic number of the material, r_e is the classical electron radius, u is the atomic mass unit, A_r is the relative atomic mass and R_rad are dimensionless functions, containing the scaled cross sections for bremsstrahlung. The index n stands for the production of bremsstrahlung in the nuclear electromagnetic field and e stands for the production of bremsstrahlung in the electromagnetic field of atomic electrons. The lost energy is converted to X-rays. The dependency of the energy loss on the material's atomic number Z is important, as it is of interest in a BIXS-system that the β decay electrons produce as much detectable radiation as possible. So for this reason, a high Z material is favorable for the X-ray producing element.

The relative intensity distribution of bremsstrahlung is shown in figure 3.3, the angular distribution is shown in figure 3.4.

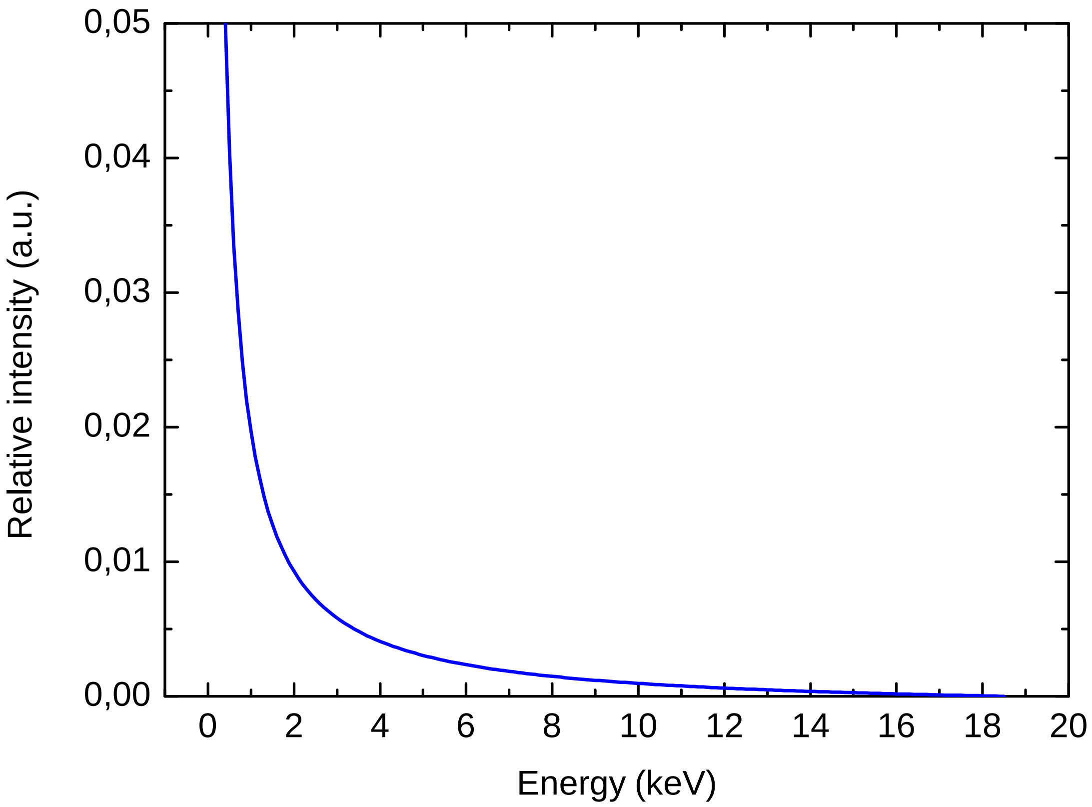

Figure 3.3: Bremsstrahlung spectrum according to Kramer's law [Lag77]. The bremsstrahlung spectrum for monoenergetic electrons of $E_{\mathrm{kin}}^{\mathrm{e}} = 18{,}6$ keV is shown in arbitrary units.

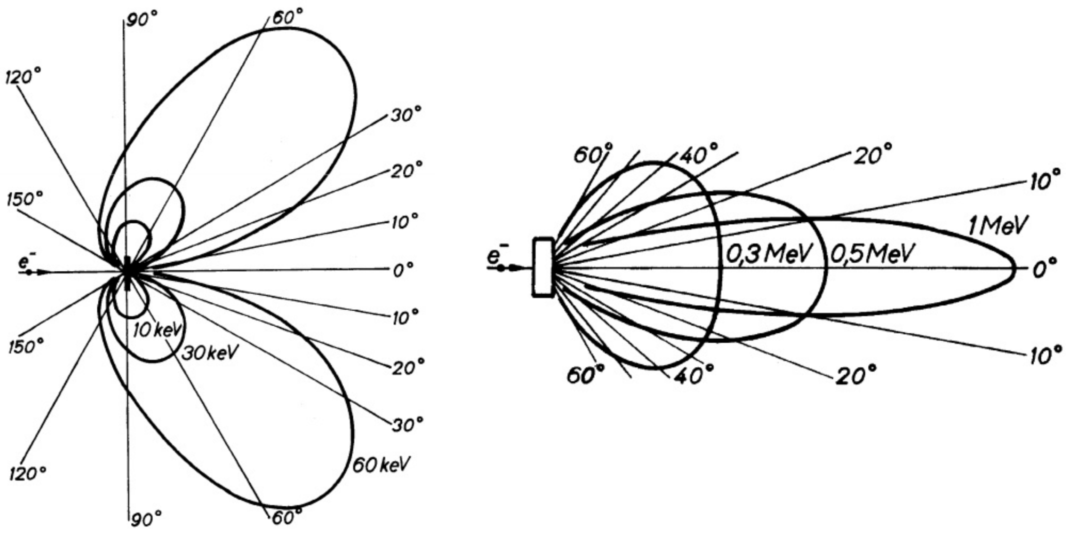

Figure 3.4: Angular distribution of bremsstrahlung. The angular distribution is shown for a thin target on the left side and for a thick target on the right side [Kri12].

3.4 Interactions of photons with matter

The following treatment of photon interactions is based on [Gru08]. As all of the photon interactions are statistical processes, it is impossible to define a range for photons. A photon beam is attenuated exponentially in matter according to:

$$I(x) = I_0 \, e^{-\mu_{\text{total}} x} \ , \tag{3.9}$$

where I is the intensity of the photon beam, I_0 is the initial intensity of the photon beam, $x = d \cdot \rho$ is an area density (penetration depth d multiplied by the density of the target material ρ) and μ is the total attenuation coefficient. The partial attenuation coefficients are related to the cross sections of the possible interactions:

$$\mu_i = \frac{N_A}{M} \, \sigma_i \ , \tag{3.10}$$

where σ_i is the cross section for one type of interaction, N_A is the Avogadro number and M is the molar mass of the target material. The total attenuation coefficient is defined by:

$$\mu_{\text{total}} = \sum_i \mu_i = \frac{N_A}{M} \sum_i \sigma_i \ . \tag{3.11}$$

There are six ways for photons to interact with matter [Dem10b]:

- photoelectric absorption,
- nuclear photoelectric absorption,
- inelastic scattering (Compton or Raman scattering),
- elastic scattering (Rayleigh or Thomson scattering),
- nuclear pair production,
- electron pair production.

The attenuation coefficients for these interactions are strongly dependent on the photon energy. Figure 3.5 shows mass attenuation coefficients for photons in gold. It becomes clear that at energies of $E_\gamma \leq 18.6$ keV photoelectric absorption and coherent scattering are the dominant processes.

During nuclear photoelectric absorption a photon is absorbed by an atomic nucleus, causing it to enter an excited state. The energies needed for this process are are much larger than the Q-value of the tritium decay. They are of the scale of nuclear binding energies (i.e. MeV) [Dem10b]. Therefore, nuclear photoelectric absorption will not be discussed.

During nuclear or electron pair production an electron positron pair is produced in the electric field of a nucleus or an atomic electron. The lower energy limit for pair production of $E_{\text{pair}}^{\text{min}} = 2 m_{\text{e}} c^2$ is larger than the tritium Q-value. So it is not possible for the β induced photons to interact by pair production. Therefore, pair production is not of interest for this work.

During photoelectric absorption, a photon of the energy $E_\gamma = hf$ is absorbed and an atomic electron is emitted. The photoelectron leaves the atom with a kinetic energy of

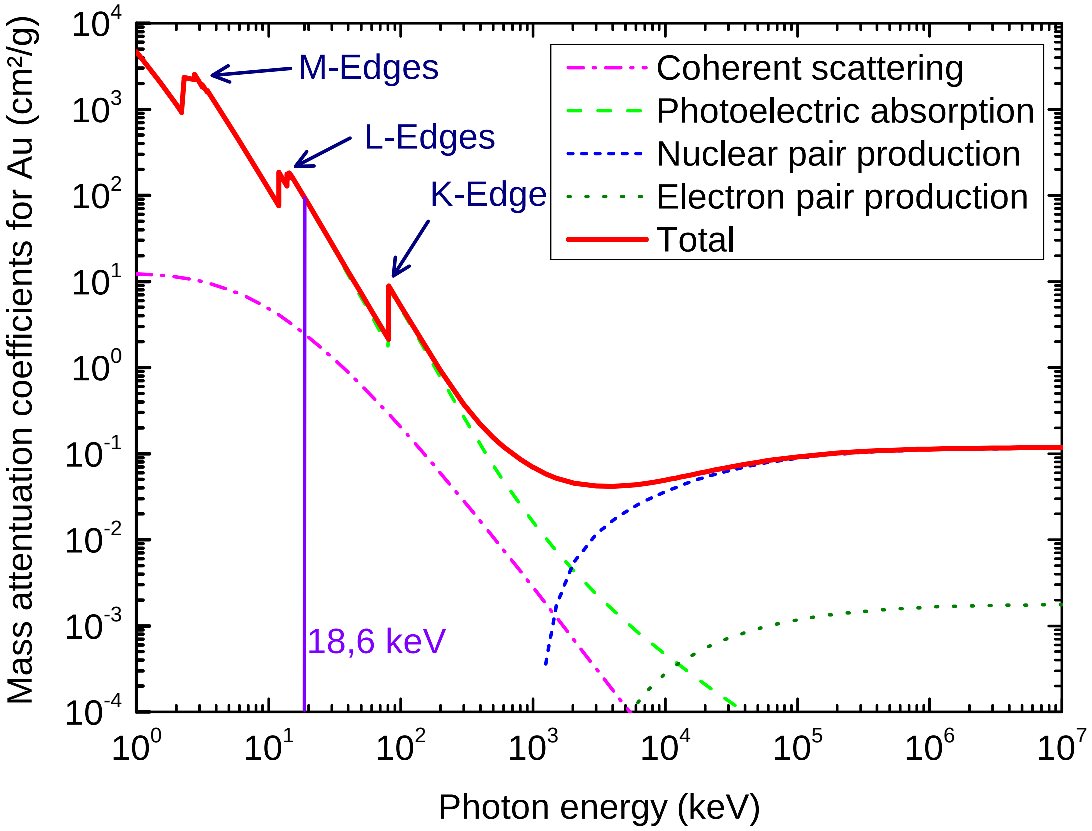

Figure 3.5: Mass attenuation coefficients for gold. The graph shows the total mass attenuation coefficient and the partial attenuation coefficients for possible photon interactions: Coherent scattering, incoherent scattering, photoelectric absorption, nuclear pair production and electron pair production. The data for this plot is taken from [Sel04].

$E_\mathrm{e} = hf - E_\mathrm{bind}$. In a non-relativistic range away from the absorption edges, the total photoelectric cross section is given by the Born-approximation [Gru08]:

$$\sigma_\mathrm{photo} = \left(\frac{32}{\epsilon^7}\right)^{\frac{1}{2}} \alpha^4 \cdot Z^5 \cdot \sigma^e_\mathrm{Th} \;, \tag{3.12}$$

where σ_photo is the total photoelectric cross section, $\epsilon = E_\gamma / m_\mathrm{e} c^2$ is the reduced photon energy, α is the fine-structure constant, Z is the atomic number of the absorbing material and $\sigma^e_\mathrm{Th} = \frac{8}{3}\pi r_\mathrm{e}^2$ is the Thomson cross section. The photoelectric absorption cross section is strongly dependent on Z and on $E_\gamma^{-7/2}$, which causes it to be the dominant interaction for low photon energies.

Compton scattering is an inelastic scattering of photons by quasi-free atomic electrons. For medium photon energies $E_\mathrm{bind} << E_\gamma << m_\mathrm{e} c^2$ the cross section for Compton scattering can be written as a Taylor series [Dem10b]:

$$\sigma_c = \frac{8}{3}\pi r_\mathrm{e}^2 \; Z \left(1 - \frac{2E_\gamma}{m_\mathrm{e}c^2} + \frac{26}{5}\left(\frac{E_\gamma}{m_\mathrm{e}c^2}\right)^2 + \ldots\right) \;, \tag{3.13}$$

where r_e is the classical electron radius, Z is the atomic number and c is the vacuum speed of light.

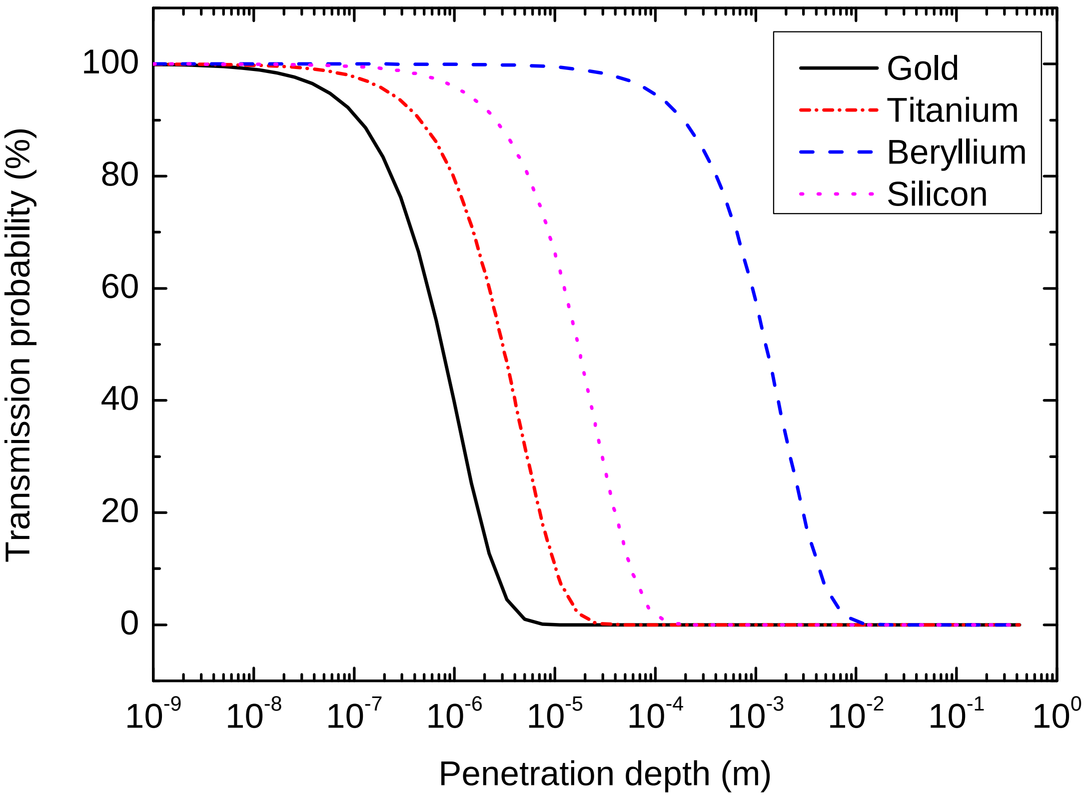

Figure 3.6: X-ray Transmission for different materials. Shown is the photon transmission probability of 5.7 keV photons for gold, titanium, beryllium and silicon as a function of the penetration depth. The data is taken from [Sel04].

Transmission of X-rays

The cross sections determine the probability of interactions of photons and thereby also absorption and transmission of X-rays through matter. Combining equations 3.9 to 3.13 one gets:

$$T = \frac{I(d)}{I_0} = e^{-\frac{N_A}{M}\sum_i \sigma_i \rho d} = e^{-\mu_{\text{tot}}\rho d} \ . \tag{3.14}$$

The transmission probability is important for two reasons when designing a BIXS system: Self absorption in the X-ray producing element should be minimized, meaning that materials with low $\mu_{\text{tot}} \cdot \rho$ are favorable for this reason. Low Z materials are more transparent to X-rays because of the strong dependency of the cross sections on Z (compare eq. 3.12 and 3.13). Therefore, low Z materials should be chosen to be used in the X-ray producing element for this reason[20].

In contrast it is favorable that a maximum of the photon energy is absorbed in the detector chip. In figure 3.6 the transmission probabilities for photons of the average β decay electron energy as an example are shown dependent on the penetration depth.

---

[20] As mentioned in section 3.3, also the production of bremsstrahlung should be maximized in the X-ray producing element, which makes a high Z material favorable. So the choice of the materials for the X-ray producing element is always a trade-off between maximizing bremsstrahlung and minimizing self absorption.

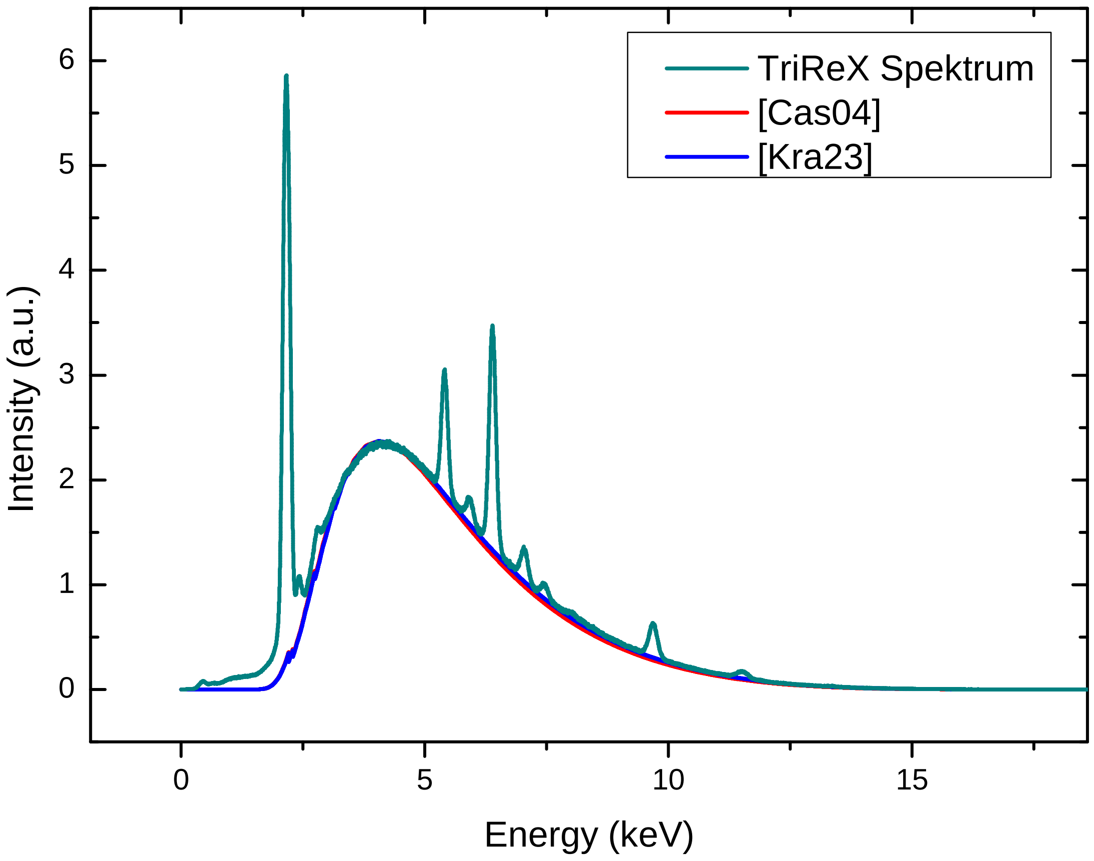

Figure 3.7: BIXS spectrum calculated for and measured by the TriReX experiment. Spectra are calculated according to [Cas04] and [Kra23]. The calculated spectra only include the continuous bremsstrahlung part of the spectrum. In the measured spectrum the continuous part is superimposed by characteristic X-rays [Röl12a].

3.5 The beta induced X-ray spectrum

In [Röl11] a spectrum for a BIXS system with tritium was calculated. It is shown in figure 3.7 together with a tritium measurement from the TriReX experiment, which is briefly described in section 3.9 and in detail in [Röl11] and [Ebe12]. As shown in the calculation in [Röl11], the shape of the continuous part of the spectrum is independent of the material the bremsstrahlung is produced in. Only the characteristic peaks in a measured spectrum allow conclusions concerning the material composition of the BIXS system.

3.6 The BIXS method for the detection of adsorbed tritium on solid surfaces

The BIXS-method can be used for the detection of tritium adsorbed on solid surfaces, as it is shown in figure 3.8. In an ideal case, the activity on the sample surface would be the only source for the signal in the detector. In this case, there would be a distinct relation between the measured count rate and surface activity. From this the

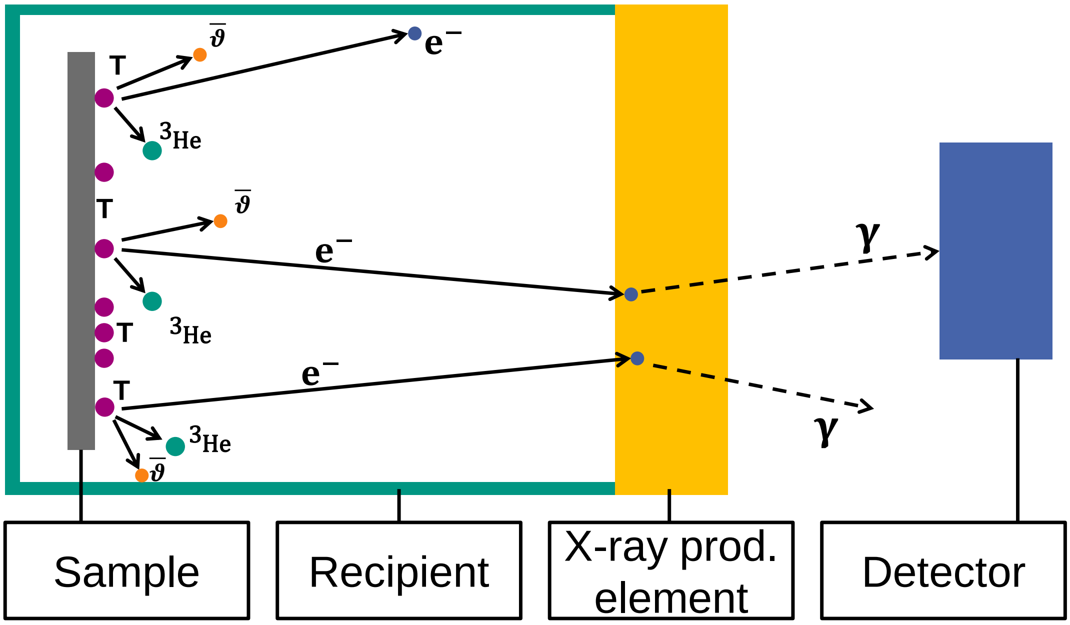

Figure 3.8: Schematic of the BIXS method for the determination of the amount of tritium adsorbed on solid surfaces. A solid sample with tritium adsorbed on its surface is placed inside the recipient. The activity of the tritium adsorbed on the sample surface is detected using the BIXS method.

amount of adsorbed tritium could be calculated. In reality background signal can result from other processes. Residual tritium located anywhere in the recipient can produce bremsstrahlung in any material used in the recipient. Tritium can be located

- adsorbed on the sample,
- adsorbed on the X-ray producing element,
- adsorbed on other surfaces of the recipient such as walls,
- in the residual gas in the recipient.

From all of these locations it is generally possible for β decay electrons to enter any material used in the recipient and to produce X-rays, which can be detected by the detector. As it is only of interest that tritium adsorbed on the sample causes a detector signal, all other possibilities of signal formation are considered as sources of background signals. In figure 3.9 an overview of the possible processes is given.

All the listed signals are dependent on pressure and temperature in the recipient and can not be measured independently. As mentioned in section 3.5, the background signals can not be identified by analysis of the shape of the continuous part of the spectrum. Although the analysis of the height of the characteristic peaks allows conclusions concerning background signals, they can not be distinguished from the signal from adsorbed tritium on the sample surface. Therefore, all sources of background signals have to be minimized in order to meet the requirements of a low detection limit (according to section 4.2.1). An additional source of background signal is the detector noise. This

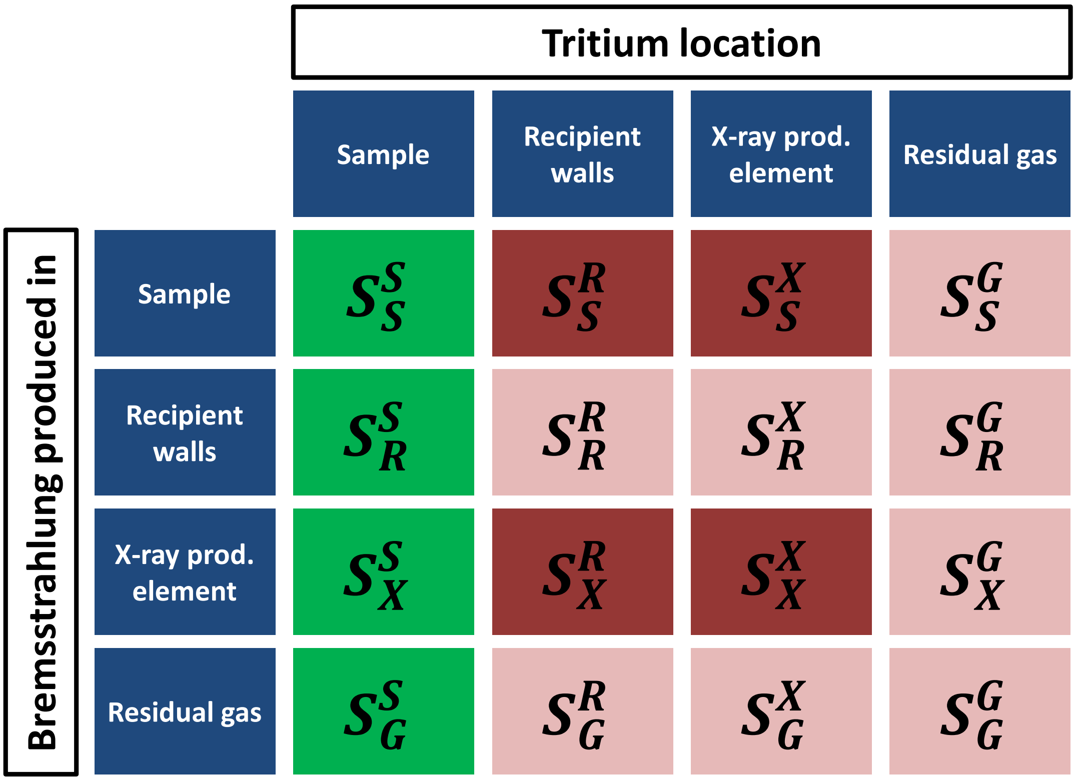

		Tritium location			
		Sample	Recipient walls	X-ray prod. element	Residual gas
Bremsstrahlung produced in	Sample	S_S^S	S_S^R	S_S^X	S_S^G
	Recipient walls	S_R^S	S_R^R	S_R^X	S_R^G
	X-ray prod. element	S_X^S	S_X^R	S_X^X	S_X^G
	Residual gas	S_G^S	S_G^R	S_G^X	S_G^G

Figure 3.9: Overview of possible processes of X-ray production. The matrix lists the possible origins of β decay electrons (the location of decaying tritium) and the locations, where these electrons can produce bremsstrahlung. S_i^j stands for the detector signal which is generated by the process where tritium in the location j decays and the β decay electrons produce X-rays in the material i. Here S stands for the sample, R stands for the recipient materials, X stands for the X-ray producing element and G stands for the residual gas. The signals S_i^S (green, i arbitrary) originate from the sample surface activity. The light red boxes are used for signals which can be reduced to a minimum by the design of the BIXS system. The dark red boxes are used for signals which can not be reduced. The influence of these signals can be simulated.

is the only background signal which can be assumed constant, as the detector temperature is stabilized and detector parameters will not be changed after the initial setup. The noise can be measured independently. In order to reduce unintended background signals, the following steps can be considered:

- Reducing the adsorption of tritium on all surfaces other than the sample by coating the surfaces: Hereby the signals S_i^R and S_i^X (for arbitrary i) could be reduced. It has to be made sure that a coating on the X-ray producing element does not reduce the number of β decay electrons entering the element.
- Electromagnetic guiding of electrons: By applying a magnetic field to the recipient, the electrons could be guided on a path which is approximately orthogonal to the plane of the X-ray producing element. By the selection of a suitable geometry, the signals S_S^R and S_X^R can be reduced.
- Restriction of detector's field of sight: As low energy photons are absorbed in matter on the mm-scale (compare section 3.4 and figure 3.6), it should be technically possible to avoid photons which were produced in the recipient materials, from entering the X-ray producing element and practically reduce the signals S_R^j (for arbitrary j) to zero.
- Low residual gas pressure: By pumping down the system to pressures as low as possible, S_i^G (arbitrary i) can be reduced. The signals S_G^j become negligible, when the density of the residual gas is very low (e.g. of the order of 10^{-15} g/l at 10^{-10} mbar for hydrogen), because the intensity of bremsstrahlung is proportional to the density of the material (compare equation 3.8). Furthermore, at low residual gas pressures, electrons from tritium on the sample surface lose less energy on their path through the residual gas.
- Baking out the system: As tritium is an isotope of hydrogen, exchange reactions of tritium with water are possible [Eic09]. This means that residual water in the system is able to bind large amounts of tritium. Baking out the system reduces the amount of residual water and thereby the amount of bound tritium in this water. So an increase of the signals $S_i^{R/X/G}$ can be avoided by baking out the system.
- Usage of low noise detector and optimization of detector parameters for low background.

The overall aim is to reduce the background signals in order to make the signals (S_i^S) which are proportional to the sample surface activity dominant. If the adsorption of tritium on one sample (e.g. on gold) is found to be negligible, the background can additionally be measured and later be subtracted from measurement data.

3.7 The BIXS method for the detection of tritium diffused into the bulk material

When tritium has diffused into material, it can still be detected by BIXS. The probabilities of β decay electrons escaping the material or producing bremsstrahlung in the

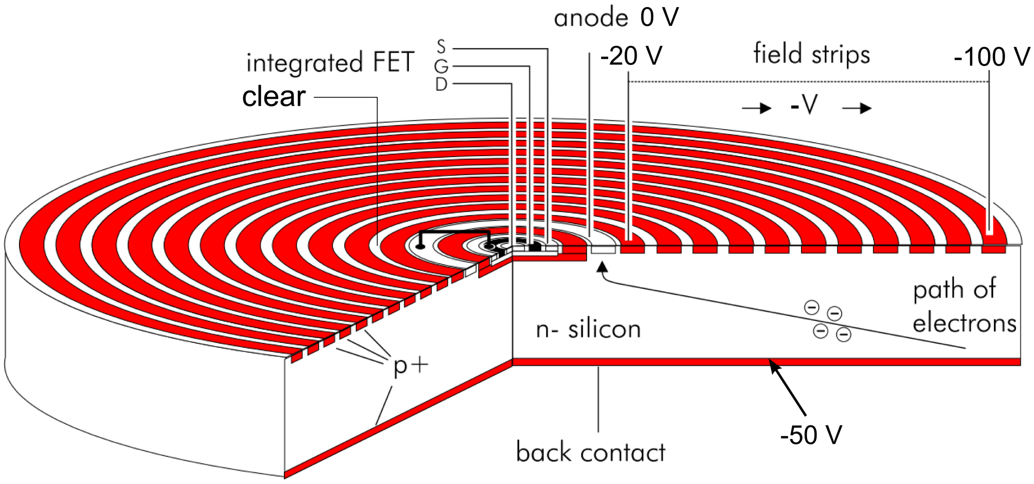

Figure 3.10: Schematic of a silicon drift detector (SDD). The figure shows the schematic setup of a silicon drift detector [Lec01]. The principle is described in the text.

material and a signal in a BIXS system are dependent on the tritium depth distribution. So a measured BIXS spectrum contains information about the tritium depth distribution. In order to use this information, the spectrum caused by thin layers (d $\leq 1\mu$m) of material containing diffused tritium close to the surface can be simulated in Monte Carlo simulations. These simulated spectra can be fitted to measured spectra. The tritium depth distribution is obtained as a series of fitting parameters in this method. This method has already been applied [Tor05], [Mat03]. It was shown that the depth of diffused tritium mainly affects the continuous bremsstrahlung spectrum. This technique can reach depths up to 0.1 mm in metals. Compared to other techniques such as acid etching methods the non destructive character of the BIXS method is an advantage, especially because no mixed radioactive and chemically hazardous waste is produced.

3.8 Silicon drift detectors for BIXS

The detector in a BIXS-system should have a low background signal (compare section 3.6), a good energy resolution (compare section 3.7) and it should have a large absorption probability for photons in the energy range of interest ($E_\gamma \leq 18.6$ keV). Furthermore, a large active volume is advantageous.

Silicon drift detectors (SDDs), which were introduced by E.Gatti and P.Rehak in 1983 [Gat84], are a suitable solution for this task, therefore an SDD will be used in TRIADE. The following section should give an insight into the principles of SDDs and why they are suitable to meet the requirements for a BIXS-system. The SDD, which will be used in TRIADE, will be described in section 4.1. The characterization measurements with the used detector are discussed in section 5.1.

Figure 3.10 shows the basic principle of a silicon drift detector. It is alike to the principle of other planar photodiodes, but an SDD has a unique electrode structure. On the backside, the SDD has a planar back contact, on the opposite side circular and

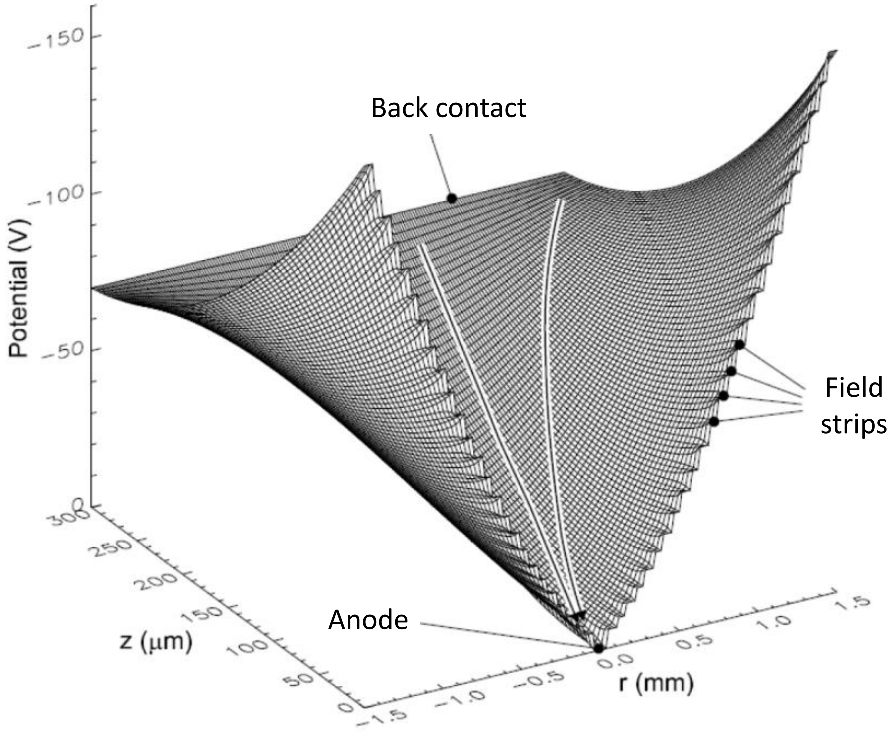

Figure 3.11: Potential in the SDD. The figure shows the Potential for free electrons, which are produced by incoming radiation in the detector chip. The Potential has its minimum in the anode of the detector [Rei12].

concentric electrodes are located. The back contact is on voltage of -50 V, the voltage of the concentric electrodes rises from -100 V of the outer ring to -20 V on the inner ring. The electrodes are p^+ doped, while the sensitive detector volume is n^- doped. The anode, which is located in the center of the detector, is n^+ doped. So a volume free of charge carriers develops. In this volume ionizing radiation causes electron hole pairs. Due to the circular structure of the electrodes and the increasing voltage towards the anode, an inhomogeneous drift field is built, which has its potential minimum in the anode for electrons. So electrons from anywhere inside the active volume drift towards the anode and produce a signal current, while positively charged holes drift towards the back contact. The potential inside the SDD is shown in figure 3.11. The anode is connected to a junction gate field-effect transistor (JFET), which serves as the first preamplifier in the system [Amp11].

The input voltage noise is the dominant source of noise in semiconductor detectors [Röl11]. This noise is proportional to the capacitance of the detector and increases at short shaping times. The capacitance of the detector and thereby the noise can be reduced by minimization of the anode area, which is achieved by the structure described before. The electrons are guided to the anode by the drift field, so the active volume of the diode is enlarged by adding more electrodes with the same anode area. The input capacitance becomes independent of the detector area [Amp11].

The capacitance can be further minimized by direct mounting the first pre-amplifier, an n-channel JFET directly on the SDD. Thereby, unnecessary capacitances originating from the connection of anode to the JFET are avoided. This further improves the signal to noise ratio. Further noise reduction can be realized by cooling. Usually SDDs are cooled by Peltier elements, as energy resolutions below 200 eV are reachable without cryogenic cooling and at comparatively short shaping times[21] [Fio08]. Short shaping times are favorable, as the shaping time limits the maximum count rate for the detector.

3.9 Experiences with BIXS from the tritium rear wall experiment (TriReX)

The TRIADE motivation and design was strongly inspired by the results of the tritium rear wall experiment (TriReX). The implementation of the TriReX experiment is shown schematically in figure 3.12 and discussed in detail in [Röl11] and [Ebe12]. There were three major tasks for the TriReX experiment:

- Activity monitoring: It had to be shown that the activity inside the KATRIN windowless gaseous tritium source could be monitored using a BIXS system. The requirements for the monitoring system were a statistical uncertainty of $\leq 0.1\%$ in a measurement period of 1000 s at a source activity of 10^{11} Bq.
- Permeation behavior of protection windows: The BIXS detectors for KATRIN have to be protected from tritium atmosphere in order to avoid contamination and fulfill the requirements (TLA[22]) for vacuum systems containing tritium. TriReX was supposed to demonstrate that no larger amounts of tritium could permeate through beryllium windows.
- Adsorption behavior of tritium: TriReX was supposed to measure how much tritium had to be expected to adsorb on the rear wall and the windows of the KATRIN BIXS detectors, because of the systematic effects of tritium adsorption on these surfaces (compare chapter 1).

The following results were found during the TriReX experiment ([Röl11],[Röl12b] and [Ebe12]):

- In the TriReX experiment it was successfully shown that BIXS is a suitable method for the activity monitoring in the KATRIN WGTS. An almost linear relation was found between the tritium activity in the volume which was seen by the detector and the measured count rate.
- After 3 months of tritium measurements, there were no signs of tritium permeation through the used beryllium window.
- It was not possible to measure tritium adsorption in TriReX. Therefore a follow-up experiment for TriReX was required. The reasons why TriReX could not measure tritium adsorption are discussed below.

---

[21] of the order of µs

[22] "Technische Liefer- und Abnahmebedingungen", technical terms of delivery and acceptance of the Tritium Laboratory Karlsruhe, [TLA12]

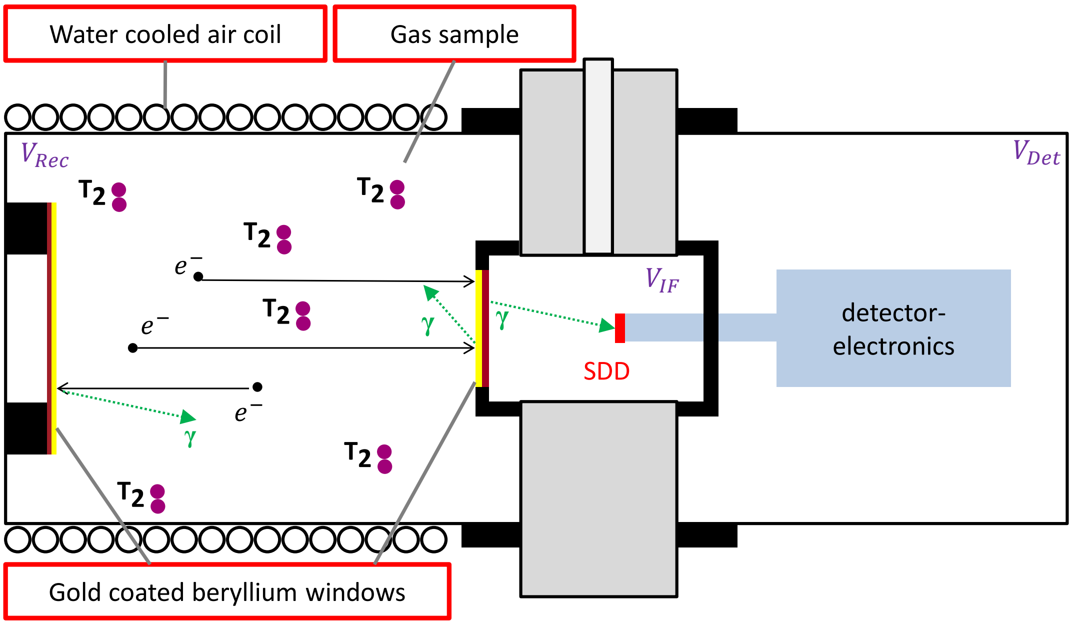

Figure 3.12: Schematic of the TriReX setup. The setup is split into three volumes: The recipient contains the gas mixture and two gold coated beryllium windows, which serve as X-ray producing elements. The left one is regarded as a model for the KATRIN rear wall. The volume in the center (V_{IF}) is located inside an intermediate flange. It contains the SDD. The third volume on the right side contains the detector electronics. The schematic also illustrates the BIXS process.

Adsorption was not measurable in the TriReX experiment, because a large memory effect was observed. The background counts increased with the number of measurements taken, as it can be seen in figure 3.13 and as it is described in [Röl12b]. One monolayer of adsorbed tritium equals an activity of roughly[23] 10^6 Bq/cm^2. The detection efficiency was of the order of 10^{-8} cps/Bq in the TriReX experiment [Röl12b] for the activity measurements for gaseous tritium. Therefore, the expected count rate for 1 monolayer of adsorbed tritium is several orders smaller than the memory effect, which was of the order of 10 cps. So the TriReX experiment was not sensitive to adsorption measurements.

The intrinsic noise of modern detectors (compare section 4.3.3) is of the order of 10^{-3}/s, so in principle it is possible to design a BIXS system which is sensitive to tritium adsorption, if the memory effect can be reduced.

Adsorbed tritium on the recipient's walls was identified as the main source of the memory effect [Röl12b]. The following lessons learned from the TriReX experiment were identified for the reduction of the memory effect. They made improvements possible for the TRIADE design:

- Gold coating of all surfaces inside the recipient: It is assumed that there is no significant tritium adsorption on gold coated surfaces (compare section 2.6). Therefore it was decided to fully coat the surfaces inside the TRIADE recipient with gold.
- Restriction of detector's field of sight: In the TriReX experiment characteristic peaks were visible in the spectrum, which were caused by X-rays produced in the stainless steel walls of the recipient. In order to reduce this signal, the detector's field of sight is restricted to the sample surface in the TRIADE experiment.
- Baking of system: The tritium adsorption capability of stainless steel is strongly connected to the amount of surface water [Eic09]. The tritium can be trapped by isotopic exchange reactions. Therefore the amount of tritium on the stainless steel walls can be reduced by baking residual water out of the system.

The TRIADE design is described in the following chapter.

---

[23] The calculation for this estimation can be found in appendix A

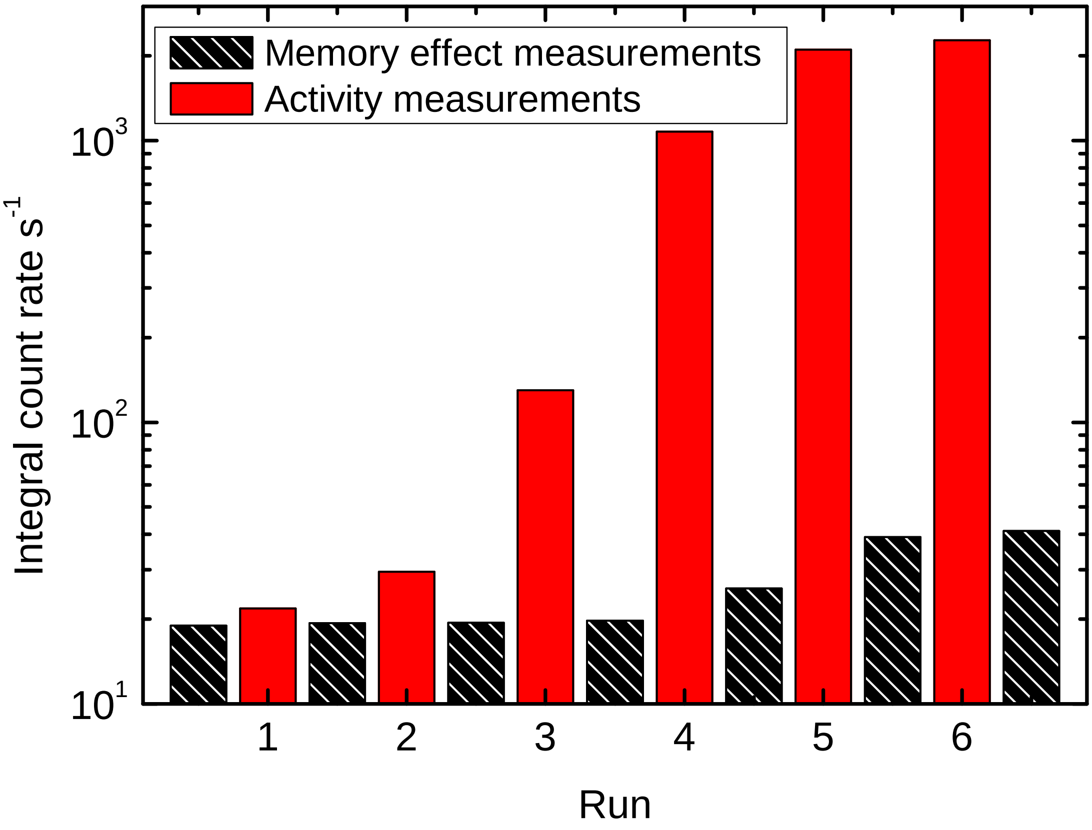

Figure 3.13: TriReX memory effect. Evolution of the background level before and after tritium measurement runs in the TriReX experiment [Röl12b]. Whenever a higher tritium activity was brought into the TriReX recipient for activity measurements, the background level which was measured after pumping down the recipient increased (black bars).

Chapter 4

Experimental setup of the Tritium Adsorption Desorption Experiment

In this chapter the experimental design and setup of the tritium adsorption desorption experiment are described. Section 4.1 gives an overview of the experimental setup. In section 4.2 the requirements for TRIADE are defined. In section 4.3 the design of the TRIADE core components is discussed and in section 4.4 the mass spectrometry setup is described. The pumping system and the procedural setup are described in sections 4.6 and 4.7.

4.1 Overview of the TRIADE experimental setup

Figure 4.1 gives an overview of the TRIADE subsystems, which are described in the following. The core components, which consist of three volumes and contain the whole BIXS setup, are described in section 4.3. Tritiated gas mixtures can be filled into the recipient through a sampling port in order to enable the gas to adsorb on the sample surface and in order to perform BIXS measurements. Gas from the recipient can be pumped through the volume of the mass spectrometer by the pumping system in order to analyze the gas mixture and desorbing atoms or molecules. The mass spectrometry setup is described in section 4.4. In order to store gas, it can be pumped into a buffer vessel and back into the recipient. Furthermore, gas can be pumped from the recipient or the buffer vessel to the TLK infrastructure, if it is no longer needed. The pumping system is described in section 4.6, the procedural setup is described in section 4.7. In order to make temperature stabilized and temperature dependent measurements possible, an adequate temperature management system is required. The cooling is implemented with a cold gas flow through a heat exchanger at the recipient. The cooling gas is produced by a cold gas system. The recipient can be heated with heating cables. The temperature management system is further described in section 4.5. The CAD model of the whole setup is shown in figure 4.2.

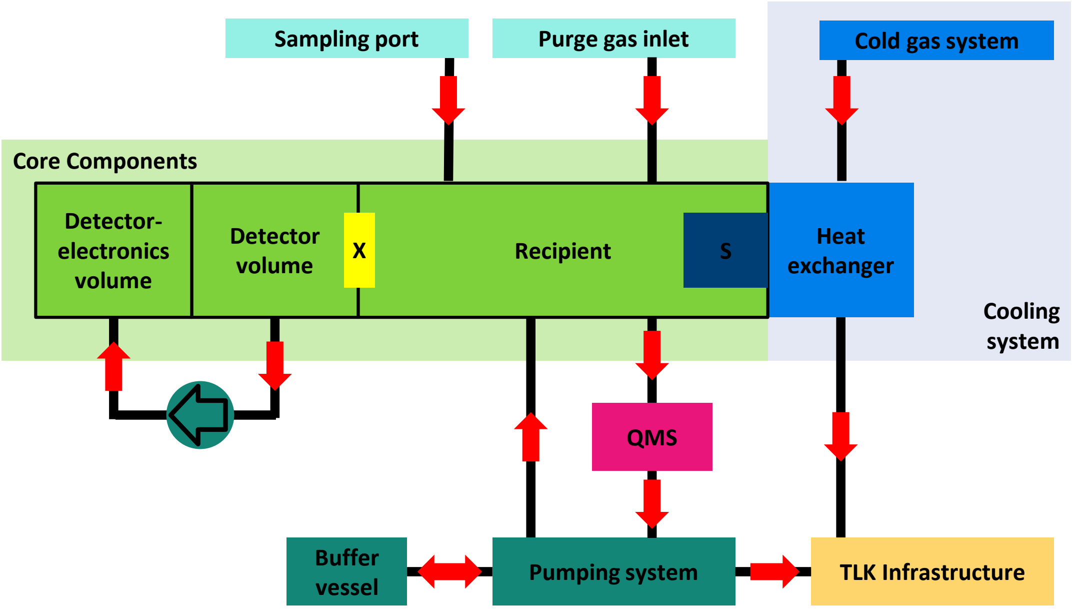

Figure 4.1: Simplified flow diagram of TRIADE. The figure gives an overview of the TRIADE subsystems. The yellow box, marked with "X" stands for the X-ray producing element. The dark blue box marked with a "S" stands for the sample. "QMS" indicates the quadrupole mass spectrometer. The red arrows indicate the directions of possible gas flows. The detailed flow diagram is shown in figure 4.13.

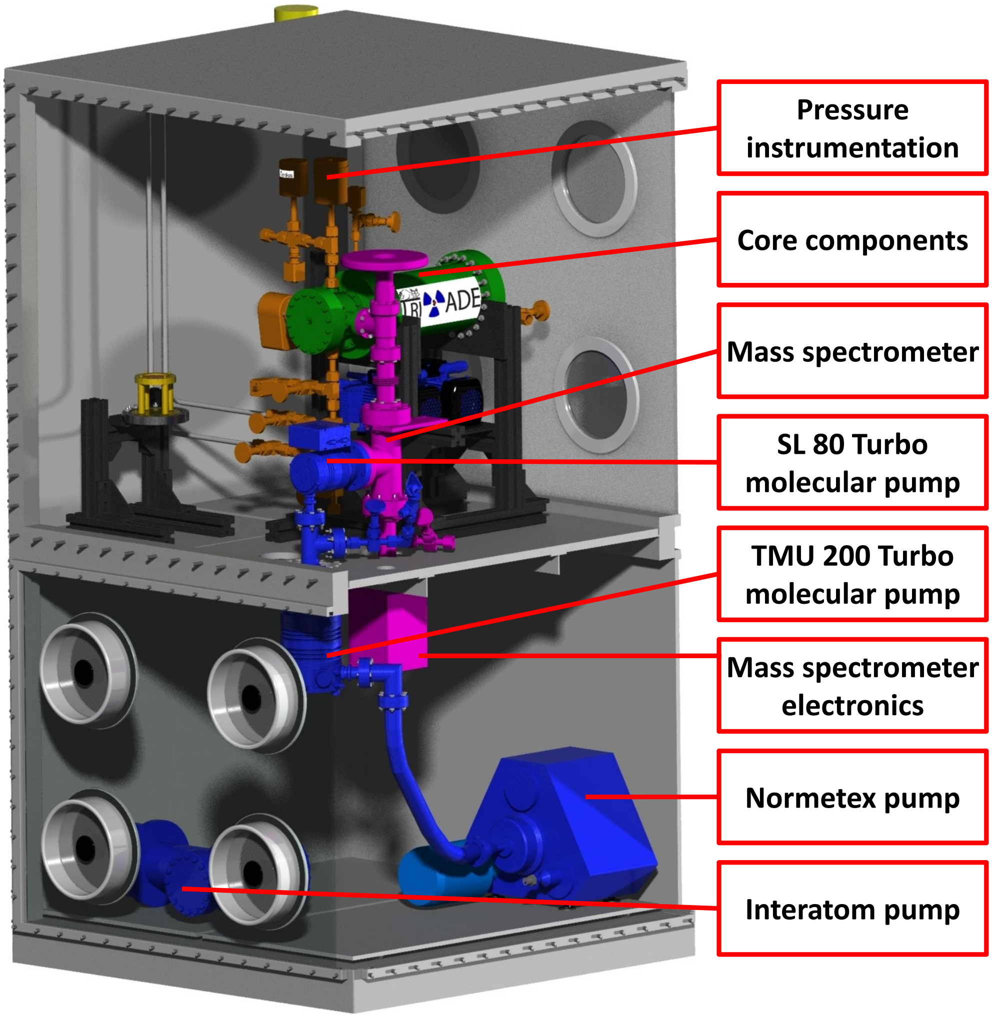

Figure 4.2: TRIADE CAD overview. The TRIADE setup was designed with Autodesk Inventor 2013©. The core components (green) are located in the upper part of the glove box. The recipient is connected to the pressure instrumentation (yellow) and the infrastructure. As many of the needed manual valves as possible are located next to the recipient, facing the same side of the box in order to optimize operability. The connection between the recipient and the pumping system (magenta) contains the mass spectrometer, whose electronics is fixed below the base plate. The length of the connections of the pumping system is minimized: The SL80 turbomolecular pump is attached to the mass spectrometer's volume, and the TMU200 turbomolecular pump is mounted to the ground plate right below the SL80. The scroll pump and the metal bellows pump are located at the bottom of the glove box. In order to simplify the sketch, some connection pipes are not visible in this overview. The procedural setup of TRIADE is discussed in section 4.7.

4.2 Requirements for TRIADE

There are physical requirements for the TRIADE experiment, which are described in section 4.2.1. The technical requirements, which result from safety regulations and the physical requirements, are described in section 4.2.2.

4.2.1 Physical requirements

In order to measure tritium adsorption with a sensitivity of < 1 monolayer, some physical requirements for the TRIADE setup must be fulfilled. The setup should be a further development of the BIXS method, as it is used in the TriReX experiment (see [Röl11] and [Ebe12]). Therefore the BIXS method should be implemented in the setup together with a second measurement method (mass spectrometry). The resulting technical requirements are described in section 4.2.2.

- General physical requirements for the implementation of the BIXS method for adsorption measurements are (compare section 3.1):
  - the possibility to expose a sample surface to tritium under controlled conditions (pressure, temperature),
  - an X-ray producing element in which the β decay electrons are fully absorbed producing bremsstrahlung, and which is as transparent to the produced X-rays as possible,
  - an X-ray spectrometer which detects the produced bremsstrahlung photons.
- In order to reach the desired detection limit of < 1 monolayer with the BIXS method, the background has to be reduced to a minimum. This means (compare section 3.6):
  - minimization of detector noise to the order of 10^{-3} cps,
  - restriction of the detector's field of sight to the sample surface by choice of a suitable geometry,
  - minimization of tritium adsorption on surfaces of the setup,
  - minimization of residual gas pressure to the order of $\leq 10^{-10}$ mbar,
  - minimization of humidity in the recipient[24].
- Physical requirements for mass spectrometric desorption measurements (compare section 2.4):
  - the possibility to analyze desorbing species with a quadrupole mass spectrometer,
  - the ability to heat the sample with a heating rate as constant as possible over a range of approximately -100°C to 200°C,
  - the minimization of the amount of desorbing atoms or molecules of the mass which is of interest from the surfaces of the setup[25].

---

[24] Water can bind tritium on the recipient's walls (as HTO or T_2O), as it was found in the TriReX experiment, compare 3.9.

[25] This can be done in two ways: It can be tried to reduce the area of the setup surface and it can be tried to avoid adsorption on the setup surfaces in the first place. Furthermore, the mass spectrometer should be located as close to the sample as possible.

- As adsorption and desorption are dependent on pressure and temperature and as these dependencies are of major interest, temperature and pressure in the sample environment should be controllable in the range of approximately −100°C to 200°C and 10^{-10} bar to 1 bar.
- The setup should have the possibility to test tritium decontamination procedures with purge gas and by baking out the system at approx. 200°C.

4.2.2 Technical requirements

There are a number of technical requirements for the experiment in order to enable the intended measurement methods (BIXS, mass spectroscopy) with the demanded sensitivity. Furthermore, there are technical requirements due to safety regulations described in the TLA [TLA12].

- The experimental setup, as well as the selection of components and materials has to meet the technical terms of delivery and acceptance ([TLA12]) of the TLK:

  The TLA include different requirements for the first[26] and the second containment of systems containing tritium. The maximum allowed integral leak rate of the primary system is $< 10^{-9}$ Pa m^3/s, the maximum allowed single leak rate of primary system components is $< 10^{-10}$ Pa m^3/s. In the primary system only fully metallic sealings are allowed. Furthermore, there are requirements concerning usable materials for the first and second containment.

  To fulfill the requirements in the TLA, usually stainless steel vacuum components are used as primary system. Connections are usually established with flanges with fully metallic sealings, such as CF[27]. The second containment is usually a glove box with a stainless steel frame and polycarbonate or aluminium walls.
- The maximum bakeout temperature must be technically limited to temperatures of $T \leq 200°C$, otherwise further safety measures are obligatory [TLA12].
- The X-ray producing element, which is placed between the detector volume and the recipient, has to separate the detector volume from the recipient (compare figure 4.3) to avoid contamination of the detector with tritium. Therefore, it has to withstand a differential pressure of 1 bar in case of a vacuum break and it has to prevent tritium permeation.
- The X-ray producing element will be implemented as a gold coated beryllium window (see section 4.3.2.1) in a DN40 CF flange. This cannot fulfill the requirements of the TLA in order to serve as a first containment. Therefore the detector has to be enclosed in the primary system.
- For the operation of the SDD and noise reduction the conduction of heat into the detector should be minimized to reduce the required cooling and to avoid a temperature rise in the detector. The SDD in TRIADE is maintained at a temperature of approximately 230 K by internal Peltier cooling. Therefore, the detector has to be operated at low pressures (of the order of mbar) to reduce thermal conduction through residual gas.

---

[26] The first tritium containment will be referred to as the primary system in the following.

[27] UHV capable flanges and gasket seals compatible to the CONFLAT© (Varian,Inc,UHV) standard. Usually the flanges are made of stainless steel and gasket seals are made of copper.

- The detector electronics used in TRIADE is not vacuum compatible and has to be placed in a separate volume using a standard CF feedthrough. As this feedthrough uses an elastomeric compression O-ring for sealing, it does not fulfill the requirements of the first containment and the detector electronics has to be placed in a volume separated from the detector but inside the primary system.

- The detector electronics needs an adequate heat sink in order to avoid the temperature to exceed the maximum operating temperature of 50°C. The temperature of the electronics needs to be monitored.

- The setup has to be connected to the TLK's tritium infrastructure, especially to the safety systems. The activity of the box atmosphere has to be monitored by an ionization chamber. Furthermore, the system needs to be able to pump gas, which is no longer needed, to the CAPER facility[28] or the ZTS[29].

- The setup needs the ability to pump gas from the recipient to a storage buffer vessel and back into the recipient.

- In order to reduce the residual pressure down to 10^{-10} mbar, an adequate pumping system is necessary. This pressure range is usually reached by turbo molecular pumps with a system of suitable fore pumps. The implementation of the pumping system is described in section 4.6.

- In order to minimize humidity in the recipient, the setup should be bakeable to temperatures as high as possible. A minimum bakeout temperature of $\approx$ 150°C is required. Due to the safety regulations, the maximum temperature should be limited to 200°C.

- To reduce tritium adsorption on the surfaces of the setup (except of the sample itself) a maximum fraction of the surfaces in the setup should be coated with gold, at least inside the recipient. The coating needs to resist the expected temperature shifts between -100°C and 150°C.

4.3 Design of the core components

A schematic view of the core components of the TRIADE setup is shown in figure 4.3. The core components consist of three volumes, as the recipient needs to be separated from the detector volume, which needs to be separated from the detector electronics volume (according to the requirements, compare section 4.2). This makes it possible to control the atmospheres around sample, detector and detector electronics independently. The X-ray producing element and the detector feedthrough do not meet the requirements of the TLA in order to serve as the first containment. Therefore the detector and the detector electronics volumes are part of the primary system. The implementation of the core components is shown in a picture of the CAD model in figure 4.5.

---

[28] The CAPER facility is TLK's three step reference process for the Tokamak Exhaust Processing (TEP) system of ITER. It is designed to remove tritium from exhaust gases. [Bor05]

[29] "Zentrales Tritium Rückhaltesystem", central tritium retention system [Bes08]

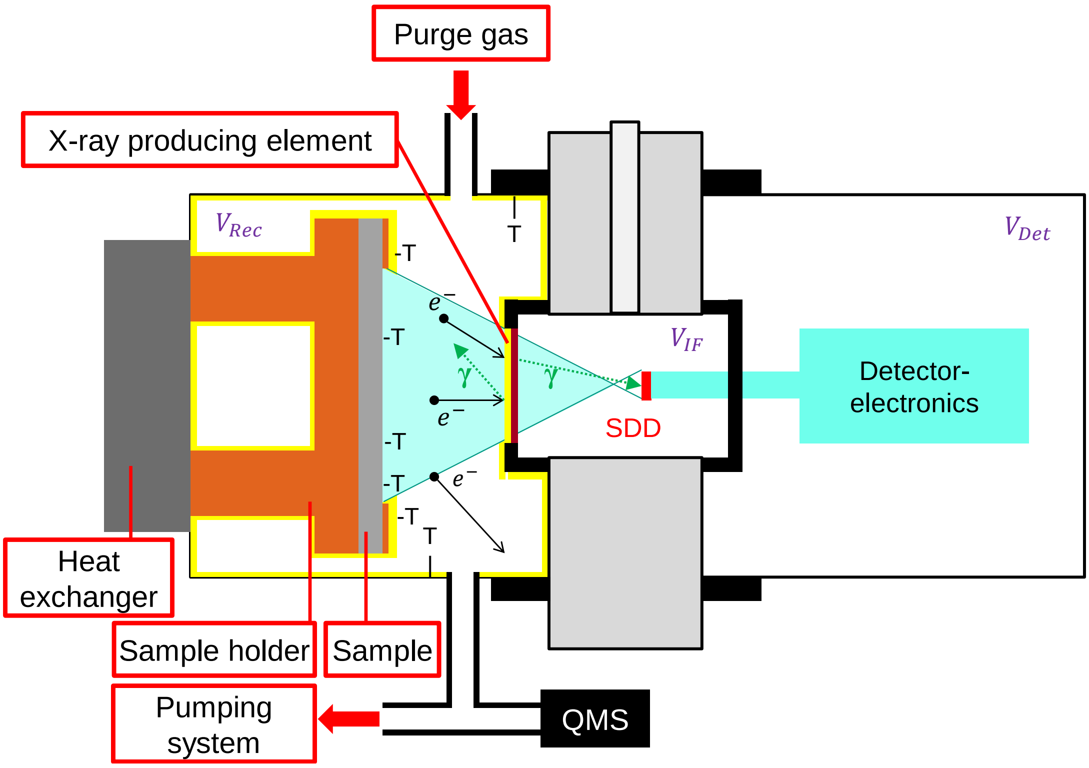

Figure 4.3: Schematic of the TRIADE core components. The schematic shows the three volumes of the TRIADE core components, which are the recipient (V_{Rec}), the intermediate flange volume (V_{IF}) and the detector electronics volume (V_{Det}). "QMS" stands for the quadrupole mass spectrometer. The recipient contains the sample, which is mounted on a sample holder. V_{IF} contains the silicon drift detector (SDD). The detector electronics is located in the volume on the right. The schematic indicates the BIXS process and the restriction of the detector's field of sight.

4.3.1 Geometry and implementation of core components

The geometry of the core setup had to be designed with respect to the following aspects:

- Restriction of detector's field of sight: As explained in section 3.6, it is of interest that the area viewed by the detector is restricted to the sample surface.
- Maximum opening angle of the detector: The recommended maximum angle of X-rays entering the detector is 45° to the perpendicular (compare figure B.15), as X-rays which enter under a larger angle might not be fully absorbed inside the active volume. This results in a signal of a reduced energy. Therefore, the entering angle for X-rays should be limited by the setup.
- Maximization of signal caused by sample surface activity: Concerning the geometry of the core components, the following characteristics are favorable for maximization of the signal:
  - large sample surface,
  - large X-ray producing element,
  - short distance between sample and detector.

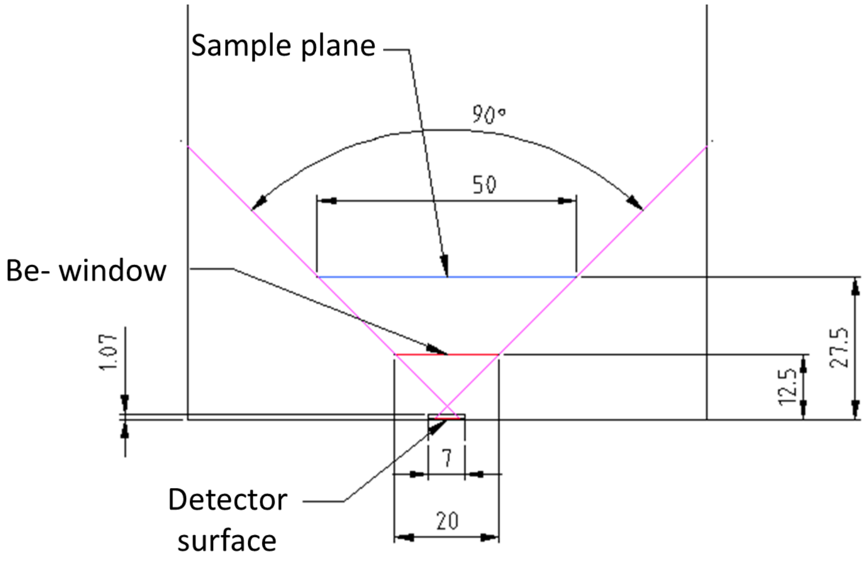

Figure 4.4: TRIADE core components geometry. The drawing shows the geometry of sample plane, beryllium window and detector surface. All distances are given in mm. The edges of the X-ray producing element restrict the area viewed by the detector. The X-ray producing element is implemented as a CF window. It can be assumed that the flange containing the window is nontransparent to photons of energies in the range of interest.

Furthermore, the use of vacuum components of standard dimensions is favorable for cost reasons. The chosen geometry is shown in figure 4.4. The implementation of this geometry is shown in figure 4.5.

The recipient is a cylindrical vacuum chamber of a DN100 CF standard diameter with two DN100 CF flanges, two DN40 CF flanges and two 1/2 inch VCR male connections, which are necessary for the connection of the recipient to instrumentation, infrastructure and pumping system (compare sections 4.6 and 4.7). The recipient is kept as short as possible in order to minimize the inner volume, which is advantageous for pumping down the system and which reduces unnecessary surfaces inside the recipient. Furthermore, the required activity for a chosen tritium partial pressure is minimized. The chosen minimum length of the recipient is determined by the space needed for the DN40 CF connections.

For positioning the sample at the desired position, a sample holder is mounted on the blind flange which closes the recipient on one side. The holder consists of a plate mounted on four staves and a holder ring, which is screwed onto the plate and fixes the sample. In order to maximize the visible sample surface, the plate diameter and the outer holder ring diameter are as large as possible in order to fit into the recipient. The inner holder ring diameter is as large as possible with respect to its stability. In order to avoid virtual leaks[30], the plate has several venting slots. The sample holder is shown in figure 4.11.

---

[30] Term for hollow spaces where gas can remain during pump down of the system. Gas slowly flowing out of hollow spaces can appear like a leak in the system and limit the ultimate pressure.

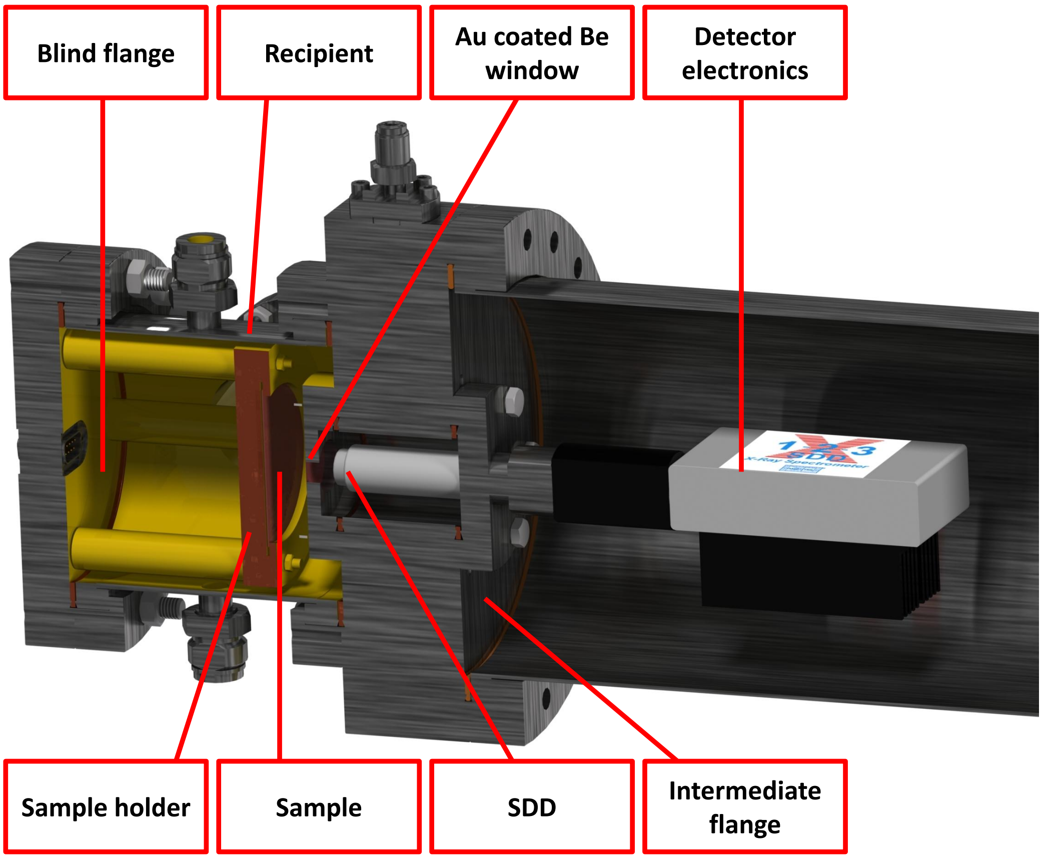

Figure 4.5: CAD model of TRIADE core components. The picture of the TRIADE CAD model shows a cut through the core components. It shows the recipient on the left side, closed by a blind flange with electrical feedthroughs. The sample holder is mounted onto the blind flange. The intermediate flange contains the detector volume and is closed by the gold coated beryllium window on the left side and the detector feedthrough on the right side (both DN40 CF flanges). On the right side, the detector electronics is visible.

The custom made intermediate flange has a centered bore, which serves as the detector volume. The detector volume is closed from both sides with DN40 CF flanges. On the side facing the recipient the gold coated beryllium foil is mounted in a DN40 CF window flange. The window restricts the area viewed by the detector. On the opposite side the detector feedthrough is mounted. Furthermore, a standard size DN160 CF pipe is mounted to the intermediate flange, which serves as the detector electronics volume. The intermediate flange furthermore has a 1/4 inch VCR male connection in order to pump down the detector volume.

The mechanical dimensions of the custom-made vacuum components and the sample holder are shown in appendix B.2.

Figure 4.6: Materion IF-1 beryllium window in DN40 CF flange. The picture shows the beryllium window before it was sputter-coated with gold. The coated window, mounted inside the recipient is shown in figure 4.7.

4.3.2 Materials used

As introduced in section 4.2, there are some special requirements concerning the materials used for the core components. The materials used in the X-ray producing element are crucial for its proper functioning. They are described in section 4.3.2.1. The coatings of the surfaces inside the recipient, which should reduce tritium adsorption on these surfaces (compare section 2.6), are described in section 4.3.2.2. The used standard and custom vacuum components are made of certified 316L stainless steel. In accordance to the TLA there has to be an individual documentation for every component used in the primary system[31]. The support structure is made of standard strut profiles[32] and custom aluminium plates.

4.3.2.1 X-ray producing element

For TRIADE it is of interest that a maximum intensity of X-rays is produced inside the X-ray producing element. Furthermore, a maximum fraction of these X-rays should transmit the X-ray producing element and be detected by the detector. As explained in section 3.3, the produced X-ray intensity goes with Z^2, where Z is the atomic number of the material used. So a high Z material is favorable. But high Z materials also have a higher attenuation coefficient for photons than low Z materials (compare section 3.4). Therefore, the thickness of the layer in which the bremsstrahlung is produced is always a trade-off between maximizing bremsstrahlung production and minimizing self-absorption.

Gold with Z=79 is a suitable high Z material, as it is solid, not radioactive, not toxic, not chemically reactive and easily available. Furthermore, low tritium adsorption on gold can be assumed (compare section 2.6). The optimization of the thickness of the gold layer for a BIXS system for tritium measurements was investigated in [Mau09]. It was found that a maximum of X-ray intensity is achieved with a layer thickness between approximately 80 and 160 nm. A layer of this thickness can only be carried by

---

[31] The chemical composition and certain physical properties have to be measured and documented in a certificate according to DIN EN 10204 (3.1).

[32] by Bosch Rexroth

a substrate in order to be mechanically stable. In order to minimize X-ray absorption, this substrate should be made of a low Z material. Apart from lithium, which reacts violently with water and can cause burns [ESIS12], beryllium is the material with lowest Z (with Z_{Be}=4) which is solid. In TRIADE a gold layer of 100 nm on a beryllium substrate of 100 µm is used with an additional adhesive layer of 10 nm of titanium between gold and beryllium. The gold and adhesive layers were sputter-coated[33] on the beryllium substrate.

The beryllium substrate was built by Materion Electrofusion[34]. Further details can be found in appendix B.5. The window was mounted inside a DN40 CF flange by diffusion bonding. It is shown in figure 4.6. The IF-1 beryllium foil used has a minimum beryllium content of 99.8%. The leak rate of the window is specified by the manufacturer as $< 1 \cdot 10^{-9}$atm$\cdot$cm^3/s. It is bakeable up to 450°C. The maximum differential pressure[35] is Δp = 1 bar. The beryllium window has to be able to withstand a vacuum break on any side. If the beryllium window breaks, the setup can not be used any more, because of the potential contamination of the system with hazardous beryllium dust and the additional contamination of the detector with tritium. If the beryllium window breaks, this can be detected by a fast pressure rise inside the detector volume. As mentioned in section 4.2.2, the beryllium foil does not meet the requirements of the TLA in order to serve as the first containment, which is why detector and detector electronics have to be placed inside the first containment.

4.3.2.2 Coatings

In order to reduce the adsorption of tritium on surfaces other than the surface of the sample (compare sections 2.6 and 3.6), the following surfaces had to be coated (compare figures 4.5 and 4.7):

- the inner side of the recipient,
- all surfaces on all individual parts of the sample holder (staves, plate and holder ring),
- the surface facing the recipient of the blind flange,
- the surface facing the recipient of the intermediate flange,
- all surfaces of the flange the beryllium foil is mounted in (the coating of the beryllium itself is described in section 4.3.2.1),
- the entire surface of the threaded bolts and screw nuts which are needed to mount the beryllium window and the holder ring of the sample holder.

The techniques for coating these surfaces had to be chosen according to the geometry of the components[36]. Furthermore, a temperature resistance of the coating was required at least for the expected temperature range of −100 to 200°C. Furthermore, a small surface roughness was considered to be advantageous in order to reduce tritium adsorption. The chosen techniques and coatings are described in the following.

---

[33] by Siegert Thinfilm Technology, Robert-Friese-Straße 3, D-07629 Hermsdorf

[34] 44036 S Grimmer Blvd, Fremont, CA 94538-6346, USA

[35] bi-directional

[36] For example it was not possible to sputter coat the inner side of the recipient.

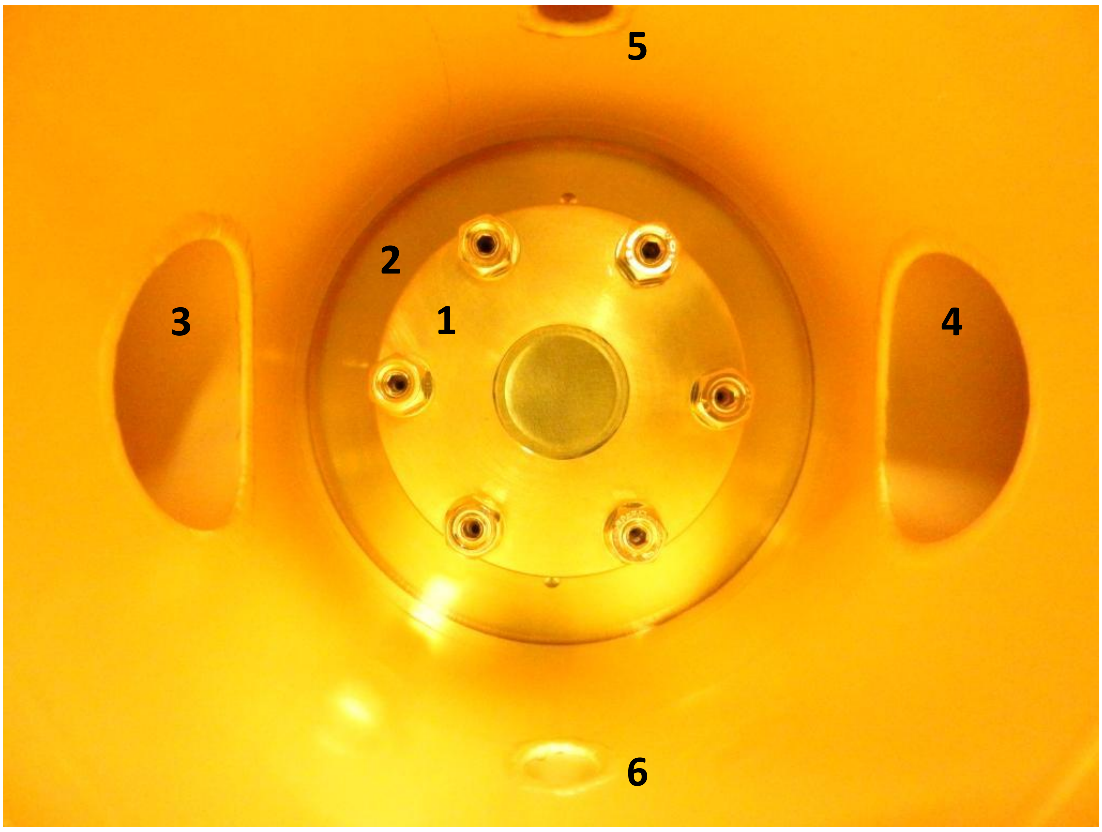

Figure 4.7: Gold coated recipient with gold coated beryllium window. The picture shows a view of the gold coated inner side of the recipient. (1) is the flange containing the gold coated beryllium window, which is mounted to the intermediate flange (2) with gold coated threaded bolts and gold coated screw nuts. The numbers (3-6) indicate the connections of the recipient to (3) the cold cathode vacuum transducer, (4) the high vacuum side of the pumping system and the volume of the quadrupole mass spectrometer, (5) pressure instrumentation and purge gas inlet and (6) sampling port and TLK infrastructure.

The recipient was electropolished by Poligrat GmbH[37], which was a requirement for the electrochemical coating of the recipient and which reduced surface roughness. The recipient was electrochemically coated by Collini AG[38]. It was coated with an adhesive layer of 2.5 µm of nickel, followed by a layer of 5 µm of gold. Three samples of the recipient material[39] were coated simultaneously to the recipient itself. Two of the samples were used by the manufacturer for a bending test and a high temperature test. The third sample is available for further investigation at TLK, for example for the investigation of the temperature resistance of the coating using γ-spectroscopy. This is of interest as the coating of the recipient will regularly be exposed to temperature shifts in the range of -100°C up to 200°C.

Blind flange, sample holder (all individual parts) and intermediate flange were sputter-coated[40] with an adhesive layer of chrome and a layer of 1 µm of gold by Siegert Thinfilm Technology[41].

The beryllium window was also sputter-coated by Siegert TFT, but using titanium as adhesive layer of approximately 10 nm thickness. Titanium was used as its characteristic peaks are not too close to peaks of favorite sample materials [Tho09].The gold layer on the beryllium has a thickness of 100 nm (compare section 4.3.2.1). In order to be temperature resistant, the gold layer on the flange has a thickness of 1 µm.

The threaded bolts and screw nuts, which are used for mounting the beryllium window onto the intermediate flange, were electrochemically coated by the KIT main workshop.

The gold coated recipient and the beryllium window, mounted onto the intermediate flange are shown in figure 4.7.

4.3.3 The Amptek X123 X-ray spectrometer

For the implementation of the BIXS method an X-ray detector is needed. As mentioned in section 3.8, the detector should have a low background signal, a good energy resolution and and it should have a large absorption probability for photons in the energy range of interest. The choice for TRIADE is a silicon drift detector which meets these requirements, as explained in the following. The principle of SDDs is described in section 3.8. A picture of the Amptek X123 is presented in figure 4.8. The Amptek X123 is a complete X-ray spectrometer, which includes

- a silicon drift detector with Peltier detector cooling,
- a preamplifier,
- a DP5 digital pulse processor,
- a multi channel analyzer (MCA).

The silicon drift detector is protected by a 12.5 µm beryllium window and can in principle be operated at ambient pressure. The geometry of the spectrometer is shown

---

[37] Valentin-Linhof-Str. 10, D-81829 München, Germany

[38] Ringstrasse 9, CH-8600 Dübendorf, Switzerland

[39] 316L stainless steel

[40] at least on all surfaces facing the recipient

[41] Robert-Friese-Straße 3, D-07629 Hermsdorf, Germany

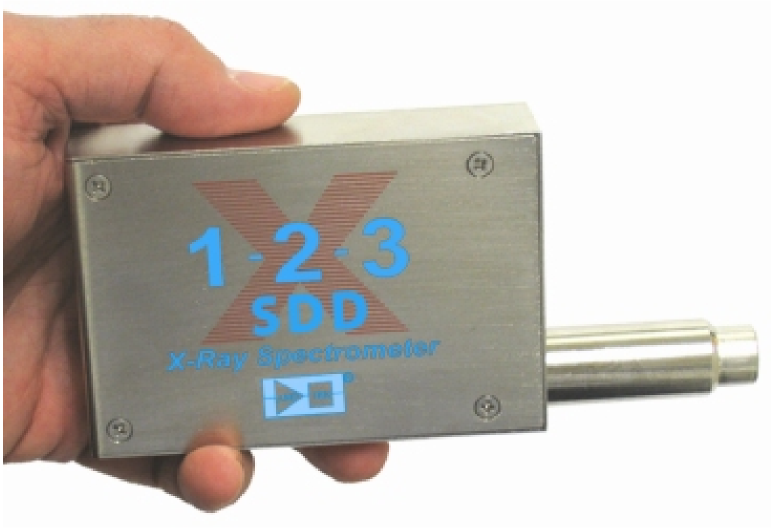

Figure 4.8: The X123 X-ray spectrometer. The SDD is located behind a beryllium window at the end of the extender. The housing contains pulse processor and multi channel analyzer.

in figure B.14 and the geometry of the detector is shown in figure B.15. Figure B.16 gives an overview of the manufacturer's specifications of the X123. The X123 has to be connected to a power supply and to a computer, using an USB, RS232 or Ethernet interface. The included software allows taking, saving and analyzing spectra.

In order to achieve the best performance with the detector, meaning to minimize the background counts and to maximize the energy resolution, the operating parameters of the detector, which are described in the following, have to be optimized, as explained in section 5.1.1.

The pulse processor in the Amptek X123 uses two parallel signal processing channels in order to accurately measure both pulse height[42] and the incoming count rate [Amp12]. The first channel, which is optimized for the detection of accurate pulse height is called the "slow" channel, because of its comparatively long peaking time[43], which is optimized for a good energy resolution of the detector.

Since photons reach the detector at random intervals it is possible that two interactions are closely spaced in time and overlap in the slow channel. This can result in the detection of one pulse of incorrect height, instead of two pulses of accurate height. In order to avoid this, the second channel uses a much shorter peaking time. It is used to detect pulses which are closely spaced in time and overlap in the slow channel. These pulses can be rejected from the spectrum[44]. Furthermore, the fast channel is used to measure the incoming count rate more accurately than in the slow channel. The fast and slow channel concept is shown in figure 4.9.

The X123 gives the user the possibility to set a large number of parameters. The choice of the parameters is important for the detector performance.

---

[42] and thereby the energy of the incoming radiation

[43] "Slow Peaking Time" (SPT), of the order of μs

[44] The function can be enabled and disabled in the software.

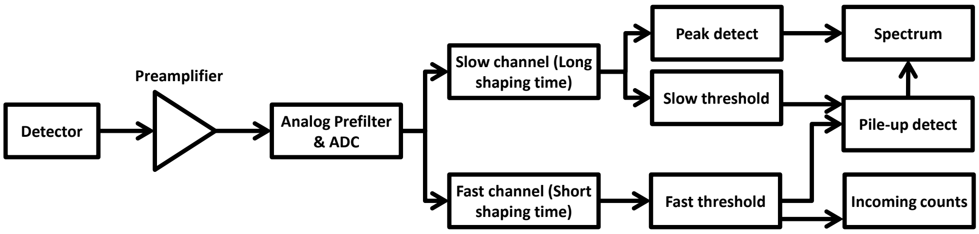

Figure 4.9: Schematic of fast and slow channel in the Amptek X123. The schematic indicates the signal processing in the digital pulse processor of the X123. The signal is amplified, filtered and digitized. The slow channel uses a long shaping time in order to optimize energy resolution. The fast channel uses a short shaping time in order to accurately detect incoming counts. The comparison of fast and slow channel is used for pile-up detection. As the different shaping times cause different noise edges, each channel has its own threshold.

The parameters which are important for TRIADE are discussed here:

- Slow/ fast peaking time: The slow/ fast peaking time are the peaking times in the slow and fast channel. It is the time required for a shaped pulse from baseline to the peak. It is usually approximately 2.4 times the shaping time constant of the shaping amplifier [Amp11]. The energy resolution of the SDD strongly depends on the slow peaking time.
- Slow/ fast threshold: In order to not misinterpret electric noise as pulses originating from radiation, a threshold has to be defined for the fast and the slow channel. Pulses with an amplitude lower than the threshold in the correspondent channel are rejected. If the threshold is set near to zero one usually observes a sharp noise edge at the low energy end of the spectrum. The threshold is usually set just above this noise edge. It can also be set slightly below the noise edge, in order to make it visible in the spectrum[45].
- Gain: The gain, set by the user, is the voltage gain of the digital processor. It determines the energy calibration and the full scale energy of the taken spectra (compare equation B.1). In TRIADE, the gain is set to a value which results in a full scale energy slightly above the end point of the tritium β spectrum (18.6 keV).
- Cooler temperature: In order to reduce electric noise, it is favorable to cool the detector to a constant temperature as low as possible. But the cooling performance of the peltier element is limited and temperature fluctuations might change the energy calibration of the SDD. So the cooler temperature should be set to a value at which the detector can be stabilized under the expected conditions.

In order to reach the desired detection limit of < 1 monolayer, the detector parameters should be optimized in order to reduce detector noise. The most important parameters concerning detector noise reduction are the thresholds, which have to be set just above the noise edge. Furthermore, the slow peaking time has to be optimized in terms of energy resolution and intrinsic detector noise. The slow peaking time should ensure a good energy resolution for analysis of characteristic radiation. The measurements for detector parameter optimization are described in section 5.1.1.

---

[45] This can be useful in order to recognize temperature drifts of the detector.

4.4 Mass spectrometry setup

In order to analyze desorbing atoms and molecules in TRIADE, a quadrupole mass spectrometer (QMS) is part of the setup. In a quadrupole mass spectrometer atoms and molecules are ionized and accelerated. They then travel into the quadrupole which consists of four parallel metal rods. The field, which is caused by a direct voltage and a superimposed radio frequency voltage between the two pairs of rods, only permits ionized atoms or molecules of a certain q/m to pass on a stable trajectory and be recorded by a detector[46]. By varying the frequency of the alternating current it is possible to scan through a range of q/m values [Dem10a].

The mass spectrometer used in TRIADE is a MKS[47] Microvision Plus. The manufacturer's specifications for this spectrometer can be found in figure B.17, the mechanical dimensions can be found in figure B.18. For the integration of the QMS into the TRIADE setup the following requirements had to be considered:

- In order to perform TDS measurements[48], the QMS should be located as close to the sample as possible (compare section 2.4). This has to be implemented with respect to BIXS being the first priority in the TRIADE setup.
- The QMS should be located between recipient and pumping system (compare section 2.4).
- The maximum pressure the QMS can be operated at is 10^{-4} mbar.

Furthermore, the QMS has to be calibrated before usage. The calibration is described in section 5.4. The mass spectrometer is mounted in the DN63 CF tee between recipient and pumping system (compare figure 4.2). Therefore, atoms or molecules desorbing from the sample are pumped through the volume containing the mass spectrometer.

The QMS will be used for the analysis of gas mixtures, for example in order to determine the tritium purity of tritiated gas mixtures provided by CAPER. Furthermore, atoms or molecules desorbing from the sample can be detected by the QMS.

As mentioned in section 2.4 it is of interest in thermal desorption spectroscopy that only atoms or molecules from the investigated surface are analyzed. As BIXS is the main measurement principle in TRIADE, this idea could not entirely be realized. The current setup has the following restrictions concerning thermal desorption spectroscopy:

- In the current setup also desorbing atoms and molecules from setup surfaces[49] might be analyzed by the mass spectrometer.
- It is not clear whether adequate heating rates can be reached with the current temperature management system (compare section 4.5). This has to be tested in performance test measurements with the temperature management system.

It has to be investigated which information can be obtained from TDS spectra taken with the TRIADE setup. In the ideal case it might be possible to draw conclusions concerning binding energies of adsorbed tritium to different sample surfaces.

---

[46] Where q is the charge and m is the mass of the ionized atoms or molecules.

[47] MKS Instruments, 2 Tech Drive, Suite 201, Andover, MA 01810, USA

[48] The principle of TDS is described in section 2.4, a schematic of an ideal TDS setup is shown in figure 2.3.

[49] such as the inner side of the recipient, the sample holder or the manual valve between recipient and the QMS volume

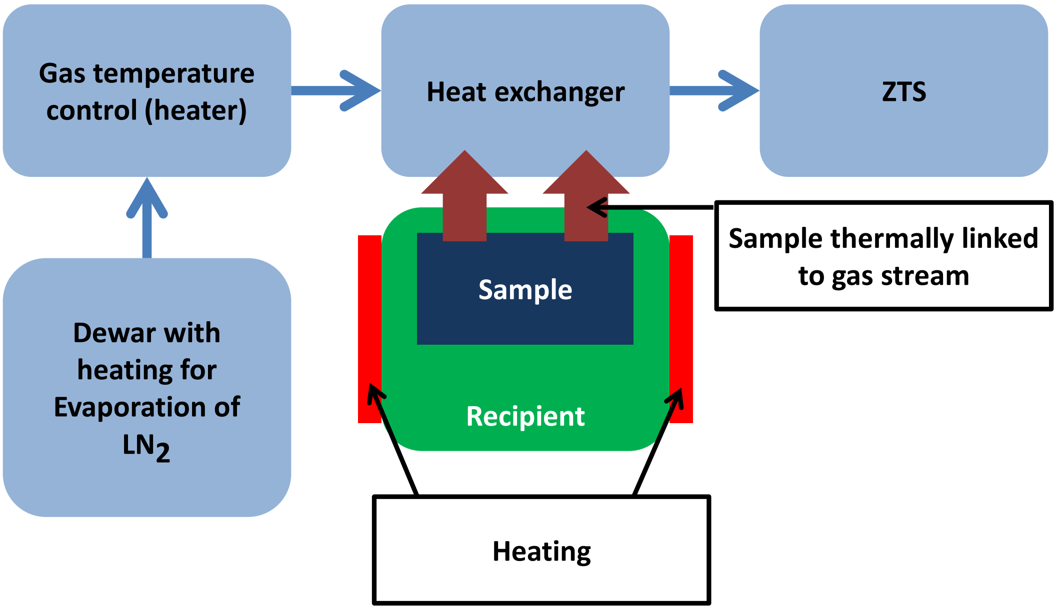

Figure 4.10: Schematic of the TRIADE temperature management system. The schematic shows the principle of cooling and heating of the sample. The blue arrows indicate gas flows, the red arrows should suggest a heat flux from the sample into the heat exchanger. More details can be found in the text.

4.5 Temperature management

In order to enable a large temperature range an adequate temperature management is necessary. The sample temperature is required to be controllable from approximately −100°C to 200°C for temperature dependent BIXS measurements and thermal desorption measurements.

Figure 4.10 gives an overview of the temperature management system. In order to cool down the sample, a cold gas system produces gaseous nitrogen of a controllable temperature between 78 K and approximately 350 K. This gas passes through a heat exchanger, which is thermally linked to the sample, and is then passed to the ZTS. The sample can be heated by heating the blind flange and the recipient with a flange heater and a heating cable.

The system can be baked out with the heating at the recipient and an additional heating cable, which is located at the mass spectrometer's volume.

The design of the heat exchanger has to take into account the technical requirements of the first containment. The heat exchanger was placed outside the first containment due to the technical complexity of the implementation of a heat exchanger inside the first containment. In this case, the cooling gas supply piping would have to fulfill the requirements of the first containment.

The temperature of the sample shall be controlled by controlling the temperature of the blind flange the sample holder is mounted to. This can be done remotely outside the primary system. The sample temperature follows the flange temperature because of the heat conduction through the sample holder. In order to maximize this effect,

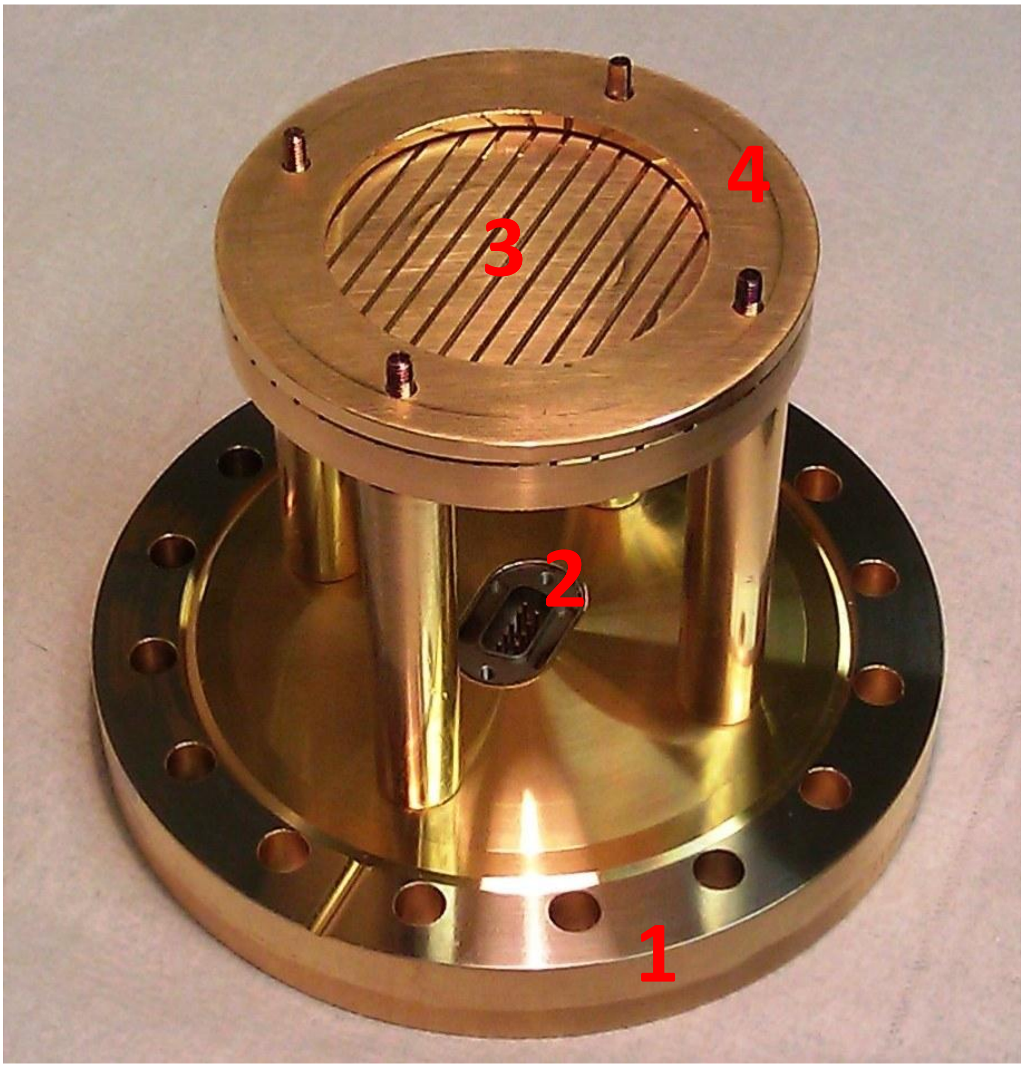

Figure 4.11: Sample holder on blind flange. (1) is the blind flange with an electrical feedthrough (2).The slots in the plate (3) of the sample holder are used to avoid virtual leaks. The sample can be fixed under the holder ring (4).

the sample holder is made of copper, which has a high thermal conductivity[50]. The recipient is designed as short as possible due to the reasons listed in section 4.3.1, so the distance between flange and sample is minimized. The idea of managing the sample temperature by managing the flange temperature was tested during two experiments (one for heating and one for cooling), which is described in section 5.2.

In order to cool the flange, a custom-made heat exchanger was developed. The setup is shown in figure 4.12. It consists of a copper plate and an aluminium plate, which are screwed together. The aluminium plate has two connections for gas pipes. On the sides of the plates which face each other, a deepening is reamed into the plates, so that gas, which is lead into the volume, is forced to stream along a certain track. The length of the track and the surface facing the gas is maximized, so the temperature of the copper

---

[50] 4.04 W/cmK compared to 0.865 W/cmK of iron at 250 K [Pow66]

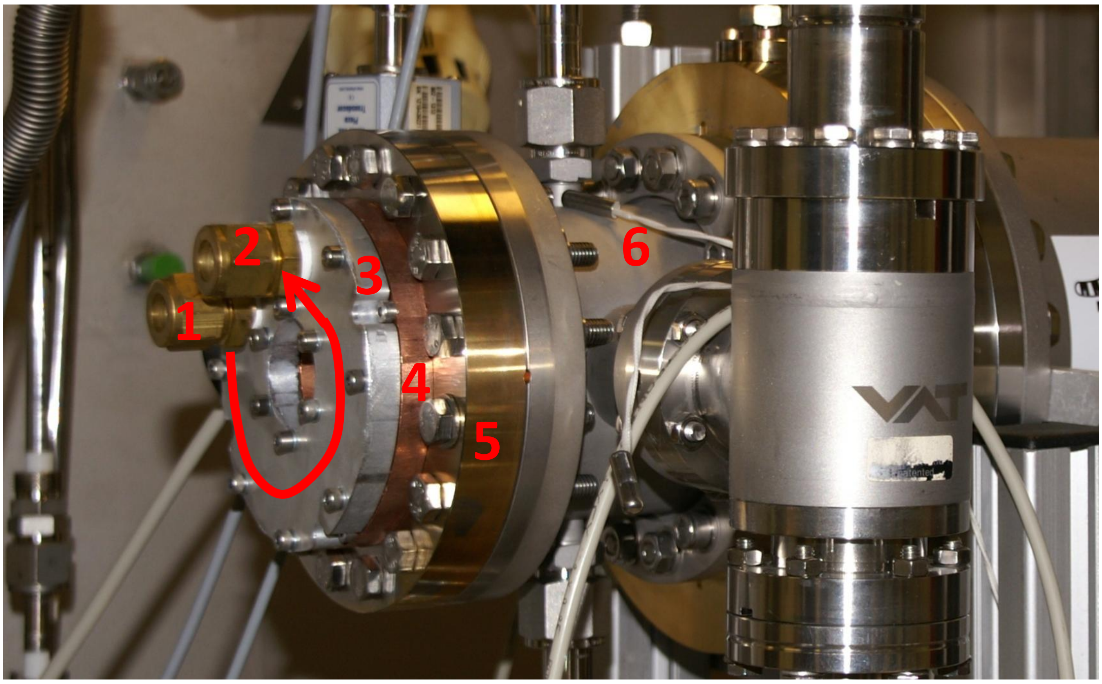

Figure 4.12: Picture of heat exchanger for cooling flange and sample. The heat exchanger, which consists of an aluminium (3) and a copper plate (4), has a gas inlet (3) and a gas outlet (2). The track the gas has to follow inside the heat exchanger is indicated by the arrow. The hole in the heat exchanger is needed for the connection of the electrical feedthrough in the blind flange (5), which is needed for the temperature measurement inside the recipient (6).

plate follows the gas temperature as closely as possible. The heat exchanger is screwed to the back of the blind flange the sample holder is mounted to with the copper plate facing the blind flange. The blind flange with the heat exchanger can be covered with styrofoam from the outside for thermal insulation.

The temperature controlled gas for TRIADE will be produced by a system provided by KGW Isotherm[51]. The principle of this system is indicated in figure 4.10. Liquid nitrogen is evaporated in a closed dewar vessel by controlled heating with a 500 W heater. The expanding gas leaves the dewar and has to pass another heater of 630 W, which can warm up the gas to a controllable temperature between the boiling point of nitrogen[52] and a temperature[53] of approximately 350 K. The gas of the desired temperature is then lead through vacuum isolated[54], jacked corrugated tubes to the heat exchanger at the blind flange with the sample holder. After passing the heat exchanger, it is released to the ZTS. Thus the cooling gas never enters the primary system.

---

[51] Gablonzer Straße. 6, D-76185 Karlsruhe,Germany

[52] 77.15 K [Zha11]

[53] specified by the manufacturer

[54] The isolation vacuum is produced by two Oerlikon Divac 0.8T diaphragm pumps (compare table B.3), one for the part of the tube outside the glove box, one for the part inside.

4.6 Design of pumping system and instrumentation

The pumping system of the TRIADE experiment is designed to enable the final pressure of $p_{\mathrm{fin}} \leq 10^{-10}$ mbar (according to section 4.2.2), which is required for background reduction during the BIXS measurements. Furthermore, the pumping system is needed to transport tritiated gas mixtures, e.g. from the recipient to a buffer vessel (compare 4.7). The pumps used in TRIADE are listed in table B.3. The arrangement of the pumps is shown in figure 4.13 and described in section 4.7. The recipient can be pumped down by two cascaded turbomolecular pumps (VA052[55] and VA053[56]), which are necessary to reach the desired ultimate pressures. The first turbomolecular pump is located as close to the recipient as possible. The high vacuum connection of the second turbomolecular pump (VA053) is located as closely to the outlet connection of the first one (VA052) as possible in order to optimize the conductivity. The fore vacuum for the turbomolecular pumps is provided by a Normetex scroll pump (VA054) and a Siemens Interatom metal bellows pump (VA055).

In order to be able to monitor the pressure in the recipient over a range from 1 bar down to 10^{-10} mbar different pressure gauges with overlapping pressure ranges are necessary. Figure 4.13 indicates the locations, the pressure is measured at in the TRIADE vacuum system. The different pressure gauges and their measurement ranges are listed in table B.1, their arrangement is discussed in section 4.7.

4.7 Procedural setup of TRIADE

The design of the vacuum system of TRIADE is shown in figure 4.13. From the experimental point of view, the recipient (BV061) is separated from the intermediate flange volume (IF-volume) by the beryllium window. From the safety-related point of view the beryllium window does not fulfill the requirements to serve as a first containment (compare section 4.2.2). Therefore, the beryllium window is drawn as a dotted line in the schematic (compare figure 4.13). The same holds for the elastomeric sealed detector feedthrough between IF-volume and detector electronics volume.

The intermediate flange used in TRIADE has the same geometry as the one which was used in the TriReX experiment (compare section 3.9 and [Röl11]). The detector feedthrough used in TriReX was also elastomerically sealed. In [Röl11] it was found that the leak rate of the elastomeric sealing of the detector feedthrough[57] was so large that a continuous pumping of the IF-volume was necessary to keep the pressure inside the IF-volume of the order of 1 mbar. It can be assumed that the sealing of the TRIADE detector feedthrough has a comparable leak rate. Therefore, the IF-volume in TRIADE is also continuously pumpable with a diaphragm pump[58] (VA051).

The recipient can be decontaminated using purge gas. The relevant part of the experiment is printed blue in figure 4.13. The system is connected to a gas bottle (BV063) containing pressurized purge gas (e.g. helium or hydrogen). In order to be able to control the purge gas stream a pressure reducer (RV043) and a flow controller (RV042)

---

[55] Leybold Oerlikon SL80

[56] Pfeiffer TMU 200

[57] determined as 10^{-7} mbar $\cdot$ l/s

[58] Divac 0.8 T by Oerlikon, Churerstrasse 120, CH-8808, Pfäffikon, Switzerland

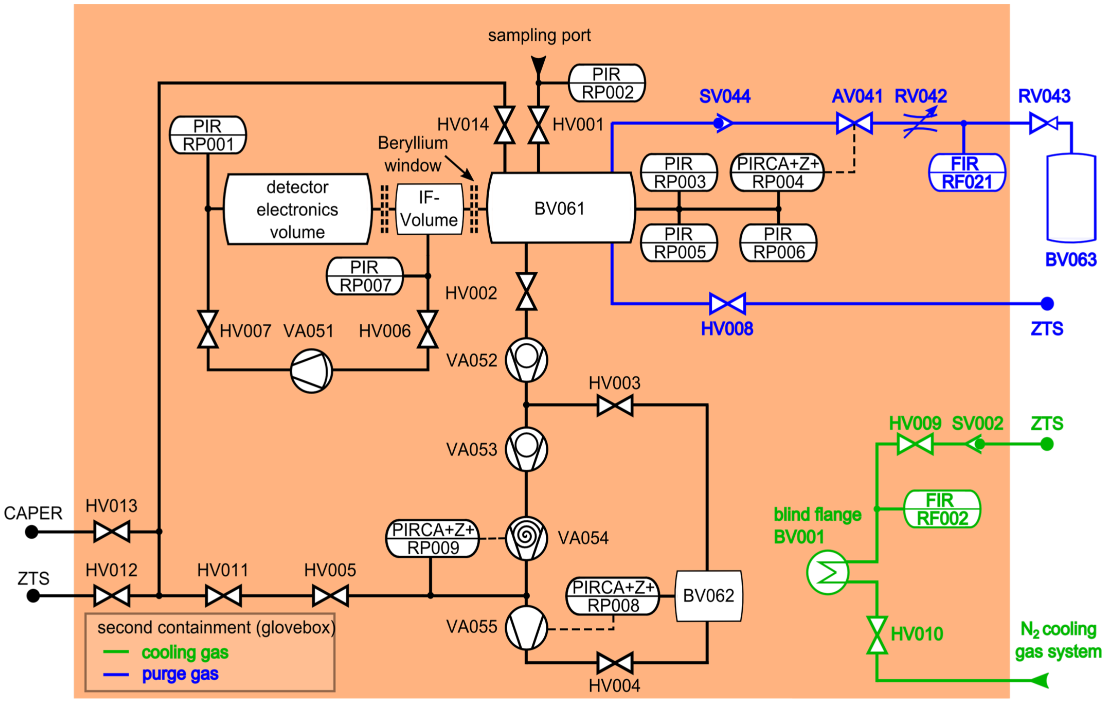

Figure 4.13: The TRIADE vacuum system. The schematic shows the TRIADE vacuum system with purge gas system (blue) and cooling gas system (green). The abbreviation for manual valves is "HV", that for pumps is "VA", that for pressure sensors is "PIR" and that for flow sensors is "FIR". The procedural setup of the experiment is further described in the text.

is integrated in the connection. In case of a pressure rise above 800 mbar inside the recipient, an automatic valve (AV041) stops the purge gas inlet, triggered by RP004 (MKS 902). The diffusion of tritium from the recipient into the gas bottle is prevented by a check valve (SV044). After passing the recipient, the purge gas can directly be led to the ZTS.

Waste gas can either be passively led or be actively pumped to the ZTS[59] or CAPER using VA052, VA053 and VA054. Furthermore, gas from the recipient can be pumped into a buffer vessel (BV062) with a volume of 16 l, using all pumps. Gas from the buffer vessel can be re-used by pumping it back into the recipient again. It can also be pumped to CAPER or the ZTS using VA053 and VA054.

The cooling gas system is fully separated from the primary system, as explained in section 4.5. In the schematic the cooling gas system is printed green. After passing the heat exchanger at the blind flange of BV061 the gas is lead into the ZTS. The cooling gas flow is monitored by a flow meter (RF002). Diffusion of tritium from the ZTS into the cooling gas system is prevented by a check valve (SV002).

Figure 4.14 shows the measurement sensors for temperature monitoring in the TRIADE setup. The temperature is measured with PT100 and PT1000 resistance temperature detectors. In order to measure the dependency of tritium adsorption and desorption on the temperature, the sample temperature is measured at the backside of the sample holder (RT016). In addition, the temperature is measured at the blind flange of the

---

[59] with respect to the restrictions on activities and quantity of gas

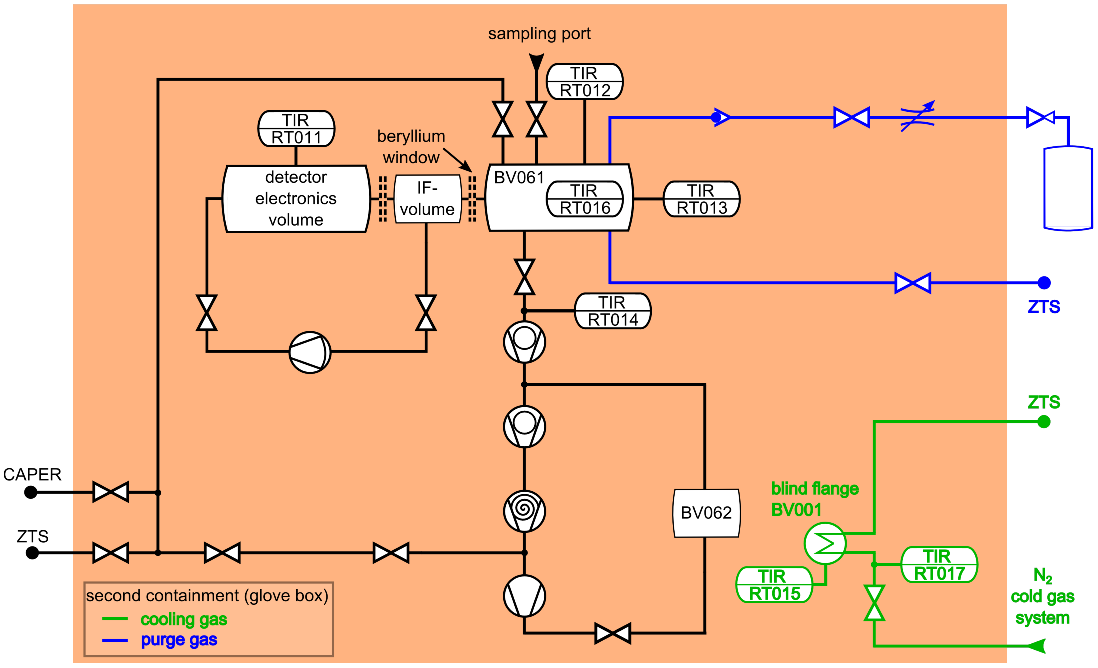

Figure 4.14: Temperature measurement in the TRIADE system. The schematic shows the locations of the measurement sensors for temperature monitoring in the TRIADE setup. A list of the sensors is given in table B.2.

recipient and at the recipient's wall for controlled heating with the flange heater and heating cable. The temperature at the gas inlet flange of VA052 is monitored in order to prevent too high temperatures at the turbomolecular pump, which can cause damage to the TMP. Furthermore, the temperature of the cold gas stream is measured as well as the temperature at the heat exchanger, in order to monitor the performance of the cold gas system. The detector electronics temperature can be read out by the detector software. Additionally, the temperature of the cooling body is measured by RT011. All temperature measurement points are listed in table B.2.

The main components of the TRIADE setup are shown in figure 4.15, a full view of the TRIADE setup is presented in figure B.2.

Figure 4.15: The TRIADE setup. The picture shows the upper part of the glove box, in which the TRIADE experiment is set up, before closing the box. The indicated components are (1) the recipient, (2) the intermediate flange, (3) the detector electronics volume, (4) the volume of the quadrupole mass spectrometer, (5) the Leybold SL80 turbomolecular pump, (6) the pressure instrumentation of the recipient and (7) two Divac 0.8T vacuum pumps (one is VA051 and one is used for the insulation vacuum of the cooling gas pipe). The buffer vessel, the TMU 200 turbomolecular pump, the Normetex scroll pump and the Interatom metal bellows pump are located in the lower part of the glove box, which is not visible in this picture. The whole setup is shown in figure B.2.

Chapter 5

Commissioning of TRIADE and first test measurements

This chapter describes the commissioning of the TRIADE experiment and the test measurements which were performed prior to the setup of TRIADE and during the commissioning. Section 5.1 describes the measurements for the characterization of the detector used in TRIADE and their results. In section 5.2 two test experiments are described, which were performed in order to gain experience for the final design of the TRIADE temperature management system. The commissioning of the vacuum system is described in section 5.3 and first measurements with the quadrupole mass spectrometer, which were performed during the commissioning of the TRIADE experiment, are discussed in section 5.4.

5.1 Detector characterization measurements

The Amptek X123 X-ray spectrometer used in the TRIADE experiment enables the user to set the values of various detector parameters (compare section 4.3.3 or [Amp12]). These parameters have a huge impact on the performance of the detector. Therefore the measurements described in section 5.1.1 were performed in order to optimize the settings and test the performance of the detector. Furthermore an energy calibration was performed, which is described in section 5.1.2.

5.1.1 Measurements for detector parameter optimization

The most important detector characteristic for the TRIADE experiment is the noise level, as the amount of adsorbed tritium will be calculated from the measured count rate. The noise level mostly depends on the detector temperature, the slow threshold and the slow peaking time (SPT, compare section 4.3.3). The detector is stabilized at a temperature of 220 K. The dependence of the noise level on the slow peaking time was measured, before the detector was integrated into the final setup. The results are shown in figure 5.1.

The noise level has its minimum of 1.95 mHz at 9.6 µs, but the variations of the noise level for slow peaking times larger than 4 µs are relatively small. So any slow peaking time above 4 µs was considered to be appropriate.

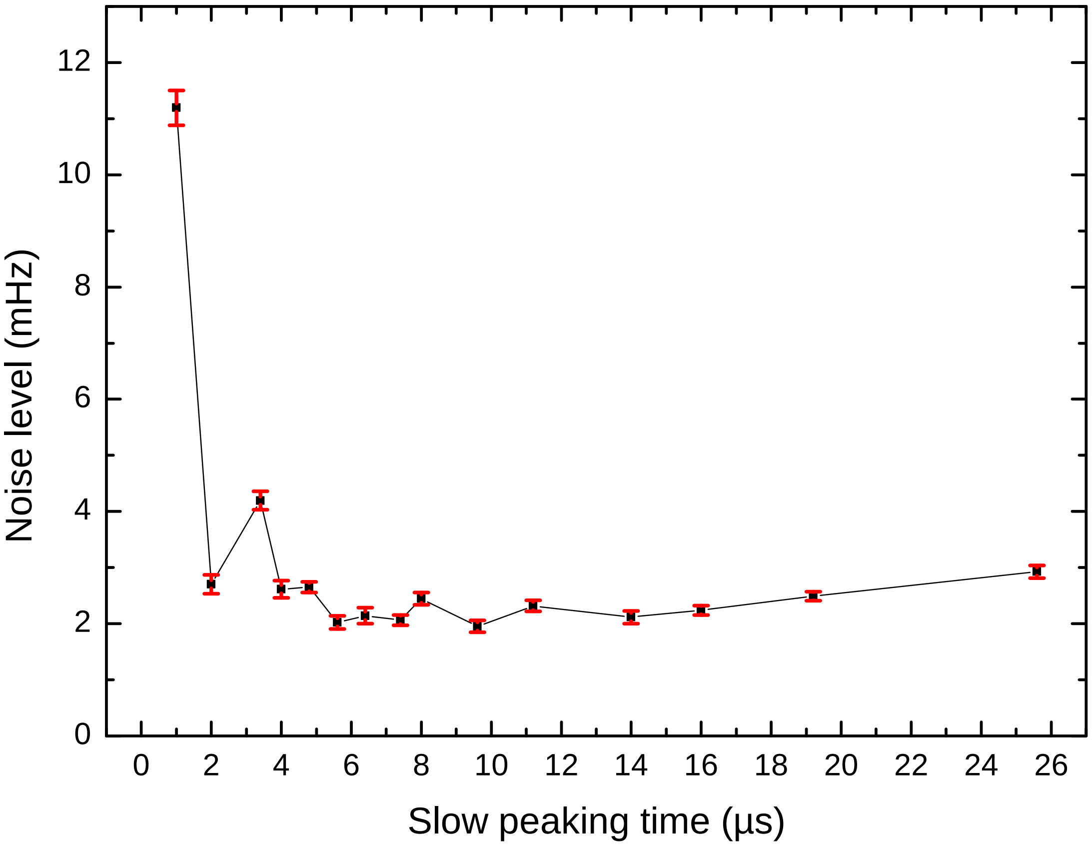

Figure 5.1: Noise level as a function of the slow peaking time. The noise was measured without any radiation source for at least 24 hours. The line is not a fit function, it is only to guide the eye. The results are consistent with the manufacturer's specification of a minimum noise level close to 10 µs [Amp12]. The threshold was manually set to channel 400 of 8192 (corresponding to approximately 1 keV). To ensure comparability the same threshold was applied to all measurements. The high value was required to cut off the noise edge in the measurements with short SPTs. The value of the measured noise level changes with the threshold used.

Apart from the noise level, the slow peaking time strongly influences the energy resolution of the detector. Therefore the energy resolution was measured for different slow peaking times. The measurements were performed with an americium-241 γ-source and a terbium foil as a target[60]. A Gaussian peak was fitted to the L$\alpha_{1/2}$-line and the FWHM was determined. The results are shown in figure 5.2.

The slow peaking time was preliminarily chosen as 11.2 µs. This setting ensures a low noise level and good energy resolution. It was used for the energy calibration of the detector, which is described in the following section. The slow peaking time can be changed during operation of the TRIADE experiment, if necessary. In this case a new energy calibration and an adjustment of the thresholds is required.

---

[60] The data sheet of this source can be found in figure B.22.

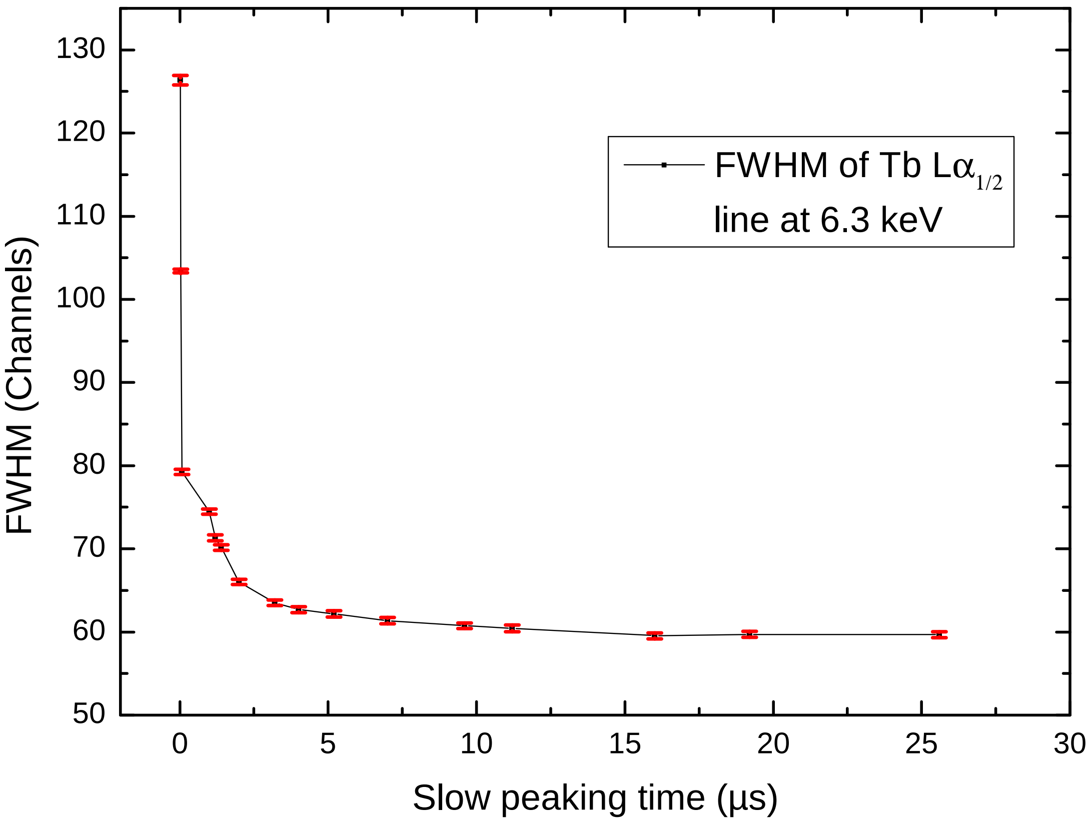

Figure 5.2: Resolution of the Amptek X123 for different slow peaking times. The full width at half maximum (FWHM) of the terbium L$\alpha_{1/2}$ line at 6.2 keV was determined using a Gaussian peak fit. Since the energy calibration depends on the SPT, the resolution is given in channels. The line is not a fit function, it is only to guide the eye.

Using the energy calibration from section 5.1.2, the previously determined resolution of 60.44 channels at the chosen peaking time of 11.2 µs corresponds to an energy resolution of:

$$\Delta E = (151.34 \pm 0.98)\ \text{eV}\ . \tag{5.1}$$

In addition to the SPT, adequate thresholds had to be determined. The slow threshold was first set to a very low value. In the spectrum which was measured with this setting the noise edge was clearly visible. The position of the noise edge was determined and the slow threshold was then set to a value slightly above the noise edge. This procedure was repeated for the fast threshold. The chosen settings can be found in appendix B.3.1.

In order to test the performance of the detector, the noise level was measured over a period of approximately 65 hours, using the SPT chosen before. The threshold was manually set to the chosen value. The noise rate S_{Noise} was determined as:

$$S_{\text{Noise}} = (4.11 \pm 0.13)\ \text{mHz}\ . \tag{5.2}$$

The value differs from that presented in figure 5.1, because of the lower threshold. The measurement of the noise level was repeated after the detector was integrated into the final TRIADE setup and after baking the system several times. The spectrum obtained in this measurement is shown in figure 5.3.

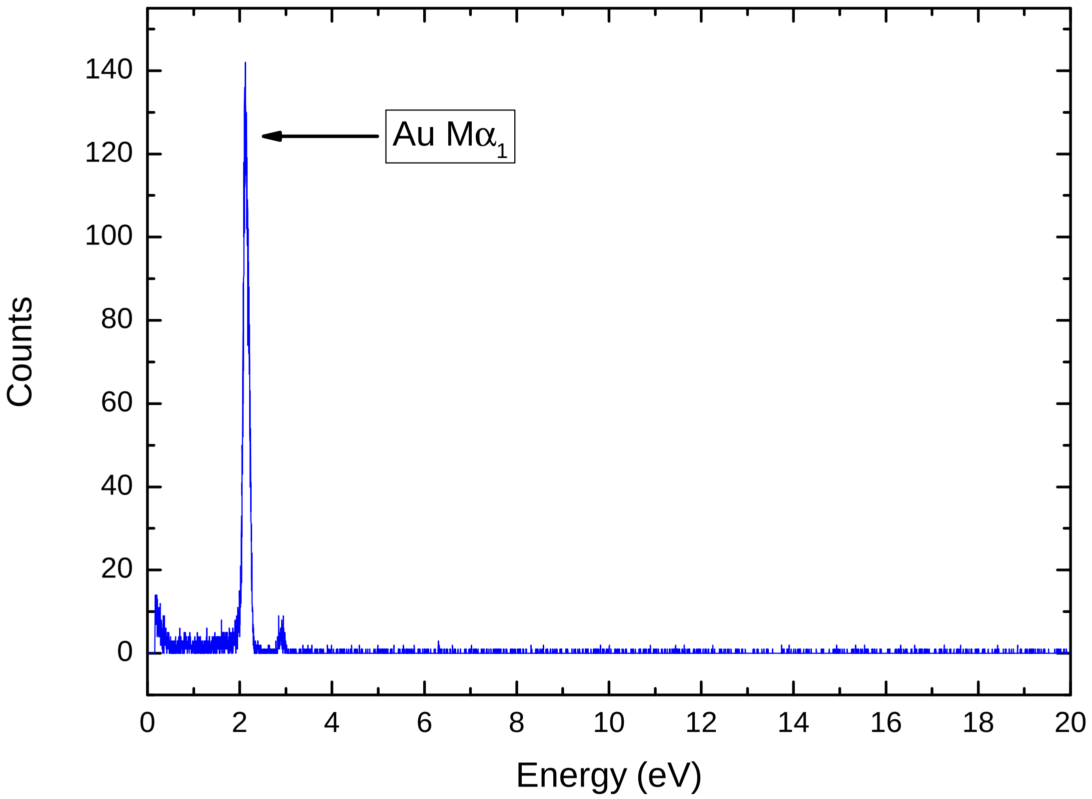

Figure 5.3: Background spectrum in the final setup. This spectrum was measured before tritium or any other source was filled into the recipient. Nevertheless, a peak is visible which is assumed to correspond to the $M\alpha_1$ line of gold. A possible explanation is given in the text.

The gold peak which occurs in the spectrum in figure 5.3 was not observed before the first bakeout of the system. A possible explanation for this peak is a radioactive substance, which naturally occurs in one of the materials used in the recipient. The radiation from this substance could cause characteristic radiation in the gold coatings, which results in the observed peak. One possibility of a radioactive substance is ^{40}K, which might have been deposited during the galvanic gold coating of the recipient and which might have gassed out of the coating during bakeout. The peak was not observed, while the recipient was being pumped by all pumps.

5.1.2 Energy calibration with X-ray tube

In order to record spectra for the energy calibration, the detector was integrated into a setup referred to as the X-ray box ("X-Box"). The X-Box consists of an Amptek[61] Mini-X X-ray tube system, a lead box as shielding and a computer for controlling the Mini-X. Furthermore, a detector can be placed inside the X-Box.

The Mini-X contains an X-ray tube, a high voltage supply, a 1 µm gold target, and an USB controller. The high voltage and the tube current are controllable in the range of 10 kV to 50 kV and 5 µA to 200 µA. A target can be mounted in front of the

---

[61] Amptek Inc., 14 De Angelo Drive, Bedford, MA. 01730 U.S.A.

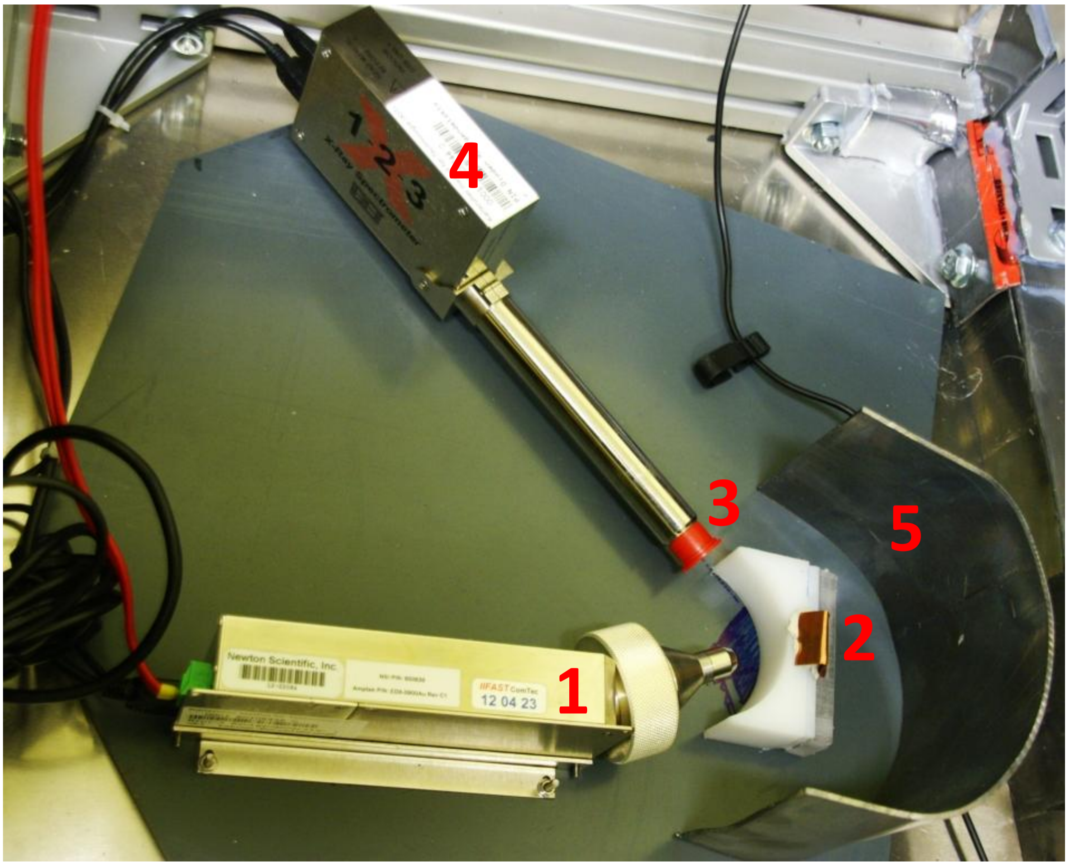

Figure 5.4: Inside view of the X-box. The figure shows the experimental setup for the measurement of spectra for the energy calibration of the Amptek X123 SDD. (1) Amptek Mini-X, (2) copper target, (3) location of the detector (not visible), (4) detector electronics, (5) shielding. The whole setup is placed in a lead-shielded box.

Mini-X. If the target is irradiated with X-rays from the Mini-X, characteristic radiation is produced inside the target (compare section 3.4). This characteristic radiation can be analyzed. If the material of the target is known, the peaks in the spectrum can often be identified and an energy calibration of the detector can be performed using literature data of the peak positions. If the detector is calibrated and the composition of the target is unknown, one can obtain information about the composition of the target material by analysis of the spectra.

Different detectors can be mounted inside the X-Box. The picture shows an Amptek X123 Si-PIN diode spectrometer[62]. The X123 SDD used for TRIADE was mounted in the same position perpendicular to the Mini-X for the calibration measurements.

In order to obtain an energy calibration for the chosen settings, a spectrum using a copper target was recorded, which is shown in figure 5.5. Beside the characteristic peaks of copper, further peaks are visible. It is assumed that these peaks are caused by characteristic radiation of iron and chrome, which are contained in the surrounding experimental setup.

---

[62] The X123 Si-PIN diode and the X123 SDD spectrometer have the same mechanical dimensions.

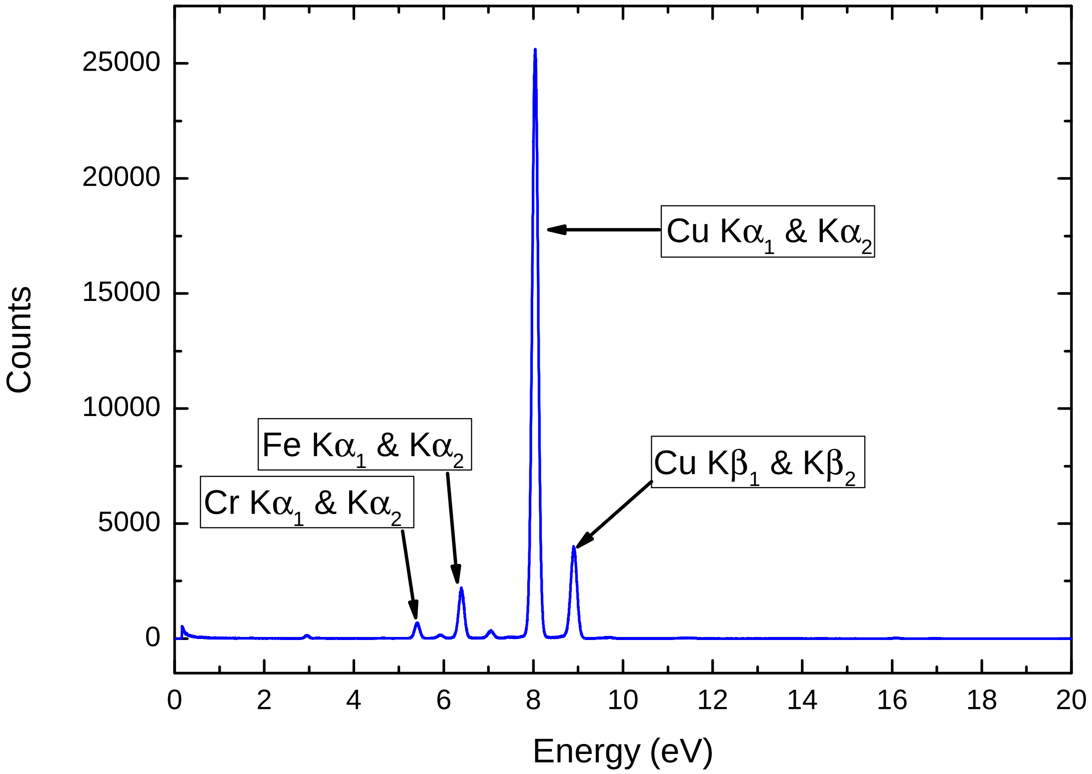

Figure 5.5: Detector calibration spectrum. The shown spectrum was used for the calibration of the TRIADE detector. The peaks indicated in the spectrum were identified based on the knowledge of the materials which are in the setup.

Table 5.1: Peak positions and characteristic energies for detector calibration. The listed energies are taken from [Tho09].

Material:	Cr	Fe	Fe	Cu	Cu
Peak:	$K\alpha_1$,$K\alpha_2$	$K\alpha_1$,$K\alpha_2$	$K\beta_1$,$K\beta_3$	$K\alpha_1$,$K\alpha_2$	$K\beta_1$,$K\beta_3$
Peak position (Ch):	2176.93	2571.03	2832.79	3227.55	3571,99
Standard error (Ch):	0.38	0.12	0.89	0.01	0.07
Energy (keV):	5411.63	6399.47	7058.00	8041.00	8905.30

In order to determine the energy calibration for the detector, Gaussian peaks were fitted to the peaks indicated in figure 5.5. The energies corresponding to these peaks were taken from [Tho09]. Table 5.1 gives an overview of the peak positions and the corresponding energies.

The energy to channel calibration was determined from a linear regression using all peaks:

$$E = (-41.175 \pm 7.871)\ \mathrm{eV} + (2.504 \pm 0.002)\ \frac{\mathrm{eV}}{\mathrm{Channel}} \cdot \mathrm{Channel\ number}\ . \tag{5.3}$$

Changing detector parameters, especially like the gain or the SPT, can change the energy calibration of the detector. Therefore, the determined calibration is only valid for the chosen settings. All settings used are documented in appendix B.3.1.

5.2 Temperature management test measurements

In the TRIADE experiment the sample should be cooled or heated by cooling or heating the blind flange, the sample holder is mounted to. To optimize heat conduction through the sample holder, it is made of copper (compare section 4.5). In order to verify the functionality of this approach, two test experiments were performed, one for the heating and one for the cooling of the sample.

For these experiments, a simplified sample holder was built and mounted onto a DN100 CF blind flange. A copper pipe was brazed to the back of the blind flange, which was mounted to a standard DN100 CF pipe. The pipe was evacuated by a turbomolecular pump before performing the experiments.

For testing the cooling concept, the copper pipe was connected to a closed dewar containing liquid nitrogen. The other end of the pipe was used as an exhaust pipe. The experiments were performed in an extractor hood. The liquid nitrogen in the dewar was heated in order to evaporate the nitrogen and let it flow through the copper pipe along the blind flange. The blind flange was covered with glass wool and aluminium foil for thermal insulation. The setup of this test experiment is shown in figure 5.6. The temperature was monitored at the sample holder and in the exhaust gas stream.

The temperature curve of the cooling test experiment is shown in figure 5.7. The nitrogen dewar was heated by a heating cartridge with a power of $P_{\mathrm{heat}} = 93$ W. The nitrogen in the dewar had to be refilled after approximately two hours. The cooling was interrupted thereby resulting in a temperature rise both at the sample holder and in the exhaust gas stream. The sample holder was then cooled for another 2.5 hours, before the temperature rapidly rose again, when the dewar was empty again. A minimum temperature of $T_{\mathrm{min}} = -30$°C was reached at the sample holder after a cooling period of approximately five hours.

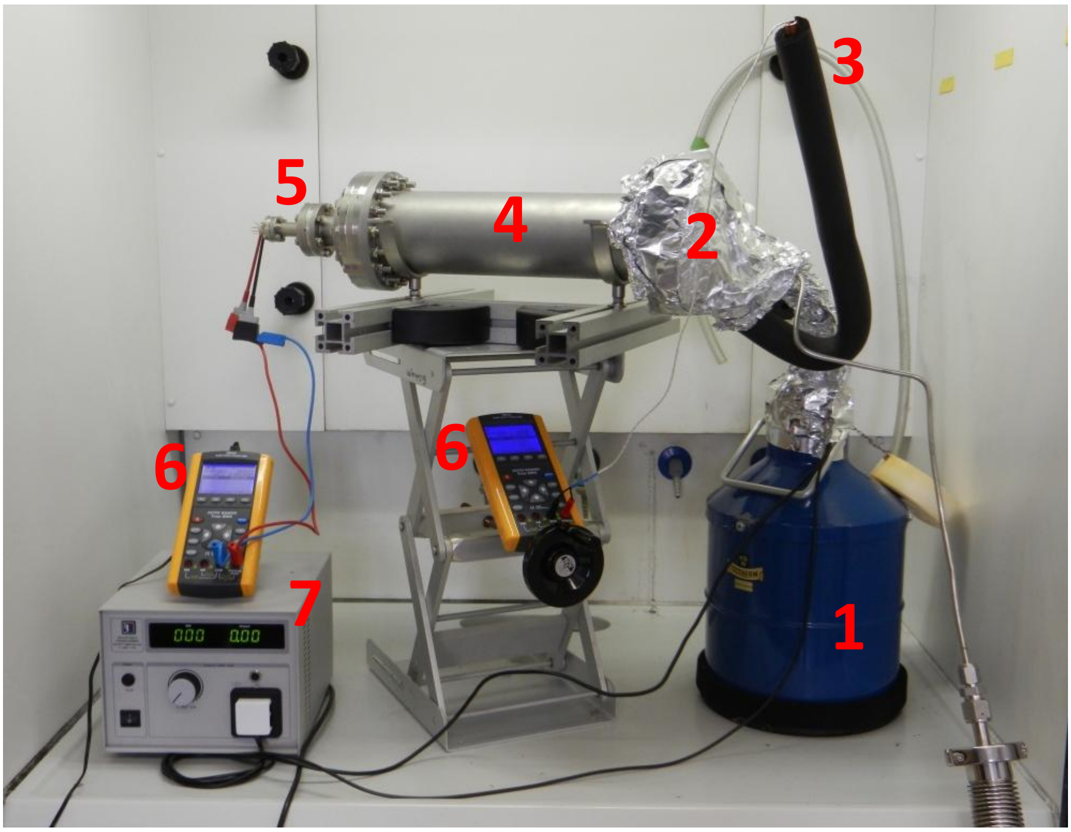

Figure 5.6: Test experiment of the sample cooling. The picture shows the test setup in the extractor hood at the "cold laboratory" at TLK. (1) dewar with liquid nitrogen (2) blind flange with sample holder on vacuum side and cooling pipe on opposing side (not visible, covered with thermal insulation material), (3) exhaust, (4) evacuated DN100 CF pipe, (5) electrical feedthrough, (6) multimeters for temperature measurement, (7) transformer for the power supply of the heating cartridge. The concept of the experiment is described in the text.

This result was considered as a proof of principle for the idea of cooling the sample by cooling the flange. The system used for the test experiment was a quick and economic setup for the proof of principle. The following limitations of the system used restricted the lowest reachable temperatures:

- The connection between dewar and copper pipe was not leak proof. A large fraction of the evaporated nitrogen was lost for the cooling process at this point.
- The contact area between cooling pipe and blind flange was very small, resulting in poor heat conduction between sample holder and cooling gas.
- The cooling pipe was entirely made of copper and only insulated by foam material and aluminium foil. So it is assumed that the nitrogen gas was warmed up in the copper pipe before passing the blind flange.

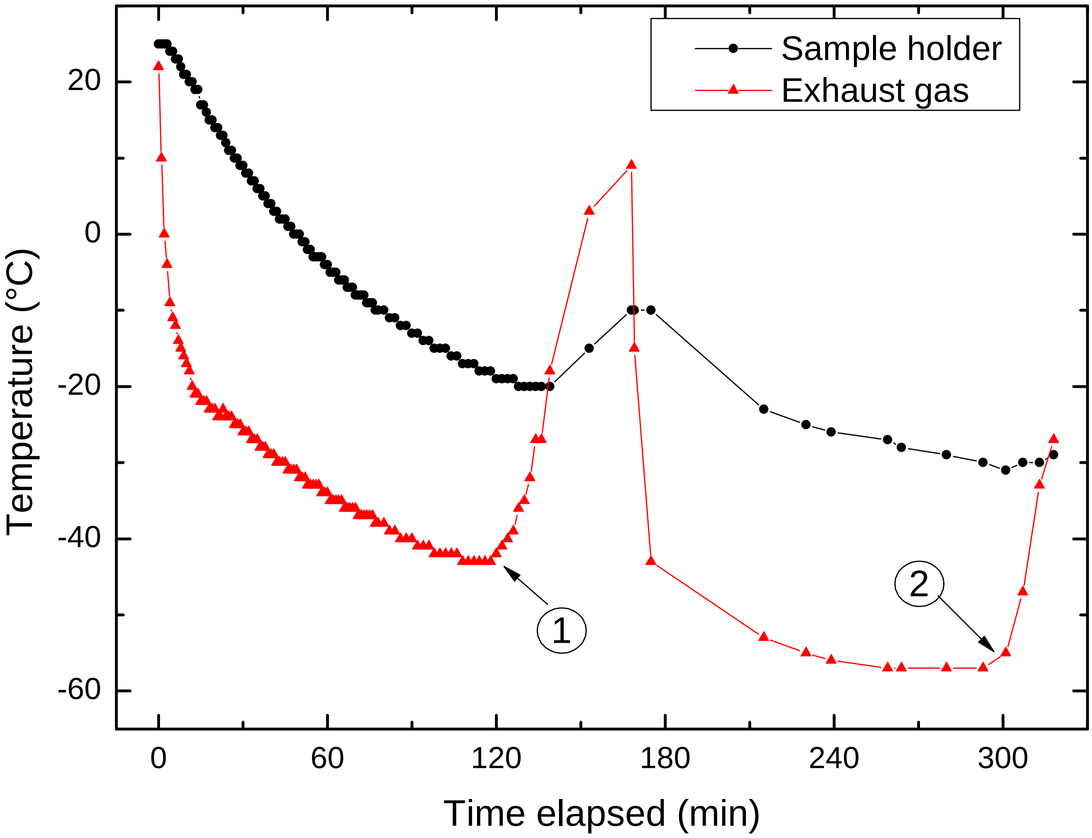

Figure 5.7: Measurement data from the sample cooling test experiment. The temperature was measured at the sample holder and in the exhaust gas stream. The cooling was interrupted when the dewar had to be refilled after approximately two hours (1). The experiment was finished after the temperature at the sample holder seemed to reach saturation and the temperature in the exhaust gas started to rise again (2).

The following improvements were implemented in the more sophisticated design of the TRIADE cooling system (compare section 4.5) in order to reach lower temperatures:

- The cold nitrogen gas is produced by a professional, leak proof system.
- The nitrogen gas is led to the heat exchanger by a vacuum insulated hose.
- A custom-made heat exchanger with large contact area is used in the final setup.

Regarding these improvements and the results of the test experiment, it is expected that a minimum temperature of $T_{\mathrm{min}}^{\mathrm{exp}} = -100°\mathrm{C}$ is reachable with the TRIADE cooling system.

The heating concept of TRIADE was tested using the same setup as for the cooling test experiment. A flange heater was used to heat the blind flange, the sample holder is mounted to. The temperature was again measured at the sample holder and furthermore directly at the blind flange at the flange heater. The heating power was controlled with a transformer and slowly increased at the beginning of the test experiment. The results of this experiment are shown in figure 5.8.

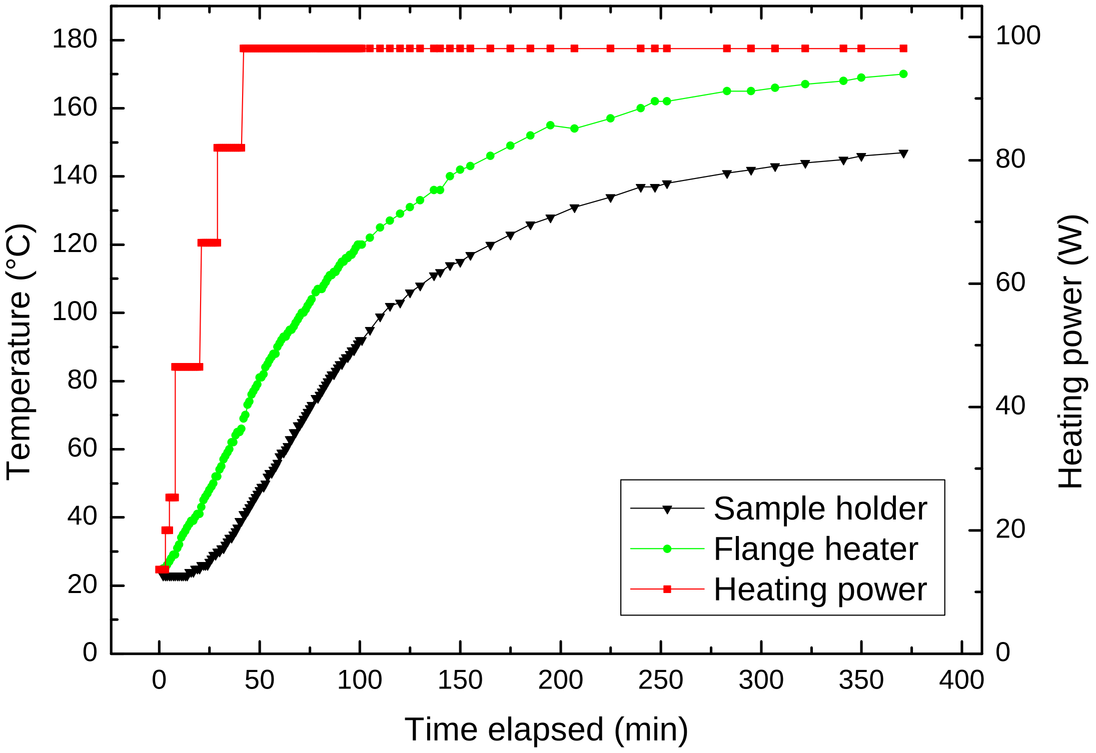

Figure 5.8: Temperature curve of the test experiment of the sample heating. The temperature at the sample holder seems to reach a saturation level at approximately 150°C. This is seen as a proof of principle for the heating concept.

After more than six hours of heating, a final temperature of 147°C was reached at the sample holder. Higher temperatures will be reachable in the final setup with additional heating cables at the recipient and the mass spectrometer volume. Both test experiments confirmed the expectation that the temperature at the sample reacts very slowly to temperature changes of the blind flange or the other surroundings. It is therefore expected that the temperature of the sample in the final setup can not rapidly be changed, and in return, only minimal fluctuations are expected, if the blind flange is constantly cooled or heated.

5.3 Commissioning of the vacuum system

All single connections of the TRIADE vacuum system were helium leak tested according to procedure A3, DIN EN 1779:1999 [DIN06]. The leak detector was connected to the connection between VA054 and VA055 and later to the sampling port (compare figure 4.13) for the leak tests. The leak detector was calibrated before the test of the system, using a calibrated leak. The tested connections were sprayed with helium gas, which was used as a tracer for leaks. All pumps were turned off during leak tests. The leak rate was lower than 10^{-10} mbar·l/s for every single connection. Thereby, the TRIADE vacuum system complies with the requirements in the TLA of the TLK (compare section 4.2.2 or [TLA12]).

The system was repeatedly pumped over several days and baked at approximately 180°C to 200°C. The lowest pressure reached after this procedure was:

$$P_{\mathrm{fin}} \approx 5 \cdot 10^{-9} \text{ mbar} . \tag{5.4}$$

This pressure is low enough to make the signal contributions $\mathrm{S}_{\mathrm{i}}^{\mathrm{G}}$ and $\mathrm{S}_{\mathrm{G}}^{\mathrm{j}}$ negligible (compare section 3.6 and figure 3.9). Measurements with the mass spectrometer, which is part of the TRIADE setup, indicate that this final pressure is still dominated by residual water in the system (compare section 5.4). The residual water originates from parts of the system which were not heated during the bakeout, such as the pressure instrumentation and their connection pipework to the recipient. Therefore, it is expected that the pressure in the recipient could still be further reduced by baking the entire system with respect to the maximum operating temperatures of the instrumentation. Figure B.1 shows the pressure ultimately reachable in the recipient dependent on the integral leak and outgassing rate of the recipient.

5.4 First measurements with the quadrupole mass spectrometer

The measurement principle of a quadrupole mass spectrometer is briefly described in section 4.4, more detailed descriptions are available in the literature (e.g. [Dem10a]). The MKS Microvision Plus quadrupole mass spectrometer (QMS) used in the TRIADE experiment was first calibrated with regard to the mass alignment. The mass spectrometer was then used for the further commissioning of the vacuum system. Both is described in this section.

All gases show different distributions of relative intensities in different masses, as for example different isotopes might occur or molecules might occur dissociated. The relative intensity distributions for different species are available in the literature. All values for relative peak heights in the following are taken from [MKS13] (compare figure B.19). Furthermore, atoms or molecules can be double-ionized by the ionization source of the QMS. These particles cause contributions in the spectrum at half of their mass with reduced relative intensity. Partial pressures for nearly all masses can be caused by different atoms or molecules (for example both D_2 and He have mass 4). In addition there is an influence of the turbomolecular pump which is located near the QMS in the TRIADE experiment. The TMP has different compression ratios and pumping speeds for different gases and therefore changes the composition of the residual gas at the high vacuum side of the pump (compare figure B.3). All of these aspects have to be considered in the analysis of mass spectra.

The calibration of the mass alignment is necessary in order to ensure correct relative peak heights. The fields in the QMS can be adjusted in order to let particles of any m/e ratio in the range of 1-100 amu/e pass the rods and be detected. A quasi continuous scan for $m/e = 1 - 20$ amu/e is shown in figure 5.9.

The peaks corresponding to one mass are not δ-distributions, but asymmetric peaks. If a discrete spectrum is recorded, the measured partial pressure corresponds to one m/e value, slightly lower or higher values are disregarded. The mass alignment calibration should ensure that every partial pressure is measured at the peak maximum. If the mass alignment is not calibrated, a wrong peak height might be determined.

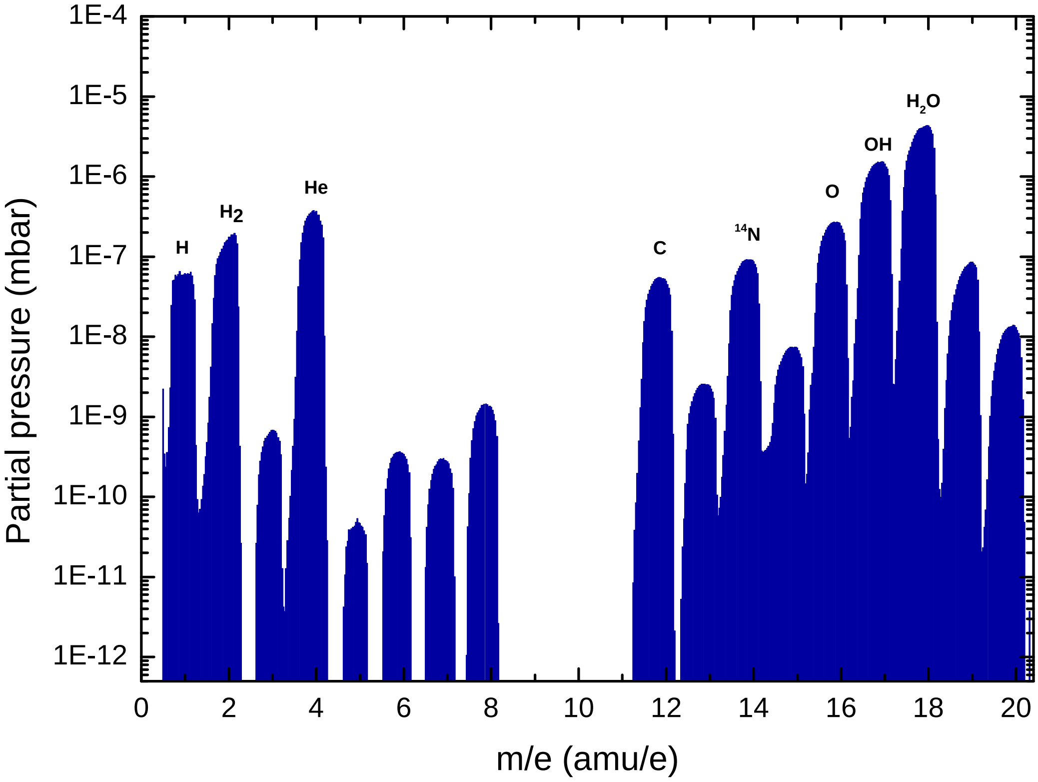

Figure 5.9: Quasi continuous QMS spectrum. The gases indicated in the spectrum are assumed to cause the dominant fraction of the partial pressure of the corresponding mass. Some contributions may originate from other gases. The shown spectrum is discussed in the text.

The calibration can be performed using the Process Eye^{TM} software provided by the manufacturer. The calibration is performed by adjusting two parameters, namely "low mass alignment" and "high mass alignment".

The calibration gas mixture, provided by Air Liquide Deutschland GmbH[63], was filled with a pressure of 1 bar into a sampling cylinder of 10 cm^3. The calibration gas was a mixture of N_2 $(32.99 \pm 0.66)\%$, CO_2 $(32.98 \pm 0.66)\%$ and He (rest). The sampling cylinder was connected to the volume, the QMS is mounted in. Prior the calibration, the system was then baked at a temperature of $T \approx 200°C$ for 17 hours. For the calibration the pumps VA052, VA053 and VA054 were pumping in a closed loop (HV002, HV005, HV011 and HV014 opened, all others closed (Compare figure 4.13).

The calibration was performed in the analog-view (compare figure 5.9) by fit-by-eye. The mass alignment parameters were varied until the partial pressures corresponding to the masses of the highest relative intensity (4 for helium, 28 for nitrogen (N_2), 44 for carbon dioxide) reached a maximum for every component of the calibration gas mixture. After the calibration the spectrum shown in figure 5.10 was obtained.

All spectra shown in the following are not calibrated concerning peak heights. Therefore only qualitative conclusions can be drawn from the spectra based on relative peak heights. Furthermore, spectra are usually normalized only for nitrogen. All gases have

---

[63] Air Liquide Deutschland GmbH, Bataverstr. 47, D-47809 Krefeld, Germany

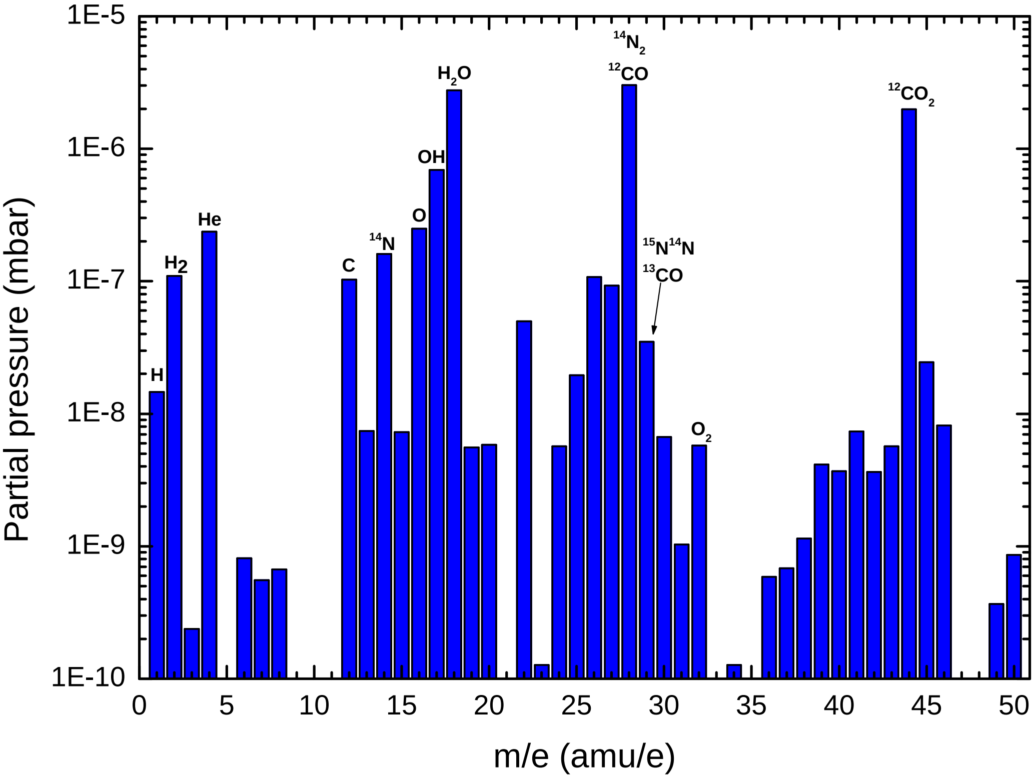

Figure 5.10: Mass spectrum with calibration gas. The gases indicated in the spectrum are assumed to cause the dominant fraction of the partial pressure of the corresponding mass. Some contributions may originate from other gases. The shown spectrum is discussed in the text.

different ionization probabilities, which make specific calibration factors necessary for every gas. The ionization probabilities for various gases can be found in figure B.20. The most important findings from the spectrum, shown in figure 5.10, are:

- Masses 28 and 44: As expected, the components of the calibration gas cause high partial pressures. The partial pressure of mass 28 is mainly caused by N_2, which also contributes to mass 14 (7% relative intensity). The partial pressure of mass 44 is caused by CO_2, which also contributes to masses 28 (11%), 16 (9%) and 12 (6%) [MKS13].
- Mass 4: The partial pressure of mass 4 is caused by helium from the calibration gas. The peak appears lower because of the low ionization probability for helium (Approximately 0.14 vs 1.0 for nitrogen, compare figure B.20).
- Masses 18, 17 and 16: The partial pressures are caused by residual water in the system. The ratio of the peak heights of masses 17 and 18 is given as 1:4 in literature [MKS13], which fits the measured spectrum very well. Water in the system is very disadvantageous, as it can bind large amounts of tritium (compare section 3.9). The amount of water in the system can be reduced by baking out the system, as it is shown in figure 5.11.

After the vacuum system had passed the final leak tests (compare section 5.3) the first spectrum shown in figure 5.11 was obtained. The highest partial pressures are caused by water in the system (masses 17 and 18). The partial pressures of hydrogen (mass 2 (100%) for molecular hydrogen and mass 1 (5%) for atomic hydrogen) are caused by outgassing of the stainless steel vacuum components. Also contributions of the calibration gas are visible (masses 28 and 44).

The second spectrum shown in figure 5.11 was obtained after baking the system at $T \approx 150°\mathrm{C}$ for approximately 16 hours. Compared to the first spectrum in figure 5.11, the partial pressures have decreased by approximately two orders of magnitude. The partial pressures at masses 18 and 17 (caused by water) have decreased by two and a half orders of magnitude, but they are still dominant. The partial pressures at masses 2 and 1 are caused by outgassing hydrogen, which can not be avoided in stainless steel vacuum systems. The other partial pressures can be explained by residual calibration gas leaking through the closed manual valve of the sampling cylinder, which was still connected to the system at that time. The spectrum indicates that there are no major leaks in the system.

After the bakeout water was still the dominant species in the TRIADE vacuum system. As it was shown, the amount of water can effectively be reduced by baking the system. Therefore this step is the most important one, when trying to reduce the final pressure in the TRIADE vacuum system. Most of the remaining water in the system probably originates from parts which are directly mounted to the recipient and were not heated (for example the pressure sensors and pipework). The residual water will be removed from the system by further pumping and baking the system, before first tritium measurements are started.

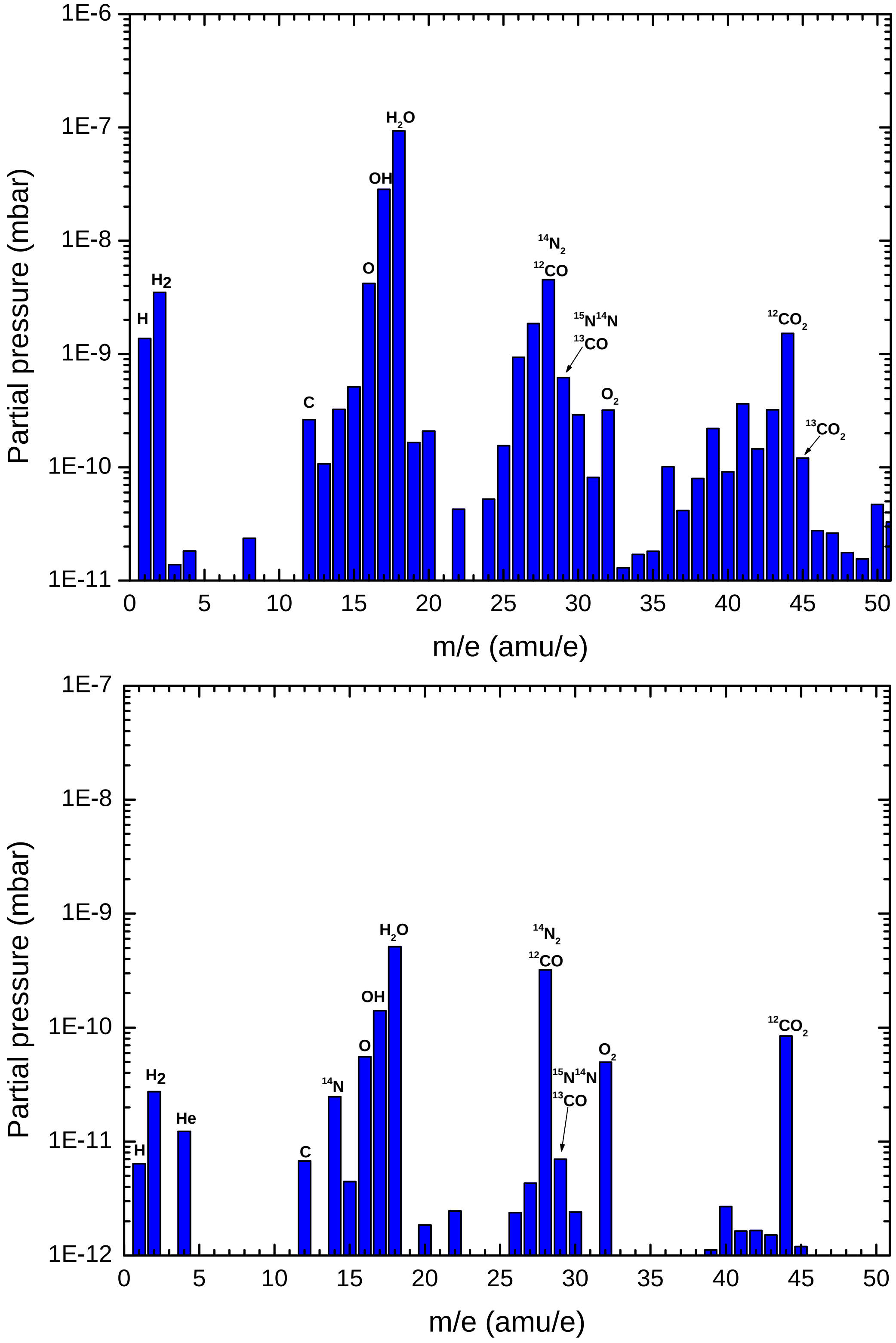

Figure 5.11: Mass spectrum before and after bakeout. The upper spectrum was taken before, the lower spectrum was taken after baking the system. The gases indicated in the spectrum are assumed to cause the dominant fraction of the partial pressure of the corresponding mass. Some contributions may originate from other gases. The shown spectra are discussed in the text.

Chapter 6

Monte Carlo simulations of the TRIADE BIXS system

In this chapter the Monte Carlo simulations of the TRIADE BIXS setup are described. These simulations are required in order to be able to analyze the signal measured by the detector. The motivation and the objectives for these simulations are described in section 6.1 and the implementation of the simulations is described in section 6.2. In section 6.3 the results of the simulations are presented.

6.1 Motivation and objectives of the simulations

As described in section 3.6, the measured detector signal is a composition of the signal originating from activity on the sample surface and background signals.

In order to be able to calculate the amount of tritium adsorbed on the sample surface from the measured count rate, the ratio between the number of decays in the adsorbate and the number of resulting events measured by the detector, needs to be determined by simulations. This ratio will be referred to as "efficiency" of tritium adsorbed on the surface causing detector events (F^i, compare equation 6.1).

Since the background contributions can not be identified in the measured spectrum, they also have to be estimated by simulations. A tritium β source can be simulated at the locations listed in figure 3.9. By assuming a value for the amount of tritium at location i, the contribution of $\sum_j S_j^i$ can be determined.

The different simulation tasks had to be prioritized. The three most important tasks, which were dealt with in the context of this work, were the simulation of

- the detector signal originating from adsorbed tritium on the sample surface,
- the background signal originating from tritium adsorbed on the X-ray producing element,
- the background signal originating from tritium in the residual gas.

The intrinsic detector noise, which is the third major source of background, was determined experimentally (compare section 5.1). With this information, it was possible to determine the expected most important contributions to the detector signal.

6.2 Implementation of the simulations

For the simulations of the TRIADE setup the PENELOPE 2008 (**PEN**etration and **E**nergy **LO**ss of **P**ositrons and **E**lectrons) code system was used [Sal08]. It allows the simulation of electron, positron and photon transport in the energy range of 50 eV to 1 GeV. The software contains a simulation algorithm based on a scattering model which uses numerical databases and analytical cross section models for the different interaction mechanisms. The following interaction mechanisms are implemented:

- Electron interactions: Elastic and inelastic scattering, bremsstrahlung emission and positron anihilation.
- Photon interactions: Rayleigh and Compton scattering, photoelectric absorption and pair production.

During the interaction of primary electrons or photons new secondary particles can be produced. Those might interact and produce further particles, forming an electromagnetic shower. New particles are produced until their energy is too low to produce further particles. The simulation of a large amount of particles requires large computing capacities. Therefore, models for the simplification of the simulations are implemented in the PENELOPE code system. The user can control how these models are used in a simulation by setting the different parameters ($C1$, $C2$, WCC, WCR). A detailed description of the PENELOPE 2008 code system is given in [Sal08].

The simulations for TRIADE were performed with the program "pencyl.exe", which is included in the PENELOPE code system. It allows the simulation of electron and photon transport in multilayered cylindrical structures. The program requires an input file containing information about the setup geometry, the source and different simulation parameters. Furthermore, the program requires files containing material properties.

The TRIADE setup geometry for the simulation was defined in an input file compatible to the pencyl.exe program. The same geometry definition was used for the simulation of all sources (tritium on sample, on window, in residual gas). Just the source definition was modified for the simulation of different sources. As an example, the input file for the simulation of tritium in the residual gas is shown in appendix C.1. For the simulation of the TRIADE setup, the following simplifications were used in the geometry definition:

- The staves of the sample holder were not included in the geometry definition, as there is no direct line of sight to the detector. The probability of interactions in the staves leading to measurable results is assumed to be negligible.
- The bodies with gold coated surfaces are assumed to entirely consist out of gold. Since the thickness of the gold coatings is of the order of µm (compare section 4.3.2.2), it is assumed that the probability of interactions taking place deeper in the bulk material leading to measurable results is negligible. Thus, no measurable effect is expected from the materials below the gold coatings.
- Geometries located behind the active volume of the detector were not defined for the simulation. It is assumed that interactions in this area are negligible.
- Minor simplifications were used concerning the shape of the components (compare figure 6.1)

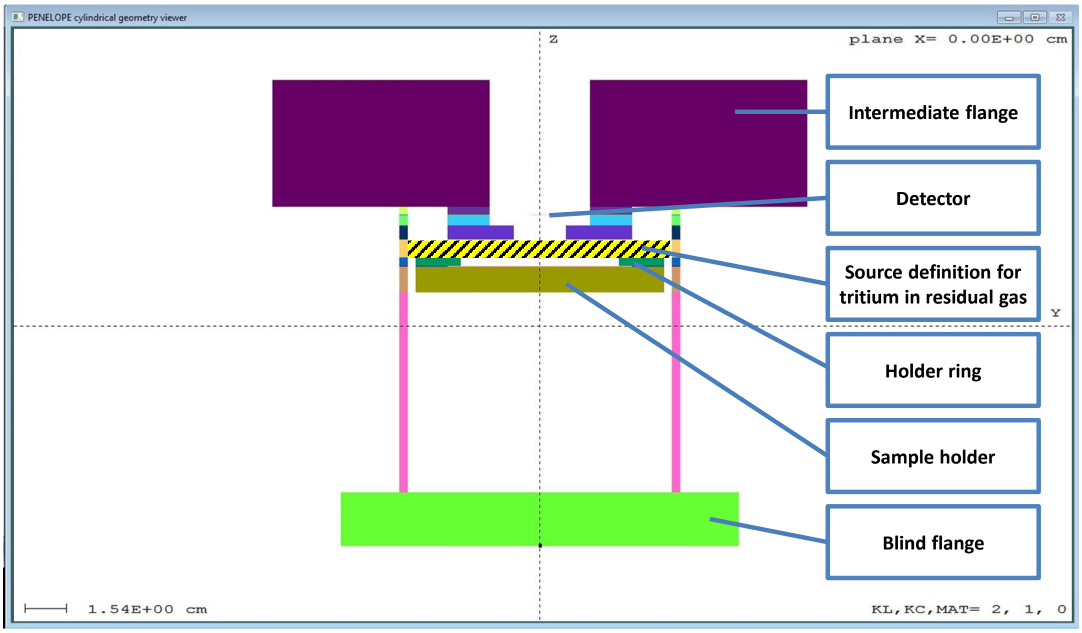

Figure 6.1: Geometry definition for the simulation of the TRIADE setup. This picture was created with the "gviewc" program, which is provided within the PENELOPE code system. The different colors indicate the different layers and bodies, used for the geometry definition. One component in the real setup might be represented by various bodies in the geometry definition.

The geometry definition is shown in figure 6.1 (compare to the experimental setup in figure 4.5). The source definition contains a calculated β spectrum and a source geometry definition. All β sources were defined with an isotropic angular distribution. The source geometries were defined as follows:

- In order to simulate tritium adsorbed on the sample surface, the β source was defined with zero thickness on the part of the sample surface which is not covered by the sample holder.
- In order to simulate tritium adsorbed on the gold coated beryllium window, the β source was defined with zero thickness on the window surface facing the recipient. Tritium adsorbed on the flange, the window is mounted in, was not simulated, as contributions from this source are expected to be negligible.
- In order to simulate tritium in the residual gas, the β source was defined in the space between the holder ring of the sample holder and the gold coated beryllium window. In this space the source is defined to cover the entire diameter of the recipient. This source definition is indicated in figure 6.1.

The definition of the sources on the sample surface and on the beryllium window represents the real situation in good approximation. The dimensions of the source simulating tritium in the residual gas was limited to the volume which is considered to be relevant in order to save on computing capacity. This source definition does not take into account that tritium will be located everywhere in the residual gas in the recipient.

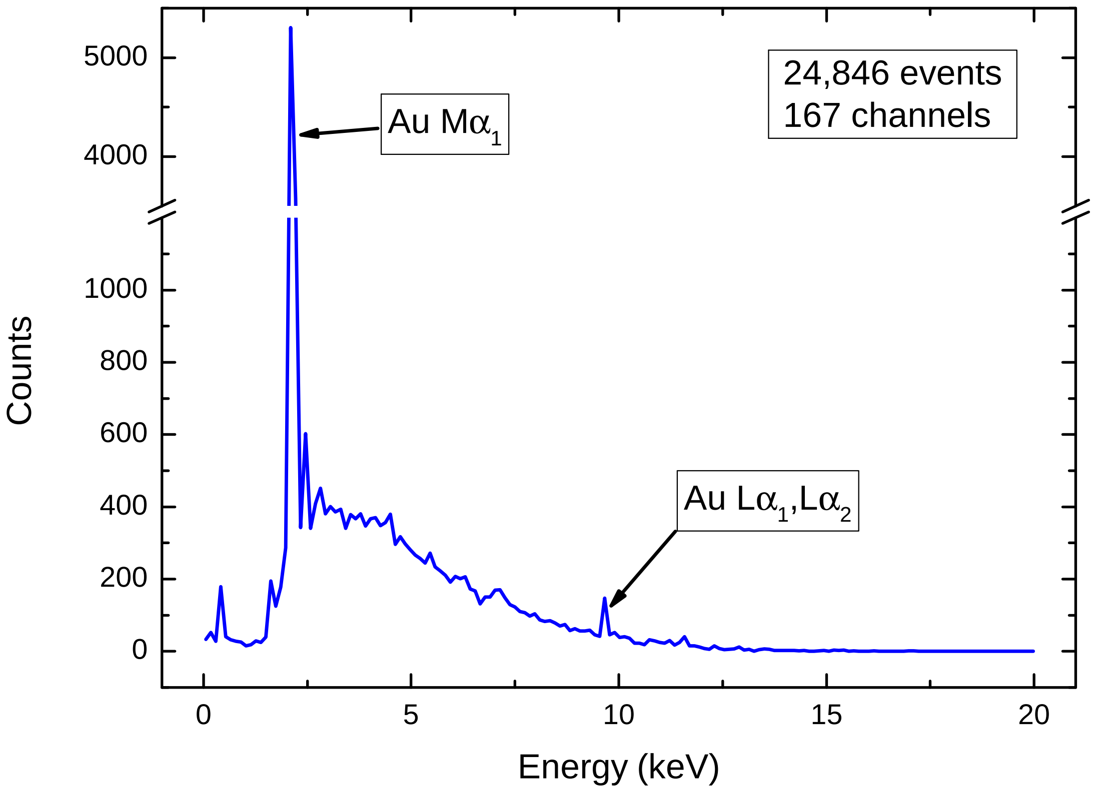

Figure 6.2: Simulated BIXS spectrum. This figure shows a simulated spectrum originating from tritium adsorbed on the gold coated beryllium window. The spectrum was obtained after simulating $2.07 \cdot 10^{10}$ primary particles.

Nevertheless, the dimensions of the defined source were limited as explained above, because a large fraction of tritium in the residual gas does not cause measurable detector signals. For example, the contributions from tritium located between the plate of the sample holder and the blind flange are assumed to be negligible.

Therefore, the results of the simulations of tritium in the residual gas only refer to gas in the defined volume. This has to be taken into account during the analysis of the simulation results.

The simulations were performed on the "Tesla" computer cluster at the IEKP[64] at the Karlsruhe Institute of Technology. The simulations for the different source definition were split into 20 individual jobs, as every job runs on only one core of the Tesla cluster. By splitting the simulations into 20 jobs, more computing capacity could be used simultaneously. The simulated spectra of the 20 jobs were summed up afterwards. Together they were treated as one simulation.

The duration of the individual jobs was limited to one week. In this period a number of $N \approx 2 \cdot 10^{10}$ primary particles were simulated for every source definition. The total computing time was approximately 10,000 hours on Xeon E 5649 cores.

---

[64] Institut für Experimentelle Kernphysik

6.3 Results of the simulations

In figure 6.2 the simulated spectrum is shown as an example for the source defined on the gold coated beryllium window. This source is closest to the detector and therefore most statistics were obtained compared to the spectra of the other source definitions. The simulated spectrum looks very similar to the spectrum measured by the TriReX experiment (compare figure 3.7). The peak at 2.1 keV corresponds to the characteristic Mα_1 peak of gold at $E_{\mathrm{M}\alpha_1} = 2.12$ keV. The peak at 9.7 keV corresponds to overlapping characteristic Lα_1 and Lα_2 peaks of gold at $E_{\mathrm{L}\alpha_1} = 9.71$ keV and $E_{\mathrm{L}\alpha_2} = 9.62$ keV [Tho09]. This result meets the expectations very well, as most bodies are defined to consist of gold in the simulation.

In order to be able to estimate the contributions to the measured signal, the detection efficiencies of the processes causing the signal were determined by the simulations. The detection efficiency F^i is defined as the number of counts measured by the detector N^i_{counts}, caused by tritium at location i, divided by the number of primary particles N_{pp}:

$$F^i = \frac{N^i_{\mathrm{counts}}}{N_{\mathrm{pp}}} \; . \tag{6.1}$$

The contribution to the measured signal from tritium at location i (S^i, compare section 3.6) can be estimated assuming a value for the amount of tritium at location i:

$$S^i = \sum_j S^i_j = F^i \cdot A^i \; , \tag{6.2}$$

where A^i is the activity of the tritium at location i. S^i_j is the signal contribution caused by the process in which an decay electron from tritium at location i causes bremsstrahlung at location j. The detection efficiencies determined from the simulations are given in table 6.1. It is important to note that these efficiencies depend on the material of the simulated sample, because measurable bremsstrahlung is produced in the sample. Therefore, the determined efficiencies are only valid for the simulated gold coated beryllium sample.

In case of tritium in the residual gas, one furthermore has to keep in mind the volume which was defined as the source for this case. When determining S^G one has to assume an activity A^G in the defined volume, not an activity in the entire recipient.

Table 6.1: Simulated detection efficiencies for tritium adsorbed on sample, on the beryllium window and tritium in the residual gas. The detection efficiencies are given as counts measured by the detector per simulated primary particle.

Tritium location:	on sample (S)	on window (X)	in residual gas (G)
Simulated particles:	$2.09 \cdot 10^{10}$	$2.07 \cdot 10^{10}$	$1.93 \cdot 10^{10}$
Efficiency F^i ($\frac{\mathrm{counts}}{\mathrm{particle}}$):	$1.07 \cdot 10^{-7}$	$1.20 \cdot 10^{-6}$	$5.40 \cdot 10^{-8}$
Stat. uncertainty:	$0.07 \cdot 10^{-7}$	$0.02 \cdot 10^{-6}$	$0.50 \cdot 10^{-8}$

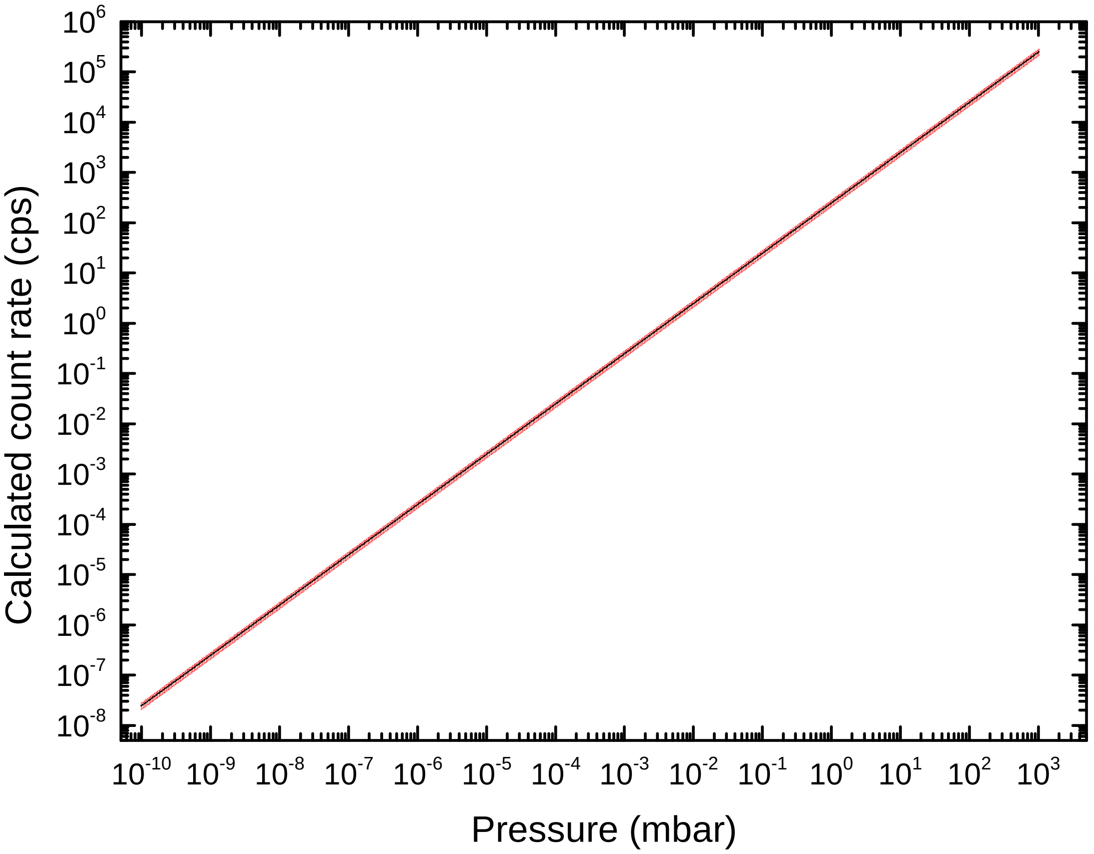

Figure 6.3: Calculated rate caused by gaseous tritium in the recipient. The expected count rate caused by gaseous tritium in the recipient was calculated in dependence on the pressure in the system. Error bars are too small to be visible. The expected rate was calculated based on the efficiency of gaseous tritium in the recipient causing events in the detector (F^G) determined from the simulation. For the calculation a temperature of 20°C in the recipient was assumed.

Using the detection efficiency for tritium in the residual gas (F^G) and the ideal gas law, the expected count rate was calculated as a function of the pressure in the recipient. The result is shown in figure 6.3. As the pumping system is designed to reach a final pressure of the order of $p_{\text{fin}} = 10^{-10}$ mbar (compare section 4.6), it becomes clear that the contribution of tritium in the residual gas is negligible. For example, at a pressure of $p \approx 10^{-8}$ mbar, which should routinely be reachable, the count rate caused by tritium in the residual gas is $S^G \approx 2.5 \cdot 10^{-6}$ cps and thereby three orders of magnitude smaller than the intrinsic detector noise.

In order to determine the expected signal contributions the adsorption of one monolayer of tritium was assumed on the sample and the window surface. The corresponding activity was determined according to the calculation in appendix A. Taking into account the geometry of the setup, one obtains the expected rates as shown in table 6.2. The expected detector noise is the value determined experimentally (compare section 5.1). The contributions from tritium adsorbed on the recipient's surface and the sample holder were not determined.

Table 6.2: Expected signal contributions determined from simulations and detector characterization measurements. The table shows the expected count rates which originate from one monolayer of tritium adsorbed on the sample and on the gold coated beryllium window, as well as tritium in the residual gas at a pressure of $P = 10^{-8}$ mbar and the detector noise, which was determined experimentally.

Simulated signal source	Expected rate (cps)
1 monolayer of T on sample	3.40 ± 0.21
1 monolayer of T on window	4.21 ± 0.08
T_2 in residual gas	$(2.50 \pm 0.36) \cdot 10^{-6}$
Detector noise	$(4.11 \pm 0.13) \cdot 10^{-3}$

The minimum detectable activity (MDA) can be calculated from the standard deviation σ_B of the total background signal, which was determined from the values in table 6.2. According to [Tso11], the MDA using a 95% confidence limit is:

$$MDA = 4.653 \cdot \sigma_\mathrm{B} = 0.37 \text{ cps} . \tag{6.3}$$

The corresponding activity on the sample surface was determined using the efficiency of the process of tritium on the sample causing detector events (F^S) determined before. By comparing this activity to the calculated activity of one monolayer (see appendix A) the detection limit was determined as:

$$\Theta_\mathrm{lim}^\mathrm{TRIADE} \approx 0.1 \text{ monolayer} . \tag{6.4}$$

The activity on the sample can be calculated from:

$$A = \frac{\dot{N} - B}{F^S} , \tag{6.5}$$

where $\dot{N}$ is the measured count rate, B is the total background count rate and F^S is the efficiency of tritium adsorbed on the sample producing detector counts. The required measurement duration for the detection of one monolayer using the constraint $\sigma_A \leq 0.05 \cdot A$ and the data from tables 6.1 and 6.2 is:

$$t_\mathrm{meas} \approx 412 \text{ s} . \tag{6.6}$$

These results confirm that the required and prospected detection limit < 1 monolayer will be reached with appropriate measurement durations. The largest contribution to the MDA originates from the statistical uncertainty of the simulations. This can be significantly reduced, if the simulations are repeated with more statistics.

Chapter 7

Summary and outlook

Tritium can adsorb on surfaces of materials used in tritium technology. There is a need in tritium technology to being able to estimate the amounts of tritium adsorbing on different surfaces. The KATRIN experiment uses high precision electron spectroscopy of the β decay of tritium for the determination of the neutrino mass. Tritium adsorption on the surfaces of the KATRIN rear wall and the BIXS detector protection windows could cause unwanted effects and it is essential to know how much tritium has to be expected to adsorb on these components. Furthermore, it has to be known how much tritium adsorbs on certain materials which will be used in future fusion reactors in order to try to avoid tritium diffusion and to enable accurate tritium accountancy.

Only few literature data are available about the adsorption of tritium on different materials. Furthermore, tritium adsorption does not only strongly depend on the materials used but also on the surrounding conditions (tritium concentration, temperature, pressure). Therefore, a new experiment had to be developed which is capable of measuring tritium adsorption on different materials under the conditions which are of interest. A detection limit of less than 1 monolayer of adsorbed tritium is required.

β induced X-ray spectroscopy, which is already in use at the TLK, is considered the most suitable method to meet these requirements. Hence, the TRItium Adsorption Desorption Experiment (TRIADE) has been initiated, which is able to answer the questions concerning tritium adsorption in the context of KATRIN and which afterwards will be used for the investigation of any material of interest in tritium technology. The aim of this work was to design and to set up the TRIADE experiment, which has successfully been achieved and which is summarized in the following.

Design and setup of the TRIADE experiment

The main measurement principle of the TRIADE experiment is β induced X-ray spectroscopy. A fraction of decay electrons from tritium adsorbed on a sample surface enters an X-ray producing element, where some electrons produce bremsstrahlung, which is detected by a silicon drift detector. The amount of tritium adsorbed on the sample can be calculated from the count rate measured by the detector.

A gold coated beryllium window is used as the X-ray producing element. Gold is the most suitable material for maximizing bremsstrahlung production, while beryllium is the most transparent material for X-rays.

All surfaces inside the recipient are coated with gold, in order to minimize background effects from tritium adsorbed on surfaces apart from the sample surface. It is assumed that tritium does not adsorb on gold under the expected conditions in the recipient. The experiment allows any solid material which can be prepared as a disk of 70 mm diameter and 1 mm thickness to be used as a sample.

Additionally to the BIXS method, a quadrupole mass spectrometer (QMS) is integrated into the setup. The QMS allows the analysis of gas compositions in the recipient. With the QMS, the setup furthermore includes all crucial components to perform thermal desorption spectroscopy. The capabilities of TDS within the TRIADE experiment are under investigation. Preparatory literature research for the analysis of TDS spectra has been performed in this work.

In the context of this work, the TRIADE experiment has been completely designed and realized. This included the physical design based on the experience of the TriReX experiment and the implementation of the experiment, including the selection of the silicon drift detector, the design of the instrumentation, the temperature management system, the mass spectrometry setup and the procedural setup of the experiment. The concepts of the temperature management system was successfully tested in two test experiments.

Current status and outlook for the TRIADE experiment

The setup of the TRIADE experiment in a glovebox at TLK was finished successfully. Figure 4.15 shows the main components, the entire setup is shown in figure B.2.

The commissioning of the setup is almost completed. The commissioning of the detector included the optimization of thresholds and the slow peaking time, as well as background measurements. The commissioning of the vacuum system is essentially completed, an ultimate pressure of $5 \cdot 10^{-9}$ mbar was reached in the recipient. Lower pressures are expected to be reached soon.

Using the results of the detector background measurements with the optimized detector parameters, it has successfully been shown by simulations (described in chapter 6) that the desired detection limit of < 1 monolayer can be reached with the TRIADE setup.

During recent background measurements in the final setup, a slightly increased background level was determined. The causes are currently investigated. Nevertheless, first measurements can start after completing the investigations and last commissioning tasks, such as an integral leak test and closing the glove box. Furthermore, the cold gas system needs to be commissioned[65].

First samples are available for measurements. Figure 7.1 shows an PF-60 beryllium sample[66], kindly provided by Materion Electrofusion[67]. Because of the special interest of the KATRIN experiment in tritium adsorption on gold coated beryllium, the sample was sputter coated with gold[68] from one side. Further samples, made of electropolished 316L stainless steel, aluminium and copper were prepared for first measurements. After answering the questions related to the KATRIN experiment, the setup will be open for other materials of interest in tritium technology.

---

[65] First measurements in the temperature range above room temperature can be performed before the commissioning of the cold gas system.

[66] minimum beryllium content 99.0%

[67] 6070 Parkland Boulevard, Mayfield Heights, OH 44124, USA

[68] by Siegert TFT, Robert-Friese-Straße 3, D-07629 Hermsdorf, Germany

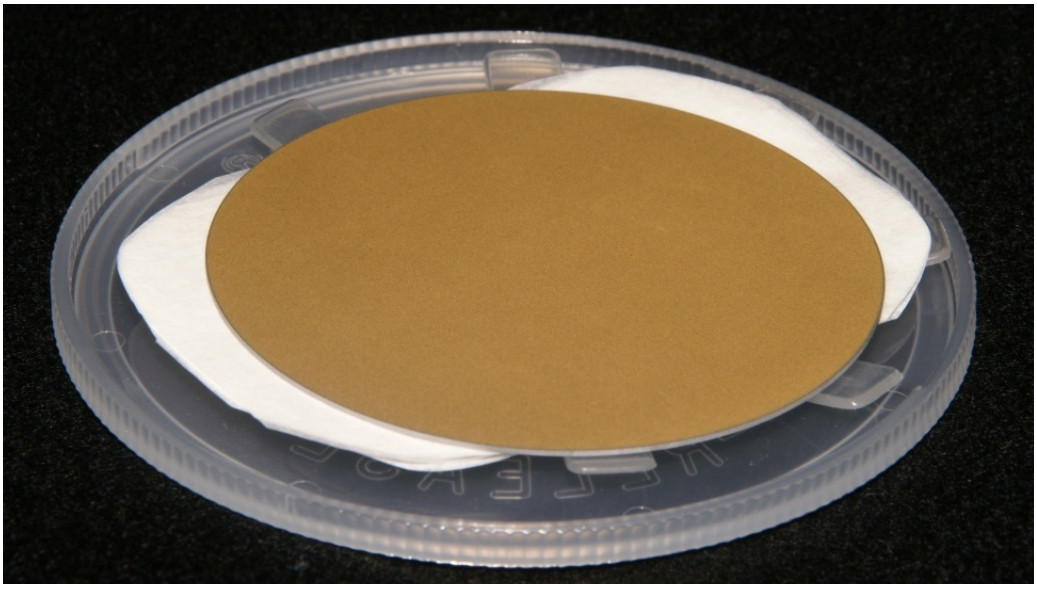

Figure 7.1: First sample for TRIADE. The picture shows the gold coated side of a PF-60 beryllium sample, which was provided by Materion Electrofusion.

The TRIADE setup has the following potential for future upgrades:

- Due to TLK safety regulations, the maximum activity which may be handled in the current setup is limited to 10^{10} Bq [TLA12]. It is planned to upgrade the setup, in order to be allowed to handle larger activities. Therefore, a tritium retention system will be procured.
- In order to be able to control the temperature of the sample faster and in order to extend the temperature range to lower temperatures, the cooling concept can be optimized. In the current setup, the heat exchanger, which is cooled by the cooling gas, is placed outside the recipient, due to the technical complexity of leading cooling gas into the recipient. In a future upgrade for the TRIADE experiment, the heat exchanger can be placed closer to the sample.
- In order to optimize the detection limit, the simulations can be repeated with more statistics. In order to get more accurate results, further simulations can be performed, using fewer simplifications concerning the experimental setup. Furthermore, the contribution of tritium adsorbed on the recipient's walls to the measured count rate can be determined.
- Being able to measure tritium adsorption enables the investigation of decontamination processes. The possibility to decontaminate a sample with purge gas is already implemented in TRIADE. Further decontamination test processes could be implemented into the setup, such as decontamination by UV-light.

In conclusion, the TRIADE experiment will soon be able to answer the open questions concerning tritium adsorption in the context of the KATRIN experiment. With the detection limit determined, it will be possible to determine at least a sufficient upper limit for the amount of adsorbed tritium, which is expected on the surfaces of interest for the KATRIN experiment. First measurements with tritium are planned to start in March 2013.

Appendix A

List of formula symbols, estimation of monolayer activity

Estimation of the activity of an adsorbed monolayer on a gold surface:

It is assumed that one gold atom on the surface can adsorb one tritium atom. So one gets:

$$\mathrm{N}_{\mathrm{Ads}}^{\mathrm{ML}} \approx \frac{1}{\mathrm{g}^2} = \frac{1}{(4 \cdot 10^{-10}\ \mathrm{m})^2} = 6.25 \cdot 10^{14}\ \frac{\text{adsorption sites}}{\mathrm{cm}^2}\ , \tag{A.1}$$

where N_{Ads}^{ML} is the number of adsorption sites per area for one monolayer of adsorbed tritium. g is the lattice parameter of gold from [Wie33]. For the activity per area one gets:

$$\mathrm{A}_{1\ \mathrm{cm}^2}^{\mathrm{ML}} = \frac{\ln 2}{\mathrm{T}_{1/2}} \cdot \mathrm{N}_{\mathrm{Ads}}^{\mathrm{ML}} = \frac{\ln 2}{12.3\ \mathrm{y}} \cdot 6.25 \cdot 10^{14}\ \frac{\text{adsorption sites}}{\mathrm{cm}^2} = 1.12 \cdot 10^{6}\ \frac{\mathrm{Bq}}{\mathrm{cm}^2}\ , \tag{A.2}$$

where $A_{1\ cm^2}^{ML}$ is the activity of one monolayer of adsorbed tritium on a gold surface of 1 cm^2 area. $\mathrm{T}_{1/2}$ is the tritium half-life from [Ott08].

Table A.1: List of formula symbols Physical quantities, their formula symbols and units (SI-units, unless otherwise indicated)

Physical quantity	Formula symbol	Unit
Activity	A	Bq
Atomic number	Z	*nondimensional*
Coverage	Θ	*nondimensional*
Cross section	σ	cm^2
Density	ρ	$\mathrm{g/cm}^2$
Distance	d	m
Efficiency	F	*nondimensional*
Energy	E	eV
Heating rate	β	K/s
Intensity	I	$\mathrm{W/m}^2$
Mass	m	kg
Molar mass	M	g/mol
Particle number	N	*nondimensional*
Pressure	P	Pa
Rate	R	1/s
Signal contribution	S_j^i	cps
Temperature	T	K
Time	t	s
Velocity	v	m/s

Appendix B

Additional information on components used

B.1 Pumping system and instrumentation

Table B.1: Overview of the pressure sensors in TRIADE.

Designation	Measurement range in mbar	Location/description	Type
RP001	$10^{-1} - 10^{3}$	detector electronics volume	MKS 902
RP002	$10^{-1} - 666$	sampling port	MKS 722B
RP003	$10^{-2} - 20$	BV061	Baratron 626B
RP004	$10^{-1} - 10^{3}$	BV061	MKS 902
RP005	$10^{-5} - 10^{-1}$	BV061	Baratron 627D
RP006	$10^{-10} - 10^{-3}$	BV061	MKS 903
RP007	$10^{-1} - 10^{3}$	IF-volume	MKS 902
RP008	$10^{-1} - 10^{3}$	BV062	MKS 902
RP009	$10^{-1} - 10^{3}$	ZTS connection	MKS 902

Table B.2: Overview of TRIADE temperature measurement points.

Designation	Measurement range (°C)	Description	Type
RT011	-30 – $+70$	heat sink detector electronics	Pt1000
RT012	0 – $+200$	heating cable BV061	Pt100
RT013	0 – $+200$	flange heater BV061	Pt100
RT014	0 – $+200$	high vacuum connection VA052	Pt100
RT015	-200 – $+200$	heating cable BV062	Pt100
RT016	-200 – $+200$	heat exchanger BV061	Pt100
RT017	0 – $+200$	cooling gas flow	Pt100

Table B.3: Overview of TRIADE pumps

Pump	Siemens Interatom	Normetex	Pfeiffer TMU200	Leybold SL80	Divac 0.8T
Designation	VA055	VA054	VA053	VA052	VA051
Max. fore vacuum (mbar)	1000	100	$\leq 10^{-1}$	12	2000
Ultimate pressure (mbar)	100	10^{-2}	10^{-8}	$< 2 \cdot 10^{-10}$	≤ 3
Pumping speed	$3\,\mathrm{m^3/h}$	$12\,\mathrm{m^3/h}$	$180\,\mathrm{l/s}$	$65\,\mathrm{l/s}$	$0.6\ \mathrm{m^3/h}$
Leak rate (mbar l/s)	$\leq 10^{-9}$	$\leq 10^{-9}$			

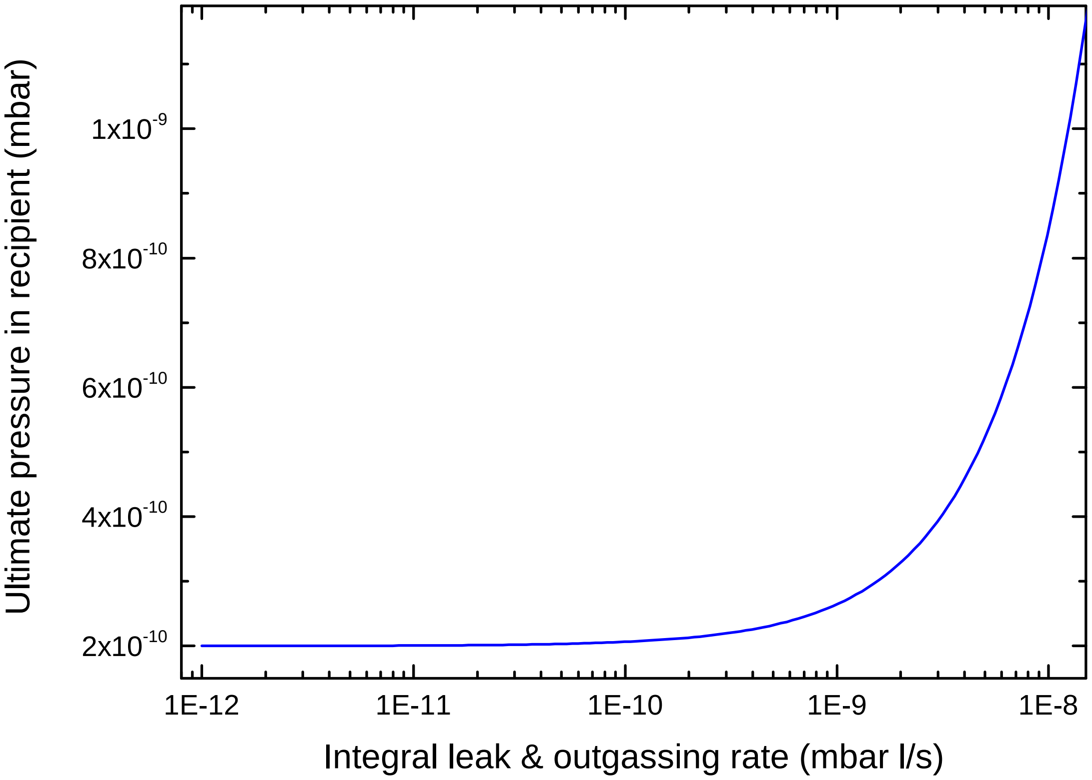

Figure B.1: Ultimate reachable pressure in recipient dependent on integral leak and outgassing rate. Calculated from an estimation of the conductivity of the connection between VA052 and the recipient (15.5 l/s, according to [Jou08]) and based on the ultimate pressure reachable by VA052 ($P_{\mathrm{Ult}}^{\mathrm{SL80}} < 2 \cdot 10^{-10}$ mbar · l/s, see figure B.3)

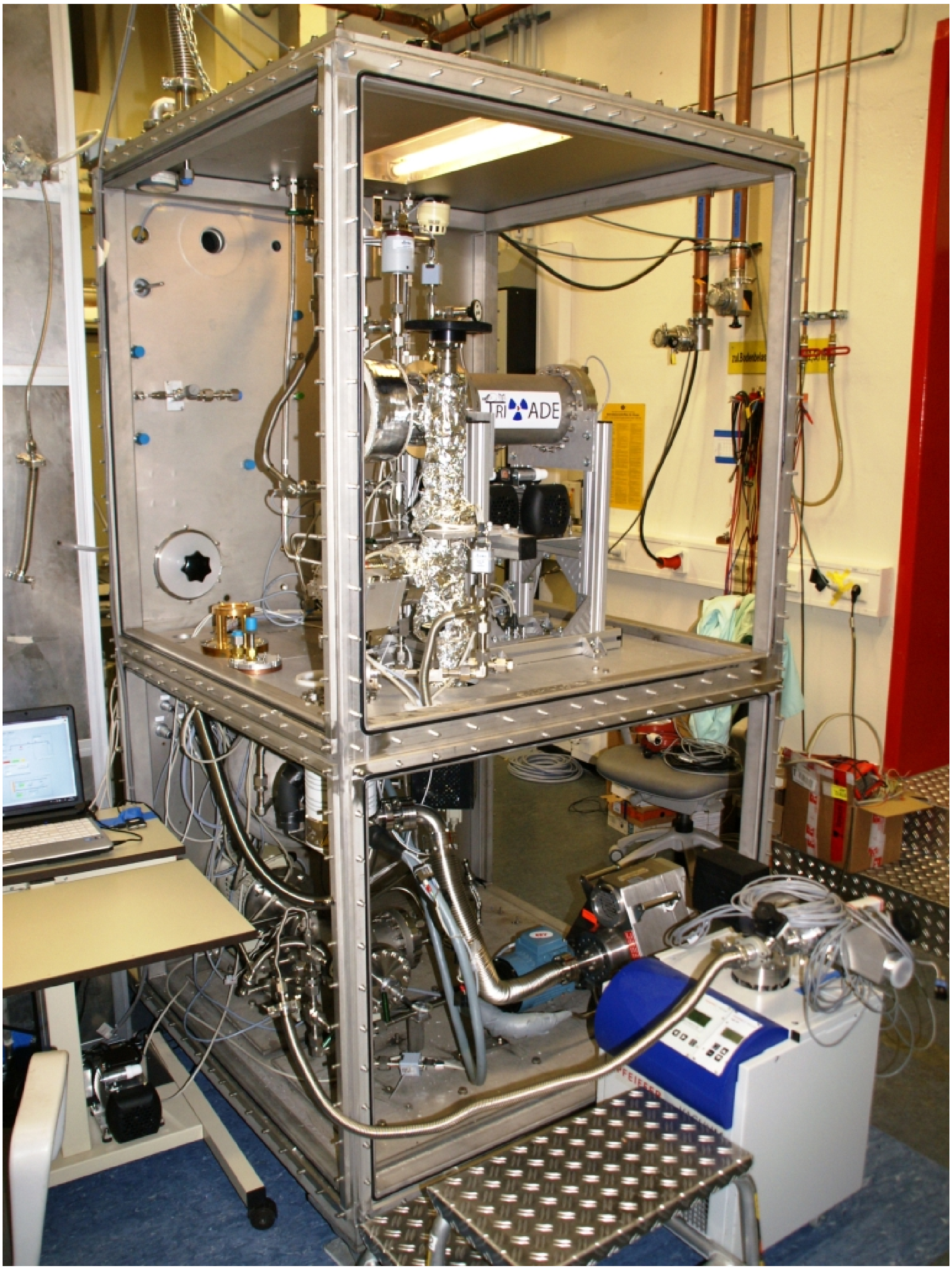

Figure B.2: Full view of the TRIADE experiment.

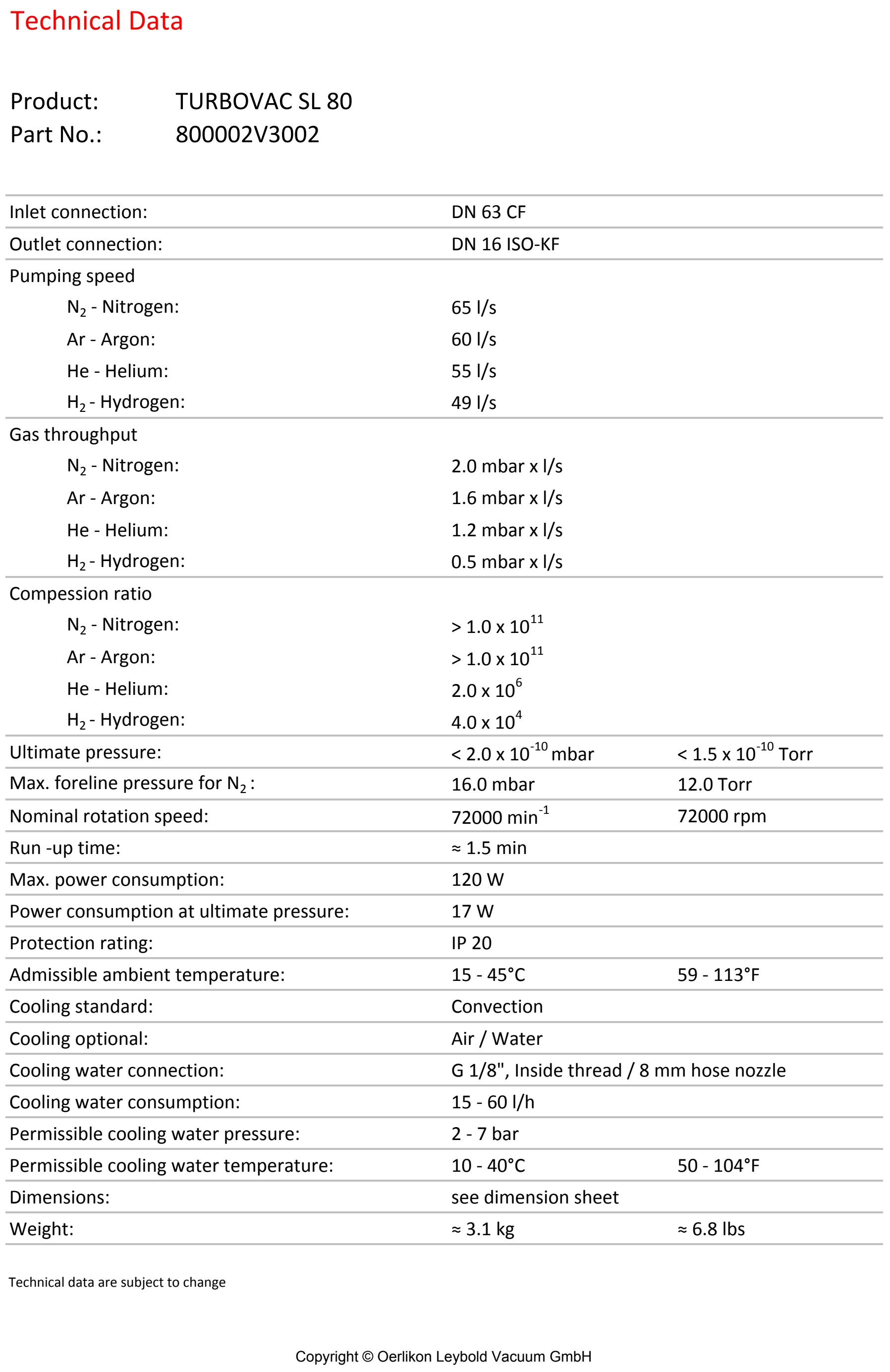

Technical Data

Product: TURBOVAC SL 80
Part No.: 800002V3002

Inlet connection:	DN 63 CF	
Outlet connection:	DN 16 ISO-KF	
Pumping speed		
N_2 - Nitrogen:	65 l/s	
Ar - Argon:	60 l/s	
He - Helium:	55 l/s	
H_2 - Hydrogen:	49 l/s	
Gas throughput		
N_2 - Nitrogen:	2.0 mbar x l/s	
Ar - Argon:	1.6 mbar x l/s	
He - Helium:	1.2 mbar x l/s	
H_2 - Hydrogen:	0.5 mbar x l/s	
Compession ratio		
N_2 - Nitrogen:	$> 1.0 \times 10^{11}$	
Ar - Argon:	$> 1.0 \times 10^{11}$	
He - Helium:	2.0×10^{6}	
H_2 - Hydrogen:	4.0×10^{4}	
Ultimate pressure:	$< 2.0 \times 10^{-10}$ mbar	$< 1.5 \times 10^{-10}$ Torr
Max. foreline pressure for N_2 :	16.0 mbar	12.0 Torr
Nominal rotation speed:	72000 min^{-1}	72000 rpm
Run -up time:	≈ 1.5 min	
Max. power consumption:	120 W	
Power consumption at ultimate pressure:	17 W	
Protection rating:	IP 20	
Admissible ambient temperature:	15 - 45°C	59 - 113°F
Cooling standard:	Convection	
Cooling optional:	Air / Water	
Cooling water connection:	G 1/8", Inside thread / 8 mm hose nozzle	
Cooling water consumption:	15 - 60 l/h	
Permissible cooling water pressure:	2 - 7 bar	
Permissible cooling water temperature:	10 - 40°C	50 - 104°F
Dimensions:	see dimension sheet	
Weight:	≈ 3.1 kg	≈ 6.8 lbs

Technical data are subject to change

Figure B.3: Data sheet of Oerlikon Leybold SL80 turbomolecular pump.

TECHNICAL DATA :

Displacement :	
¥ 50 Hz operation	15 m³/h (8.8 ft³.min⁻¹)
¥ 60 Hz operation	18 m³/h (10.6 ft³.min⁻¹)
Peak pumping speed (50 Hz operation) :	12 m³/h (7.1 ft³.min⁻¹)
Ultimate vacuum (with backing pump) :	5.10^{-3} mbar
Connections :	Meeting your need
Motor power	0.37 kW
Enclosure rating	IP 55
Motor voltage :	
¥ 3-phase 50 Hz	230-400 V
¥ 3-phase 60 Hz	240-480 V
Other voltage	On application
Weight	67 kg (148 lb)
Noise	51,5 dB(A)
Leak tightness (helium)	< 10^{-8} mbar.l.s⁻¹

PERFORMANCES :

For the tests, the pump was connected to an elastomer diaphragm backing pump (Pumping rated speed : 22 Nl/min - 0.78 ft³.min⁻¹ - and ultimate vacuum : 2 mbar abs)

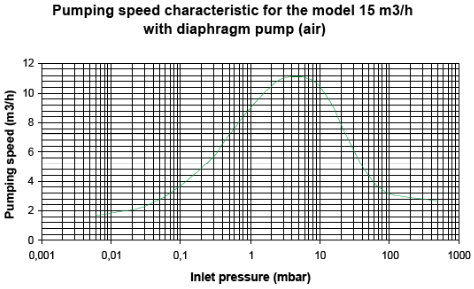

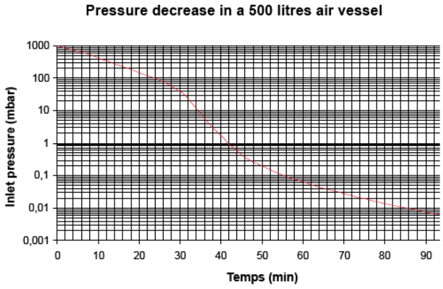

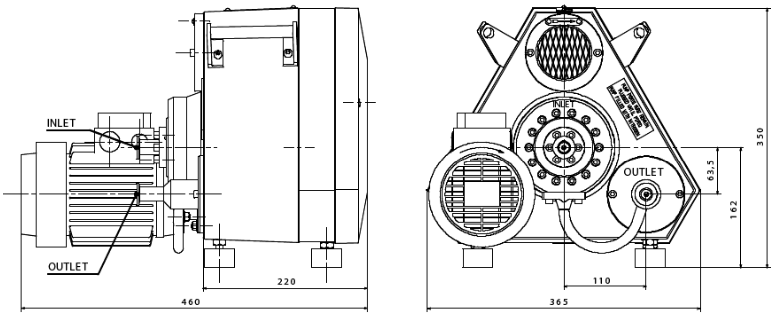

NORMETEX
POMPES

Authorized US Distributor:

Covenant Distributors, Inc
1227 Augusta West Pkwy
Augusta, Georgia 30909
1-706-854-8444
World Wide Web: http://www.eCovenant.net

Figure B.4: Technical data of the Normetex scroll pump.

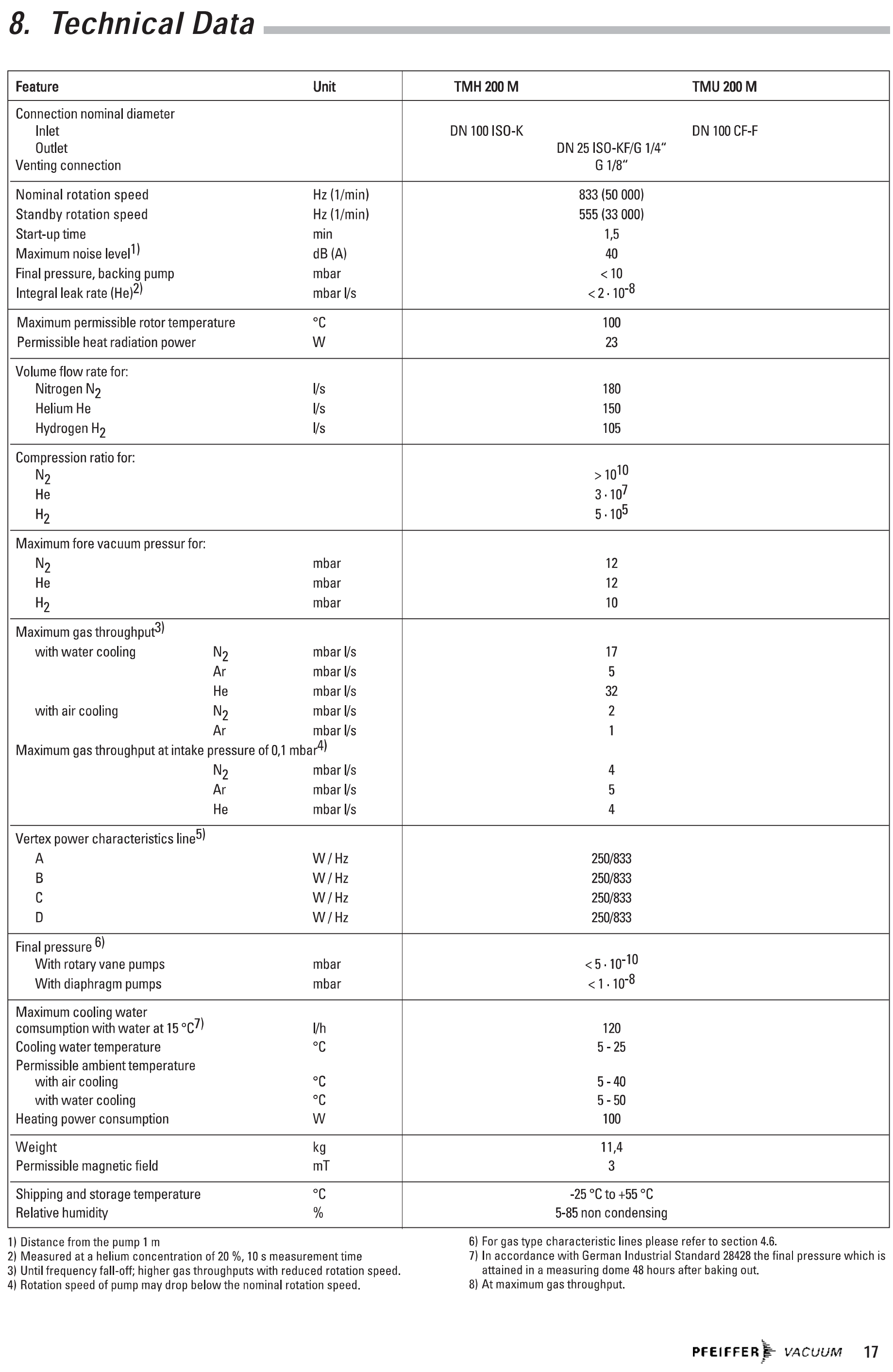

8. Technical Data

Feature		Unit	TMH 200 M	TMU 200 M
Connection nominal diameter				
Inlet			DN 100 ISO-K	DN 100 CF-F
Outlet			DN 25 ISO-KF/G 1/4“	
Venting connection			G 1/8“	
Nominal rotation speed		Hz (1/min)	833 (50 000)	
Standby rotation speed		Hz (1/min)	555 (33 000)	
Start-up time		min	1,5	
Maximum noise level[1]		dB (A)	40	
Final pressure, backing pump		mbar	< 10	
Integral leak rate (He)[2]		mbar l/s	$< 2 \cdot 10^{-8}$	
Maximum permissible rotor temperature		°C	100	
Permissible heat radiation power		W	23	
Volume flow rate for:				
Nitrogen N_2		l/s	180	
Helium He		l/s	150	
Hydrogen H_2		l/s	105	
Compression ratio for:				
N_2			$> 10^{10}$	
He			$3 \cdot 10^{7}$	
H_2			$5 \cdot 10^{5}$	
Maximum fore vacuum pressur for:				
N_2		mbar	12	
He		mbar	12	
H_2		mbar	10	
Maximum gas throughput[3]				
with water cooling	N_2	mbar l/s	17	
	Ar	mbar l/s	5	
	He	mbar l/s	32	
with air cooling	N_2	mbar l/s	2	
	Ar	mbar l/s	1	
Maximum gas throughput at intake pressure of 0,1 mbar[4]				
	N_2	mbar l/s	4	
	Ar	mbar l/s	5	
	He	mbar l/s	4	
Vertex power characteristics line[5]				
A		W / Hz	250/833	
B		W / Hz	250/833	
C		W / Hz	250/833	
D		W / Hz	250/833	
Final pressure [6]				
With rotary vane pumps		mbar	$< 5 \cdot 10^{-10}$	
With diaphragm pumps		mbar	$< 1 \cdot 10^{-8}$	
Maximum cooling water comsumption with water at 15 °C[7]		l/h	120	
Cooling water temperature		°C	5 - 25	
Permissible ambient temperature				
with air cooling		°C	5 - 40	
with water cooling		°C	5 - 50	
Heating power consumption		W	100	
Weight		kg	11,4	
Permissible magnetic field		mT	3	
Shipping and storage temperature		°C	-25 °C to +55 °C	
Relative humidity		%	5-85 non condensing	

1) Distance from the pump 1 m
2) Measured at a helium concentration of 20 %, 10 s measurement time
3) Until frequency fall-off; higher gas throughputs with reduced rotation speed.
4) Rotation speed of pump may drop below the nominal rotation speed.
6) For gas type characteristic lines please refer to section 4.6.
7) In accordance with German Industrial Standard 28428 the final pressure which is attained in a measuring dome 48 hours after baking out.
8) At maximum gas throughput.

PFEIFFER VACUUM 17

Figure B.5: Technical data of the Pfeiffer TMU200 turbomolecular pump.

8.1. Dimensions

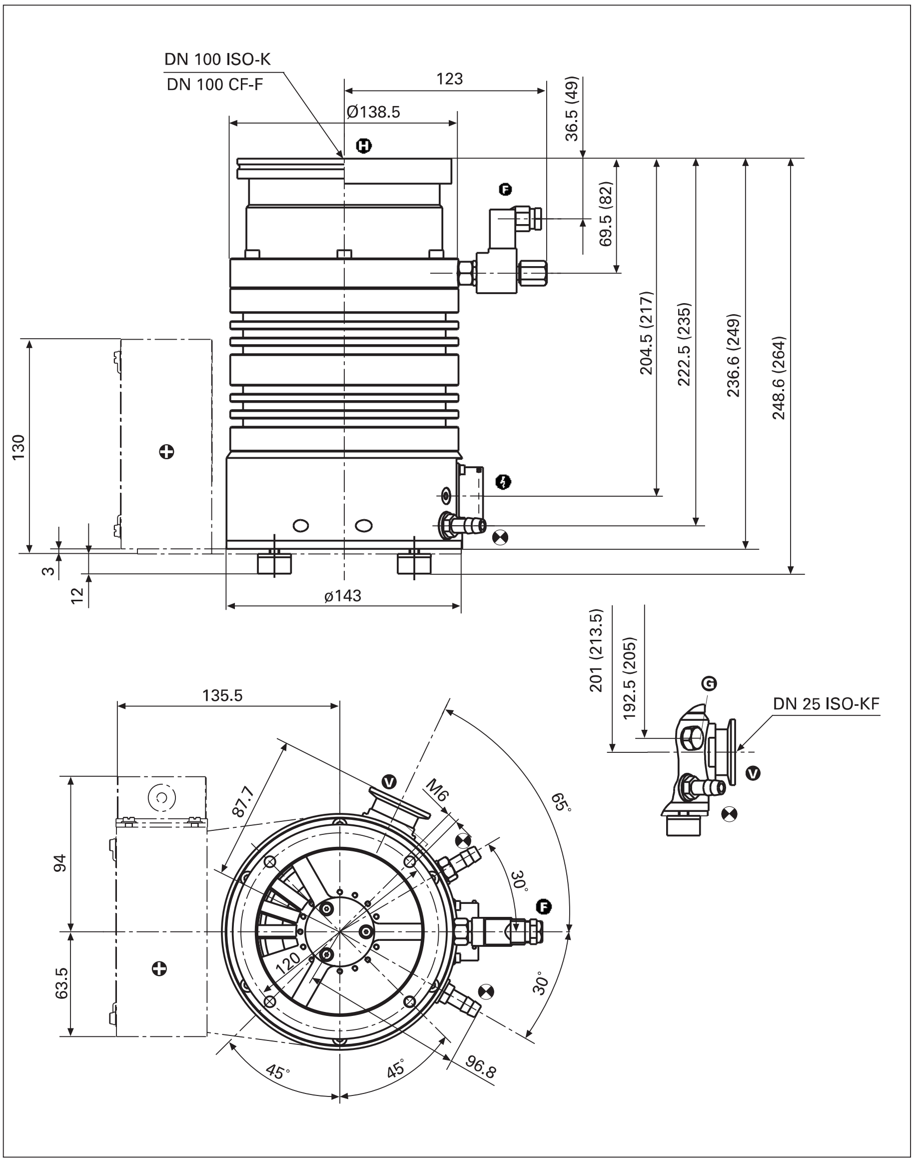

Values in brackets be for TMU 200M (DN 100 CF-F).

18 PFEIFFER VACUUM

Figure B.6: Mechanical dimensions of the Pfeiffer TMU200 turbomolecular pump. Taken from [TMU12]

B.2 Custom-made components

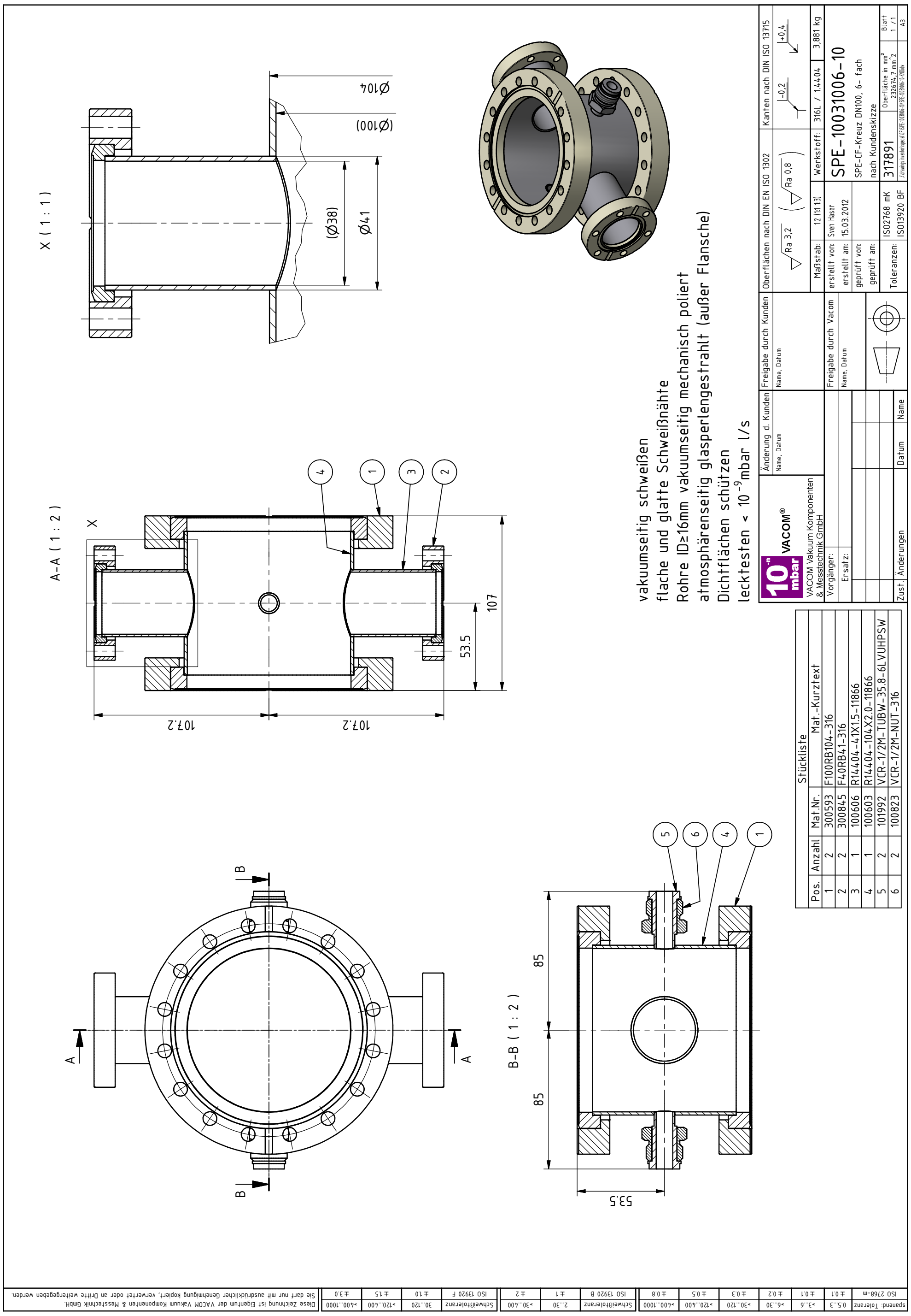

Stückliste

Pos.	Anzahl	Mat.Nr.	Mat.-Kurztext
1	2	300593	F100RB104-316
2	2	300845	F40RB41-316
3	1	100606	R14404-41X1.5-11866
4	1	100603	R14404-104X2.0-11866
5	2	101992	VCR-1/2M-TUBW-35.8-6LVUHPSW
6	2	100823	VCR-1/2M-NUT-316

Figure B.7: Mechanical dimensions of the custom-made recipient. Drawing by VACOM Vakuum Komponenten & Messtechnik GmbH, all dimensions in mm.

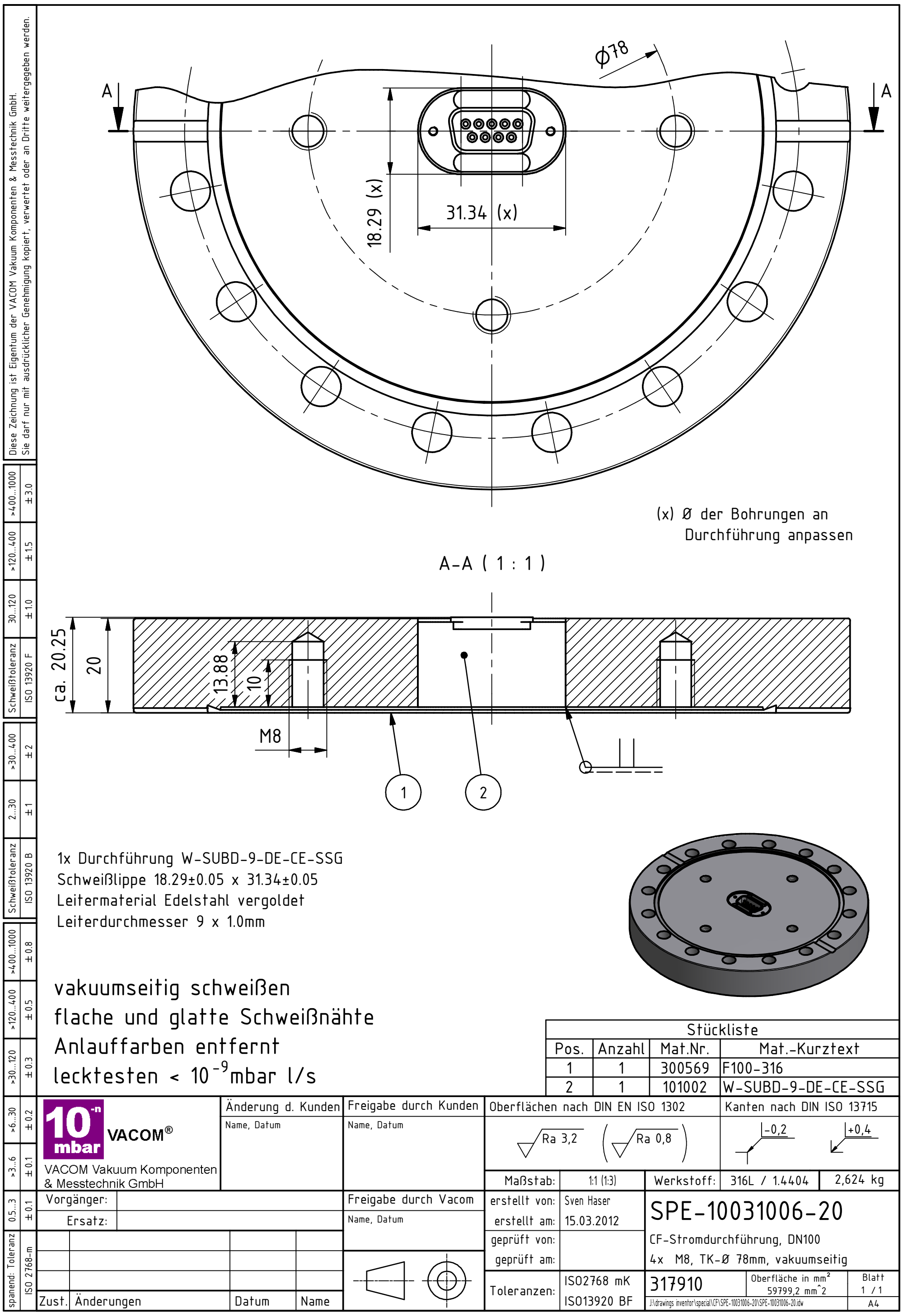

Diese Zeichnung ist Eigentum der VACOM Vakuum Komponenten & Messtechnik GmbH.
Sie darf nur mit ausdrücklicher Genehmigung kopiert, verwertet oder an Dritte weitergegeben werden.

spanend: Toleranz ISO 2768-m	0.5...3 ± 0.1	>3...6 ± 0.1	>6...30 ± 0.2	>30...120 ± 0.3	>120...400 ± 0.5	>400...1000 ± 0.8
Schweißtoleranz ISO 13920 B	2...30 ± 1	>30...400 ± 2				
Schweißtoleranz ISO 13920 F	30...120 ± 1.0	>120...400 ± 1.5	>400...1000 ± 3.0			

(x) Ø der Bohrungen an
Durchführung anpassen

1x Durchführung W-SUBD-9-DE-CE-SSG
Schweißlippe 18.29±0.05 x 31.34±0.05
Leitermaterial Edelstahl vergoldet
Leiterdurchmesser 9 x 1.0mm

vakuumseitig schweißen
flache und glatte Schweißnähte
Anlauffarben entfernt
lecktesten < 10^{-9}mbar l/s

Stückliste

Pos.	Anzahl	Mat.Nr.	Mat.-Kurztext
1	1	300569	F100-316
2	1	101002	W-SUBD-9-DE-CE-SSG

VACOM®
VACOM Vakuum Komponenten
& Messtechnik GmbH

Änderung d. Kunden Name, Datum	Freigabe durch Kunden Name, Datum	Oberflächen nach DIN EN ISO 1302 Ra 3,2 (Ra 0,8)	Kanten nach DIN ISO 13715 -0,2 +0,4
Vorgänger:		Maßstab: 1:1 (1:3)	Werkstoff: 316L / 1.4404 — 2,624 kg
Ersatz:	Freigabe durch Vacom Name, Datum	erstellt von: Sven Haser	SPE-10031006-20
		erstellt am: 15.03.2012	CF-Stromdurchführung, DN100
		geprüft von:	4x M8, TK-Ø 78mm, vakuumseitig
		geprüft am:	
Zust. Änderungen Datum Name		Toleranzen: ISO2768 mK ISO13920 BF	317910 — Oberfläche in mm²: 59799,2 mm^2 — Blatt 1 / 1
			J:\drawings inventor\special\CF\SPE-10031006-20\SPE-10031006-20.idw — A4

Figure B.8: **Mechanical dimensions of the custom-made blind flange for closing the recipient.** Drawing by VACOM Vakuum Komponenten & Messtechnik GmbH, all dimensions in mm.

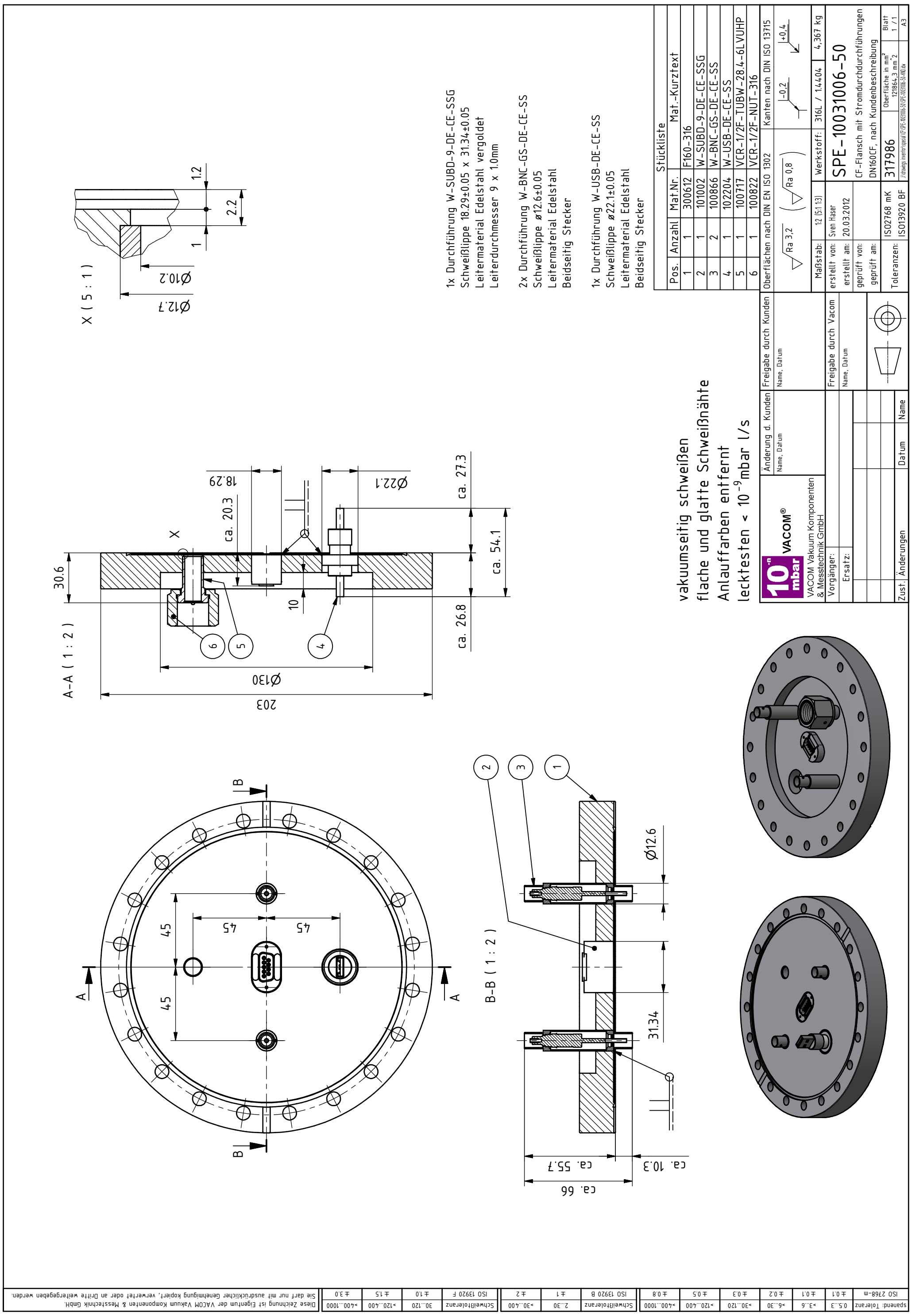

Figure B.9: Mechanical dimensions of the custom-made flange used for closing the detector electronics volume. Drawing by VACOM Vakuum Komponenten & Messtechnik GmbH, all dimensions in mm.
]

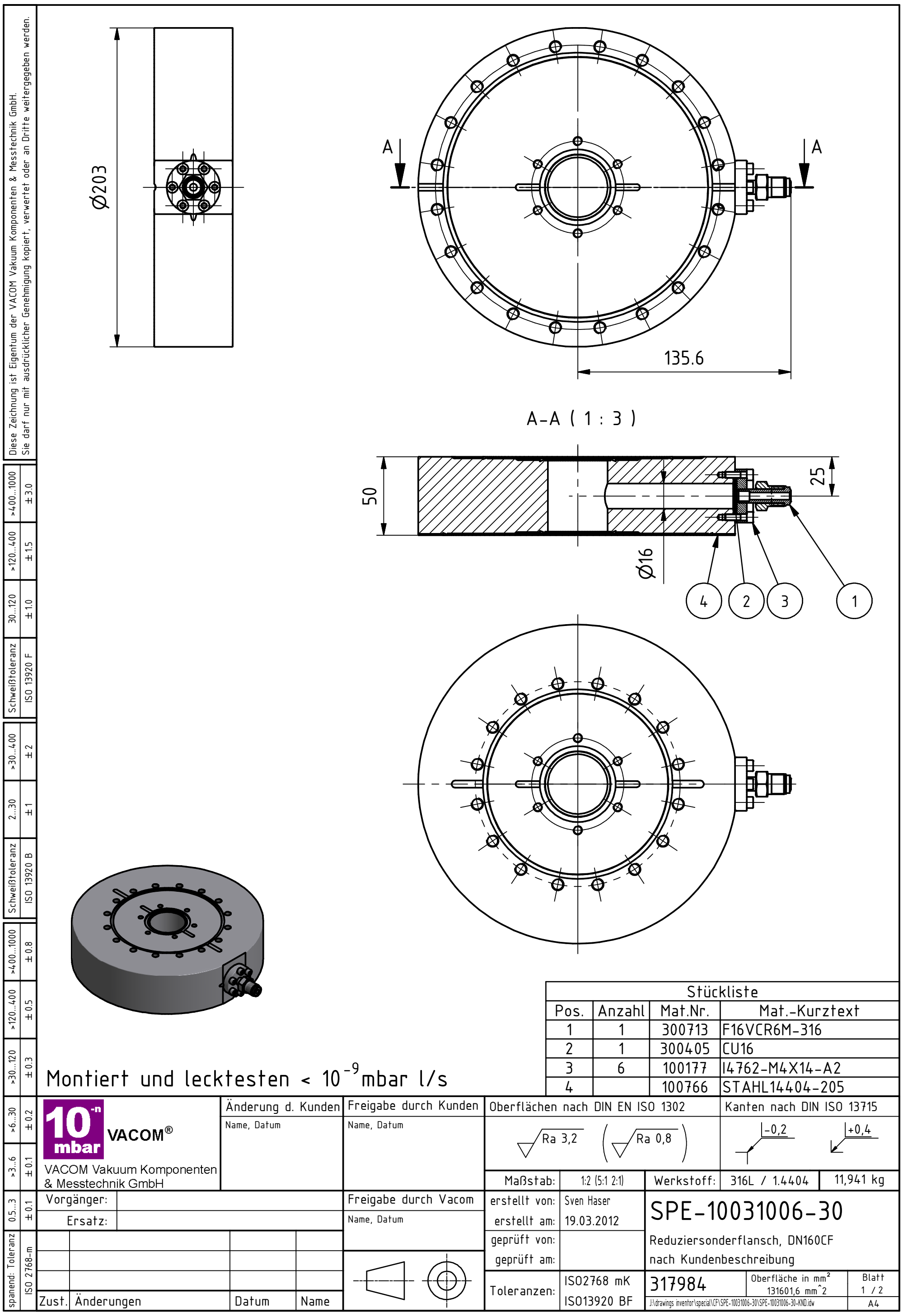

Figure B.10: Mechanical dimensions of the custom-made intermediate flange. Drawing by VACOM Vakuum Komponenten & Messtechnik GmbH, all dimensions in mm.

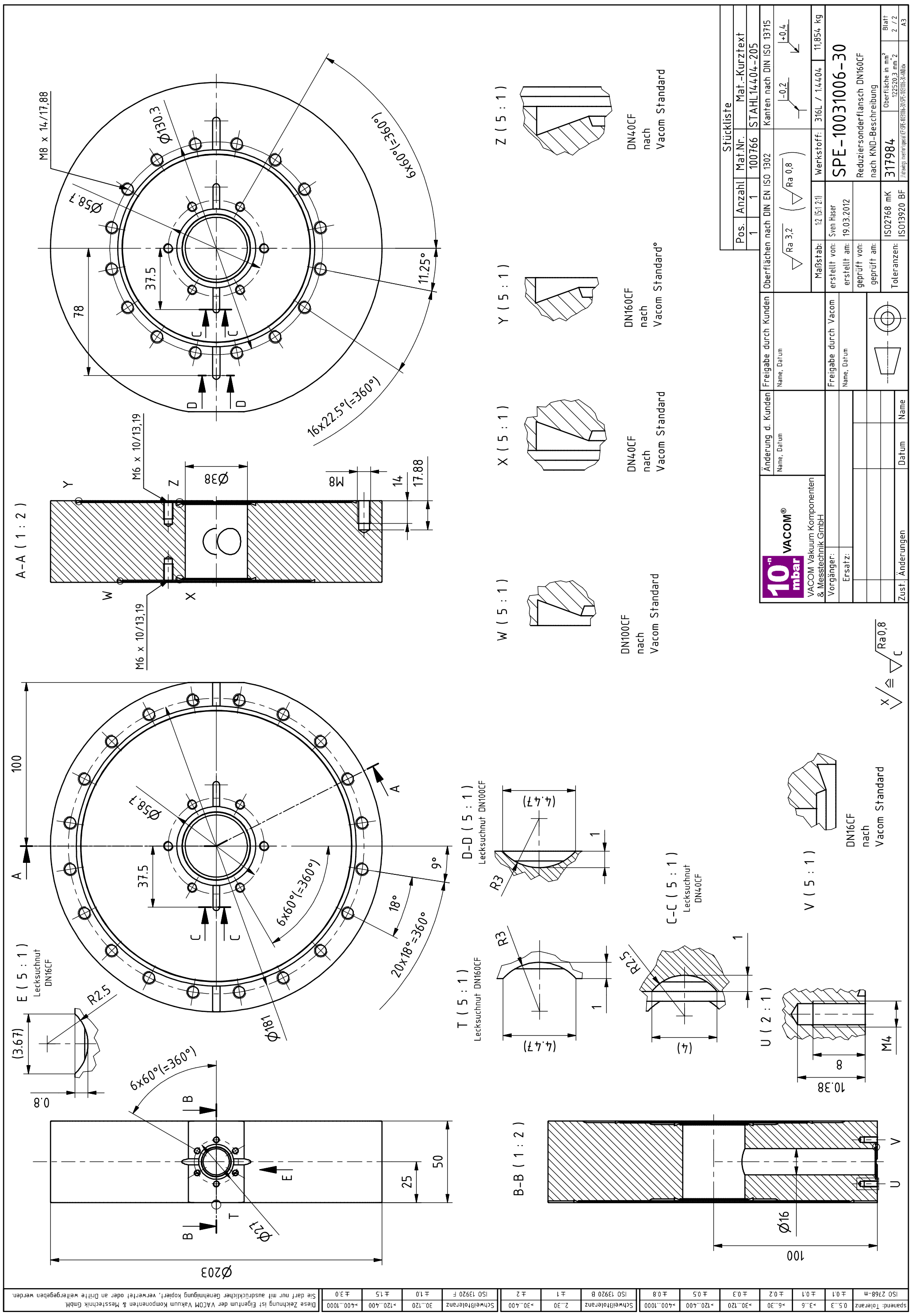

Figure B.11: Mechanical dimensions of the custom-made intermediate flange (2). Drawing by VACOM Vakuum Komponenten & Messtechnik GmbH, all dimensions in mm.

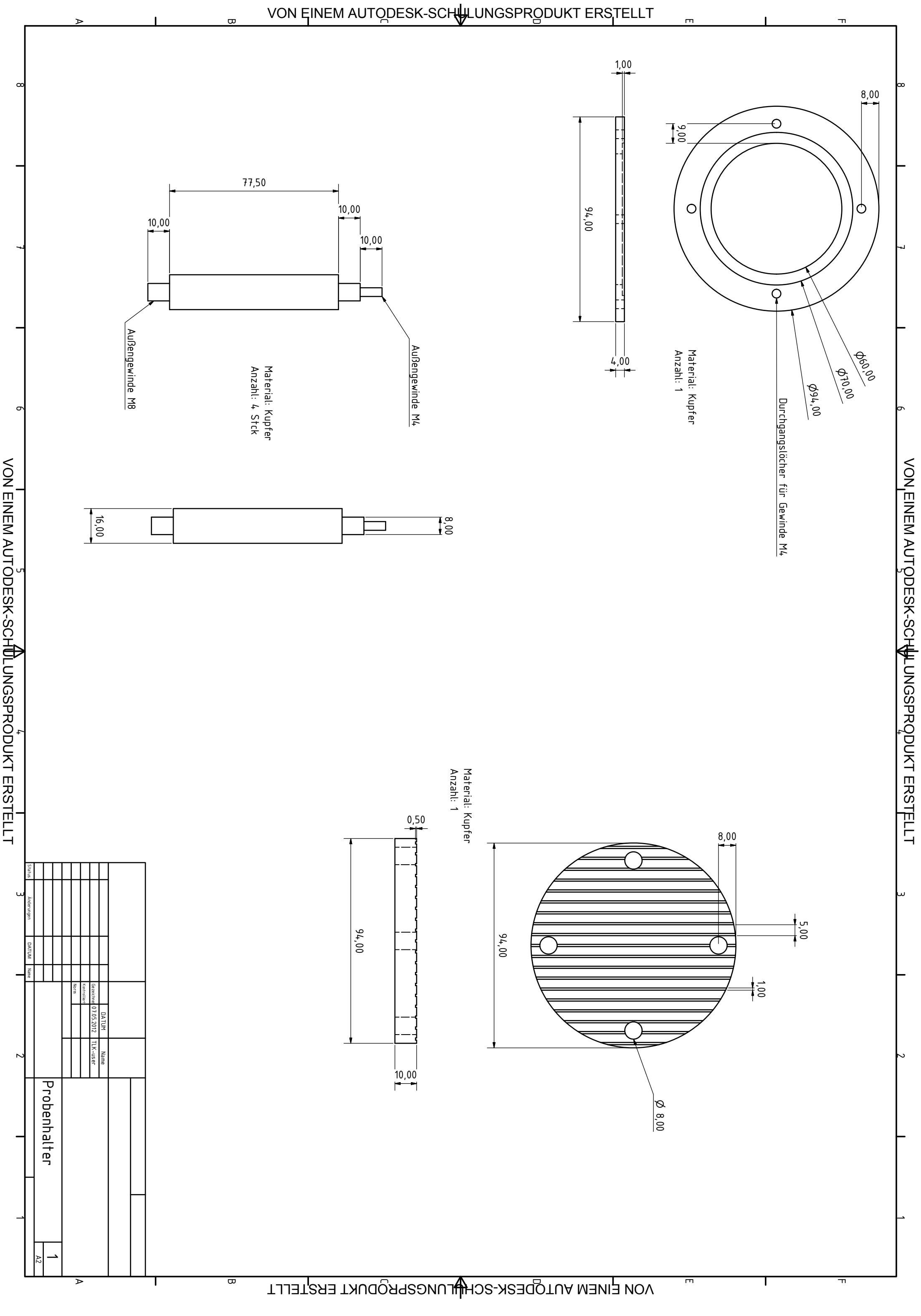

Figure B.12: Mechanical dimensions of the custom-made sample holder. All dimensions in mm.

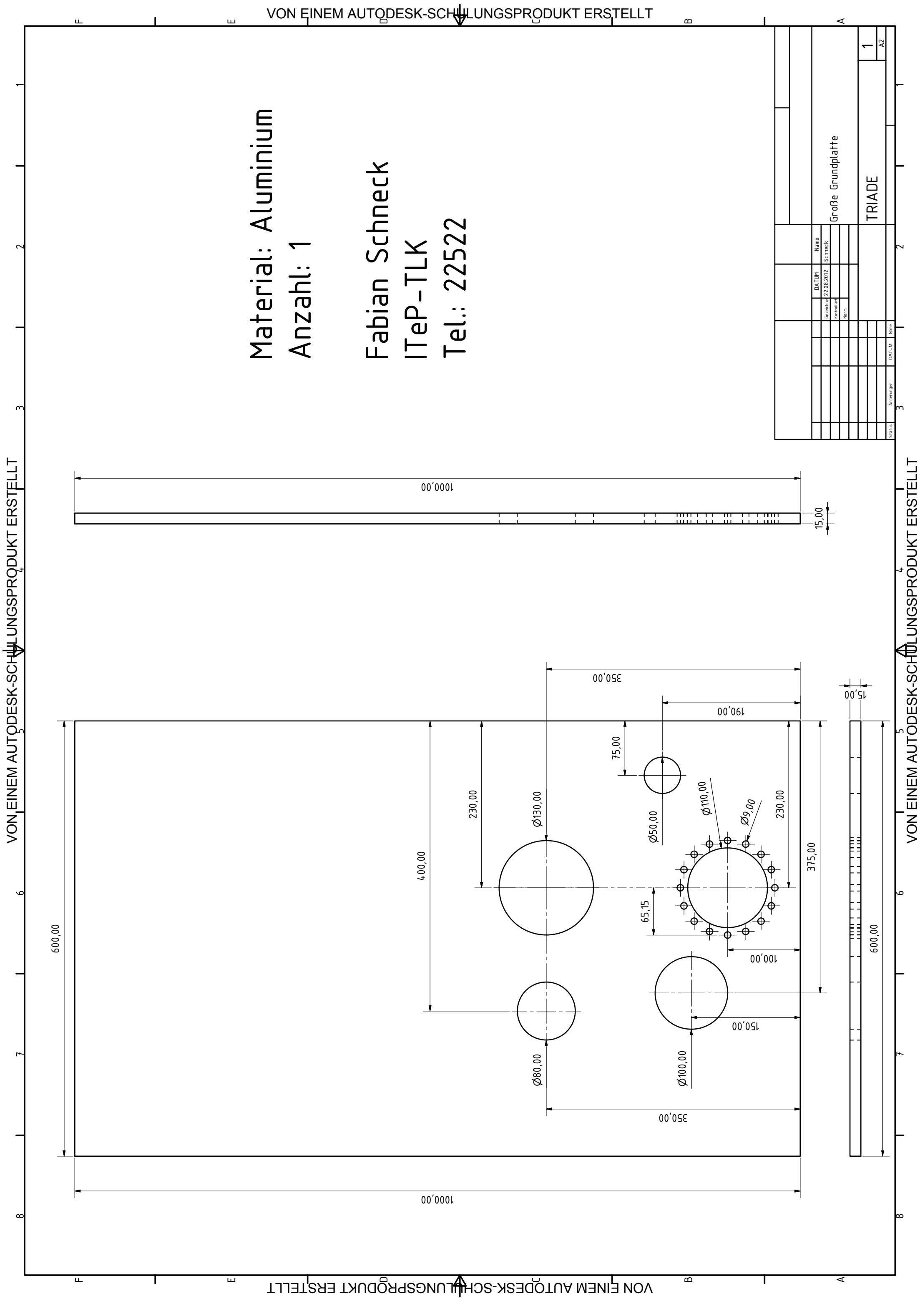

Figure B.13: Mechanical dimensions of the custom-made base plate. All dimensions in mm.

B.3 Amptek X123

Gain and energy calibration: The output channel for an energy E_{dep}, deposited in the detector is given by:

$$C = \left(\frac{E_{dep}}{\epsilon_{pair}}\right)\left(\frac{1}{q_e C_F}\right)(G_{Shape}G_{DPP})\left(\frac{N_{chan}}{V_{max}}\right) \tag{B.1}$$

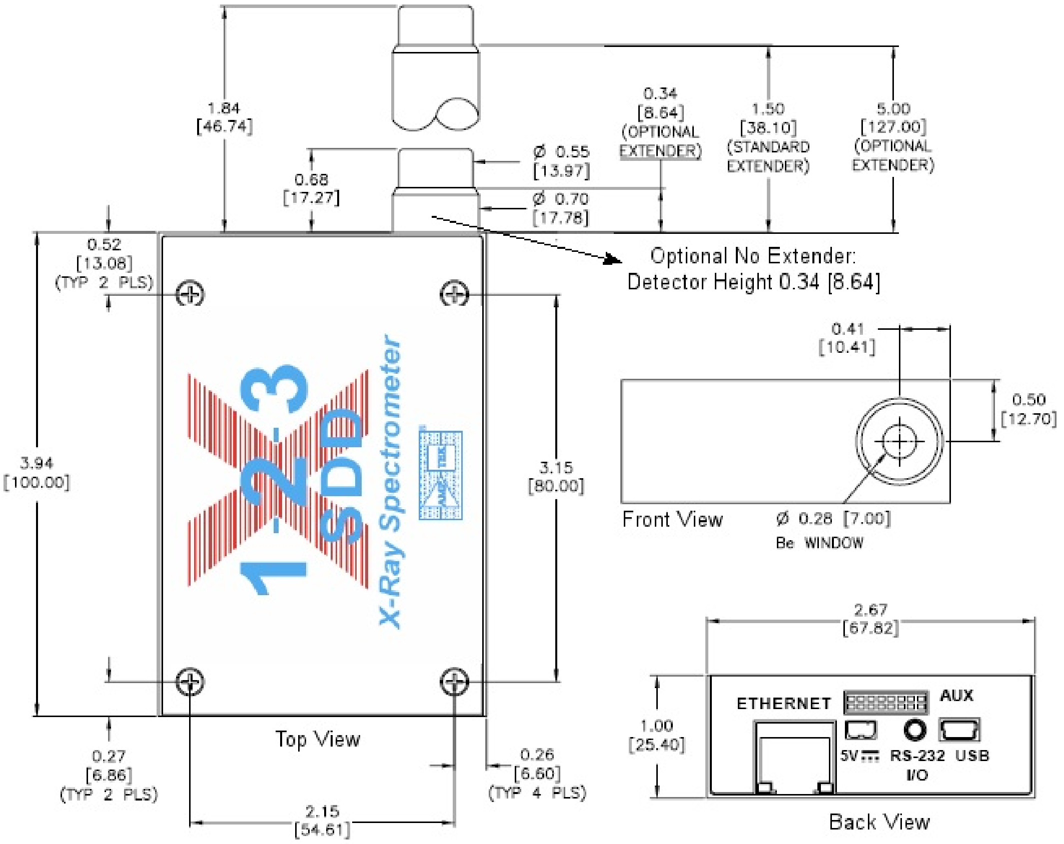

Figure B.14: Mechanical dimensions of the X123 X-ray spectrometer: All dimensions in inches (mm)

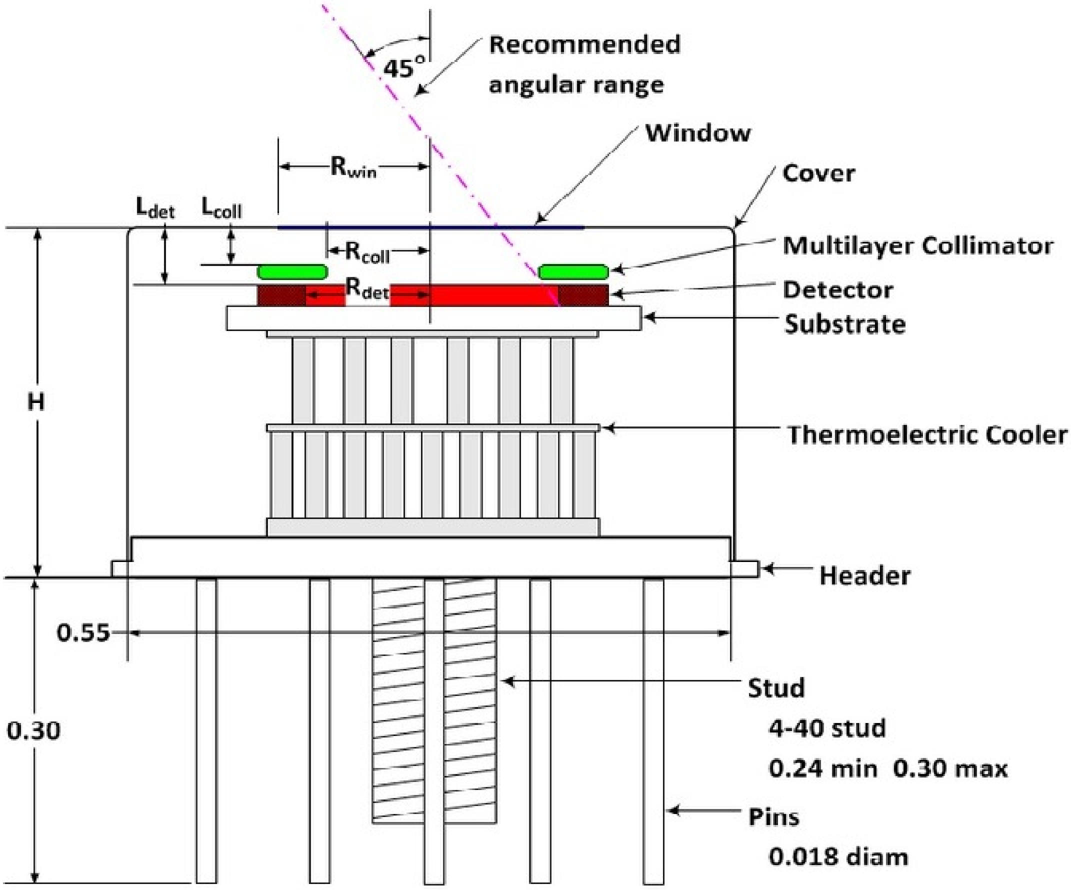

Figure B.15: Mechanical dimensions of the XR100 silicon drift detector: All dimensions in inches

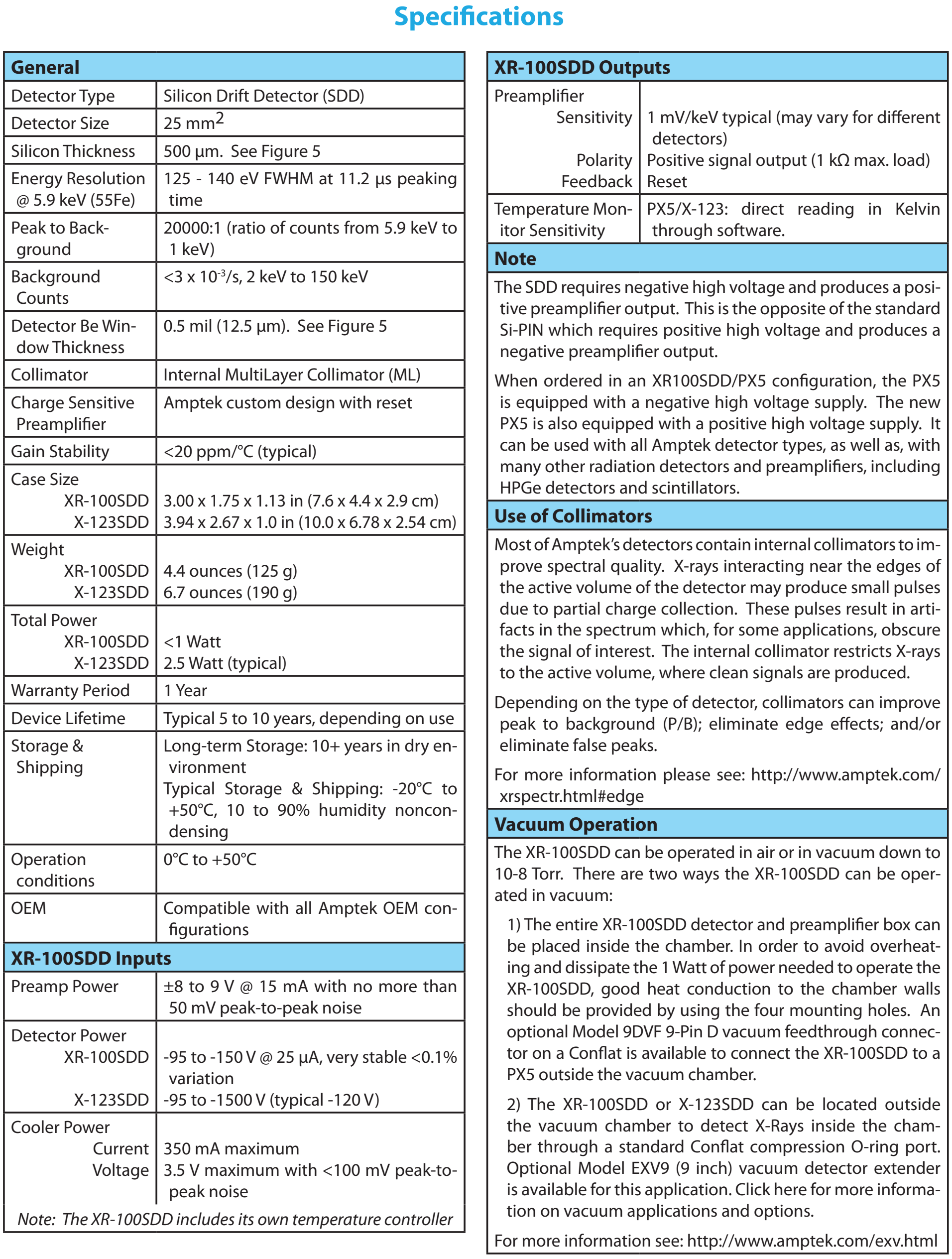

Specifications

General

Detector Type	Silicon Drift Detector (SDD)
Detector Size	25 mm^2
Silicon Thickness	500 µm. See Figure 5
Energy Resolution @ 5.9 keV (55Fe)	125 - 140 eV FWHM at 11.2 µs peaking time
Peak to Background	20000:1 (ratio of counts from 5.9 keV to 1 keV)
Background Counts	<3 x 10^{-3}/s, 2 keV to 150 keV
Detector Be Window Thickness	0.5 mil (12.5 µm). See Figure 5
Collimator	Internal MultiLayer Collimator (ML)
Charge Sensitive Preamplifier	Amptek custom design with reset
Gain Stability	<20 ppm/°C (typical)
Case Size	
XR-100SDD	3.00 x 1.75 x 1.13 in (7.6 x 4.4 x 2.9 cm)
X-123SDD	3.94 x 2.67 x 1.0 in (10.0 x 6.78 x 2.54 cm)
Weight	
XR-100SDD	4.4 ounces (125 g)
X-123SDD	6.7 ounces (190 g)
Total Power	
XR-100SDD	<1 Watt
X-123SDD	2.5 Watt (typical)
Warranty Period	1 Year
Device Lifetime	Typical 5 to 10 years, depending on use
Storage & Shipping	Long-term Storage: 10+ years in dry environment Typical Storage & Shipping: -20°C to +50°C, 10 to 90% humidity noncondensing
Operation conditions	0°C to +50°C
OEM	Compatible with all Amptek OEM configurations

XR-100SDD Inputs

Preamp Power	±8 to 9 V @ 15 mA with no more than 50 mV peak-to-peak noise
Detector Power	
XR-100SDD	-95 to -150 V @ 25 µA, very stable <0.1% variation
X-123SDD	-95 to -1500 V (typical -120 V)
Cooler Power	
Current	350 mA maximum
Voltage	3.5 V maximum with <100 mV peak-to-peak noise

Note: The XR-100SDD includes its own temperature controller

XR-100SDD Outputs

Preamplifier	
Sensitivity	1 mV/keV typical (may vary for different detectors)
Polarity	Positive signal output (1 kΩ max. load)
Feedback	Reset
Temperature Monitor Sensitivity	PX5/X-123: direct reading in Kelvin through software.

Note

The SDD requires negative high voltage and produces a positive preamplifier output. This is the opposite of the standard Si-PIN which requires positive high voltage and produces a negative preamplifier output.

When ordered in an XR100SDD/PX5 configuration, the PX5 is equipped with a negative high voltage supply. The new PX5 is also equipped with a positive high voltage supply. It can be used with all Amptek detector types, as well as, with many other radiation detectors and preamplifiers, including HPGe detectors and scintillators.

Use of Collimators

Most of Amptek's detectors contain internal collimators to improve spectral quality. X-rays interacting near the edges of the active volume of the detector may produce small pulses due to partial charge collection. These pulses result in artifacts in the spectrum which, for some applications, obscure the signal of interest. The internal collimator restricts X-rays to the active volume, where clean signals are produced.

Depending on the type of detector, collimators can improve peak to background (P/B); eliminate edge effects; and/or eliminate false peaks.

For more information please see: http://www.amptek.com/xrspectr.html#edge

Vacuum Operation

The XR-100SDD can be operated in air or in vacuum down to 10-8 Torr. There are two ways the XR-100SDD can be operated in vacuum:

1) The entire XR-100SDD detector and preamplifier box can be placed inside the chamber. In order to avoid overheating and dissipate the 1 Watt of power needed to operate the XR-100SDD, good heat conduction to the chamber walls should be provided by using the four mounting holes. An optional Model 9DVF 9-Pin D vacuum feedthrough connector on a Conflat is available to connect the XR-100SDD to a PX5 outside the vacuum chamber.

2) The XR-100SDD or X-123SDD can be located outside the vacuum chamber to detect X-Rays inside the chamber through a standard Conflat compression O-ring port. Optional Model EXV9 (9 inch) vacuum detector extender is available for this application. Click here for more information on vacuum applications and options.

For more information see: http://www.amptek.com/exv.html

Figure B.16: Data sheet of the X123 SDD.

B.3.1 Detector settings for energy calibration

```
RESC=?; Reset Configuration
CLCK=80; 20MHz/80MHz
TPEA=11.200; Peaking Time
GAIF=1.0447;
GAIN=69.115; Total Gain (Analog * Fine)
RESL=204; Detector Reset Lockout
TFLA=0.200; Flat Top
TPFA=100; Fast Channel Peaking Time
PURE=ON; PUR Interval On/Off
RTDE=OFF; RTD On/Off
MCAS=NORM; MCA Source
MCAC=8192; MCA/MCS Channels
SOFF=OFF; Set Spectrum Offset
AINP=POS; Analog Input Pos/Neg
INOF=DEF; Input Offset
GAIA=15;
CUSP=0; Non-Trapezoidal Shaping
PDMD=NORM; Peak Detect Mode
THSL=0.976; Slow Threshold
TLLD=OFF; LLD Threshold
THFA=56.25; Fast Threshold
DACO=SHAPED; DAC Output
DACF=0; DAC Offset
RTDS=0; RTD Sensitivity
RTDT=0.00; RTD Threshold
BLRM=1; BLR Mode
BLRD=3; BLR Down Correction
BLRU=0; BLR Up Correction
GATE=OFF; Gate Control
AUO1=ICR; AUXOUT Selection
PRET=OFF; Preset Time
PRER=OFF; Preset Real Time
PREC=OFF; Preset Counts
PRCL=1; Preset Counts Low Threshold
PRCH=8191; Preset Counts High Threshold
HVSE=-110; HV Set
TECS=220; TEC Set
PAPS=ON; Preamp 8.5/5 (N/A)
SCOE=RI; Scope Trigger Edge
SCOT=12; Scope Trigger Position
SCOG=16; Digital Scope Gain
MCSL=1; MCS Low Threshold
MCSH=8191; MCS High Threshold
MCST=0.00; MCS Timebase
AUO2=ICR; AUXOUT2 Selection
TPMO=OFF; Test Pulser On/Off
GPED=RI; G.P. Counter Edge
GPIN=AUX1; G.P. Counter Input
GPME=ON; G.P. Counter Uses MCAEN?
GPGA=ON; G.P. Counter Uses GATE?
GPMC=ON; G.P. Counter Cleared With MCA Counters?
MCAE=ON; MCA/MCS Enable
BOOT=ON; Turn Supplies On/Off At Power Up
«DP5 CONFIGURATION END»
«DPP STATUS»
Device Type: DP5
Serial Number: 11120
Firmware: 6.06
FPGA: 5.13
Fast Count: 2456482
Slow Count: 2280433
Accumulation Time: 814.394000
Real Time: 816.990000
Dead Time: 7.19HV Volt: -112V
TEC Temp: 223K
Board Temp: 44Â°C
```

B.4 MKS Microvision Plus

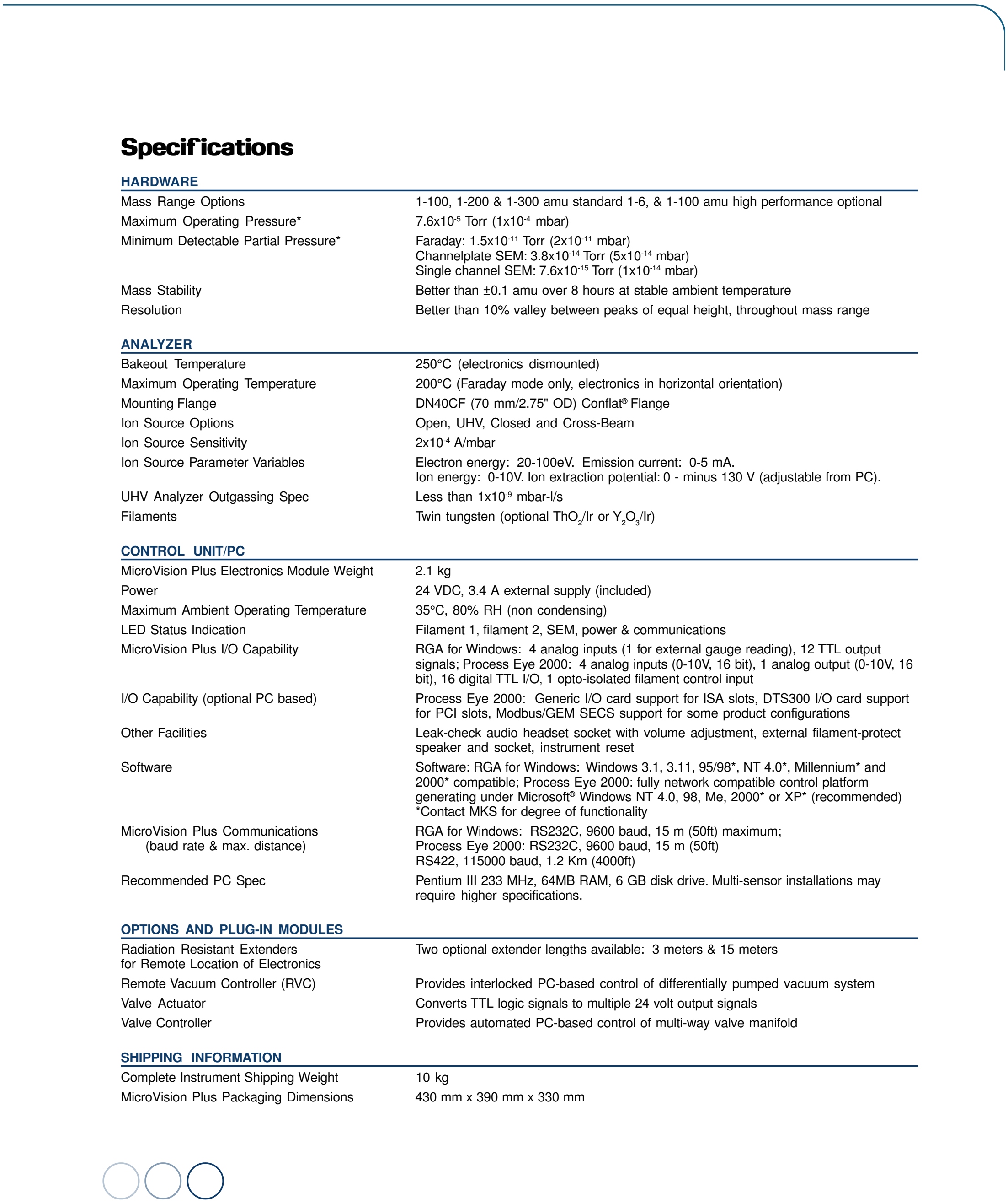

Specifications

HARDWARE

Mass Range Options	1-100, 1-200 & 1-300 amu standard 1-6, & 1-100 amu high performance optional
Maximum Operating Pressure*	7.6×10^{-5} Torr (1×10^{-4} mbar)
Minimum Detectable Partial Pressure*	Faraday: 1.5×10^{-11} Torr (2×10^{-11} mbar) Channelplate SEM: 3.8×10^{-14} Torr (5×10^{-14} mbar) Single channel SEM: 7.6×10^{-15} Torr (1×10^{-14} mbar)
Mass Stability	Better than ±0.1 amu over 8 hours at stable ambient temperature
Resolution	Better than 10% valley between peaks of equal height, throughout mass range

ANALYZER

Bakeout Temperature	250°C (electronics dismounted)
Maximum Operating Temperature	200°C (Faraday mode only, electronics in horizontal orientation)
Mounting Flange	DN40CF (70 mm/2.75" OD) Conflat® Flange
Ion Source Options	Open, UHV, Closed and Cross-Beam
Ion Source Sensitivity	2×10^{-4} A/mbar
Ion Source Parameter Variables	Electron energy: 20-100eV. Emission current: 0-5 mA. Ion energy: 0-10V. Ion extraction potential: 0 - minus 130 V (adjustable from PC).
UHV Analyzer Outgassing Spec	Less than 1×10^{-9} mbar-l/s
Filaments	Twin tungsten (optional ThO_2/Ir or Y_2O_3/Ir)

CONTROL UNIT/PC

MicroVision Plus Electronics Module Weight	2.1 kg
Power	24 VDC, 3.4 A external supply (included)
Maximum Ambient Operating Temperature	35°C, 80% RH (non condensing)
LED Status Indication	Filament 1, filament 2, SEM, power & communications
MicroVision Plus I/O Capability	RGA for Windows: 4 analog inputs (1 for external gauge reading), 12 TTL output signals; Process Eye 2000: 4 analog inputs (0-10V, 16 bit), 1 analog output (0-10V, 16 bit), 16 digital TTL I/O, 1 opto-isolated filament control input
I/O Capability (optional PC based)	Process Eye 2000: Generic I/O card support for ISA slots, DTS300 I/O card support for PCI slots, Modbus/GEM SECS support for some product configurations
Other Facilities	Leak-check audio headset socket with volume adjustment, external filament-protect speaker and socket, instrument reset
Software	Software: RGA for Windows: Windows 3.1, 3.11, 95/98*, NT 4.0*, Millennium* and 2000* compatible; Process Eye 2000: fully network compatible control platform generating under Microsoft® Windows NT 4.0, 98, Me, 2000* or XP* (recommended) *Contact MKS for degree of functionality
MicroVision Plus Communications (baud rate & max. distance)	RGA for Windows: RS232C, 9600 baud, 15 m (50ft) maximum; Process Eye 2000: RS232C, 9600 baud, 15 m (50ft) RS422, 115000 baud, 1.2 Km (4000ft)
Recommended PC Spec	Pentium III 233 MHz, 64MB RAM, 6 GB disk drive. Multi-sensor installations may require higher specifications.

OPTIONS AND PLUG-IN MODULES

Radiation Resistant Extenders for Remote Location of Electronics	Two optional extender lengths available: 3 meters & 15 meters
Remote Vacuum Controller (RVC)	Provides interlocked PC-based control of differentially pumped vacuum system
Valve Actuator	Converts TTL logic signals to multiple 24 volt output signals
Valve Controller	Provides automated PC-based control of multi-way valve manifold

SHIPPING INFORMATION

Complete Instrument Shipping Weight	10 kg
MicroVision Plus Packaging Dimensions	430 mm x 390 mm x 330 mm

Figure B.17: MKS Microvision Plus specifications

Dimensional Drawing

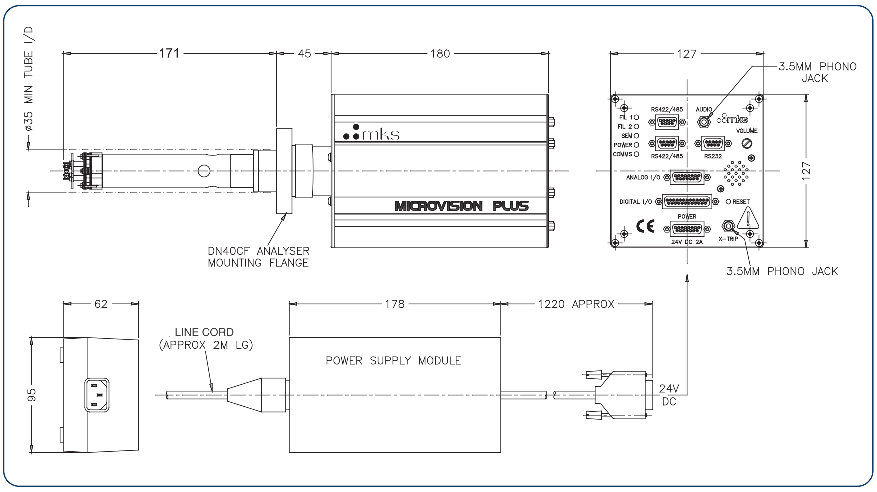

Note: Unless otherwise specified, dimensions are nominal values in millimeters.

Figure B.18: MKS Microvision Plus mechanical dimensions

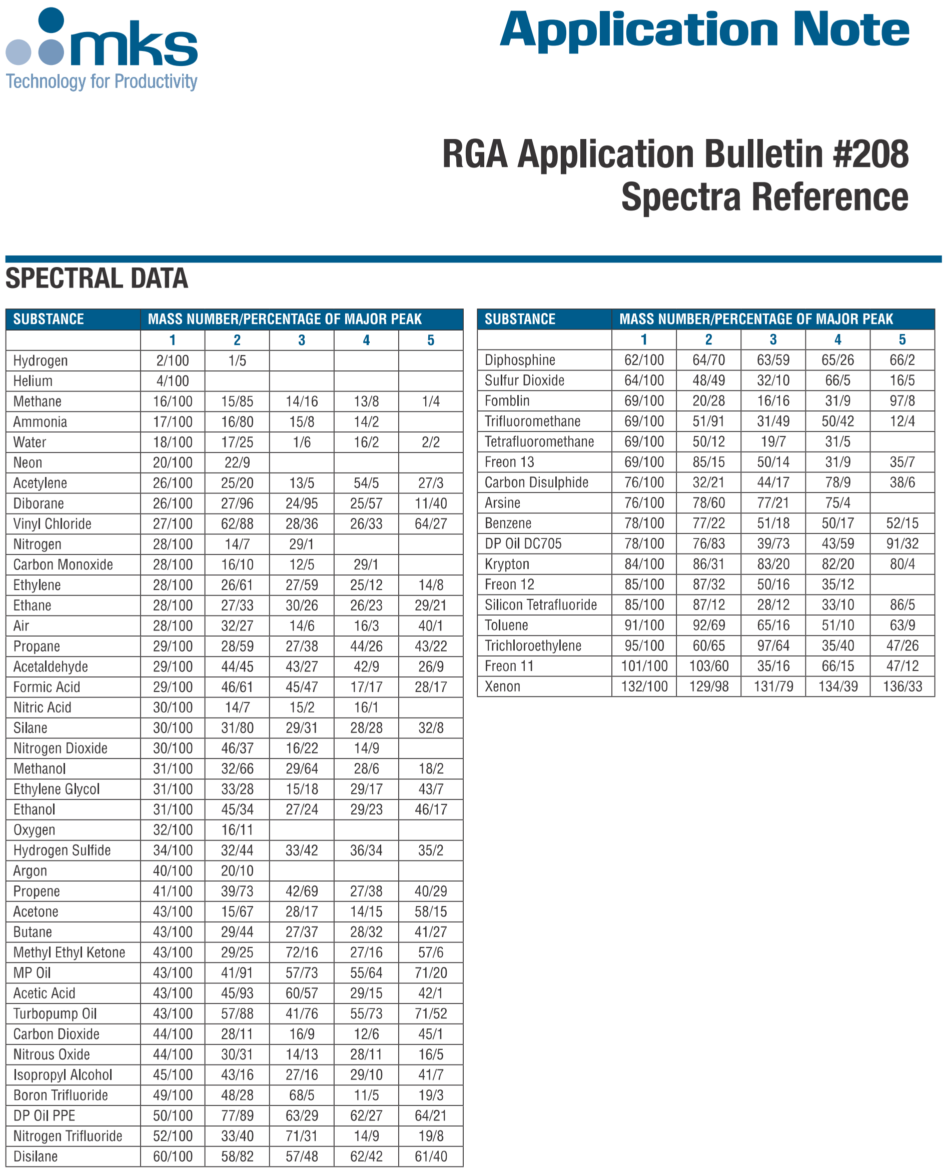

mks
Technology for Productivity

Application Note

RGA Application Bulletin #208
Spectra Reference

SPECTRAL DATA

SUBSTANCE	MASS NUMBER/PERCENTAGE OF MAJOR PEAK				
	1	2	3	4	5
Hydrogen	2/100	1/5			
Helium	4/100				
Methane	16/100	15/85	14/16	13/8	1/4
Ammonia	17/100	16/80	15/8	14/2	
Water	18/100	17/25	1/6	16/2	2/2
Neon	20/100	22/9			
Acetylene	26/100	25/20	13/5	54/5	27/3
Diborane	26/100	27/96	24/95	25/57	11/40
Vinyl Chloride	27/100	62/88	28/36	26/33	64/27
Nitrogen	28/100	14/7	29/1		
Carbon Monoxide	28/100	16/10	12/5	29/1	
Ethylene	28/100	26/61	27/59	25/12	14/8
Ethane	28/100	27/33	30/26	26/23	29/21
Air	28/100	32/27	14/6	16/3	40/1
Propane	29/100	28/59	27/38	44/26	43/22
Acetaldehyde	29/100	44/45	43/27	42/9	26/9
Formic Acid	29/100	46/61	45/47	17/17	28/17
Nitric Acid	30/100	14/7	15/2	16/1	
Silane	30/100	31/80	29/31	28/28	32/8
Nitrogen Dioxide	30/100	46/37	16/22	14/9	
Methanol	31/100	32/66	29/64	28/6	18/2
Ethylene Glycol	31/100	33/28	15/18	29/17	43/7
Ethanol	31/100	45/34	27/24	29/23	46/17
Oxygen	32/100	16/11			
Hydrogen Sulfide	34/100	32/44	33/42	36/34	35/2
Argon	40/100	20/10			
Propene	41/100	39/73	42/69	27/38	40/29
Acetone	43/100	15/67	28/17	14/15	58/15
Butane	43/100	29/44	27/37	28/32	41/27
Methyl Ethyl Ketone	43/100	29/25	72/16	27/16	57/6
MP Oil	43/100	41/91	57/73	55/64	71/20
Acetic Acid	43/100	45/93	60/57	29/15	42/1
Turbopump Oil	43/100	57/88	41/76	55/73	71/52
Carbon Dioxide	44/100	28/11	16/9	12/6	45/1
Nitrous Oxide	44/100	30/31	14/13	28/11	16/5
Isopropyl Alcohol	45/100	43/16	27/16	29/10	41/7
Boron Trifluoride	49/100	48/28	68/5	11/5	19/3
DP Oil PPE	50/100	77/89	63/29	62/27	64/21
Nitrogen Trifluoride	52/100	33/40	71/31	14/9	19/8
Disilane	60/100	58/82	57/48	62/42	61/40

SUBSTANCE	MASS NUMBER/PERCENTAGE OF MAJOR PEAK				
	1	2	3	4	5
Diphosphine	62/100	64/70	63/59	65/26	66/2
Sulfur Dioxide	64/100	48/49	32/10	66/5	16/5
Fomblin	69/100	20/28	16/16	31/9	97/8
Trifluoromethane	69/100	51/91	31/49	50/42	12/4
Tetrafluoromethane	69/100	50/12	19/7	31/5	
Freon 13	69/100	85/15	50/14	31/9	35/7
Carbon Disulphide	76/100	32/21	44/17	78/9	38/6
Arsine	76/100	78/60	77/21	75/4	
Benzene	78/100	77/22	51/18	50/17	52/15
DP Oil DC705	78/100	76/83	39/73	43/59	91/32
Krypton	84/100	86/31	83/20	82/20	80/4
Freon 12	85/100	87/32	50/16	35/12	
Silicon Tetrafluoride	85/100	87/12	28/12	33/10	86/5
Toluene	91/100	92/69	65/16	51/10	63/9
Trichloroethylene	95/100	60/65	97/64	35/40	47/26
Freon 11	101/100	103/60	35/16	66/15	47/12
Xenon	132/100	129/98	131/79	134/39	136/33

Figure B.19: Relative peak heights spectral data

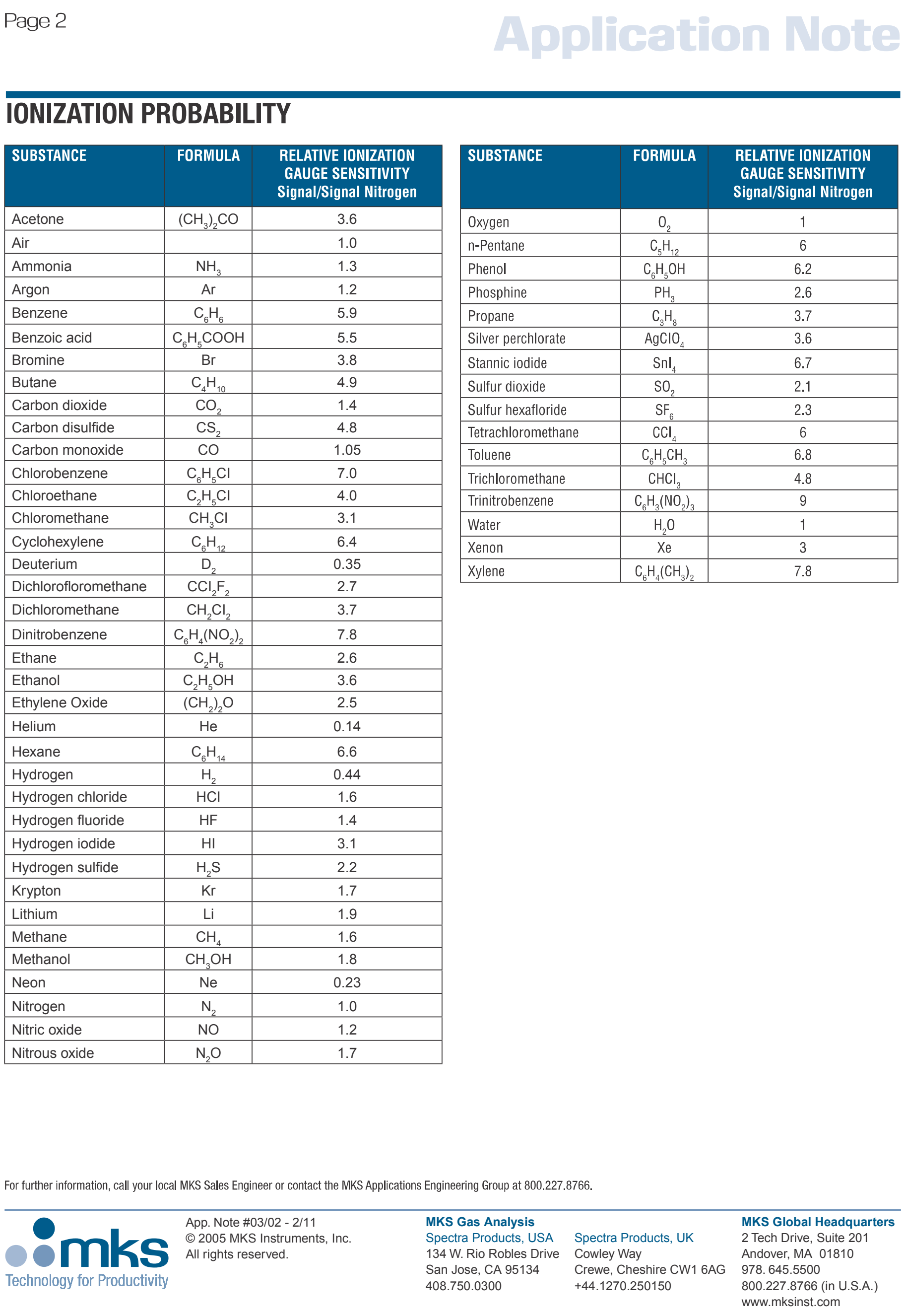

Page 2

Application Note

IONIZATION PROBABILITY

SUBSTANCE	FORMULA	RELATIVE IONIZATION GAUGE SENSITIVITY Signal/Signal Nitrogen
Acetone	$(CH_3)_2CO$	3.6
Air		1.0
Ammonia	NH_3	1.3
Argon	Ar	1.2
Benzene	C_6H_6	5.9
Benzoic acid	C_6H_5COOH	5.5
Bromine	Br	3.8
Butane	C_4H_{10}	4.9
Carbon dioxide	CO_2	1.4
Carbon disulfide	CS_2	4.8
Carbon monoxide	CO	1.05
Chlorobenzene	C_6H_5Cl	7.0
Chloroethane	C_2H_5Cl	4.0
Chloromethane	CH_3Cl	3.1
Cyclohexylene	C_6H_{12}	6.4
Deuterium	D_2	0.35
Dichloroflorometane	CCl_2F_2	2.7
Dichloromethane	CH_2Cl_2	3.7
Dinitrobenzene	$C_6H_4(NO_2)_2$	7.8
Ethane	C_2H_6	2.6
Ethanol	C_2H_5OH	3.6
Ethylene Oxide	$(CH_2)_2O$	2.5
Helium	He	0.14
Hexane	C_6H_{14}	6.6
Hydrogen	H_2	0.44
Hydrogen chloride	HCl	1.6
Hydrogen fluoride	HF	1.4
Hydrogen iodide	HI	3.1
Hydrogen sulfide	H_2S	2.2
Krypton	Kr	1.7
Lithium	Li	1.9
Methane	CH_4	1.6
Methanol	CH_3OH	1.8
Neon	Ne	0.23
Nitrogen	N_2	1.0
Nitric oxide	NO	1.2
Nitrous oxide	N_2O	1.7
Oxygen	O_2	1
n-Pentane	C_5H_{12}	6
Phenol	C_6H_5OH	6.2
Phosphine	PH_3	2.6
Propane	C_3H_8	3.7
Silver perchlorate	$AgClO_4$	3.6
Stannic iodide	SnI_4	6.7
Sulfur dioxide	SO_2	2.1
Sulfur hexafloride	SF_6	2.3
Tetrachloromethane	CCl_4	6
Toluene	$C_6H_5CH_3$	6.8
Trichloromethane	$CHCl_3$	4.8
Trinitrobenzene	$C_6H_3(NO_2)_3$	9
Water	H_2O	1
Xenon	Xe	3
Xylene	$C_6H_4(CH_3)_2$	7.8

For further information, call your local MKS Sales Engineer or contact the MKS Applications Engineering Group at 800.227.8766.

App. Note #03/02 - 2/11

MKS Gas Analysis

Spectra Products, USA
134 W. Rio Robles Drive
San Jose, CA 95134
408.750.0300

Spectra Products, UK
Cowley Way
Crewe, Cheshire CW1 6AG
+44.1270.250150

MKS Global Headquarters
2 Tech Drive, Suite 201
Andover, MA 01810
978. 645.5500
800.227.8766 (in U.S.A.)
www.mksinst.com

Figure B.20: Ionization probabilities

B.5 IF-1 beryllium window

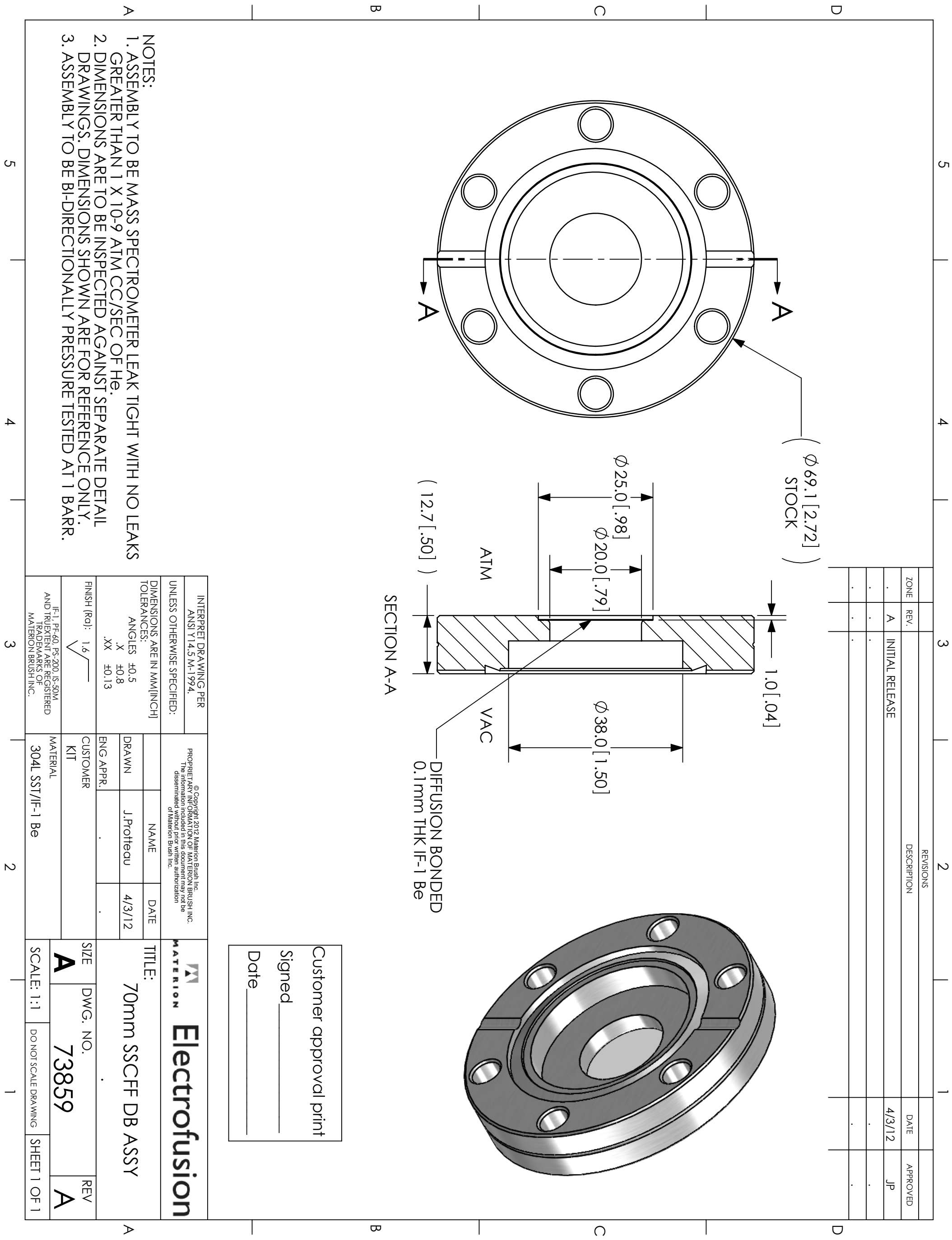

Figure B.21: Mechanical dimensions of the Materion IF-1 beryllium window. Dimensions in mm (inch). Drawing by Materion Brush Inc.

B.6 Americium-241 source

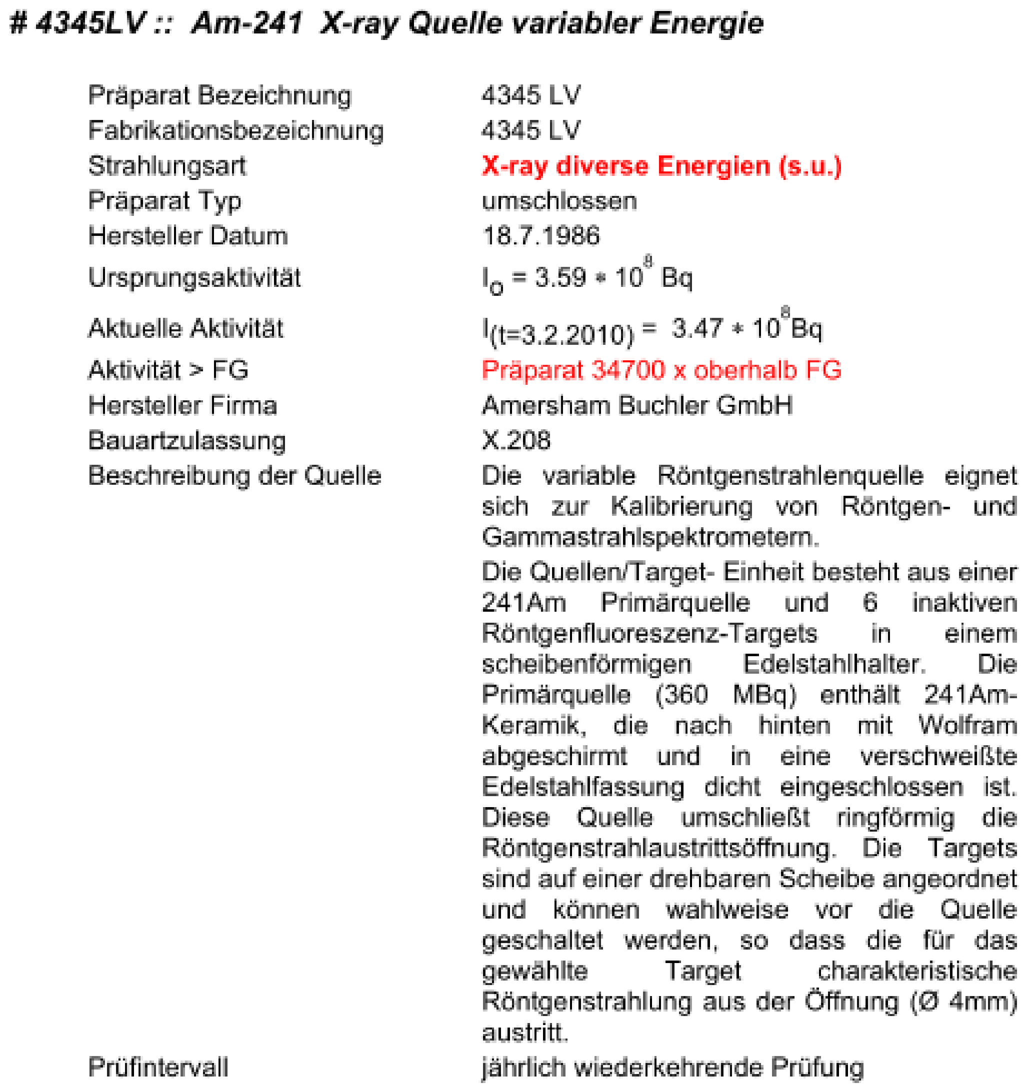

 # 4345LV :: Am-241 X-ray Quelle variabler Energie

Präparat Bezeichnung	4345 LV
Fabrikationsbezeichnung	4345 LV
Strahlungsart	**X-ray diverse Energien (s.u.)**
Präparat Typ	umschlossen
Hersteller Datum	18.7.1986
Ursprungsaktivität	$I_0 = 3.59 * 10^8$ Bq
Aktuelle Aktivität	$I_{(t=3.2.2010)} = 3.47 * 10^8$Bq
Aktivität > FG	Präparat 34700 x oberhalb FG
Hersteller Firma	Amersham Buchler GmbH
Bauartzulassung	X.208
Beschreibung der Quelle	Die variable Röntgenstrahlenquelle eignet sich zur Kalibrierung von Röntgen- und Gammastrahlspektrometern. Die Quellen/Target- Einheit besteht aus einer 241Am Primärquelle und 6 inaktiven Röntgenfluoreszenz-Targets in einem scheibenförmigen Edelstahlhalter. Die Primärquelle (360 MBq) enthält 241Am-Keramik, die nach hinten mit Wolfram abgeschirmt und in eine verschweißte Edelstahlfassung dicht eingeschlossen ist. Diese Quelle umschließt ringförmig die Röntgenstrahlaustrittsöffnung. Die Targets sind auf einer drehbaren Scheibe angeordnet und können wahlweise vor die Quelle geschaltet werden, so dass die für das gewählte Target charakteristische Röntgenstrahlung aus der Öffnung (Ø 4mm) austritt.
Prüfintervall	jährlich wiederkehrende Prüfung

Figure B.22: Data sheet of the Am-241 source.

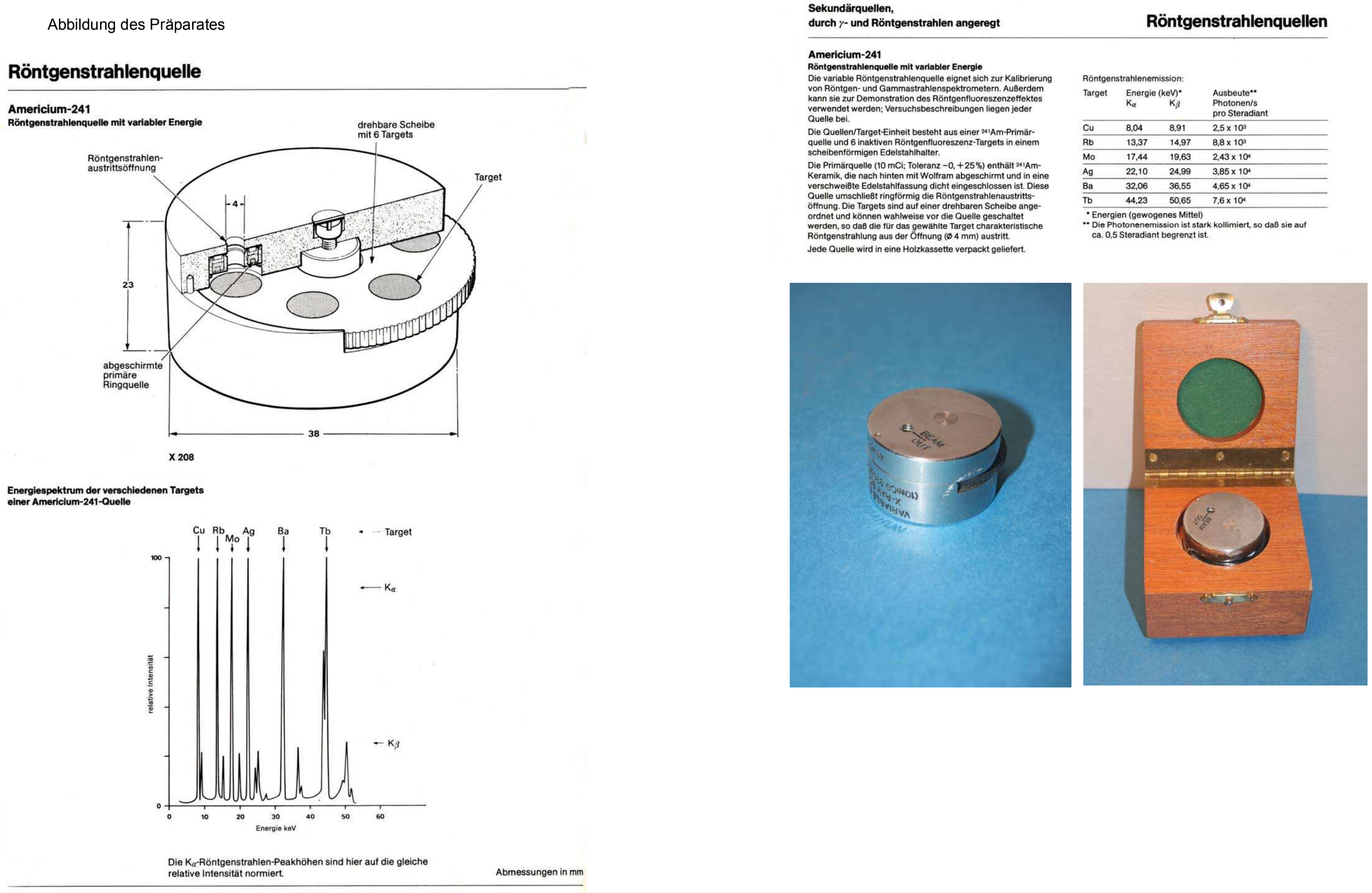

Abbildung des Präparates

Röntgenstrahlenquelle

Americium-241
Röntgenstrahlenquelle mit variabler Energie

X 208

Energiespektrum der verschiedenen Targets einer Americium-241-Quelle

Die K_α-Röntgenstrahlen-Peakhöhen sind hier auf die gleiche relative Intensität normiert.

Abmessungen in mm

Sekundärquellen, durch γ- und Röntgenstrahlen angeregt

Röntgenstrahlenquellen

Americium-241
Röntgenstrahlenquelle mit variabler Energie

Die variable Röntgenstrahlenquelle eignet sich zur Kalibrierung von Röntgen- und Gammastrahlenspektrometern. Außerdem kann sie zur Demonstration des Röntgenfluoreszenzeffektes verwendet werden; Versuchsbeschreibungen liegen jeder Quelle bei.

Die Quellen/Target-Einheit besteht aus einer ^{241}Am-Primärquelle und 6 inaktiven Röntgenfluoreszenz-Targets in einem scheibenförmigen Edelstahlhalter.

Die Primärquelle (10 mCi; Toleranz −0, +25 %) enthält ^{241}Am-Keramik, die nach hinten mit Wolfram abgeschirmt und in eine verschweißte Edelstahlfassung dicht eingeschlossen ist. Diese Quelle umschließt ringförmig die Röntgenstrahlenaustrittsöffnung. Die Targets sind auf einer drehbaren Scheibe angeordnet und können wahlweise vor die Quelle geschaltet werden, so daß die für das gewählte Target charakteristische Röntgenstrahlung aus der Öffnung (ø 4 mm) austritt.

Jede Quelle wird in eine Holzkassette verpackt geliefert.

Röntgenstrahlenemission:

Target	Energie (keV)* K_α	K_β	Ausbeute** Photonen/s pro Steradiant
Cu	8,04	8,91	$2{,}5 \times 10^3$
Rb	13,37	14,97	$8{,}8 \times 10^3$
Mo	17,44	19,63	$2{,}43 \times 10^4$
Ag	22,10	24,99	$3{,}85 \times 10^4$
Ba	32,06	36,55	$4{,}65 \times 10^4$
Tb	44,23	50,65	$7{,}6 \times 10^4$

* Energien (gewogenes Mittel)
** Die Photonenemission ist stark kollimiert, so daß sie auf ca. 0,5 Steradiant begrenzt ist.

Figure B.23: Further information on the Am-241 source.

Appendix C

Additional information on Penelope 2008 simulations

C.1 pencyl.exe input file

Input file for the simulation of tritium in the residual gas:

```
TITLE  TRIADE Simulation with activity in gas volume
       .
GSTART >>>>>>>> Beginning of the geometry definition list.
LAYER        0.00  1.88  1 Start
CYLIND   1   0.00  7.50
LAYER        1.88  8.85  2 Recipient
CYLIND   1   5.00  5.20
LAYER        8.85  9.85  3 Plate of sample holder
CYLIND   1   0.00  4.70
CYLIND   1   5.00  5.20
LAYER        9.85  9.95  4 Probe layer
CYLIND   3   0.00  3.50
CYLIND   1   3.50  4.70
CYLIND   1   5.00  5.20
LAYER        9.95 10.25  5 Holder ring
CYLIND   1   3.00  4.70
CYLIND   1   5.00  5.20
LAYER        10.25  11.55  6 Space between holder and window
CYLIND   1   5.00  5.20
LAYER        11.55  11.55001  7 Gold coating
CYLIND   1   0.00  1.00
CYLIND   1   5.00  5.20
LAYER        11.55001  11.550011 8 Adhesive layer
CYLIND   2   0.00  1.00
CYLIND   1   5.00  5.20
LAYER        11.550011 11.560011 9 Be
CYLIND   3   0.00  1.00
CYLIND   1   1.00  3.50
CYLIND   1   5.00  5.20
LAYER        11.560011 12.00 10 Window (small inner radius)
CYLIND   1   1.00  3.50
CYLIND   1   5.00  5.20
LAYER        12.00  12.803 11 Fenster (large inner radius)
CYLIND   1   1.90  3.50
CYLIND   1   5.00  5.20
LAYER        12.803 12.853 12      Detector-layer
CYLIND   4   0.00  0.233
CYLIND   1   1.90  3.50
CYLIND   1   5.00  5.20
LAYER        12.853  17.7 13 Rest IF
CENTRE       0.00  0.00
CYLIND   1   1.90  10.10
GEND   <<<<<<<< End of the geometry definition list.
       .
       >>>>>>>> Source definition.
SKPAR  1[Primary particles: 1=electron, 2=photon, 3=positron]
       .
SPECTR 100.000 8.27E-03[E bin: lower-end and probability]
SPECTR 200.00  8.42E-03
SPECTR 300.00 8.61E-03
SPECTR 400.00  8.80E-03
SPECTR 500.00  8.98E-03
SPECTR 600.00  9.15E-03
SPECTR 700.00 9.30E-03
SPECTR 800.00 9.43E-03
SPECTR 900.00 9.56E-03
SPECTR 1000.00 9.67E-03
SPECTR 1100.00 9.77E-03
SPECTR 1200.00 9.86E-03
SPECTR 1300.00 9.94E-03
SPECTR 1400.00 1.00E-02
SPECTR 1500.00 1.01E-02
SPECTR 1600.00 1.01E-02
SPECTR 1700.00 1.02E-02
SPECTR 1800.00 1.02E-02
SPECTR 1900.00 1.03E-02
SPECTR 2000.00 1.03E-02
SPECTR 2100.00 1.03E-02
SPECTR 2200.00 1.03E-02
SPECTR 2300.00 1.03E-02
SPECTR 2400.00 1.03E-02
SPECTR 2500.00 1.03E-02
SPECTR 2600.00 1.03E-02
SPECTR 2700.00 1.03E-02
SPECTR 2800.00 1.03E-02
SPECTR 2900.00 1.03E-02
SPECTR 3000.00 1.03E-02
SPECTR 3100.00 1.03E-02
SPECTR 3200.00 1.02E-02
SPECTR 3300.00 1.02E-02
SPECTR 3400.00 1.02E-02
SPECTR 3500.00 1.01E-02
SPECTR 3600.00 1.01E-02
SPECTR 3700.00 1.01E-02
SPECTR 3800.00 1.00E-02
SPECTR 3900.00 9.98E-03
SPECTR 4000.00 9.93E-03
SPECTR 4100.00 9.88E-03
SPECTR 4200.00 9.83E-03
SPECTR 4300.00 9.77E-03
SPECTR 4400.00 9.72E-03
SPECTR 4500.00 9.66E-03
SPECTR 4600.00 9.60E-03
SPECTR 4700.00 9.53E-03
SPECTR 4800.00 9.47E-03
SPECTR 4900.00 9.40E-03
```

```
SPECTR 5000.00 9.33E-03
SPECTR 5100.00 9.27E-03
SPECTR 5200.00 9.19E-03
SPECTR 5300.00 9.12E-03
SPECTR 5400.00 9.05E-03
SPECTR 5500.00 8.97E-03
SPECTR 5600.00 8.90E-03
SPECTR 5700.00 8.82E-03
SPECTR 5800.00 8.74E-03
SPECTR 5900.00 8.66E-03
SPECTR 6000.00 8.58E-03
SPECTR 6100.00 8.50E-03
SPECTR 6200.00 8.41E-03
SPECTR 6300.00 8.33E-03
SPECTR 6400.00 8.24E-03
SPECTR 6500.00 8.16E-03
SPECTR 6600.00 8.07E-03
SPECTR 6700.00 7.98E-03
SPECTR 6800.00 7.90E-03
SPECTR 6900.00 7.81E-03
SPECTR 7000.00 7.72E-03
SPECTR 7100.00 7.63E-03
SPECTR 7200.00 7.54E-03
SPECTR 7300.00 7.45E-03
SPECTR 7400.00 7.35E-03
SPECTR 7500.00 7.26E-03
SPECTR 7600.00 7.17E-03
SPECTR 7700.00 7.08E-03
SPECTR 7800.00 6.98E-03
SPECTR 7900.00 6.89E-03
SPECTR 8000.00 6.80E-03
SPECTR 8100.00 6.70E-03
SPECTR 8200.00 6.61E-03
SPECTR 8300.00 6.51E-03
SPECTR 8400.00 6.42E-03
SPECTR 8500.00 6.32E-03
SPECTR 8600.00 6.23E-03
SPECTR 8700.00 6.13E-03
SPECTR 8800.00 6.04E-03
SPECTR 8900.00 5.94E-03
SPECTR 9000.00 5.85E-03
SPECTR 9100.00 5.75E-03
SPECTR 9200.00 5.66E-03
SPECTR 9300.00 5.56E-03
SPECTR 9400.00 5.47E-03
SPECTR 9500.00 5.37E-03
SPECTR 9600.00 5.28E-03
SPECTR 9700.00 5.18E-03
SPECTR 9800.00 5.09E-03
SPECTR 9900.00 5.00E-03
SPECTR 10000.00 4.90E-03
SPECTR 10100.00 4.81E-03
SPECTR 10200.00 4.72E-03
SPECTR 10300.00 4.62E-03
SPECTR 10400.00 4.53E-03
SPECTR 10500.00 4.44E-03
SPECTR 10600.00 4.35E-03
SPECTR 10700.00 4.26E-03
SPECTR 10800.00 4.17E-03
SPECTR 10900.00 4.08E-03
SPECTR 11000.00 3.99E-03
SPECTR 11100.00 3.90E-03
SPECTR 11200.00 3.81E-03
SPECTR 11300.00 3.72E-03
SPECTR 11400.00 3.63E-03
SPECTR 11500.00 3.55E-03
SPECTR 11600.00 3.46E-03
SPECTR 11700.00 3.37E-03
SPECTR 11800.00 3.29E-03
SPECTR 11900.00 3.20E-03
SPECTR 12000.00 3.12E-03
SPECTR 12100.00 3.04E-03
SPECTR 12200.00 2.95E-03
SPECTR 12300.00 2.87E-03
SPECTR 12400.00 2.79E-03
SPECTR 12500.00 2.71E-03
SPECTR 12600.00 2.63E-03
SPECTR 12700.00 2.56E-03
SPECTR 12800.00 2.48E-03
SPECTR 12900.00 2.40E-03
SPECTR 13000.00 2.33E-03
SPECTR 13100.00 2.25E-03
SPECTR 13200.00 2.18E-03
SPECTR 13300.00 2.10E-03
SPECTR 13400.00 2.03E-03
SPECTR 13500.00 1.96E-03
SPECTR 13600.00 1.89E-03
SPECTR 13700.00 1.82E-03
SPECTR 13800.00 1.75E-03
SPECTR 13900.00 1.69E-03
SPECTR 14000.00 1.62E-03
SPECTR 14100.00 1.56E-03
SPECTR 14200.00 1.49E-03
SPECTR 14300.00 1.43E-03
SPECTR 14400.00 1.37E-03
SPECTR 14500.00 1.31E-03
SPECTR 14600.00 1.25E-03
SPECTR 14700.00 1.19E-03
SPECTR 14800.00 1.13E-03
SPECTR 14900.00 1.08E-03
SPECTR 15000.00 1.02E-03
SPECTR 15100.00 9.71E-04
SPECTR 15200.00 9.19E-04
SPECTR 15300.00 8.68E-04
SPECTR 15400.00 8.19E-04
SPECTR 15500.00 7.71E-04
SPECTR 15600.00 7.24E-04
SPECTR 15700.00 6.78E-04
SPECTR 15800.00 6.34E-04
SPECTR 15900.00 5.91E-04
SPECTR 16000.00 5.50E-04
SPECTR 16100.00 5.10E-04
SPECTR 16200.00 4.71E-04
SPECTR 16300.00 4.34E-04
SPECTR 16400.00 3.98E-04
SPECTR 16500.00 3.64E-04
SPECTR 16600.00 3.31E-04
SPECTR 16700.00 3.00E-04
SPECTR 16800.00 2.70E-04
SPECTR 16900.00 2.41E-04
SPECTR 17000.00 2.14E-04
SPECTR 17100.00 1.89E-04
SPECTR 17200.00 1.65E-04
SPECTR 17300.00 1.43E-04
SPECTR 17400.00 1.22E-04
SPECTR 17500.00 1.03E-04
SPECTR 17600.00 8.50E-05
SPECTR 17700.00 6.90E-05
SPECTR 17800.00 5.47E-05
SPECTR 17900.00 4.20E-05
SPECTR 18000.00 3.09E-05
SPECTR 18100.00 2.15E-05
SPECTR 18200.00 1.38E-05
SPECTR 18300.00 7.79E-06
SPECTR 18400.00 3.47E-06
SPECTR 18500.00 8.70E-07
SPECTR 18600.00 -1.00E+00
       .
STHICK 1.3   [External source thickness]
SRADII 0 5                             [Source inner and outer radii]
SPOSIT 0 0 10.9                    [Coordinates of the source centre]
SCONE  0 0 180                          [Conical beam; angles in deg]
       .
       >>>>>>>> Material data and simulation parameters.
MFNAME Gold.mat                       [Material file, up to 20 chars]
MSIMPA 1.0e2 1.0e2 1.0e2 0.05 0.05 1e2 1e2  [EABS(1:3),C1,C2,WCC,WCR]
MFNAME Titanium.mat                   [Material file, up to 20 chars]
MSIMPA 1.0e2 1.0e2 1.0e2 0.05 0.05 1e2 1e2  [EABS(1:3),C1,C2,WCC,WCR]
MFNAME Beryllium.mat                  [Material file, up to 20 chars]
MSIMPA 1.0e2 1.0e2 1.0e2 0.05 0.05 1e2 1e2  [EABS(1:3),C1,C2,WCC,WCR]
MFNAME Silicon.mat                    [Material file, up to 20 chars]
MSIMPA 1.0e2 1.0e2 1.0e2 0.05 0.05 1e2 1e2  [EABS(1:3),C1,C2,WCC,WCR]
       .
       >>>>>>>> Counter array dimensions and pdf ranges.
NBTL   0 0.15 150          [Track-length interval and no. of TL-bins]
       .
       >>>>>>>> Energy-deposition detectors (up to 25).
ENDETC 0.0 2.e4 500                [Energy window and number of bins]
EDSPC  Spectrum1001.dat         [Output spectrum file name, 20 chars]
EDBODY 12 1                     [Active body; one line for each body]
       .
       >>>>>>>> Dose and charge distributions.
DOSE2D 12 1 100 100   [Tally 2D dose and charge dists. in body KL,KC]
       .
       >>>>>>>> Job properties
RESUME dump.dmp                [Resume from this dump file, 20 chars]
DUMPTO dump.dmp                   [Generate this dump file, 20 chars]
DUMPP  60                                    [Dumping period, in sec]
       .
RSEED  1 1               [Seeds  of  the  random-number  generator]
NSIMSH 2e12                     [Desired number of simulated showers]
TIME   6e5                         [Allotted simulation time, in sec]
       .
END                                  [Ends the reading of input data]
```

Source geometry definition for the simulation of tritium adsorbed on the sample:

```
STHICK 0                   [External source thickness]
SRADII 0 3              [Source inner and outer radii]
SPOSIT 0 0 9.9500001  [Coordinates of the source centre]
SCONE  0 0 180            [Conical beam; angles in deg]
```

Source geometry definition for the simulation of tritium adsorbed on the gold coated beryllium window:

```
STHICK 0                   [External source thickness]
SRADII 0 1              [Source inner and outer radii]
SPOSIT 0 0 11.4999999 [Coordinates of the source centre]
SCONE  0 0 180            [Conical beam; angles in deg]
```

Bibliography

[Alt03] G. H. Altarelli, editor, *Neutrino mass*, Springer tracts in modern physics ; 190, Springer, Berlin (2003).

[Amp11] Amptek, *Amptek silicon drift detectors*, Amptek application Notes (2011).

[Amp12] Amptek, *DppMCA Help*, Amptek DppMCA Software Help (2012).

[Ase11] V. N. Aseev et al., *Upper limit on the electron antineutrino mass from the Troitsk experiment*, Phys. Rev. D **84** (2011) 112003.

[Bab12] M. Babutzka et al., *Monitoring of the operating parameters of the KATRIN Windowless Gaseous Tritium Source*, New Journal of Physics **14**, 10 (2012) 103046.

[Bar11] G. Barnes et al., *Interfacial science : an introduction*, Oxford University Press, Oxford, 2. ed. edition (2011), previous ed.: 2005. - Includes bibliographical references and index; Erscheint: 01. Februar 2011.

[Bes08] U. Besserer et al., *Tritium confinement, retention, and releases at the tritium laboratory Karlsruhe*, Fusion Science and Technology **54**, 1 (2008) 160–163.

[Boh98] J. Boh et al., *Adsorption and abstraction of atomic hydrogen (deuterium) on Al(100)*, Surface Science **395**, 1 (1998) 98 – 110.

[Bor05] B. Bornschein et al., *Successful experimental verification of the tokamak exhaust processing concept of ITER with the CAPER facility*, Fusion Science and Technology **48**, 1 (2005) 11–16.

[Bor11] B. Bornschein, *Between Fusion and Cosmology - The Future of the Tritium Laboratory Karlsruhe*, Fusion Science and Technology **60**, 3 (2011) 1088–1091.

[Bru38] S. Brunauer et al., *Adsorption of Gases in Multimolecular Layers*, Journal of the American Chemical Society **60**, 2 (1938) 309–319.

[Cas04] G. Castellano et al., *Analytical model for the bremsstrahlung spectrum in the 0.25-20 keV photon energy range*, Spectrochimica Acta Part B: Atomic Spectroscopy **59**, 3 (2004) 313 – 319.

[Che10] W. Cheng et al., *Evaluation of natural recharge of Chingshui geothermal reservoir using tritium as a tracer*, Radiation Measurements **45**, 1 (2010) 110 – 117.

[Chr88] K. Christmann, *Interaction of hydrogen with solid surfaces*, Surface Science Reports **9**, 1-3 (1988) 1 – 163.

[Chr91] K. Christmann, *Introduction to surface physical chemistry*, Topics in physical chemistry ; 1, Steinkopff, Darmstadt (1991).

[Cla70] A. Clark, *The theory of adsorption and catalysis*, Physical chemistry ; 18, Acad. Pr., New York [u.a.] (1970).

[Dem10a] W. Demtröder, *Experimentalphysik 3 : Atome-, Moleküle- und Festkörper*, Springer-Lehrbuch, Springer-Verlag Berlin Heidelberg (2010).

[Dem10b] W. Demtröder, *Experimentalphysik 4 : Kern-, Teilchen- und Astrophysik*, Springer-Lehrbuch, Springer-Verlag Berlin Heidelberg (2010).

[Dem12] D. Demange et al., *Overview of R&D at TLK for process and analytical issues on tritium management in breeder blankets of ITER and DEMO*, Fusion Engineering and Design **87**, 7 - 8 (2012) 1206 – 1213.

[DIN06] DIN, *Materialprüfnormen für metallische Werkstoffe*, volume 1: Mechanisch-technologische Prüfverfahren (erzeugnisformunabhängig), Prüfmaschinen, Bescheinigungen of *DIN-Taschenbuch ; 19*, Beuth, Berlin, 15. aufl. stand der abgedr. normen: mai 2006 edition (2006).

[Ebe12] S. R. Ebenhöch, *Systematische Untersuchungen eines Röntgendetektorsystems zur Überwachung der KATRIN-Tritiumquelle*, Bachelor thesis, Karlsruhe Institute of Technology (2012).

[Eic09] F. Eichelhardt, *Measurement of the Tritium Pumping Properties of a 4.2 K Argon Condensate for the Cryogenic Pumping Section of KATRIN*, Dissertation, Verlag Karlsruhe (2009).

[Ein74] K. Einarsson et al., *Randomly tritium-labelled chenodeoxycholic acid as tracer in the determination of bile acid turnover in man*, Clinica Chimica Acta **56**, 3 (1974) 235 – 239.

[ESIS12] European Comission, Joint research center, Institute for Health and Consumer Protection (IHCP), *European chemical substances Information System (ESIS)*, 2012.

[Fio08] C. Fiorini et al., *Semiconductor drift detectors for X- and gamma-ray spectroscopy and imaging*, Nuclear Instruments and Methods in Physics Research Section B: Beam Interactions with Materials and Atoms **266**, 10 (2008) 2173 – 2181.

[Gam09] D. Gambier, *Fusion for Energy: A new European organization for the development of fusion energy*, Fusion Engineering and Design **84**, 2 - 6 (2009) 138 – 142.

[Gat84] E. Gatti et al., *Semiconductor drift chamber - An application of a novel charge transport scheme*, Nuclear Instruments and Methods in Physics Research **225**, 3 (1984) 608 – 614.

[Gru08] C. Grupen et al., *Particle detectors*, Cambridge monographs on particle physics, nuclear physics, and cosmology ; 26, Cambridge University Press, New York, NY, 2. ed. edition (2008), previous ed.: published as by Claus Grupen with the cooperation of Armin Böhrer and Ludek Smolík. 1996.

[Han10] S. Hannestad, *Neutrino physics from precision cosmology*, Progress in Particle and Nuclear Physics **65**, 2 (2010) 185 – 208.

[Hen91] M. Henzler et al., *Oberflächenphysik des Festkörpers*, Teubner-Studienbücher : Physik, Teubner, Stuttgart (1991).

[Hir84] T. Hirabayashi et al., *Sorption of gaseous tritium on the surface of type 316 stainless steel*, Journal of Nuclear Materials **120**, 2 - 3 (1984) 309 – 315.

[Iba06] H. Ibach, *Physics of surfaces and interfaces*, Springer, Berlin (2006).

[Jou08] K. H. Jousten, editor, *Handbook of vacuum technology*, WILEY-VCH, Weinheim (2008).

[KAT05] KATRIN Collaboration, *KATRIN Design Report 2004*, Forschungszentrum Karlsruhe (Karlsruher Institut für Technologie) (2005).

[KAT12] KATRIN rear section working group, *KATRIN Rear Section Technical Design Report 2012*, Technical report, KATRIN Collaboration (2012).

[Kra23] H. A. Kramers, *XCIII. On the theory of X-ray absorption and of the continuous X-ray spectrum*, Philosophical Magazine Series 6 **46**, 275 (1923) 836–871.

[Kri12] H. Krieger, *Grundlagen der Strahlungsphysik und des Strahlenschutzes*, SpringerLink : Bücher, Vieweg+Teubner Verlag, Wiesbaden, 4. Aufl. 2012. überarb. u. erw edition (2012).

[Lag77] D. Laguitton et al., *Experimental spectral distribution versus Kramers' law for quantitative X-ray fluorescence by the fundamental parameters method*, X-Ray Spectrometry **6**, 4 (1977) 201–203.

[Lec01] P. Lechner et al., *Silicon drift detectors for high count rate X-ray spectroscopy at room temperature*, Nuclear Instruments and Methods in Physics Research Section A: Accelerators, Spectrometers, Detectors and Associated Equipment **458**, 1 - 2 (2001) 281 – 287.

[Mat85] M. Matsuyama et al., *Contamination of ionization chamber due to tritium exposure*, The International Journal of Applied Radiation and Isotopes **36**, 7 (1985) 595.

[Mat03] M. Matsuyama et al., *Non-destructive tritium measurements of Mk IIA divertor tile by BIXS*, Journal of Nuclear Materials **313 - 316**, 0 (2003) 491 – 495.

[Mau09] D. Maurel, *Designstudien zur Messung der Aktivität der Tritiumquelle im KATRIN-Experiment mit Röntgenstrahlung*, Diploma thesis, Karlsruhe Institute of Technology (2009).

[MKS13] MKS Instruments, *RGA Application Bulletin*, Application Notes **208** (2013).

[Nag06] S. Nagy et al., *On the Q -value of the tritium ß-decay*, EPL (Europhysics Letters) **74**, 3 (2006) 404.

[Ott08] E. Otten et al., *Neutrino mass limit from tritium β-decay*, Reports on Progress in Physics **71** (2008) 086201.

[Pau30] W. Pauli, *Offener Brief an die Gruppe der Radioaktiven bei der Gauvereins-Tagung zu Tübingen*, Reproduced in: R. Kronig and V. Weisskopf (Eds.), Wolfgang Pauli, Collected Scientific Papers, Vol. 2, Interscience, New York (1964) 1316 - 1317 (1930).

[Pow66] R. Powell et al., *Thermal conductivity of selected materials*, National Standard Reference Data Series **NSRDS-NBS 8** (1966).

[Pri12] F. Priester et al., *TriToP - A compatibility experiment with turbomolecular pumps under tritium atmosphere*, Vacuum (2012), in press.

[Red62] P. Redhead, *Thermal desorption of gases*, Vacuum **12**, 4 (1962) 203 – 211.

[Rei56] F. Reines et al., *The Neutrino*, Nature **178** (1956).

[Rei12] A. Rein, *Inbetriebnahme und Grundlagen-Charakterisierung eines Silicon-Drift-Detector für Messungen der Tritiumkonzentrationen in Wasser*, Bachelor thesis, Karlsruhe Institute of Technology (2012).

[Röl11] M. Röllig, *Studien zu einem Röntgendetektorsystem zur Überwachung der Aktivität in der KARTIN Tritiumquelle*, Diploma thesis, Institute for Experimental Nuclear Physics, Karlsruhe Institute of Technology (2011).

[Röl12a] M. Röllig, *Calculations and Spectrum kindly provided by M.Röllig* (2012).

[Röl12b] M. Röllig et al., *Activity monitoring of a gaseous tritium source by beta induced X-ray spectrometry*, Fusion Engineering and Design (2012).

[Sal08] F. Salvat et al., *PENELOPE 2008: A Code System for Monte Carlo Simulation of Electron and Photon Transport* (2008).

[Sch91] P. Schira et al., *The Tritium Laboratory Karlsruhe: Laboratory design and equipment*, Fusion Engineering and Design **18**, 0 (1991) 19 – 26.

[Sel04] S. Seltzer, *NIST Standard Reference Database 126* (2004).

[Sto92] L. Stobinski et al., *Atomic hydrogen adsorption on thin gold films*, Surface Science **269/270**, 0 (1992) 383 – 388.

[Sto94] L. Stobinski et al., *Model of atomic hydrogen adsorption on thin gold film surface*, Vacuum **45**, 2 - 3 (1994) 299 – 301.

[Sto96] L. Stobinski, *Molecular and atomic deuterium chemisorption on thin gold films at 78 K: an isotope effect*, Applied Surface Science **103**, 4 (1996) 503 – 508.

[Sto99] L. Stobinski et al., *Molecular hydrogen interactions with discontinuous and continuous thin gold films*, Applied Surface Science **141**, 3/4 (1999) 319 – 325.

[Stu10] M. Sturm et al., *Monitoring of all hydrogen isotopologues at tritium laboratory Karlsruhe using Raman spectroscopy*, Laser Physics **20** (2010) 493–507.

[Tho09] A. C. Thompson, editor, *X-ray data booklet*, Lawrence Berkeley National Lab., Berkeley, Calif., 3. ed. edition (2009).

[TLA12] TLA, *Technische Liefer- und Abnahmebedingungen*, Internal document of the TLK (2012).

[TMU12] *Turbomolecular Drag Pumps With Magnetic Bearings Manual.*

[Tor05] Y. Torikai et al., *Tritium distribution in JET Mark IIA type divertor tiles analysed by BIXS*, Journal of Nuclear Materials **337/339**, 0 (2005) 575 – 579.

[Tso11] N. Tsoulfanidis et al., *Measurement and detection of radiation*, CRC Press, Boca Raton, Fla. [u.a.], 3. ed. edition (2011).

[Vei12] H.-M. Veith, *Strahlenschutzverordnung : unter Berücksichtigung der Änderungen durch die Novellierung 2011; Textausgabe mit einer erläuternden Einführung*, Bundesanzeiger, Köln, 9. aktualis. Aufl., Stand: 1. November 2011 edition (2012), erscheint: November 2011.

[Wan01] Z. Wang et al., *Estimating pre-exponential factors for desorption from semiconductors: consequences for a priori process modeling*, Applied Surface Science **181**, 1 - 2 (2001) 111 – 120.

[Wes60] T. Westermark et al., *On the use of bremsstrahlung for the determination of tritium in aqueous and organic systems*, Nuclear Instruments and Methods **9**, 2 (1960) 141 – 144.

[Wie33] P. Wiest, *Gitterkonstante und Korngröße bei Gold-Silberlegierungen*, Zeitschrift für Physik **81** (1933) 121–128.

[Zha11] Y. Zhang et al., *Corrected Values for Boiling Points and Enthalpies of Vaporization of Elements in Handbooks*, Journal of Chemical and Engineering Data **56**, 2 (2011) 328–337.

[Zhu89] X. Zhu et al., *Laser-induced thermal desorption of CO on Ni(111): Determination of pre-exponential factor and heat of desorption*, Chemical Physics Letters **155**, 4-5 (1989) 459 – 462.

Danksagung

An dieser Stelle möchte ich allen Personen danken, die diese Arbeit ermöglicht haben und die mich während der Zeit meines Studiums und insbesondere während der Zeit am TLK unterstützt haben. Ich danke allen Personen auf der nachfolgenden, sicher unvollständigen Liste herzlich:

- Prof. Dr. Guido Drexlin für die interessante Aufgabenstellung und dafür, dass er diese Arbeit erst ermöglicht hat.
- Prof. Dr. Ulrich Husemann für die Übernahme der Zweitkorrektur.
- Florian Priester und Marco Röllig für ihre Betreuung.
- Dr. Beate Bornschein für ihr außergewöhnliches Engagement für die Studenten am Tritiumlabor, sowie für ihre intensive Betreuung bei der Korrektur dieser Arbeit.
- Dr. Christopher Dorn und der Materion Brush Inc. für die Bereitstellung der ersten Berylliumprobe für das TRIADE Experiment.
- Florian Kassel und Alexander Beck für ihre Motivation zum Frühsport, sowie für ihre Offenheit für Diskussionen über die wichtigen Dinge im Leben.
- Sebastian Fischer für seine Hilfsbereitschaft und seine entscheidende Unterstützung bei zahlreichen Herausforderungen.
- Martin Babutzka für das Korrekturlesen von Teilen dieser Arbeit und seine Unterstützung in IT-Fragen. Ich danke Magnus Schlösser für seine Korrekturen zu später Stunde und sein Engagement für die körperliche Ertüchtigung der Studenten und Mitarbeiter am TLK, sowie Kerstin Schönung für ihre leckeren Backwaren.
- Allen Studenten und Mitarbeitern des TLK, insbesondere: Dr. Uwe Besserer, Dr. Jürgen Wendel, Dirk Osenberg, Dr. Michael Sturm, Dr. Woo Sik Gil, Stefan Welte, Robert Wagner, Manfred Göckel, Norbert Kernert, Luisa La Cascio, Beate Kloppe, Sylvia Krieger, Eva Porter, Nancy Lohr, Hans-Dieter Adami, Robin Grössle, Robert Michling, Simon Niemes, Vera Schäfer, Simone Rupp, Bennet Krasch und Sylvia Ebenhöch für ihre Unterstützung und die angenehme Atmosphäre am TLK.
- Dr. Michael Notheisen für das Korrekturlesen großer Teile dieser Arbeit und viele nützliche Hinweise.
- Sebastian Ziegler, der mich durch das gesamte Studium begleitet hat, für viel Motivation und produktive Diskussionen.
- Marcel Sattler für entspannte Kaffeepausen während intensiver Lernphasen.
- Thomas Mendelssohn für das Design des TRIADE-Logos und viel Hilfe in IT-Fragen, sowie Kristian Kordsmeyer für seine Kreativität.

Ich danke meinen Eltern und meiner Schwester Louisa für den immer dagewesenen Rückhalt und ganz besonders Laura für ihr Verständnis und ihre Unterstützung während der intensiven Lern- und Schreibphasen.